

JUN 10 2004

REPORT DOCUMENTATION PAGE			Form Approved OMB No. 0704-0188	
Public reporting burden for this collection of information is estimated to average 1 hour per response, including the time for reviewing instructions, searching existing data sources, gathering and maintaining the data needed, and completing and reviewing the collection of information. Send comments regarding this burden estimate or any other aspect of this collection of information, including suggestions for reducing this burden, to Washington Headquarters Services, Directorate for Information Operations and Reports, 1215 Jefferson Davis Highway, Suite 1204, Arlington, VA 22202-4302, and to the Office of Management and Budget, Paperwork Reduction Project (0704-0188), Washington, DC 20503.				
1. AGENCY USE ONLY (Leave blank)	2. REPORT DATE 9.Jun.04	3. REPORT TYPE AND DATES COVERED THESIS		
4. TITLE AND SUBTITLE SUCTION SIDE ROUGHNESS EFFECTS ON FILM COOLING HEAT TRANSFER ON A TURBINE VANE		5. FUNDING NUMBERS		
6. AUTHOR(S) 2D LT RUTLEDGE JAMES L				
7. PERFORMING ORGANIZATION NAME(S) AND ADDRESS(ES) UNIVERSITY OF TEXAS AT AUSTIN		8. PERFORMING ORGANIZATION REPORT NUMBER  CI04-361		
9. SPONSORING/MONITORING AGENCY NAME(S) AND ADDRESS(ES) THE DEPARTMENT OF THE AIR FORCE AFIT/CIA, BLDG 125 2950 P STREET WPAFB OH 45433		10. SPONSORING/MONITORING AGENCY REPORT NUMBER		
11. SUPPLEMENTARY NOTES				
12a. DISTRIBUTION AVAILABILITY STATEMENT Unlimited distribution In Accordance With AFI 35-205/AFIT Sup 1		12b. DISTRIBUTION CODE		
13. ABSTRACT (Maximum 200 words)				
<p style="font-size: 2em; margin: 0;">20040615 052</p> <p style="margin: 10px 0 0 0;"><b>DISTRIBUTION STATEMENT A</b> Approved for Public Release Distribution Unlimited</p>				
14. SUBJECT TERMS		15. NUMBER OF PAGES 217		
		16. PRICE CODE		
17. SECURITY CLASSIFICATION OF REPORT	18. SECURITY CLASSIFICATION OF THIS PAGE	19. SECURITY CLASSIFICATION OF ABSTRACT	20. LIMITATION OF ABSTRACT	

**The views expressed in this article are those of the author and do not reflect the official policy or position of the United States Air Force, Department of Defense, or the U.S. Government**

Copyright

by

James Lloyd Rutledge

2004

*The views expressed in this article are those of the author and do not reflect the official policy or position of the United States Air Force, Department of Defense, or the U.S. Government.*

**Suction Side Roughness Effects on Film Cooling Heat Transfer  
on a Turbine Vane**

**by**

**James Lloyd Rutledge, B.S.M.E.**

**Thesis**

Presented to the Faculty of the Graduate School of

The University of Texas at Austin

in Partial Fulfillment

of the Requirements

for the Degree of

**Master of Science in Engineering**

**The University of Texas at Austin**

**May 2004**



**Suction Side Roughness Effects on Film Cooling Heat Transfer  
on a Turbine Vane**

**Approved by  
Supervising Committee:**

---

**David G. Bogard**

---

**Michael E. Crawford**

Dedicated to my parents.

## **ACKNOWLEDGEMENTS**

A great number of people have made this thesis possible. I would like to thank Dr. David Bogard for constantly challenging me on nearly every aspect of this thesis. I am honored to have him as my thesis advisor. I also thank Dr. Michael Crawford for reviewing this thesis. Thanks go out to the US Air Force and the College of Engineering for their support of my graduate education. A number of graduate students including Jason Albert, Krishna Varadarajan, Elon Terrell, Brian Mouzon, Dan Warren, and Tricia Demling have made the Turbulence and Turbine Cooling Research Laboratory an exciting place to work. Special thanks go to my fellow Big Tunnel Guys, Sean Jenkins and David Robertson, with whom I have spent countless hours getting things working and running experiments. I would especially like to thank Colleen who was always there and my parents for their love and support.

## ABSTRACT

### **Suction Side Roughness Effects on Film Cooling Heat Transfer on a Turbine Vane**

by

James Lloyd Rutledge, M.S.E.

The University of Texas at Austin, 2004

Supervisor: David G. Bogard

An experimental study was conducted in a simulated three vane linear cascade to determine the effects of surface roughness and film cooling on the heat transfer coefficient distribution in the region downstream of the first row of suction side coolant holes. Suction side film cooling was operated in the range  $0 \leq M \leq 1.4$ . The showerhead was tested at  $M_{sh} = 1.6$ . In addition to the completely smooth condition, simulated airfoil roughness was used upstream of the coolant holes, downstream of the coolant holes, and both upstream and downstream of the coolant holes. Two levels of mainstream turbulence intensity were tested. The heat transfer measurements were conducted by application of a uniform heat flux in the region downstream of the coolant holes. The resulting surface temperature distributions were measured with infrared thermography. Because the upstream region was unheated, the influence of film cooling on the heat transfer coefficient was due only to hydrodynamic effects and not thermal effects. The coolant to mainstream density ratio of the majority of the experiments was unity; however, a single experiment was conducted at a density ratio of  $DR = 1.6$  to determine how the coolant to mainstream density ratio affects heat transfer. Net heat flux

reduction calculations were performed by combining the heat transfer coefficient measurements of the present study with adiabatic effectiveness measurements of a separate study. In order to gain insight into the hydrodynamics that affect the heat transfer, boundary layer measurements were conducted using hot-wire anemometry.

## TABLE OF CONTENTS

NOMENCLATURE.....	xi
CHAPTER ONE: INTRODUCTION .....	1
1.1 BACKGROUND OF GAS TURBINE FILM COOLING .....	1
1.2 FILM COOLING PARAMETERS.....	3
1.3 REVIEW OF LITERATURE .....	7
1.3.1 Surface Roughness Characterization.....	7
1.3.2 Roughness Modeling.....	9
1.3.3 Adiabatic Effectiveness.....	12
1.3.4 Heat Transfer Boundary Conditions .....	13
1.3.5 Heat Transfer Studies Without Film Cooling .....	14
1.3.5.1 Effects of a Step Change in Surface Roughness .....	15
1.3.5.2 Airfoil Heat Transfer.....	15
1.3.6 Heat Transfer Studies With Film Cooling .....	16
1.3.6.1 Flat Plate Film Cooling Heat Transfer.....	17
1.3.6.2 Effects of High Density Ratio .....	18
1.3.6.3 Film Cooled Airfoil Heat Transfer.....	20
1.3.7 Effects of Elevated Freestream Turbulence on $h$ and $\eta$ .....	21
1.3.8 Boundary Layer Measurements .....	23
1.4 OBJECTIVES OF THE CURRENT STUDY .....	24
CHAPTER TWO: EXPERIMENTAL FACILITY AND PROCEDURES .....	27
2.1 EXPERIMENTAL FACILITY.....	27
2.1.1 Test Section.....	27
2.1.2 Mainstream Flow Loop.....	28
2.1.3 Secondary Flow Loop .....	30
2.2 AIRFOIL GEOMETRY .....	32
2.3 SURFACE ROUGHNESS DESIGN .....	34

2.4 THE UNIFORM HEAT FLUX PLATE .....	37
2.5 HEAT TRANSFER TESTS .....	39
2.5.1 Heat Transfer Test Preparation .....	39
2.5.2 Heat Transfer Test Procedure.....	43
2.6 DATA REDUCTION METHODS .....	46
2.6.1 Conduction and Radiation Correction.....	47
2.6.1.1 Conduction Correction .....	48
2.6.1.2 Radiation Correction .....	51
2.6.2 High Density Ratio Tests .....	51
2.6.3 Net Heat Flux Reduction.....	57
2.7 BOUNDARY LAYER MEASUREMENTS .....	58
2.8 UNCERTAINTY ANALYSIS .....	61
2.8.1 IR Camera Resolution.....	61
2.8.2 Mainstream Velocity.....	62
2.8.3 Coolant Flow Rates .....	62
2.8.4 Surface Temperature .....	63
2.8.5 Heat Transfer Coefficient (Low Density Ratio).....	64
2.8.6 Heat Transfer Coefficient (High Density Ratio).....	65
2.8.7 Repeatability Within a Test.....	66
2.8.8 Repeatability Between Tests .....	66
2.8.9 Hot Wire Measurements .....	66
CHAPTER THREE: EXPERIMENTAL RESULTS .....	78
3.1 TEST CONDITIONS.....	78
3.2 BOUNDARY LAYER MEASUREMENTS .....	80
3.2.1 $s/C = 0.19$ Smooth Surface Check .....	81
3.2.2 $s/C = 0.19$ Tests With Low Turbulence Baseline .....	82
3.2.3 $s/C = 0.19$ Tests With High Turbulence Baseline.....	86
3.2.4 Measurements Downstream of the Row of Holes.....	88
3.2.5 Measurements at $s/C = 0.35$ .....	89

3.3 SMOOTH VANE HEAT TRANSFER RESULTS .....	91
3.3.1 Smooth Heat Transfer Without Showerhead Blowing .....	91
3.3.2 Smooth Heat Transfer With Showerhead Blowing.....	95
3.3.3 Trip Rod Effects on Heat Transfer.....	96
3.3.4 Surface Imperfections .....	96
3.4 HEAT TRANSFER RESULTS WITH DOWNSTREAM ROUGHNESS .....	97
3.4.1 Downstream Rough Heat Transfer Without Showerhead Blowing.....	97
3.4.2 Downstream Rough Heat Transfer With Showerhead Blowing.....	100
3.5 UPSTREAM ROUGHNESS EFFECTS ON HEAT TRANSFER....	102
3.5.1 Downstream Smooth.....	102
3.5.2 Downstream Rough.....	104
3.6 HIGH DENSITY RATIO EFFECTS ON HEAT TRANSFER.....	106
3.7 NET HEAT FLUX REDUCTION.....	108
CHAPTER FOUR: CONCLUSIONS.....	202
4.1 SUMMARY OF RESULTS.....	202
4.2 RECOMMENDATIONS FOR FUTURE WORK .....	204
4.2.1 The Effect of a Heated Starting Length .....	205
4.2.2 High Density Ratio Effects on a Smooth Surface .....	206
4.2.3 Different Roughness Characteristics .....	206
4.2.4 Heat Transfer Downstream of the Second Row of Coolant Holes .....	206
APPENDIX A: ROUGHNESS REYNOLDS NUMBER .....	208
APPENDIX B: BUS BAR SOLDERING.....	210
APPENDIX C: HEAT TRANSFER TEST PROCEDURE.....	212
REFERENCES.....	213
VITA .....	217



## NOMENCLATURE

### Symbols

$A$	area
$C$	true chord length
$c_f$	skin friction coefficient
$c_p$	specific heat
$DR$	density ratio, $\frac{\rho_c}{\rho_\infty}$
$D$	simulated roughness diameter
$d$	film cooling hole diameter
$f$	friction factor
$h$	heat transfer coefficient
$I$	momentum flux ratio, $\frac{\rho_c U_j^2}{\rho_\infty U_\infty^2}$ , or electrical current
$k$	height of simulated roughness elements or thermal conductivity
$k_s$	equivalent sand grain roughness
$L$	thickness of vane wall
$m$	order of curve fit
$M$	blowing ratio, $\frac{\rho_c U_j}{\rho_\infty U_\infty}$
$N$	number of measurements
$Pr$	Prandtl number, $\frac{\mu c_p}{k}$
$p$	hole-to-hole pitch, or pitch of roughness elements
$q''$	heat flux
$R$	resistance
$R_a$	centerline average roughness
$R_z$	average peak to valley roughness height
$Re$	Reynolds number based on chord, $\frac{UC}{\nu}$
$Re_k$	roughness Reynolds number, $\frac{u_\tau k_s}{\nu}$
$Re_x$	Reynolds number based on $x$ , $\frac{Ux}{\nu}$
$R_z$	peak-to-valley roughness height
$r$	recovery factor
$s$	streamwise surface distance from the stagnation line
$S$	reference area of the surface if no roughness were present

$S_f$	total projected frontal area of the roughness elements
$St$	Stanton number, $\frac{h}{\rho c_p U_{in}}$
$T$	temperature
$Tu$	turbulence intensity, $\frac{u_{rms}}{u_{mean}}$
$U$	flow velocity
$U_c$	overall internal heat transfer coefficient
$u$	local velocity
$u_\tau$	shear velocity
$V$	voltage
$VR$	velocity ratio, $\frac{U_j}{U_\infty}$
$x$	streamwise surface distance from the first row of suction side coolant holes or distance from leading edge of flat plate
$y$	spanwise distance along vane, measured from a suction side coolant hole
$z$	distance normal to the vane surface

#### Sigal and Danberg Parameters

$S$	reference area of the surface if no roughness were present
$S_f$	total projected frontal area of the roughness elements
$A_f$	projected frontal surface area of a roughness element
$A_s$	windward wetted surface area of a roughness element
$\Lambda_s$	roughness density parameter

#### Greek

$\beta$	injection angle from surface
$\Delta q_r$	net heat flux reduction
$\delta$	momentum boundary layer thickness
$\varepsilon$	emissivity
$\eta$	adiabatic effectiveness, $\frac{T_\infty - T_{aw}}{T_\infty - T_c}$
$\eta'$	conduction corrected nondimensional temperature with uniform heat flux
$\Lambda_f$	turbulence integral length scale
$\rho$	density

$\sigma$	Stefan-Boltzmann constant, $5.6697 \times 10^{-8}$ , or standard deviation
$\tau$	shear stress
$\phi$	overall effectiveness, $\frac{T_{\infty} - T_w}{T_{\infty} - T_c}$

#### Subscripts

<i>aw</i>	adiabatic wall
<i>c</i>	coolant
<i>e</i>	edge
<i>f</i>	with film cooling
<i>HF</i>	with heat flux
<i>HFP</i>	heat flux plate
<i>i</i>	inside
<i>in</i>	inlet
<i>j</i>	jet
<i>o</i>	without film cooling
<i>s</i>	surface
<i>sh</i>	showerhead
<i>w</i>	wall
$\infty$	mainstream
$-$	spanwise averaged

## **CHAPTER ONE**

### **INTRODUCTION**

#### **1.1 BACKGROUND OF GAS TURBINE FILM COOLING**

Charles Curtis received the first patent on a gas turbine engine in 1865. The first gas turbine engine was built by Aegidius Elling in 1903 and produced 11 horsepower. The usefulness of the gas turbine engine was not realized until the 1930s when the aviation industry began gas turbine engine research. Also at that time, people began to use the engine for stationary power generation.

Gas turbine engines are based on the Brayton cycle. Atmospheric air is compressed, at which point heat is added by combustion. The hot, high pressure gas expands through a turbine providing mechanical energy to power the compressor and other devices as required by the application. For example, the mechanical power from land based gas turbine engines drives generators to provide electricity. In the case of turbojet aircraft, a minimal amount of energy is extracted by the turbine, as the thrust from the expanding gases is desirable for propulsion. Turbofan engines use power from the turbine to operate the fan used for propulsion.

Although the efficiency of the ideal Brayton cycle is dictated only by pressure ratio across the compressor, increasing the firing temperature in the combustor directly increases the efficiency of a real engine with non-isentropic components. However, the primary incentive for high firing temperatures is the increase in specific power output.

Early gas turbine engines had relatively low combustion temperatures, but those temperatures were increased until the thermal capabilities of downstream turbine components limited the temperature to about 1200 K. By 1960, simple cooling schemes were being used in order to allow the turbine to

operate in an otherwise inhospitable environment. Modern thermal protection methods allow the turbine inlet temperature to reach 2000 K (Mattingly, 1996).

Since modern gas turbine engines rely on internal combustion, the fuel supply must be kept clean in order to minimize the erosion of hot gas path components. Aero engines are generally fed much cleaner (and more expensive) fuel than land based engines. Cooling the turbine components has the added advantage of helping them survive longer with lower quality fuel. The detrimental effects of the erosive, corrosive, high temperature, and high stress environment of the turbine stage may be mitigated with cooling. With current engine technology, one may double the life of a turbine blade by reducing its temperature by 30 K (Han et al. (2000)). Thus cooling schemes are requisite for engine reliability.

The simplest cooling schemes consist of running relatively cool air from the compressor through the turbine blades and vanes to provide internal convection cooling. In order to provide efficient cooling, some channel designs have become increasingly complex and are aptly called serpentine cooling schemes. Film cooling is the process of ejecting coolant through small holes on the surfaces of blades and vanes with the goal of having the coolant form a cool film on the surface to provide thermal protection. Advancements in materials have also helped protect turbine components. For example, thermal barrier coatings (TBC) are often applied to turbine components in order to insulate the metal from the hot gases.

An added complication for engine designers is that film cooling designs must take into consideration the effects of age on the parts to be protected. After just a few hundred hours of operation, a turbine component may show significant signs of wear. The surfaces will be roughened due to corrosion, erosion, fuel deposits, and thermal barrier coating spallation. Rough surfaces affect film cooling by changing the dynamics of the flow and the associated

heat transfer characteristics. If the film cooling schemes can no longer function as planned, the components will continue to deteriorate at an accelerating rate.

The focus of this research is on the film cooling aspects of first stage nozzle guide vanes. These first stage nozzle guide vanes sit motionless directly downstream of the combustors and are exposed to the harshest environment in the engine. The flow across a film cooled turbine vane is sufficiently complex that wind tunnel tests are required to accurately predict the performance of a new airfoil design or determine what is actually happening with a current design.

## 1.2 FILM COOLING PARAMETERS

Two important measures of an airfoil's thermal performance are the adiabatic effectiveness,  $\eta$ , and the heat transfer coefficient,  $h$ . The adiabatic effectiveness (Equation 1.2.1) is a nondimensionalized version of the adiabatic wall temperature,  $T_{aw}$ , which is the temperature distribution that would occur on the surface of the airfoil if there were no heat transfer into the vane. The following equation defines  $\eta$ :

$$\eta \equiv \frac{T_{\infty} - T_{aw}}{T_{\infty} - T_c} \quad (1.2.1)$$

where  $T_{\infty}$  is the mainstream temperature and  $T_c$  is the coolant temperature.

With a real, non-adiabatic vane, there is both convective heat transfer from the mainstream into the vane and conduction within the vane. The adiabatic effectiveness is important because it defines the driving potential for the convective heat transfer. The second measurement that must be made is of the heat transfer coefficient which describes the amount of convection heat

transfer into the vane for a given driving potential. The heat transfer coefficient is related to the convective heat transfer through the following equation:

$$h \equiv \frac{q''}{T_w - T_{aw}} \quad (1.2.2)$$

Indeed, the definition of  $h$  implies that the surface would assume the adiabatic wall temperature in the absence of heat transfer. The adiabatic wall temperature is given by Mills (1999) as follows:

$$T_{aw} = T_{\infty} + r \frac{u_{\infty}^2}{2c_p} \quad (1.2.3)$$

where  $T_{\infty}$  is the freestream temperature,  $u_{\infty}$  is the freestream velocity, and  $r$  is the recovery factor which is  $r = Pr^{1/3}$  for a turbulent boundary layer. The second term in Equation 1.2.3 accounts for the viscous dissipation. Viscous dissipation is negligible at the low speeds used in the facility of this study. In the absence of film cooling (for which  $\eta = 0$ ) and neglecting viscous dissipation, the adiabatic wall temperature would be the mainstream temperature. With film cooling, an adiabatic vane would assume a temperature distribution that corresponds to the temperature of the coolant at the wall. In the film cooling case,  $T_{aw}$  is the coolant temperature at the wall.

The presence of film cooling holes on the vane surface and the jets themselves potentially alter the heat transfer coefficient. If the adiabatic wall temperatures are unchanged, an airfoil with a higher heat transfer coefficient will experience a greater heat load, thus reducing its life. However, the lower adiabatic wall temperature due to the cool jets generally more than offsets the

negative effects due to an increase in heat transfer coefficient. Unfortunately, this is not always the case. Knowledge of both the adiabatic effectiveness and heat transfer coefficients is needed to predict the net benefit of film cooling.

Another parameter is the overall effectiveness,  $\phi$ . The overall film cooling effectiveness is the actual temperature distribution on a real, non-adiabatic surface. The definition of  $\phi$  is as follows:

$$\phi \equiv \frac{T_{\infty} - T_w}{T_{\infty} - T_c} \quad (1.2.4)$$

A realistic value in modern engines is  $\phi = 0.6$ .

Considering the overall film cooling effectiveness to be an engine design parameter dictated by such things as material selection and desired engine life, the heat load on a vane can be calculated if both the adiabatic effectiveness and the heat transfer coefficient are known. Engine designers are often interested in the amount of heat flux reduction provided by the film cooling schemes relative to no film cooling. The net heat flux reduction,  $\Delta q_r$ , is defined as:

$$\Delta q_r \equiv 1 - \frac{q_f''}{q_0''} = 1 - \frac{h_f(T_{aw} - T_w)}{h_0(T_{\infty} - T_w)} \quad (1.2.5)$$

A negative net heat flux reduction indicates that the heat flux is increased by film cooling and is clearly undesirable. Some algebraic manipulation will show:

$$\Delta q_r = 1 - \frac{h_f}{h_0} \left(1 - \frac{\eta}{\phi}\right) \quad (1.2.6)$$



Engine designers must pay close attention to the amount of coolant that is being used. Since the coolant is extracted from the compressor stage, but bypasses the combustion stage, increasing the amount of coolant decreases the engine efficiency. Efficiency is further reduced by the irreversible mixing that occurs between the coolant and the mainstream flow. Coolant flow rates are normalized against the mainstream flow rate in several ways. The mass flux ratio, or blowing ratio, is the ratio of the coolant to mainstream mass fluxes defined as:

$$M \equiv \frac{\rho_c U_j}{\rho_\infty U_\infty} \quad (1.2.7)$$

where  $U_\infty$  is the mainstream velocity at the hole and  $U_j$  is the coolant velocity at the hole exit. In the case of showerhead cooling (cooling at the stagnation point), we replace  $U_\infty$  with  $U_{approach}$ , the approach velocity. The blowing ratio is the most common way of expressing blowing rates. Another widely used method of characterizing coolant flow rate is through the momentum flux ratio defined as:

$$I \equiv \frac{\rho_c U_j^2}{\rho_\infty U_\infty^2} \quad (1.2.8)$$

Ethridge et al. (2001) suggested that  $I$  scaled adiabatic effectiveness well on the suction side of a vane for  $I > 0.4$ . At lower blowing rates,  $M$  was preferred. The simplest method of characterizing blowing rates is the velocity ratio. The velocity ratio ( $VR$ ) is defined as:

$$VR \equiv \frac{U_j}{U_\infty} \quad (1.2.9)$$

Ammari et al. (1990) suggested using  $VR$  for characterizing the heat transfer behavior of inclined jets at nonrealistic density ratios. This work is discussed in greater detail in Section 1.3.6.1.

### 1.3 REVIEW OF LITERATURE

A great deal of gas turbine engine research focuses on improving the thermal performance of hot gas path components through improved film cooling schemes. This section presents a review of modern research that is relevant to this study. Older studies that provide a historical basis for some of the techniques used in this study are also presented.

#### 1.3.1 Surface Roughness Characterization

The first significant research relating surface roughness to fluid flow was performed by Nikuradse (1933). Nikuradse coated the inner surfaces of pipes with closely packed sand grains of recorded mean diameter and conducted skin friction measurements in the pipe. From his data, three different flow regimes were characterized as follows:

Hydrodynamically Smooth:  $0 < Re_k \leq 5$  (1.3.1.1)

Transitionally Rough:  $5 < Re_k \leq 70$  (1.3.1.2)

Fully Rough:  $70 < Re_k$  (1.3.1.3)

The roughness Reynolds number can be written:

$$Re_k = \frac{u_\tau k_s}{\nu} \quad (1.3.1.4)$$

where

$$u_\tau = \sqrt{\frac{\tau_w}{\rho}} \quad (1.3.1.5)$$

The term  $u_\tau$  is known as the shear velocity.

In 1936, Schlichting expanded on Nikuradse's work by measuring the skin friction on surfaces with surface features of various sizes, shapes, and spacing. Schlichting proposed the use of the equivalent sand grain roughness,  $k_s$ , which is the size of sand grain in Nikuradse's experiment that would be needed in order to obtain the same skin friction characteristics of the particular surface being investigated.

With very little analytical work concerning roughness available to Schlichting at the time of his experiments, he made some assumptions in his work that Coleman et al. (1984) suggested were inaccurate. Coleman et al. (1984) replaced those questionable assumptions with more accurate approximations using recent analytical and computational advances and re-evaluated the original data using the superior techniques. Schlichting's original estimates of skin friction coefficients and equivalent sand grain roughness were found to both be higher (0.5 to 73 percent and 26 to 555 percent, respectively) than the corrected values.

Armed with the re-evaluated data from Schlichting, Sigal and Danberg (1990) proposed a correlation that predicts the equivalent sand grain roughness

of a surface with a regular roughness array. The correlation involves the use of a roughness density parameter defined as

$$\Lambda_s = \frac{S}{S_f} \left( \frac{A_f}{A_s} \right)^{-1.6} \quad (1.3.1.6)$$

where  $S$  is the reference area of the surface if no roughness were present,  $S_f$  is the total projected frontal area of the roughness elements,  $A_f$  is the projected frontal surface area of a roughness element, and  $A_s$  is the windward wetted surface area of a roughness element. The roughness density parameter and the equivalent sand grain roughness for three dimensional roughness elements were plotted and followed the relation:

$$\log\left(\frac{k_s}{k}\right) = -1.31 \log(\Lambda_s) + 2.15 \quad (1.3.1.7)$$

where  $k$  is the roughness height. Equation 1.3.1.7 is applicable for  $20 < \Lambda_s < 100$ .

### 1.3.2 Roughness Modeling

Bogard et al. (1998) studied first-stage vane samples taken from two military aero-engines that had been operated in different locations in excess of 500 hours. The surface roughness was analyzed extensively. Among the notable information that can be concluded from their figures was that foreign material deposits inside film cooling holes and that regions in the downstream paths of film cooling holes exhibit different roughness characteristics than the

surrounding area. Data from profilometer traces of the pressure sides were used to design a surface roughness that could be used for laboratory simulation. The pressure sides were used because they experience a greater level of foreign material deposition than the suction side. The centerline average roughness heights and the average peak roughness values of the two vanes differed by a factor of two; however, both vanes had the same roughness shape/density parameter (from the Sigal-Danberg correlation). Simulated roughness using protruding cones was created that matched the mentioned parameters. The authors compared the convective heat transfer coefficients of flat plates that incorporated the simulated roughness. Even though the values of  $R_a$  and  $k$  each differed by a factor of two, the heat transfer coefficients were found to be the essentially the same for the two types of simulated roughness. The authors also demonstrated that two surfaces can have matching  $R_a$  and  $k$  values, but with roughness Reynolds numbers that differ by an order of magnitude. Consequently, the authors suggest that the traditionally used roughness parameters ( $R_a$  and  $k$ ) are inadequate for roughness characterization. Although not explicitly mentioned by the authors, the data suggests that  $\Lambda_s$  is more appropriate for characterizing the convective heat transfer properties of roughness.

Bons et al. (2001) studied the roughness characteristics of nearly 100 worn turbine components from four land-based turbine manufacturers. The component surfaces had undergone some combination of pitting, erosion, spallation, and foreign material deposition. The authors created 3 dimensional surface maps of the surfaces to facilitate the analysis. Pitting and erosion was generally found on the suction surface trailing edge with pits sometimes over 50  $\mu\text{m}$  deep. The authors found that thermal barrier coating spallation was the most significant form of roughness, with height variations of 100 to 400  $\mu\text{m}$ .

Spallation was primarily found on the suction surface leading edge, pressure surface trailing edge, and in the vicinity of film cooling holes. Uncoated metal experiences a monotonically increasing surface roughness over the life of the metal; however, coated metal experiences a peak in roughness when spallation craters are large. As the coating continues to wear off and the bare metal becomes increasingly exposed, the roughness decreases. Once the bare metal is completely exposed, roughness then monotonically increases. A particularly interesting find was the presence of periodic furrows downstream of film cooling holes. The depth of the furrows ranged from 50  $\mu\text{m}$  to 500  $\mu\text{m}$ . These furrows sometimes exhibited elevated surface roughness.

Bons (2002) studied the skin friction coefficient and Stanton number augmentation from real turbine roughness and compared it to simulated roughness. Concerning skin friction, the author found that the relation proposed by Sigal and Danberg between the roughness shape/density parameter,  $\Lambda_s$ , and  $k_s/k$  fits “real” roughness data well for  $\Lambda_s < 100$ . This finding supports the use of regular roughness arrays designed to match the equivalent sand grain roughness of “real” roughness. However, the author also suggested that an ordered roughness array designed to simulate real roughness may either model skin friction behavior or heat transfer behavior, but not both. Standard correlations were found to over predict the Stanton number for the real rough surfaces by about 10%. Bons hypothesized that this phenomenon may be a result of ordered roughness arrays causing vertical secondary flows that enhance heat transfer while having little effect on the skin friction. Random roughness may have the tendency of breaking up these secondary flows.

### 1.3.3 Adiabatic Effectiveness

Schmidt et al. (1996) measured adiabatic effectiveness levels on a film cooled flat plate with two levels of surface roughness in addition to an aerodynamically smooth surface. In all cases, the region upstream of the holes was smooth and adiabatic. The two rough surfaces had roughness Reynolds numbers of  $40 < Re_k < 60$  and  $90 < Re_k < 120$ , thus one was transitionally rough and the other was fully rough. Roughness was simulated with protruding cones. The film cooling holes were aligned in the streamwise direction and had injection angles of  $\beta = 30^\circ$ . Adiabatic effectiveness was generally slightly reduced by both levels of roughness. However, for cases of very high momentum flux ratios (those that caused the jets to detach from the surface), the roughness was found to increase adiabatic effectiveness.

Snook (2002) studied roughness effects on adiabatic effectiveness downstream of the first row of suction side film cooling holes on a simulated vane. A conical roughness array was used upstream and downstream of the first row of suction side coolant holes. In addition to the fully rough condition, roughness was also used only upstream of the coolant holes and only downstream of the coolant holes. At reasonable blowing rates, roughness was found to decrease the adiabatic effectiveness for both high and low turbulence and with and without showerhead cooling. Roughness upstream of the row of holes was found to cause a greater deterioration in adiabatic effectiveness than the downstream roughness, probably due to its effects on the approach boundary layer. Upstream roughness caused a decrease in area averaged adiabatic effectiveness of approximately 33%. Downstream roughness decreased the adiabatic effectiveness by 21% at the optimum blowing ratio. Combined upstream and downstream roughness caused a decrease in adiabatic effectiveness of 29% relative to the smooth condition. At blowing rates that caused separation of the coolant flow, downstream roughness was found to

slightly increase adiabatic effectiveness, presumably because the increased mixing in the rough wall boundary layer tended to bring separated coolant back to the surface.

Robertson (2004) revisited the work of Snook, filling some gaps in Snook's data. Using the same facility as Snook, Robertson performed a comprehensive study of combined upstream / downstream roughness effects and showerhead effects. Robertson also improved upon some of Snook's experimental methods, yielding data with a greater degree of accuracy. Robertson's data was used in the preparation of the net heat flux reduction data presented in this thesis.

#### **1.3.4 Heat Transfer Boundary Conditions**

Two boundary conditions on the wall are frequently used for heat transfer experiments on both flat plates and simulated airfoils—the isothermal surface and the constant heat flux surface. Due to the high thermal conductivity of actual turbine airfoils, the proper boundary condition, at least in a small region, would best be approximated by the isothermal boundary condition. In the laboratory, the isothermal condition may be simulated directly by preconditioning the test surface to a uniform temperature before insertion into a mainstream of a different temperature. The heat flux is then measured with heat flux gauges before significant temperature nonuniformities occur on the surface. An indirect way of measuring the heat transfer coefficient on an isothermal surface is the use of the mass transfer analogy. Some mass transfer measurement techniques include the naphthalene sublimation technique, swollen polymer technique, and pressure sensitive paint techniques. With the naphthalene sublimation technique, the surface is coated with a layer of naphthalene and exposed to flow. The uniform concentration of naphthalene on the surface represents a uniform temperature distribution. The mass transfer is



measured by measuring the mass of naphthalene that was sublimed during the test. Unfortunately, mass transfer techniques are difficult to perform with rough surfaces because the roughness characteristics necessarily change over the course of the test. Furthermore, the surface must be analyzed and reconditioned after each experimental condition. Uniform heat flux tests may be performed by applying electrical heating to the test surface and are more compatible with rough surfaces. Whitaker (1972) found that the following correlation describes isothermal flat plate heat transfer across a turbulent boundary layer:

$$Nu_x = 0.029 Re_x^{0.8} Pr^{0.43} \quad (1.3.4.1)$$

valid for  $0.7 < Pr < 400$  and  $5 \times 10^5 < Re_x < 3 \times 10^7$

If instead the flat plate has a uniform heat flux, Kays and Crawford (1993) recommend the following correlation:

$$Nu_x = 0.030 Re_x^{0.8} Pr^{0.43} \quad (1.3.4.2)$$

valid for  $0.5 < Pr < 400$  and  $5 \times 10^5 < Re_x < 5 \times 10^6$

These two correlations differ by only 4%, although larger differences are found for laminar boundary layers. Thus for determining the heat transfer characteristics of a nearly isothermal object (such as a turbine vane), a uniform heat flux may be used for the measurements on a model, provided that the boundary layer is turbulent.

### 1.3.5 Heat Transfer Studies Without Film Cooling

This section presents some heat transfer studies without film cooling that are relevant to the study of heat transfer on rough turbine surfaces.

#### ***1.3.5.1 Effects of a Step Change in Surface Roughness***

Heat transfer measurements may be made directly on actual turbine airfoils through the use of heat flux gauges. Taylor et al. (1991) questioned whether heat transfer measurements from smooth heat flux gauges accurately indicate the heat transfer in the surrounding area where the airfoil surface is rough. To help answer that question, the authors studied heat transfer in the turbulent boundary layer on a flat plate with a step decrease in surface roughness. The first 0.9 m of the test surface was covered with a staggered array of hemispheres, downstream of which was nominally smooth. The authors found that the heat transfer coefficient dropped dramatically (~50%) immediately downstream of the roughness. In fact, for fully rough flows the heat transfer coefficient dropped below the value for the smooth upstream condition before eventually equilibrating to the smooth wall value.

#### ***1.3.5.2 Airfoil Heat Transfer***

Blair (1994) studied heat transfer on rotors and rotor passages using a rotating blade cascade. One level of roughness (max to min roughness height of 0.41% of the chord length) in addition to “near smooth” (max to min roughness height of 0.032% of the chord length) and “smooth” (max to min roughness height of 0.0047% of the chord length) surface finishes were tested. The Reynolds number was varied but no film cooling was used. He found that roughness increased the heat transfer coefficient everywhere, with a maximum increase of about 100% in the forechord region of the suction surface.

Abuaf et al. (1998) performed a study on the heat transfer effects of surface roughness on a linear vane cascade, focusing on the as-manufactured surface roughness. Three levels of roughness were studied on a five vane cascade with axial chord length of 4.8 cm. The roughest airfoil ( $R_a = 2.33 \mu\text{m}$ ) was vapor grit blasted and coated with an oxidation resistant coating called

Codep. The next airfoil ( $R_a = 1.03 \mu\text{m}$ ) was vapor grit blasted, tumbled, and coated with chemical vapor deposited (CVD) aluminide. The smoothest airfoil ( $R_a = 0.81 \mu\text{m}$ ) was vapor grit blasted, tumbled, polished, coated with CVD aluminide, and polished again. The effects of film cooling were not studied. This study found that the heat transfer on the suction side region was the most sensitive region to roughness, particularly at high exit Reynolds numbers. The additional processing required to go from  $R_a = 2.33 \mu\text{m}$  to  $R_a = 1.03 \mu\text{m}$  resulted in a maximum decrease in the heat transfer coefficient of about 13%. However, a further reduction in surface roughness to  $R_a = 0.81 \mu\text{m}$  resulted in very little improvement in heat transfer.

Boyle et al. (2001) used an infrared camera to obtain high spatial resolution heat transfer coefficient data on the suction side and forechord pressure side of a vane. The vane was made of insulating foam in the area of interest and copper bus bars were bonded to the foam. An electrically powered heat flux surface was created by spraying electrically conductive silver paint on the surface thereby completing a circuit between the two bus bars. Because the foam was rough, the painted surface was also rough. Tests were performed at various Mach and Reynolds numbers and at two turbulence intensities. At the higher turbulence intensity and  $Re > 61,000$  the heat transfer coefficient at the rear portion of the suction side was approximately double the expected smooth wall value. Contour plots of the Nusselt number distribution show considerable spanwise nonuniformity. The authors suggest that some of the nonuniformity was due to nonuniformities in the surface roughness.

### **1.3.6 Heat Transfer Studies With Film Cooling**

A great deal of research effort has attempted to determine heat transfer coefficient characteristics that are applicable to a film cooled turbine environment. A few of the relevant studies are presented in this section.

### ***1.3.6.1 Flat Plate Film Cooling Heat Transfer***

In addition to adiabatic effectiveness, Schmidt et al. (1996) also measured heat transfer coefficients at  $DR = 1.0$ . Heat transfer coefficients were measured by application of a uniform heat flux in the region downstream of the coolant holes. A trip rod was used to induce a turbulent boundary layer upstream of the holes. The data are representative of flat plate film cooling heat transfer without a heated starting length. Roughness was found to increase heat transfer coefficients by about 50%. Film cooling had little influence on the heat transfer coefficient especially for  $x/d > 10$ . In the companion study, Schmidt and Bogard (1996) reported centerline heat transfer coefficient ratios ( $h_f/h_o$ ) for  $I = 0.3$  and  $I = 1.1$  and all turbulence and roughness conditions. Turbulence intensity had no effect on  $h_f/h_o$ , although blowing had a small effect in the vicinity of the holes. Blowing at  $I = 1.1$  increased the heat transfer coefficient by approximately 15% near the hole, whereas blowing at  $I = 0.3$  decreased the heat transfer coefficient by approximately 10%. These conclusions were valid for all tested roughness and turbulence conditions.

Sen et al. (1996) studied the effects of compound angle injection on the heat transfer coefficient using the facility and techniques of Schmidt et al. (1996). Four hole geometries were studied—streamwise directed cylindrical holes, cylindrical holes with  $60^\circ$  compound angle, streamwise directed forward diffused holes, and forward diffused holes with  $60^\circ$  compound angle. All holes were inclined  $35^\circ$  from the surface. The forward diffused holes were expanded  $15^\circ$  at the hole exit. As with Schmidt et al. (1996), little lateral variation in the heat transfer coefficient was detected with the streamwise directed holes. However, the compound angle holes were shown to strongly influence the heat transfer coefficient. At  $x/d = 3$  and  $I = 1.0$ , the compound angle cylindrical holes caused a local increase in  $h$  of nearly 30%, whereas the streamwise directed cylindrical holes caused a maximum local increase in  $h$  of less than

10%. The forward diffused holes with compound angle showed local increases in  $h$  of 70% at  $x/d = 3$ . Thus it can be concluded that hole geometry is critical to heat transfer behavior, with compound angle holes causing greater  $h$  augmentation than streamwise directed holes.

#### ***1.3.6.2 Effects of High Density Ratio***

In an actual engine, the coolant density can be approximately double the density of the mainstream flow. Robertson (2004) used a large temperature difference between the coolant and the mainstream in order to obtain a density ratio of 1.6 for his adiabatic effectiveness tests. High density ratio film cooling tests may also be performed using an injectant that is a foreign gas of a density higher than that of the mainstream. Teekaram et al. (1988) verified that both techniques yield equivalent results. However, both of these techniques cause additional difficulty for the heat transfer experimentalist. By forcing the adiabatic wall temperature to be the mainstream temperature (and uniform), the experimentalist avoids the uncertainty involved in determining a nonuniform adiabatic wall temperature distribution. Another problem with temperature induced high density ratio tests is that metal heat flux plates exhibit undesirable thermal expansion / contraction effects when in the presence of strong temperature gradients. For these reasons, the coolant temperature is usually held at the mainstream temperature. So that leaves the heavy foreign gas option to obtain high density ratios. With foreign gas injectants, tests are limited in duration in a recirculating wind tunnel due to the gradual contamination of mainstream flow.

The effect of density ratio on the heat transfer coefficient on a film cooled flat plate (with a turbulent boundary layer) was studied by Ammari et al. (1990). A mass transfer technique was used and a "heated" starting length was utilized. Density ratios of 1.0, 1.38, and 1.52 were obtained by the use of air,

argon, and carbon dioxide respectively as the coolant. Blowing ratios of  $M = 0.5, 1.0, 1.5,$  and  $2.0$  were used. Two types of film cooling holes were used—normal injection holes and holes inclined  $35^\circ$  from the surface (with no compound angle). Heat transfer measurements were conducted using the swollen polymer mass transfer analog technique. The data of Ammari et al. not only provide a means for evaluating the effects of density ratio, but are also representative of flat plate film cooling heat transfer with a heated starting length. Film cooling always had the tendency of increasing the heat transfer coefficient. The authors found that the blowing ratio,  $M$ , correlated the data well when the coolant was injected normal to the plate. At  $M = 2.0$ , normal injection gave rise to 100% increases in the local heat transfer coefficient at  $2 d$  downstream of injection. At  $M = 0.5$ , the increase in  $h$  was 70% at the same location. However, at  $10 d$  downstream, the increases in  $h$  were 25% and 10% for  $M = 2.0$  and  $0.5$ , respectively. The heat transfer coefficient was somewhat dependent on the density ratio at fixed blowing ratio when the coolant was injected through the row of inclined holes. At a blowing ratio of  $M = 1.5$ , differences in  $h_f$  were approximately 10%, with the lower density coolant giving rise to the higher heat transfer coefficient. Although spatial data from the inclined jets at lower blowing ratios was not presented, it can be deduced from spanwise averaged data that the difference in  $h_f$  due to density ratio effects at a more typical blowing ratio of  $M = 0.5$  was considerably less than 10%. Coolant injection from angled holes caused increases as high as 60% in the local heat transfer coefficient at  $M = 1.5$  with the lower density coolant. However, at  $10 d$  downstream, the increase in  $h$  was approximately 20%. At  $M = 0.5$ , the increase in  $\bar{h}$  was negligible at  $x/d = 10$  with both density ratios. The authors indicate that use of the velocity ratio collapsed the data in the case of angled injection better than the blowing ratio or the momentum flux ratio. Also noted was the

observation that a row of coolant holes produced a greater spanwise averaged heat transfer coefficient than a single hole. This was because mixing between neighboring jets caused localized areas of high heat transfer coefficient between the jets. This phenomenon is unfortunate because these regions of high heat transfer coefficient augmentation receive little or no benefit of film cooling.

#### ***1.3.6.3 Film Cooled Airfoil Heat Transfer***

Studies of heat transfer on film cooled airfoils are very limited and have all been performed at the same facility. Two of these studies are presented in this section.

Guo et al. (2000) performed a limited study of the effects of surface roughness on a fully film cooled nozzle guide vane with respect to adiabatic effectiveness and heat transfer. The authors used a thermochromic liquid crystal coating with a mean roughness height of 25  $\mu\text{m}$  to simulate surface roughness. The vane model had a chord length of 0.0664 m, which was 1.4 times engine scale. The roughness was selected to simulate the roughness of a thermal barrier coating. An equivalent sand grain roughness was not measured, thus an appropriately constructed roughness Reynolds number was not reported. Thin film gauges and direct heat flux gauges were used to make measurements on the nominally smooth surfaces. Both the heat transfer coefficient and adiabatic effectiveness were measured using transient techniques. Tests were done on two nozzle guide vane geometries—one with cylindrical cooling holes and the other with fan shaped cooling holes. The low level of roughness the authors used did not have a significant effect on the adiabatic effectiveness. Heat transfer data is sparse at the leading edge and forechord regions, but the authors did show that the roughness increased the heat transfer coefficient by nearly a factor of two with the cylindrical holes at downstream regions of the vane. Roughness increased the heat transfer coefficient by a lesser degree for

the case of fan shaped cooling holes, purportedly due to a lower shear velocity resulting from the diffusing nature of the fan shaped holes.

Guo et al. (1998) studied the effects of film cooling using the same geometry as Guo et al. (2000), but without the roughness. Only one level of film cooling was studied, that which gave a coolant to mainstream pressure ratio of 1.02. The ejection of coolant into the turbulent boundary layer on the pressure side was shown to provide local increases in the heat transfer coefficient, especially in the vicinity directly downstream of the coolant holes. At some pressure side rows, the increase was as high as 100% with the cylindrical holes. On the suction side, local increases in  $h$  were also observed directly downstream of cylindrical holes, but by approximately 25%. At  $s/C \approx 0.5$  (over 0.1  $C$  downstream of the last row of coolant holes on the suction side),  $h_f$  dropped below  $h_o$  by approximately 25%. The authors hypothesized that this unusual find could have been caused by a thickening of the boundary layer due to the jets on the suction side. Similar results were found for the fan-shaped coolant holes with the exception of smaller  $h$  augmentations ( $\approx 50\%$  instead of 100%) on the pressure side.

### **1.3.7 Effects of Elevated Freestream Turbulence on $h$ and $\eta$**

The flow entering the turbine stage is turbulent. Researchers have placed the turbulence intensity at between 7% and 30% (see Zimmerman (1979), Goldstein (1983), and Kuotmos and McGuirk (1989)) and is dependent on the geometry of the combustor and the turbine inlet. Ames (1997) reported that the turbulence length scale was typically 1/3 to 1/2 of the inlet passage. This section discusses some of the research involving how turbulence characteristics influence heat transfer and film cooling.

In a companion study to Schmidt et al. (1996) (see Section 1.3.6.1), Schmidt and Bogard (1996) studied how three levels of turbulence ( $Tu = 0.3\%$ ,



10%, and 17%) affected film cooling adiabatic effectiveness and heat transfer. Additionally, the lower level of roughness ( $40 < Re_k < 60$ ) was tested with the variety of turbulence levels. At low momentum flux ratios ( $I < 1$ ), the increase from  $Tu = 0.3\%$  to  $Tu = 10\%$  caused adiabatic effectiveness to decrease by more than 50% near the hole, and even greater farther downstream. A further increase in turbulence to  $Tu = 17\%$  caused a much smaller decrease in adiabatic effectiveness. A reverse trend was observed for higher momentum flux ratios ( $I > 1$ ), for which high turbulence levels increased adiabatic effectiveness. Presumably, the additional turbulent mixing allowed some coolant from the detached jets to return to the surface. All surface conditions (rough / smooth, film cooled / uncooled) experienced increases in the heat transfer coefficient from 15% to 30% due to high freestream turbulence. Combined roughness and high turbulence gave increases in heat transfer of up to 100%.

Ames (1997) performed heat transfer measurements on a subsonic vane cascade. The author used turbulence intensities of  $Tu = 8\%$  and  $12\%$ . The integral length scale to cascade pitch ratio was varied between 0.10 and 0.18. Increased turbulence intensity was found to increase the heat transfer coefficient, particularly where the boundary layer was laminar under low freestream turbulence conditions. Increasing the freestream turbulence intensity moved the location of transition upstream on the suction side, but it also increased the heat transfer coefficient by approximately 25% in the region between the stagnation line and transition. Downstream of transition, the heat transfer coefficient was insensitive to the turbulence intensity.

Similarly, Radomsky (2000) found that elevating the freestream turbulence increases the heat transfer over the entire vane surface. Radomsky used the same vane geometry as was used in the present study. The main effect on the suction side was to move the onset of transition upstream. For the lowest

tested turbulence intensity of  $Tu = 0.6\%$ , transition started near  $s/C = 1.0$ . At  $Tu = 19.5\%$ , transition started near  $s/C = 0.5$ .

Snook (2002) conducted adiabatic effectiveness tests as described in Section 1.3.3 at turbulence intensities of 0.5% and 20%. For all blowing rates, the adiabatic effectiveness was always lower for the high turbulence condition. The primary effect of turbulence was to cause a higher degradation rate of spanwise averaged adiabatic effectiveness with distance downstream. The increased mixing from the high turbulence causes the coolant to dissipate away from the surface.

### 1.3.8 Boundary Layer Measurements

Radomsky and Thole (2002) used a two-component laser Doppler velocimeter (LDV) to perform boundary layer measurements on a large-scale test vane. Tests were performed at  $Tu = 0.6\%$  and  $Tu = 19.5\%$ . Measurements were made at four locations on the pressure side and five locations on the suction side. The thinnest boundary layer was found at  $s/C = 0.21$  (the forechord region of the suction side) where  $\delta/C \approx 0.0010$  for both high and low turbulence conditions. The boundary layer thickness increased downstream of that location, particularly in the region of adverse pressure gradient. The high turbulence test condition caused the boundary layer thickness to grow much greater than the low turbulence condition. At low turbulence, the boundary layer thickness was approximately constant on the pressure side as a result of the nearly constant favorable pressure gradient. However, high freestream turbulence caused the boundary layer thickness to grow on the pressure side. Transition began as early as  $s/C = 0.5$  or as late as  $s/C = 1.0$ , depending on the freestream turbulence. Even at  $s/C = 0.21$ , where the boundary layer always exhibited laminar behavior, the turbulence intensity reached 14% (based on  $U_e$ )

within the boundary layer for the low and high freestream turbulence conditions, respectively.

#### **1.4 OBJECTIVES OF THE CURRENT STUDY**

There were two primary objectives of this research. The first objective was to determine how roughness, showerhead film cooling, and turbulence intensity affect heat transfer on the suction side of a vane. Secondly, the effects of suction side film cooling from streamwise directed holes on suction side heat transfer were studied. Additionally, a limited study of the effects of density ratio on film cooling heat transfer was performed. To date, the data for a film cooled rough vane heat transfer coefficients is lacking. Guo et al. (2000) did consider film cooling and roughness, but the low resolution of the data does not allow the influence of the jets to be understood. Furthermore, data was not presented for an uncooled vane and the heated starting length utilized in that study masked the hydrodynamic effects of the jets. Boyle (2001) obtained high resolution  $h$  distributions on a rough airfoil, but without film cooling or a smooth baseline condition for comparison purposes. The data of Schmidt and Bogard (1996) demonstrated that inclined cylindrical holes without compound angle caused at most a 15% effect on the local heat transfer coefficient on a flat plate without a heated starting length. Without knowing how curvature and pressure gradient affect heat transfer with film cooling, it is difficult to predict whether a similar effect on  $h$  would be observed on the suction side of a vane. To date, there is also an absence of literature regarding showerhead effects on suction side heat transfer.

Several researchers have shown that increasing the freestream turbulence intensity increases the heat transfer coefficient. However, it has also been shown that freestream turbulence affects the behavior of film cooling jets.

Because this study involved determining how film cooling jets affect  $h$ , turbulence effects were necessarily studied.

In this research, high spatial resolution infrared thermography techniques were employed to obtain heat transfer coefficient distributions between the first and second row of holes on the suction side of a 9 times scale model of a first stage nozzle guide vane. A comprehensive understanding of the influence of roughness was obtained by making measurements with upstream roughness only, downstream roughness only, and both upstream and downstream roughness. The research also considered the individual and combined effects of mainstream turbulence, showerhead cooling, and suction side cooling. The region that was studied on the suction side of the vane is critical as previous researchers (including Abuaf et al. (1998) and Blair (1994)) have found that it experiences relatively high heat transfer coefficients compared to the rest of the vane along with the highest sensitivity to roughness. In addition to the aforementioned parameters, a coolant blowing ratio ranging from  $M = 0$  to 1.4 was tested.

A number of film cooling heat transfer studies have been performed with heated starting lengths (including Ammari et al. (1990), Guo et al. (1998), and Guo et al. (2000)). In these experiments, the coolant was the same temperature as the mainstream flow. The coolant exited the film cooling holes, displacing the thermal boundary layer, and initiating a new thermal boundary layer. In regions immediately downstream of the holes where the film cooling adiabatic effectiveness was extremely high, the heat flux surfaces assume temperatures nearly the same as the mainstream temperature. In those locations, the film cooling was reported to cause an increase in the heat transfer coefficient. The nature of the increases in  $h$  could have been caused by thermal and / or hydrodynamic effects, but it is impossible to determine the relative contributions. The strong effect of a heated starting length on  $h_f/h_o$  is evident by

comparing the data of the relatively large values of  $h_f/h_o$  measured by Ammari et al. (1990) to the smaller values of Schmidt and Bogard (1996).

There is no heat transfer coefficient data in the literature that was acquired on simulated airfoils with film cooling and without a heated starting length. In order to obtain heat transfer coefficient data influenced only by the hydrodynamic effects of film cooling, the present study did not utilize a heated starting length. Instead, heat flux was only applied downstream of the first row of suction side coolant holes.

To complement the heat transfer data, a number of velocity and turbulence profiles were measured in the boundary layer in the region of interest. This boundary layer data provides fundamental insight into the mechanisms that affect the heat transfer.

Knowledge of the heat transfer coefficients and the adiabatic effectiveness at identical conditions allow one to calculate the net heat flux reduction due to film cooling or due to a change in surface roughness. By using the adiabatic effectiveness data of Robertson (2004), I determined how the heat load on an actual vane would be affected by roughness and film cooling.

## **CHAPTER TWO**

### **EXPERIMENTAL FACILITY AND PROCEDURES**

This chapter describes the laboratory facility used to conduct the experiments and the procedures by which the data was acquired and analyzed.

#### **2.1 EXPERIMENTAL FACILITY**

Tests were conducted in a closed loop wind tunnel manufactured by Engineering Laboratory Design Inc. The state of the tunnel used in this study was a significant departure from ELD's original design. Figure 2.1 is a schematic of the tunnel as it was used for the present study.

The heat transfer experiments required high spatial resolution temperature measurements. These measurements were achieved by employing a FLIR ThermoCAM P20 infrared camera. Because the Plexiglas test section was opaque to infrared wavelengths, a NaCl (salt) window with high infrared transmissivity was sealed in a hole in the outer wall of the test section for all tests involving infrared imaging.

##### **2.1.1 Test Section**

The test section was at one corner of the tunnel and consisted of a simulated three-vane linear cascade as shown in Figure 2.2. Two complete airfoils were within the test section and the outer wall of the test section simulated a third vane. Adjustable bypasses provided a means to equalize the flow through the passages on either side of the test vane. The test section was also built with an adjustable outer wall and an adjustable tailboard to ensure the proper pressure distribution along the suction side of the test vane. The pressure distribution was adjusted to match the acceleration of the flow around a real vane. The pressure distribution that corresponds to this condition was last

verified by Daniel Snook, who began his research in 2001. The cascade inlet velocity was 5.8 m/s and the exit velocity was 32 m/s, yielding an exit Reynolds number of  $1.06 \times 10^6$  (based on a chord of 59.4 cm) to match realistic engine conditions. Information regarding the airfoil geometry is presented in Section 2.2

### **2.1.2 Mainstream Flow Loop**

The main flow of the tunnel was driven by a 50 hp fan. Both the fan speed and blade pitch were adjustable; however, the blade pitch was adjusted infrequently in order to maintain a good seal at the fan blade pitch adjustment lever. Mainstream velocity was maintained at 5.8 m/s at the test section inlet. In general, adjustments were only required when the turbulence level was changed.

A wooden rack that held desiccant packs was located downstream of the fan. Preparation for high density ratio tests required insertion of dry desiccant into the tunnel in order to reduce the humidity in the tunnel. Because the coolant temperature during high density ratio tests was maintained below 190 K, fairly dry tunnel air was necessary to mitigate frost buildup on the airfoil. To supplement the desiccant, the tunnel air would be purged with dry nitrogen to further reduce frost problems. A thorough description of the dehumidification procedure is given in Robertson (2004).

Downstream of the desiccant rack was a water heat exchanger necessary to control the mainstream temperature. The heat exchanger consisted of twenty vertical copper tubes in parallel that each made four passes across the height of the tunnel. Prior to experimentation, the cause of a nonuniform temperature profile at the test section was traced back to some blocked heat exchanger tubes. The two heat exchanger plenums were removed to facilitate cleaning and replaced in a fashion that allowed access to any tubes desired. Additionally,

valves were placed on each tube to allow the tubes to be flushed individually periodically and for adjusting the heat exchanger to equalize flow through the tubes.

In line with the test section, a 4:1 contraction accelerated the mainstream flow. At the inlet of the contraction, there was a section with a honeycomb flow straightener and two mesh screens. At the top of the honeycomb / mesh screen section, there were two 4 cm diameter holes that could be exposed in order to allow the pressure there to equilibrate with the ambient pressure. After the contraction, the flow passed through the hot streak generator section. A concurrent study on hot streak dynamics made use of the hot streak generator. See Jenkins et al. (2004) for more information on the hot streak generator. A Pitot-static tube located approximately 19 cm from the end of the contraction wall was used to measure the mainstream velocity. The Pitot-static measurement was made in order to obtain a consistent velocity profile at the inlet to the test vane, which is discussed later. The Pitot-static pressure measurement was performed with an Omega PX164 pressure transducer.

The hot streak generator was adjustable in the pitchwise direction, but fixed midspan. Since the horizontal supporting rods disrupt the flow, additional horizontal rods were located above and below the hot streak generator to ensure a uniform flow. The hot streak generator was positioned at the extreme pressure side for all heat transfer tests. Flow disruption caused by the hot streak generator dictated the lower limit of the attainable turbulence intensity. Studies at the same facility that took place before February 2002 were not influenced by the hot streak generator, thus those "low turbulence" conditions are not comparable to the "low turbulence" condition of this study. After it passed through the hot streak generator section, the flow went through a wire screen and into the test section.



A passive turbulence generator in the test section was used to create the high turbulence condition. Twelve metal rods with a pitch of 8.5 cm covered with 3.8 cm outside diameter foam were located 50 cm upstream of the vane cascade. The turbulence rod array was designed to simulate the turbulence intensity and integral length scale of actual engine conditions. Prior to this study the turbulence characteristics were reported in Cutbirth (2000), before the hot streak generator had been installed. Previously, the turbulence intensity was  $Tu_{\infty} = 20\%$  and  $\Lambda_f/C = 0.069$  at  $0.14 C$  upstream of the test vane's leading edge. Using the techniques described in Section 2.7, the turbulence was determined during this study to be  $20\% < Tu_{\infty} < 26\%$  with  $\Lambda_f/C \approx 0.069$  at  $0.18 C$  upstream of the test vane's leading edge. The average turbulence intensity was  $Tu_{\infty} = 21\%$ . The "low" turbulence condition was created by removing the foam covers and sliding the rods out of the mainstream flow. For this low turbulence condition, the turbulence intensity was  $Tu_{\infty} = 5.2\%$  with a length scale of  $\Lambda_f/C \approx 0.074$ . Before the hot streak generator was installed, the low turbulence condition was only  $Tu_{\infty} = 0.5\%$ . The velocity profile was also confirmed immediately before beginning this study. The velocity profile at  $0.18 C$  upstream of the cascade is presented in Figure 2.3.

Downstream of the test section, the flow passed through a diffuser. Immediately upstream of the diffuser, a copper tube entered through the roof of the tunnel. This tube was used for nitrogen purging in preparation for high density ratio tests. The mainstream flow made one final turn before entering the fan.

### 2.1.3 Secondary Flow Loop

The secondary flow loop supplied the coolant to the test section and is represented by the schematic in Figure 2.4. A 7.5 hp centrifugal blower removed air from the mainstream immediately upstream of the mainstream fan.

The secondary loop flow was split downstream of the centrifugal blower. One branch returned to the tunnel at a point adjacent to where the secondary flow loop removed air from the mainstream. The other branch went to a heat exchanger. Two butterfly valves controlled how much air went to the heat exchanger and how much went directly back into the tunnel.

The primary use of the heat exchanger was to cool the air so it could be used as coolant for the adiabatic effectiveness tests. Liquid nitrogen entered the heat exchanger and followed a serpentine path of copper tubing before it was mixed with the secondary loop air at the upstream end of the heat exchanger. Cooling of the air was fairly efficient due to this mixing box arrangement. For heat transfer tests, the coolant temperature was set to be the same as the mainstream temperature; therefore, at most, short bursts of liquid nitrogen were used in order to make minor adjustments to the coolant temperature. Cooling of the coolant was required infrequently. Usually the coolant required heating, probably because the warm mainstream air lost heat to the surroundings during its residence time in the secondary loop. For that reason, a heating element was installed inside the heat exchanger at the downstream end. The heating element was a stove burner suspended by wire. Power to the heating element was controlled through a Variac Type 3PN1010V.

Once the air exited the heat exchanger, it was split into three paths, one each for the showerhead, the suction side, and the pressure side plenums in the vane. Coolant was adjusted individually through the use of valves on those pipes. Due to the relatively low flow rates through the suction side, a needle valve was placed parallel to a globe valve in order to provide adequate control over the suction side flow rate. Orifice flow meters were located on each coolant line to measure the coolant flow rates. The pressure transducers on the showerhead and suction side lines were Omega PX142 and Omega PX2650 pressure transducers, respectively.

PVC tees immediately downstream of each valve forced the coolant to turn  $90^\circ$  on its path to the test section. The straight legs of the tees were capped during normal operation; however, the caps could be removed in order to allow some of the coolant to exit into the laboratory. This purging was useful to allow a much higher flow rate than would be allowed if the coolant were forced to go through the test section and out the coolant holes. Increasing the coolant flow rate through individual pipes was frequently necessary in order to make large temperature changes in a reasonable length of time. Since the blower forced air out of the tunnel during purging, the air needed to be replaced in order to avoid tunnel implosion. Thus, the holes on top of the honeycomb / mesh screen section were left open for heat transfer tests.

## 2.2 AIRFOIL GEOMETRY

The airfoil simulated a Pratt & Whitney first stage nozzle guide vane scaled up nine times. The test airfoil dimensions were 59.4 cm chord length, 54.9 cm span height, and 13.7 mm wall thickness. The vane cascade had a pitch of 45.7 cm. The vane was made of Last-A-Foam, a polyurethane foam, produced by General Plastics Mfg. Co. The thermal conductivity of the foam was  $k = 0.048$  W/m-K. Figure 2.5 is a schematic of the vane geometry. Details regarding the coolant hole configuration are in Table 2.1. The injection angle is the angle subtended by the axis of the hole and the airfoil surface. The streamwise angle is the angle in the plane of the vane between the hole axis and the streamwise direction. All holes were cylindrical with a diameter of 4.11 mm and a pitch to diameter ratio of  $p/d = 5.55$ . Coolant rows were staggered such that a hole in one row would line up halfway between two holes in adjacent rows. The curious reader should refer to Polanka (1999) for a more complete description of the vane geometry.

Table 2.1 Film Cooling Row Locations

Region	Film Cooling Row	s/d distance from stag	s/C Location	Streamwise Angle	Injection Angle
Showerhead	Stagnation Row	0	0	90°	25°
	Pressure Row 1	-3.33	-0.023	90°	25°
	Pressure Row 2	-6.66	0.046	90°	25°
	Suction Row 1	3.33	0.023	90°	25°
	Suction Row 2	6.66	0.046	90°	25°
	Suction Row 3	10	0.069	90°	25°
Suction Side	Suction Row 4	30	0.208	0°	56°
	Suction Row 5	53	0.367	55°	33°
	Suction Row 6	84	0.581	53°	26°
Pressure Side	Pressure Row 3	-25	-0.173	30°	45°
	Pressure Row 4	-45	0.311	30°	45°

The three coolant pipes entered the test vane through the bottom of the tunnel and opened into three plenums that fed the showerhead coolant holes, suction side coolant holes, and the pressure side coolant holes. An impingement plate was used on the suction side of the vane to ensure proper coolant flow into the coolant holes. The impingement plate was made of 1 mm thick stainless steel and was located 5.5 mm from the interior surface of the vane. The impingement holes were 0.78 cm in diameter and were pitched 2.28 cm, the same pitch as the coolant holes. For all tests involving the use of the showerhead, the average showerhead blowing ratio was set to  $M_{sh} = 1.6$ . Cutbirth and Bogard (2002) reported that the individual showerhead jets merge at this blowing ratio, forming a continuous film of coolant.

A removable vane section, the “hatch,” encompassed the area around the three rows of suction side coolant holes. This removable section facilitated

access to the suction side region for instrumentation, roughness installation and removal, and heat flux plate installation and removal.

### 2.3 SURFACE ROUGHNESS DESIGN

Bons et al. (2001) demonstrated that turbine airfoil roughness is not uniform across the surface of an airfoil. Surface roughness characteristics change over time and are even dependent on the operating environment. The roughness design was used in Bogard et al. (2003) and was based on typical turbine roughness. This section describes the development of the simulated roughness.

One goal of the roughness simulation was to match the ratio of the centerline average roughness,  $R_a$  to the average peak-to-valley roughness height,  $R_z$ . The centerline average roughness,  $R_a$ , is defined as the average distance between the local surface height to the mean height while  $R_z$  is defined as the average peak to valley roughness height ( $R_z \approx k$ ). Bogard et al. (1998) found  $R_a$  to range from 8 to 50  $\mu\text{m}$ . Bons et al. (2001) found a similar range of  $R_a$  values, but his larger sample size contained some areas with  $R_a < 4 \mu\text{m}$ . A typical value of  $R_a = 22 \mu\text{m}$  was chosen for the simulated roughness. Bogard et al. (1998) found that  $R_z / R_a \approx 5$ . This finding is fairly consistent with Bons (2002), who found  $R_z / R_a$  ranged from 5 to 10. The ratio  $R_z / R_a$  was chosen to be 5 for the roughness design. With  $R_a = 22 \mu\text{m}$ , this corresponds to  $R_z = k = 110 \mu\text{m}$ .

The most critical roughness parameter to match was the equivalent sand grain roughness,  $k_s$ . By definition, this parameter was intended to allow one to match the skin friction characteristics. As discussed in Chapter 1, Sigal and Danberg (1990) related  $k_s/k$  to the roughness shape / density parameter,  $\Lambda_s$  (Equations 1.3.1.6 and 1.3.1.7). Bogard et al. (1998) found  $\Lambda_s \approx 60$  for both vane samples. Bons et al. (2001) found  $\Lambda_s$  ranging from 20 to 1000, with a

mode of approximately 150. A range of  $\Lambda_s$  from 60 to 150 corresponds to  $k_s/k$  of 0.7 to 0.2. A  $k_s/k$  value of 0.5 was selected for the simulated roughness. With  $k = 110 \mu\text{m}$ , we now have  $k_s = 55 \mu\text{m}$ . When scaled up nine times for the simulated vane, the final values are  $k_s = 0.5 \text{ mm}$  and  $k = 1 \text{ mm}$ . From equation 1.3.1.7, we find that  $k_s/k = 0.5$  corresponds to  $\Lambda_s = 3$  or 70. The value of  $\Lambda_s = 70$  was chosen as it is a better representation of actual turbine roughness.

Many roughness geometries may be developed that all meet the established criteria. A conical array (as shown in Figure 2.6) was selected due to earlier success with this type of roughness. Among its benefits are its ease of adapting into a uniform heat flux plate, manufacturability, and absence of areas that may be obscured from the view of an infrared camera. In order to keep the heat flux plate thickness as uniform as possible, a large cone base to cone height ratio was desired. As a result, this somewhat arbitrary  $D/k$  ratio was chosen to be 4, setting  $D = 4 \text{ mm}$ . The roughness parameters can now be calculated with the Sigal and Danberg equation:

$$\Lambda_s = \frac{S}{S_f} \left( \frac{A_f}{A_s} \right)^{-1.6} \quad (2.3.1)$$

where:

$S$  is the reference area of the surface if no roughness were present,

$S_f$  is the total projected frontal area of the roughness elements,

$A_f$  is the projected frontal surface area of a roughness element, and

$A_s$  is the windward wetted surface area of a roughness element.

The windward wetted surface area of each roughness element is half of the lateral surface area of a cone, or

$$A_s = \frac{\pi D}{4} \sqrt{\left(\frac{D}{2}\right)^2 + k^2} \quad (2.3.2)$$

The projected frontal surface area of a roughness element is simply the area of the triangular cross section of the cone given by

$$A_f = \frac{1}{2} Dk \quad (2.3.3)$$

The ratio  $A_s/A_f$  may be determined to be

$$\frac{A_s}{A_f} = \frac{\pi}{2} \sqrt{5} \approx 3.5 \quad (2.3.4)$$

When substituting this ratio and  $\Lambda_s = 70$  into equation 2.3.1, we find that  $S/S_f$  must be 9.43. Figure 2.7 shows the smallest repeating area of the rough surface (assuming equal element spacing in both the streamwise and spanwise directions) that can be used for determining the physical representation of  $S/S_f$ . Considering the cell in Figure 2.7,  $S$  is the area of the cell, or

$$S = p^2 \quad (2.3.5)$$

$S_f$  is the total projected frontal area of the cones in the cell, or

$$S_f = \frac{1}{2} Dk \quad (2.3.6)$$

yielding:

$$\frac{S}{S_f} = \frac{2p^2}{Dk} \quad (2.3.7)$$

Since  $D = 4$  mm and  $k = 1$  mm, the pitch,  $p$  must be 4.3 mm. The actual surface area of the simulated roughness is 8% larger than the plan form area.

As Bons et al. (2001) demonstrates, real turbine surface roughness is widely varied. The simulated roughness used in this experimentation was selected to represent a typical level of roughness. As such, the 10% discrepancy noted by Bons (2002) in modeling both skin friction and heat transfer behavior is a non-issue.

As discussed in Section 1.3.1, the roughness Reynolds number characterizes the flow as being hydraulically smooth, transitionally rough, or fully rough. The roughness Reynolds number was determined to be  $Re_k \approx 50$ , indicating that the flow is in the transitionally rough regime. A description of the techniques used to determine  $Re_k$  are in Appendix A.

## 2.4 THE UNIFORM HEAT FLUX PLATE

A uniform heat flux was applied at the surface of the vane through electrical heating of a thin metallic sheet. Two of these heat flux plates were used—one with the simulated roughness stamped into it, and another one that was smooth. Both heat flux plates were made of type 302 stainless steel, selected for its high electrical resistivity. The rough heat flux plate was 0.002” thick and the smooth heat flux plate was 0.004” thick. The rough plate had to



be thin enough that an accurate impression of the roughness could be stamped into it. Such a thin plate could not be used for the smooth surface because the structural rigidity was insufficient to prevent wrinkles in the heat flux plate. Nearly imperceptible wrinkles were sufficient to cause anomalous local heat transfer coefficients.

The heat flux plate material was sold as shim stock. The stainless steel was cut to the desired size (approximately 19 cm x 9 cm) by using a paper cutter. The rough heat flux plate had 18 rows of roughness in the streamwise direction and 42 rows in the spanwise direction. The conical roughness elements were staggered such that the spanwise location of each cone was directly between the two upstream cones. Two copper bus bars that ran along the ends of the heat flux plate ensured a one-dimensional current flow through the heat flux plate. The bus bars were made of 10 gauge copper wire that was pounded flat and bent to match the curvature of the surface of the vane. David Robertson and I developed a technique for soldering the copper bus bars to the stainless steel. The technique is described in detail in Appendix B.

A DC power supply provided electrical power for the heat flux plate. A shunt resistor ( $R = 3.33 \pm 0.01 \text{ m}\Omega$ ) was in series with the circuit. Measurement of the voltage drop across the shunt resistor allowed for the electrical current to be determined. Additionally, the voltage drop across the heat flux plate was measured. To ensure that only the voltage drop across the heat flux plate was measured (and not the wires with nonzero resistance), the voltmeter leads were placed on the bus bars immediately adjacent to the heat flux plate. The electrical heating per unit area was calculated via the following equation:

$$q''_{\text{electrical}} = \frac{V_{HFP} I}{A_{HFP}} \quad (2.4.1)$$

## **2.5 HEAT TRANSFER TESTS**

Heat transfer tests were time consuming and required a day of preparation in addition to a day to run the actual experiment. These two phases are discussed in this section.

### **2.5.1 Heat Transfer Test Preparation**

The removable section of the vane's suction side, the "hatch," was prepared before each test. A thermocouple was placed inside the hatch near the first row of coolant holes, but off of the interior surface. Because this thermocouple was used to measure the coolant temperature, it was kept off of the interior surface so as to avoid influence due to conduction. Weather stripping was used on the interior perimeter of the hatch so that the hatch could maintain a good seal with the rest of the vane when installed. Sealing was necessary to prevent coolant leaks that would result in erroneous blowing rates. Likewise, it was necessary to ensure that coolant could only exit the hatch through the first row of suction side coolant holes. The other two rows of coolant holes were plugged with clay and taped from the inside of the hatch. If all three rows of holes were left open, the flow rate distribution would be dictated by the exterior pressure distribution and there would be additional uncertainty in the blowing ratio of the first row of coolant holes.

Two type E ribbon thermocouples were epoxied to the underside of the desired heat flux plate (smooth or rough) that was at least primed if not already painted. These two thermocouples were used for calibrating the infrared camera. The locations of the thermocouples were marked on the outer surface of the heat flux plate so they could be located later. The heat flux plate was attached to the hatch through the use of double sided tape (3M 401, 0.2 mm thick) and high temperature hot glue. The double sided tape could withstand the high temperature environment created by the heat flux, but hot glue did a

superior job of holding the leading edge of the heat flux plate against the surface of the hatch. The double sided tape was used to completely cover the underside of the heat flux plate except for the leading 1 cm of the plate. The heat flux plate was carefully attached within  $0.5 d$  of the first row of coolant holes. It was important to prevent pockets of air from being trapped under the heat flux plate. At this point, the leading edge of the heat flux plate had not yet been attached. High temperature hot glue was injected under the front of the plate using a hot glue gun. A rubber stamp roller (available at art supply stores) was used to press the front edge down onto the hatch surface. The hot glue would be reheated as necessary using a heat gun, and the excess wiped away. Applied properly, the hot glue would hold the leading edge down reliably, whereas the tape held the bulk of the plate down where temperatures were too high for hot glue were reached. Once the heat flux plate had been attached in its final position, the locations of the calibration thermocouples would be noted.

The heat transfer coefficient on the smooth heat flux plate was found to be very sensitive to the step change in surface height at the leading edge of the heat flux plate. In order to eliminate this step, the surface upstream of the heat flux plate was built up to the height of the heat flux plate. The surface was built up to the appropriate height by placing 3M Scotch 395 duct tape on the hatch surface and then placing double sided 3M 401 on top, leaving the backing on the exposed surface of the tape. Film cooling holes were cut in the tape at the appropriate locations.

Some tests involved the use of roughness upstream of the heat flux plate. For these tests, the upstream roughness was attached within  $0.5 d$  upstream of the coolant holes. The upstream roughness consisted of 8 rows of 42 roughness cones.

A uniform coat of flat black spray paint (Krylon Ultra-Flat Black) was applied to the heat flux plate. The black paint had an emissivity of  $\varepsilon \approx 0.95$

and prevented stray thermal radiation from being reflected to the infrared detector. The emissivity of the paint was determined by elevating the temperature of a painted object with a thermocouple attached to the surface and adjusting the emissivity setting of the infrared camera until the temperature measured by the camera matched the temperature measured by the thermocouple. The paint also exhibited sufficiently isotropic radiation emission such that differences in view angles across the surface need not be accounted. The isotropic behavior was verified by viewing a painted object at a variety of angles with the infrared camera and observing that the infrared camera's temperature measurement was independent of angle. When painting, it was important to tape over the edges of the heat flux plate as paint would otherwise destroy the adhesive properties of the tape and hot glue.

The hatch was then installed on the rest of the test vane. The seams and screw holes in the vane were completely covered with duct tape (0.3 mm thick, 3M Scotch 395) to prevent coolant leakage. The two surface thermocouple wires and the hatch coolant thermocouple were routed out of the wind tunnel and plugged into the data acquisition system. The infrared camera was mounted on a tripod and focused on the heat flux plate through the salt window. Once the camera was secured, several benchmark images were saved. These benchmark images would provide pixel values that could later be associated with physical locations. A thin bare wire heated with body heat stood out well against a room temperature vane. Hole locations and reference positions for the calibration thermocouples were marked with this "hot stick." A strip of masking tape with increments every centimeter was attached to the heat flux plate, with the zero marker at the trailing edge of the first row of suction side film cooling holes. Originally, a hot stick was used to point out the locations of the marks to the infrared camera. Later on, thin strips of foil were attached to the tape in one centimeter increments. The strong difference in emissivity

between the foil and the tape allowed the foil to be seen clearly with the infrared camera.

The infrared camera detected not only infrared emissions from a surface, but also infrared reflections. Reflections could jeopardize the data from a test. Therefore, a cardboard box was installed around the infrared camera in order to prevent infrared reflections off of the salt window.

The mainstream temperature was a critical measurement because the difference between it and the surface temperature appears in the bottom of the heat transfer coefficient equation (Equation 1.2.2). A type E thermocouple was suspended approximately two inches off of the surface of the vane above the hatch. Special care was taken to ensure that the mainstream temperature measurement could not be influenced by the showerhead temperature.

Null tests were used to verify that a uniform heat flux was indeed present at the heat flux plate. The null tests were performed without mainstream flow. A heat flux was applied and natural convection cooled the heat flux plate. Once at steady state, the temperature was confirmed to be horizontally uniform and increasing in the upward direction. This procedure was performed for all heat flux plates used in the experimentation.

Another test was used to verify that the suction side coolant temperature measurement was correct. The mainstream flow would be turned on and coolant ejected from the suction side coolant holes at  $M=0.7$ . If the coolant temperature was different from the mainstream temperature, coolant plumes could be detected. In this manner, it was verified that the measured difference between the mainstream temperature and the coolant temperature was accurate.

A limited number of tests were performed with a 1.59 mm diameter trip rod placed approximately  $7d$  upstream of the first row of suction side coolant holes. The trip rod was not in place during normal operation, but was installed

on occasion to determine its effects on the heat transfer coefficient and the boundary layer.

### **2.5.2 Heat Transfer Test Procedure**

The checklist in Appendix C was followed closely for each test. The checklist goes through the procedure of starting up the wind tunnel for the test. The rather involved process of taking data has been omitted from that checklist, but is presented in this section along with other details.

Small wrinkles in the heat flux plate have the potential of causing anomalies in the heat transfer coefficient distribution. To check for the existence of the wrinkles, duct tape was placed over the film cooling holes to eliminate disturbances in the flow caused by the holes, the wind tunnel was turned on, and a heat flux was applied. Ideally, the temperature distribution should be laterally uniform under these conditions.

Before taking any data, the heat flux plate was on and at steady state. Between 40 and 60 amps have been used with good results. Depending on the heat flux plate, this amperage could provide between  $2000 \text{ W/m}^2$  and  $4000 \text{ W/m}^2$ . The key was to ensure that the temperature of the heat flux plate was sufficiently different from the mainstream temperature that a value for  $\Delta T$  may be used in the heat transfer coefficient calculations without the introduction of significant error. A typical value for the maximum  $\Delta T$  was 25 K. Five minutes was sufficient time for the heat flux plate to reach a steady temperature distribution. It took this much time to reach steady state because the foam substrate required heating (see Section 2.6.1.1 for information on the conduction correction).

The most challenging aspect of running a test was the maintenance of the coolant temperature. The coolant was held at about the same temperature as the mainstream temperature. With practice, it was quite reasonable to obtain

coolant temperatures within 0.2 K of the mainstream temperature, significantly less than the uncertainty of the infrared camera calibration. Liquid nitrogen could be introduced into the secondary flow through the heat exchanger / mixing box. Only a small amount of nitrogen was needed to reduce the temperature of the coolant by several degrees. When the coolant needed to be heated, the electrical heating element inside the heat exchanger was activated. Variable power was applied through the use of a Variac. Because there was only one heat exchanger and it was located upstream of the split between the pressure side, showerhead, and suction side coolant paths, it could be difficult to maintain the proper temperature for two coolant paths at once. However, temperature control was straightforward for any one coolant path. When operating both the showerhead and the suction side coolant, the showerhead generally responded faster to corrections made at the heat exchanger. The faster showerhead response was due to a much higher mass flow rate through the showerhead than a single row of suction side coolant holes. Likewise, because the residence time of coolant in the showerhead pipes was less than the residence time of the coolant in the suction side pipes, the showerhead coolant had less time to exchange heat with the surroundings. This characteristic was obvious especially when running high density ratio tests. As a result, the showerhead coolant lines were left uninsulated. Because the ratio of coolant mass flow dictated which coolant feed received the largest effect of a heat exchanger adjustment, the temperature in one coolant feed could be changed while having a relatively small effect on the other by opening up the valve for the feed that needed the adjustment while shutting off the feed that did not need the adjustment. Large flow rates could be achieved by opening the valve wide open and removing the end cap at the 90° bend downstream of the valve. This allowed the coolant to exit into the laboratory at a high rate. Although the coolant would not enter the vane during this purge operation, the coolant

upstream of the cap would be conditioned to a more appropriate temperature in short order.

When the blowing ratio was adjusted as desired and the heat flux plate was at equilibrium, data was taken. The camera operator would take a picture with the infrared camera at the same time the computer operator would save the thermocouple and pressure transducer readings. During the course of my experiments, a differential amplifier (a device used in the measurement of a voltage across an ungrounded resistor) was not available for the data acquisition computer to record the shunt resistor voltage and heat flux plate voltage. Instead, those voltages were displayed on digital voltmeters and recorded manually. Typically, tests were run at high and low turbulence and with and without showerhead cooling. When used, the showerhead was always set to  $M = 1.6$ . The turbulence generator rods were slid in and out of the tunnel with the tunnel running and the heat flux plate operating, so that equilibrium need not be reestablished. Whenever the showerhead was not in use, duct tape was placed over the showerhead holes in order to eliminate any effect of the showerhead holes on the flow.

It was found that the influence of upstream roughness on heat transfer was subtle enough that data needed to be taken with and without the roughness during the same test. As with all other in-test adjustments, the heat flux plate would be left operating the entire time.

Once all the desired data was taken, it was necessary to calibrate the infrared camera. All of the data taken during the test was used for the calibration, but since the heat flux was generally held constant, the calibration thermocouples were not exposed to a wide range of temperatures. The calibration thermocouples were placed near the downstream edge of the heat flux plate so that they were exposed to some of the highest temperatures on the plate. To be sure that the calibration curve extended to sufficiently high



temperatures, the heat flux rate was increased slightly for some calibration data. Data was still acquired by taking infrared images at the same time thermocouple data was saved on the data acquisition computer. For this data, however, only surface temperatures were important so thermal equilibrium did not need to be established nor did the shunt resistor and heat flux plate voltages need to be recorded. Calibration data was taken as the heat flux was slowly reduced until there was no heat flux and the heat flux plate temperature assumed the mainstream temperature.

## **2.6 DATA REDUCTION METHODS**

The FLIR ThermoCAM P20 infrared camera saved data digitally as .jpg files that were stored on a CompactFlash card until they were transferred to a computer. When the .jpg files were viewed with standard image viewing software, the display as seen through the camera's viewfinder would be displayed. However, the .jpg images could be processed with the ThermoCAM Researcher Pro 2.7 software to obtain temperature data. Among the software's features was the ability to export the temperature data to .mat files, which were readable by Matlab. ThermoCam Researcher could easily produce those Matlab files for each image taken during a test. I wrote a Matlab script that batch processed those Matlab files for data reduction purposes.

Sometime during each test, certain geographic features were pointed out to the camera by a pointer that has a slightly different temperature than the background and / or a high reflectivity. Film cooling hole locations, thermocouple locations, and  $x/d$  measurements were made in this fashion. A linear curve fit was used to correlate the y-pixel values to actual spanwise locations in terms of  $y/d$ . Streamwise positions were correlated with x-pixel values through the use of a quadratic (necessary due to streamwise surface curvature) equation.

The Matlab code was first executed to extract IR temperature values from the pixels in each image where there was a thermocouple. The temperature as reported by the IR camera was only a rough approximation of the actual temperature, mostly because the IR window interfered with the thermal radiation passing through it. A second order polynomial correlated the IR temperature with the actual temperature as determined by the surface thermocouples. That calibration curve was input into the Matlab program, which scanned an entire user-specified region on each image, converting the IR temperatures to actual temperatures. At this point, the program also saved spanwise averaged temperatures which were useful for creating spanwise averaged adiabatic effectiveness plots for other researchers.

For heat transfer coefficient calculations, the Matlab program used the actual surface temperatures to determine the amount of radiative and conductive heat flux at every pixel using the methods discussed in Section 2.6.1. The radiative and conductive heat fluxes were subtracted from the total heat flux to determine the convective heat flux at every pixel. Spatial heat transfer coefficients were then calculated and spanwise averaged.

### 2.6.1 Conduction and Radiation Correction

By measuring the electrical current through the heat flux plate and the voltage drop across the heat flux plate, the total heat flux out of the plate was determined. The heat transfer out of the plate occurred by means of convection, conduction, and radiation. In order to determine the convection heat transfer coefficient,  $h$ , the amount of convection heat transfer was required.

Conservation of energy dictates the following:

$$q''_{convection} = q''_{total} - q''_{conduction} - q''_{radiation}$$

The conduction correction procedure at high density ratio was much different from the procedure used at  $DR = 1.0$ . The high density ratio procedure is discussed in Section 2.6.2. This section describes how the necessary terms were found for data acquired while the system was at steady state (which was all of the heat transfer data).

#### **2.6.1.1 Conduction Correction**

The first step in determining the amount of conduction through the substrate was to choose an appropriate conduction model. In general, thermal conduction is three-dimensional. The heat flux has components in the spanwise, streamwise and normal directions. The only regions where there were significant spanwise temperature gradients were those at the edges of the plate at the bus bars. Since no data was collected from these regions, thermal conduction was assumed to be at most two-dimensional in the region of interest.

To determine the characteristics of the thermal conduction through the substrate, I wrote a Matlab program that used second order central differencing and Gauss-Siedel iteration to solve for the temperature profile and the conductive heat flux on the top surface. The analysis assumed that the surface was flat. A typical spanwise average temperature distribution on a heat flux plate of 9 cm streamwise length was used for the boundary condition on the top of the foam substrate. The applied electrical heat flux was  $1619 \text{ W/m}^2$ . A 4 cm length upstream of the heat flux plate was set at the mainstream temperature. The inner surface temperature was set at  $T_s - 0.8(T_s(x) - T_c)$ , based on experimentation. The remaining boundaries were set to be adiabatic. Figure 2.8 is the computed temperature profile within the substrate.

A simpler one dimensional conduction model assumes that the temperature gradients in the streamwise direction are negligible. According to

Figure 2.8, streamwise temperature gradients were significant only near the edges of the heat flux plate. Figure 2.9 compares the surface conductive heat flux computed by the one dimensional and two dimensional approximations. The conductive heat loss predicted by the one dimensional approximation was at most 5% of the electrical heat input.

The negative conductive heat flux calculated by the two dimensional conduction model represents conduction out of the substrate. The heat flux plate heats the foam in the vicinity of the plate. Adjacent to the plate, the warm foam was cooled by convection, thus heat was lost by the foam. In general, the surface temperature varies in the spanwise direction, thus to be applied properly, the two dimensional conduction correction must be applied repeatedly along the spanwise direction. Furthermore, the amount of predicted conduction near the end of the plate was extremely sensitive to the chosen boundary conditions. The one dimensional model was sufficient throughout much of the heat flux plate. The two approximations were within 10% of each other within the entire area except for the leading 1 cm and the trailing 1.5 cm. Therefore, the conduction correction is valid in the range  $3 < x/d < 18$ .

Accurate determination of the conduction would require either the inner surface temperature or the heat transfer coefficient inside the hatch. A ribbon thermocouple was placed on the inside surface of the hatch to help determine the unknown information. We can write the equations that govern the conduction heat transfer through the hatch by balancing the conduction with the internal convection.

$$q'' = \frac{k}{L}(T_s - T_{si}) = h(T_{si} - T_c) \quad (2.6.1.1.1)$$

From this relation we can find an expression for the inner surface temperature.

$$T_{si} = \frac{\frac{k}{L}T_s + hT_c}{h + \frac{k}{L}} \quad (2.6.1.1.2)$$

Substitute this expression for the inner surface temperature into the conduction equation from Equation 2.6.1.1.1.

$$q'' = \frac{k}{L}(T_s - T_{si})$$

$$q'' = \frac{k}{L} \left( T_s - \frac{\frac{k}{L}T_s + hT_c}{h + \frac{k}{L}} \right) \quad (2.6.1.1.3)$$

Algebraic manipulation gives the following:

$$q'' = \frac{k}{L} \left( \frac{h}{h + \frac{k}{L}} \right) (T_s - T_c) \quad (2.6.1.1.4)$$

Several measurements were made of the inner surface temperature of the hatch.

Therefore, it was possible to obtain heat fluxes with those temperature

measurements and determine the value of  $\left( \frac{h}{h + \frac{k}{L}} \right)$ . The quantity  $\left( \frac{h}{h + \frac{k}{L}} \right)$  was

found to be about 0.8 (for which  $h \approx 20 \text{ W}/(\text{m}^2 \text{ K})$ ). This value of  $\left( \frac{h}{h + \frac{k}{L}} \right)$  can

be off by as much as 20% before it has an effect greater than 1% on the calculated external heat transfer coefficients.

### **2.6.1.2 Radiation Correction**

The radiation correction employed the assumption that the both the heat flux plate and the walls of the tunnel were diffuse gray surfaces. Conveniently, the Plexiglas walls had approximately the same emissivity as the flat black paint ( $\varepsilon \approx 0.95$ ). The walls of the tunnel were assumed to have a uniform temperature equal to that of the mainstream. These assumptions were verified experimentally.

With the preceding assumptions, the local radiation heat transfer out of the heat flux plate may be written:

$$q''_{rad} = \varepsilon \sigma (T_s^4 - T_\infty^4) \quad (2.6.1.2.1)$$

where the  $T_s$  is the local surface temperature on the heat flux plate. The maximum heat loss due to radiation was typically 9% of the electrical heat flux.

### **2.6.2 High Density Ratio Tests**

A high density test was performed to complement the low density ratio data. A density ratio of  $DR = 1.6$  was obtained by cooling the coolant to 187 K while the mainstream was held at 300 K. With the  $DR = 1.0$  tests, the coolant temperature was the same as the mainstream temperature so that the adiabatic wall temperature was the mainstream temperature. However, that simplicity was not applicable with the high density ratio tests so adiabatic effectiveness measurements were taken before any heat transfer data. Details of the adiabatic effectiveness test procedure are found in Robertson (2004). Following the adiabatic effectiveness tests, the constant heat flux plate was activated and allowed to reach steady state before infrared images were acquired again.

The data was reduced using the procedure given in Robertson (2004). The output of Robertson's procedure was spatial  $\eta$  values. Data acquired while the heat flux plate was on will be called  $\eta'$  since it is definitely *not* the adiabatic effectiveness, but rather a different type of nondimensional temperature distribution. Recall the definition of  $\eta$  and extend it to the definition of  $\eta'$ .

$$\eta \equiv \frac{T_{aw} - T_{\infty}}{T_c - T_{\infty}} \quad (2.6.2.1)$$

and

$$\eta' \equiv \frac{T_w - T_{\infty}}{T_c - T_{\infty}} \quad (2.6.2.2)$$

where  $T_w$  is the surface temperature that occurs for a given heat flux.

Although the foam vane model had low thermal conductivity, it was not adiabatic. This aspect necessitated consideration of conduction effects in the determination of the adiabatic wall temperature. Robertson's procedure of accounting for the effect of conduction involved determining the wall temperature while there was no film cooling, but while the coolant inside the vane was at operating temperature. This task was accomplished by taping over the holes in the camera's field of view, but continuing to run coolant through the open holes. If the hatch were truly adiabatic, the wall would assume the mainstream temperature. But since a small amount of heat transferred into the hatch due to the coolant on the inside, the outside wall temperature was slightly cooler than the mainstream temperature. Let  $T_{s0}$  be the surface temperature

measured with no film cooling and let  $\eta_0$  be the effectiveness measured under such conditions as follows:

$$\eta_0 \equiv \frac{T_\infty - T_{s0}}{T_\infty - T_c} \quad (2.6.2.3)$$

During adiabatic effectiveness measurements, there was no heat flux at the surface, thus an energy balance yields:

$$q_{convection} = q_{conduction} \quad (2.6.2.4)$$

Allow  $U_c$  to represent the overall internal heat transfer coefficient that accounts for both conductive and internal convective thermal resistance such that

$$q_{conduction} = U_c (T_{surf} - T_c) \quad (2.6.2.5)$$

Rewriting the energy balance:

$$h(T_\infty - T_{s0}) = U_c (T_{s0} - T_c) \quad (2.6.2.6)$$

Replacing  $T_{s0}$  with the equivalent expression in terms of  $\eta_0$  and some algebraic manipulation (the details of which are in Robertson (2004)) will show:

$$\frac{U_c}{h} = \frac{\eta_0}{1 - \eta_0} \quad (2.6.2.7)$$



With film cooling, the driving potential for external convection is  $(T_{AW} - T_s)$ , for which the adiabatic wall temperature is not the mainstream temperature. The energy balance for the film cooled case is as follows:

$$h(T_{aw} - T_s) = U_c(T_s - T_c) \quad (2.6.2.8)$$

Define another effectiveness value that represents the measured effectiveness with film cooling.

$$\eta_s = \frac{T_\infty - T_s}{T_\infty - T_c} \quad (2.6.2.9)$$

A great deal of algebraic manipulation and utilization of Equation 2.6.2.7 gives the final result for the true adiabatic wall temperature in terms of the surface temperatures with and without film cooling. See Robertson (2004) for the details of the algebra.

$$\eta = \frac{\eta_s - \eta_0}{1 - \eta_0} \quad (2.6.2.10)$$

All of Robertson's reported  $\eta$  values are corrected for conduction in this manner. The next task was to determine the heat transfer coefficient with the known wall temperature with heat flux and the adiabatic effectiveness. Recall the definition of the convective heat transfer coefficient,

$$h = \frac{q''_{convection}}{T_{aw} - T_w} \quad (2.6.2.11)$$

where

$$q''_{convection} = q''_{applied} - q''_{conduction} - q''_{rad} \quad (2.6.2.12)$$

The applied heat flux is uniform electrical heat flux. Let  $T_{s,HF}$  represent the surface temperature with heat flux and let  $\eta_{HF}$  be the nondimensionalized form such that

$$\eta_{HF} \equiv \frac{T_{\infty} - T_{s,HF}}{T_{\infty} - T_c} \quad (2.6.2.13)$$

Continuing with the energy balance:

$$\begin{aligned} q_{applied}'' - q''_{rad} &= q_{conduction}'' + q_{convection}'' \\ q_{applied}'' - q''_{rad} &= U_c(T_{s,HF} - T_c) + h(T_{s,HF} - T_{AW}) \\ q_{applied}'' - q''_{rad} &= U_c(T_{\infty} - \eta_{HF}(T_{\infty} - T_c) - T_c) + h(T_{\infty} - \eta_{HF}(T_{\infty} - T_c) - T_{AW}) \\ q_{applied}'' - q''_{rad} &= U_c(1 - \eta_{HF})(T_{\infty} - T_c) + h[\eta(T_{\infty} - T_c) - \eta_{HF}(T_{\infty} - T_c)] \\ q_{applied}'' - q''_{rad} &= (T_{\infty} - T_c)[U_c(1 - \eta_{HF}) + h\eta - h\eta_{HF}] \\ \frac{q_{applied}'' - q''_{rad}}{h} &= (T_{\infty} - T_c)\left[\frac{U_c}{h}(1 - \eta_{HF}) + \eta - \eta_{HF}\right] \end{aligned}$$

Substitute Equation 2.6.2.7 for  $\frac{U_c}{h}$

$$\frac{q_{\text{applied}} - q''_{\text{rad}}}{h} = (T_{\infty} - T_c) \left[ \frac{\eta_0}{1 - \eta_0} (1 - \eta_{HF}) + \eta - \eta_{HF} \right]$$

$$\frac{q_{\text{applied}} - q''_{\text{rad}}}{h} = (T_{\infty} - T_c) \left[ \frac{\eta_0}{1 - \eta_0} - \frac{\eta_0}{1 - \eta_0} \eta_{HF} + \eta - \eta_{HF} \right]$$

$$\frac{q_{\text{applied}} - q''_{\text{rad}}}{h} = (T_{\infty} - T_c) \left[ \frac{\eta_0 - \eta_0 \eta_{HF} - (1 - \eta_0) \eta_{HF}}{1 - \eta_0} + \eta \right]$$

Finally, we have the following:

$$\frac{q_{\text{applied}} - q''_{\text{rad}}}{h} = (T_{\infty} - T_c) \left[ -\frac{(\eta_{HF} - \eta_0)}{1 - \eta_0} + \eta \right] \quad (2.6.2.14)$$

The first term in brackets is of the same form as Equation 2.6.2.10. It can be thought of as the conduction corrected nondimensional wall temperature with heat flux, or the temperature the wall would assume if all of the electrical heating is carried away only by convection. Define  $\eta'$  as this conduction corrected version of  $\eta_{HF}$ .

$$\eta' = \frac{\eta_{HF} - \eta_0}{1 - \eta_0} \quad (2.6.2.15)$$

Thus,

$$\frac{q_{\text{applied}} - q''_{\text{rad}}}{h} = (T_{\infty} - T_c)(\eta - \eta') \quad (2.6.2.16)$$

The final form of the equation for the heat transfer coefficient is now written.

$$h = \frac{q_{\text{applied}}'' - q_{\text{rad}}''}{(T_{\infty} - T_c)(\eta - \eta')} \quad (2.6.2.17)$$

It is fortuitous that the required temperature data is in the conduction corrected nondimensional form. Because Robertson's data reduction procedure automatically corrects all nondimensional temperatures for conduction, direct application of his data reduction procedure was used to find  $\eta$  and  $\eta'$  from the raw temperature data.

### 2.6.3 Net Heat Flux Reduction

In order to fully understand the heat load at a particular location on an actual vane, both the heat transfer coefficient and the adiabatic effectiveness must be known. Equation 1.2.6 describes the net heat flux reduction that is achieved due to film cooling, taking into consideration the negative consequences of film cooling on the heat transfer coefficient. The technique can be adapted to determine the influence of roughness on the heat load. In the following development,  $\Delta q_{r, \text{rough}}$  designates the net heat flux reduction as modified for comparing rough surfaces to smooth surfaces.

We start with modifying Equation 1.2.5 to deal with heat transfer to film cooled rough and smooth surfaces.

$$\Delta q_{r, \text{rough}} \equiv 1 - \frac{q_{f, \text{rough}}''}{q_{f, \text{smooth}}''} = 1 - \frac{h_{f, \text{rough}}(T_{aw, \text{rough}} - T_w)}{h_{f, \text{smooth}}(T_{aw, \text{smooth}} - T_w)} \quad (2.6.3.1)$$

Substitute the definitions of adiabatic effectiveness and overall effectiveness, Equations 1.2.1 and 1.2.4.

$$\Delta q_{r,rough} = 1 - \frac{h_{f,rough}(\eta_{rough}(T_c - T_\infty) + T_w - \phi(T_c - T_\infty) - T_w)}{h_{f,smooth}(\eta_{smooth}(T_c - T_\infty) + T_w - \phi(T_c - T_\infty) - T_w)}$$

$$\Delta q_{r,rough} = 1 - \frac{h_{f,rough}(\eta_{rough} - \phi)}{h_{f,smooth}(\eta_{smooth} - \phi)} \quad (2.6.3.2)$$

Equation 2.6.3.2 is the final form of the equation for the net heat flux reduction relevant for comparing rough surfaces to smooth surfaces. Since roughness is typically detrimental to the heat load, we expect  $\Delta q_{r,rough} < 0$ , indicating a net heat flux *increase*.

It must be stressed that both forms of the net heat flux reduction require an appropriate reference condition. For example, when determining the net heat flux reduction due to only suction side film cooling at a particular blowing ratio, the reference condition without suction side film cooling has the same turbulence intensity, same surface roughness, etc.

The net heat flux reduction analysis was possible because compatible adiabatic effectiveness data and heat transfer coefficient data is now available. I measured the required heat transfer coefficients and my colleague, David Robertson measured the adiabatic effectiveness distributions. For detailed information regarding the adiabatic effectiveness data, the reader is referred to Robertson (2004).

## 2.7 BOUNDARY LAYER MEASUREMENTS

Because this research investigated hydrodynamic effects on heat transfer, it was desirable to consider the structure of the boundary layer on the vane. A constant temperature hot wire anemometer was used to measure

velocity and turbulence intensity profiles near the vane surface. The boundary layer measurement procedure is detailed in this section.

A boundary layer hot-wire probe (one that is bent upstream as shown in Figure 2.10) was used in conjunction with an A. A. Lab Systems Ltd. AN-1003 hot wire / hot film anemometry system. The hot-wire was 5  $\mu\text{m}$  in diameter and made of platinum coated tungsten. The bridge balancing and damping adjustment was performed according to the instructions described in the accompanying user's manual. An overheat ratio of 1.5 was used for all measurements.

Because a wide range of velocities needed to be obtained, two locations in the wind tunnel were used for calibrating the hot wire anemometer—a high speed location in the vane passage and a low speed location in the entrance region. The two locations were selected based on their low velocity gradients and the ability to reach both of them and the suction side surface without disconnecting any anemometry equipment. Each location was marked in three dimensional space by placing markings on the Plexiglas wind tunnel test section. A hand held thermo-anemometer (Dwyer Series 471) was placed at each location to determine how the mean velocity at each location corresponded to the entrance velocity as measured by the fixed pitot-static probe. At the slow location, the velocity was 1.05 times the velocity at the pitot-static probe and at the fast location, the velocity was 3.60 times faster than the velocity at the pitot-static probe. The linear relationship was confirmed by varying the tunnel velocity and measuring several data points at each location.

The in situ calibration of the hot wire anemometer was performed as follows. The hot-wire was placed in one of the calibration locations. The tunnel was run for approximately 20 minutes to allow the tunnel air to reach an equilibrium temperature (it was important to maintain a constant mainstream temperature throughout the calibration and all measurements due to the nature

of the constant temperature anemometer). Calibration data were taken as the tunnel entrance velocity was varied between 4 m/s and 7 m/s. The hot-wire was then moved to the other location and the calibration continued. To obtain a zero velocity point, the tunnel was turned off and allowed to settle before taking the data. The tunnel was then turned back on to prepare for measurements.

The calibration relating the anemometer voltage output to velocity was produced using a fourth order curve fit less the cubic and linear terms as hot-wire anemometer theory suggests. I wrote a Matlab routine to do the curve fitting and plot the results as a sanity check. The script automatically used the Labview output files from the calibration procedure and saved the calibration coefficients in a file that Labview accessed when it was time to begin measurements.

Once calibration was completed, the hot-wire probe was moved into position and measurements would be made. Data was taken at a sample rate of 10,000 Hz over a period of 20 seconds in order to obtain a time history of velocity suitable for determining the integral length scale at a later time. However, the Labview system calculated and displayed the mean velocity and turbulence intensity as each data point is taken.

Turbulence intensity was measured by dividing the RMS velocity by the mean velocity as shown in the following equation:

$$Tu = \frac{\sqrt{\frac{1}{N} \sum_{i=1}^N (u_i - u_{mean})^2}}{u_{mean}} \quad (2.7.1)$$

The integral time scale of the turbulence could be determined by autocorrelating the time history of the velocity and integrating the output of the autocorrelation from  $x = 0$  to where the autocorrelation data first crossed the x-

axis. The integral length scale was then calculated by multiplying the integral time scale by the mean velocity.

## **2.8 UNCERTAINTY ANALYSIS**

The uncertainties in the experimental results were dependent upon the precision of the temperature measurements and the uncertainty of the mainstream and coolant flow rates. This section presents an analysis of this uncertainty. All reported uncertainties correspond to a 95% confidence interval.

### **2.8.1 IR Camera Resolution**

The IR camera digitally saved temperature data in a 320 x 240 pixel array. The camera's horizontal field of view was 1/3 greater than its vertical field of view, therefore each pixel represented equal horizontal and vertical angles. Ideally, the temperature given at each pixel would be determined by integrating over only the area covered by that pixel and thus independent of adjacent pixels. However, the nature of digital photography is such that adjacent pixels are not independent. The true resolution of the camera was determined by imaging sharp-edged objects with temperatures different from the background temperature so that a step change in temperature was imaged. By analyzing the temperature data across the step change, the resolution was found to be three pixels in both the x and y directions. Taking the curvature of the vane into consideration, this resolution corresponded to about 2 mm in the x direction at the upstream edge of the heat flux plate, 1 mm in the x direction at the trailing edge of the heat flux plate, and 1.3 mm in the y direction.



### 2.8.2 Mainstream Velocity

The mainstream velocity was measured using a pitot-static probe. Knowledge of the difference between the static and stagnation pressures combined with knowledge of the density of air allows one to calculate the velocity by application of Bernoulli's equation. A pressure transducer with a calibration uncertainty of  $\pm 1.99$  Pa and a precision uncertainty of  $\pm 0.34$  Pa was used to measure the pressure difference. The density as a function of the air temperature was determined by the ideal gas law. By using ice bath, boiling water, and boiling nitrogen tests, the thermocouples were found to have a total precision uncertainty of  $\pm 0.15$  K and a bias error of  $\pm 0.5$  K. This thermocouple uncertainty corresponded to a mainstream density uncertainty of  $5.8 \times 10^{-4}$  kg/m<sup>3</sup>. The resulting bias uncertainty in the velocity measurement was  $\pm 0.3$  m/s. The precision uncertainty was  $\pm 0.008$  m/s. Additionally, the wind tunnel fan control unit introduced fluctuations in the mainstream velocity. Data was never taken if the tunnel velocity had drifted more than 0.05 m/s from the desired velocity.

### 2.8.3 Coolant Flow Rates

The coolant flow rate was calculated by measuring the pressure across an orifice flow meter and the temperature at the orifice flow meter. The blowing ratio depended on this coolant flow rate, the mainstream velocity, and the mainstream density. Because an iterative technique was employed for the coolant flow rate calculation, the method of sequential perturbation was used to determine the uncertainty in blowing ratio due to uncertainty in the pressured drop across the orifice meter and the temperature at the orifice meter. The pressure transducer used with the suction side orifice meter had a calibration uncertainty of  $\pm 0.86$  Pa and the pressure transducer used with the showerhead orifice meter has an uncertainty of  $\pm 27.4$  Pa. The root sum of the squares of the

contributions to the blowing ratio uncertainty gives the total uncertainty in blowing ratio. The suction side blowing ratio bias uncertainty (due to the pressure transducer calibration) was  $\delta M = \pm 0.036$  at  $M = 0.3$  and  $\delta M = \pm 0.072$  at  $M = 1.4$ . The precision uncertainty is  $\delta M = \pm 0.0005$  at  $M = 0.3$  and  $\delta M = \pm 0.0018$  at  $M = 1.4$ . The bias uncertainty in the showerhead blowing ratio was  $\delta M = \pm 0.085$  ( $M = 1.6$ ) and the precision uncertainty was  $\delta M = \pm 0.002$ .

#### 2.8.4 Surface Temperature

The surface temperature was measured with an FLIR Model P20 infrared camera that was calibrated in situ using two type E ribbon thermocouples on the heat flux plate. Because a critical measurement in heat transfer tests is the difference between the mainstream temperature and the surface temperature, bias error was removed between the surface and mainstream thermocouples. The uncertainty in the calibration is determined via the standard deviation given by:

$$\sigma = \sqrt{\frac{\sum_{i=1}^N (T_{Measured} - T_{Calculated})_i^2}{N - (m + 1)}} \quad (2.8.4.1)$$

where  $N$  was the total number of data points and  $m$  was the order of the curve fit. Because the camera's output was a temperature, the curve fit was nearly linear. However, to better account for the influence of the salt window, second order curve fits were used. Typical infrared camera calibrations resulted in an uncertainty of  $\delta T = \pm 0.5$  K.

### 2.8.5 Heat Transfer Coefficient (Low Density Ratio)

The local heat transfer coefficient was determined by dividing the local convective heat flux by the difference between the surface temperature and the mainstream temperature. The surface temperature measurement error was determined by the accuracy of the infrared camera calibration. The heat flux was measured by using two voltmeters. The voltmeter used to measure the voltage across the shunt resistor had an uncertainty of 0.5% of the reading plus four in the last displayed digit. The voltmeter used to measure the voltage across the heat flux plate had an uncertainty of 0.5% of the reading plus one in the last digit. Additionally, there was an error associated with the area of the heat flux plate. The length and width were each known within 1 mm. The total typical error associated with the heat flux was typically  $\pm 55 \text{ W/m}^2$ , or 3 % of the measured heat flux. The uncertainty analysis using the method of Kline and McClintock (1953) was programmed into the Matlab data reduction script, allowing the uncertainty to be computed at each pixel. The uncertainty in the heat transfer coefficient was dominated by the uncertainty in the surface temperature measurement. Since the surface temperature was relatively constant in the spanwise direction, the error was relatively constant in the spanwise direction. If the uncertainties at each pixel were independent, the process of spanwise averaging the data would reduce the uncertainty by a factor of  $\frac{N}{\sqrt{N}}$ . However, much of the uncertainty was not random uncertainty. For example, there is a certain amount of error in the heat flux measurement, but it is the same at every pixel for each image, therefore that error does not decrease with spanwise averaging. The error reported at each x/d location is the average of the errors at that x/d location. The uncertainty varies very little between images. Since each test was performed at a nearly constant heat flux and the different conditions during each test had only very small effects on the surface

temperature, the uncertainty as a function of  $x/d$  was nearly constant through each test. The uncertainties for each test are reported in Figure 2.11. The uncertainties are displayed as percentages in Figure 2.12.

### 2.8.6 Heat Transfer Coefficient (High Density Ratio)

The uncertainty of the heat transfer coefficient obtained under high density ratio conditions was dependent on the uncertainty in the adiabatic effectiveness measurements. Robertson (2004) reported an uncertainty of  $\delta\eta = 0.02$ . Likewise, the uncertainty in the nondimensional temperature with heat transfer was  $\delta\eta' = 0.02$ . The method of Kline and McClintock was applied to Equation 2.6.2.17 to determine the uncertainty as a function of the heat transfer coefficient. The result was a dimensional equation that relates the heat transfer coefficient to the uncertainty in that heat transfer coefficient:

$$\delta h = 0.0005 \sqrt{1087h^2 + h^4} \quad (2.8.6.1)$$

where  $[h] = \frac{W}{m^2 K}$

Application of this uncertainty in a similar fashion as described in Section 2.8.5 gives the uncertainty presented in Figure 2.11 and 2.12. The uncertainty with the high density ratio test was approximately double that of the low density ratio tests. Most of the uncertainty in the high density ratio test was due to the surface temperature measurements and the high density ratio tests required two surface temperature measurements—one to obtain the wall temperature with heat flux and the other to obtain the adiabatic wall temperature. Furthermore, the wide surface temperature range of the high density ratio test contributed to a larger uncertainty in the temperature measurements.

### 2.8.7 Repeatability Within a Test

During the course of each heat transfer experiment, several operating conditions were repeated in order to gauge the repeatability of the data. Repeated spanwise averaged heat transfer coefficient curves were averaged and the maximum deviation from the average was noted. The leading region and trailing region of the heat flux plate was ignored due to the unreliability of the data in this region due to two-dimensional conduction effects. This process was performed on 15 separate repeated data points. The 95% confidence interval on the repeatability within a test is  $3.5 \text{ W}/(\text{m}^2 \text{ K})$ . This confidence interval corresponds to about 4.5% for the low end of the measured  $h$  values, or 1.8% for the high end of the measured  $h$  values. Figure 2.13 is a sample plot of data taken with the same test condition at two different times.

### 2.8.8 Repeatability Between Tests

Several test conditions were duplicated on different days. The same procedure used to find the repeatability within a test was used to find the repeatability between tests. The 95% confidence interval on the repeatability between tests was found to be  $7 \text{ W}/(\text{m}^2 \text{ K})$ , or between 3.5% and 9.5% depending on the magnitude of the heat transfer coefficient. Figure 2.14 is a sample plot of data taken with the same test condition on two different days.

### 2.8.9 Hot Wire Measurements

Precision error in the hot wire measurements was determined by logging hot wire data for a period of several minutes and calculating the standard deviations of the results. The precision error in velocity was  $\pm 0.026 \text{ m/s}$  (0.5% of the measured velocity) and the precision error in turbulence intensity was  $\delta Tu = \pm 0.14\%$  (3% of the measured turbulence intensity).

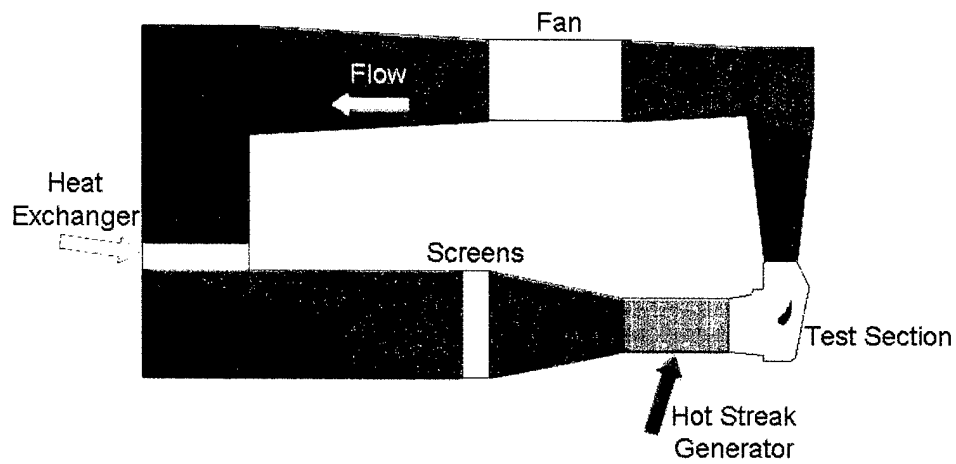


Figure 2.1: Schematic of the Closed-Loop Wind Tunnel Facility

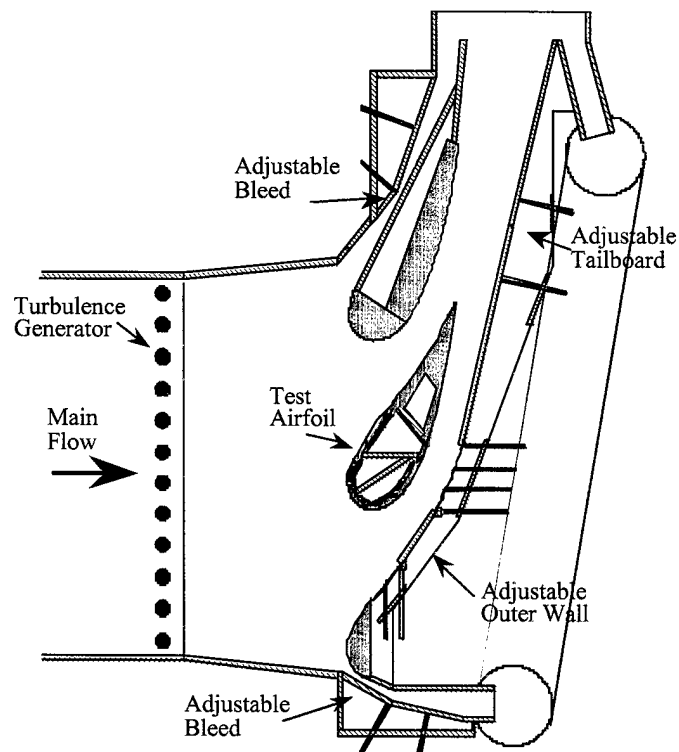


Figure 2.2: Schematic of the Turbine Vane Test Section

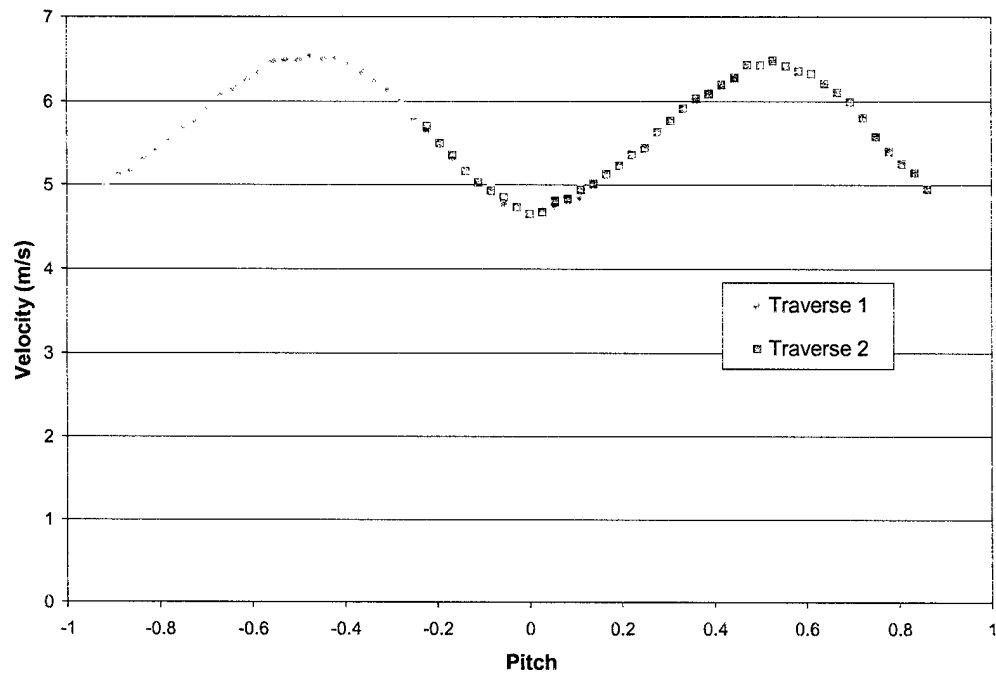


Figure 2.3: Velocity Profile 0.18c Upstream of the Vane Cascade

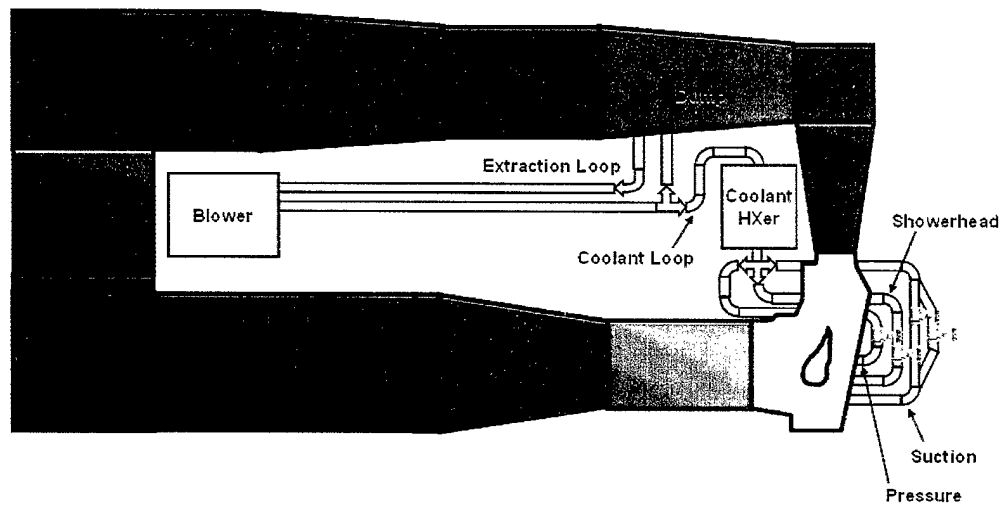


Figure 2.4: Schematic of the Secondary Loop

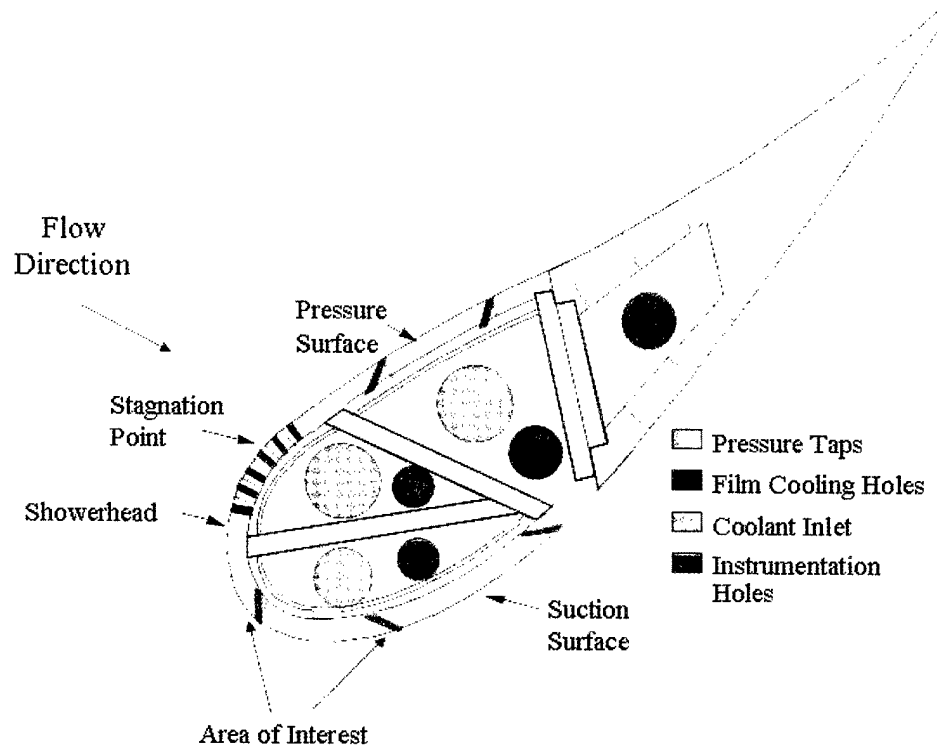


Figure 2.5: Test Vane Schematic



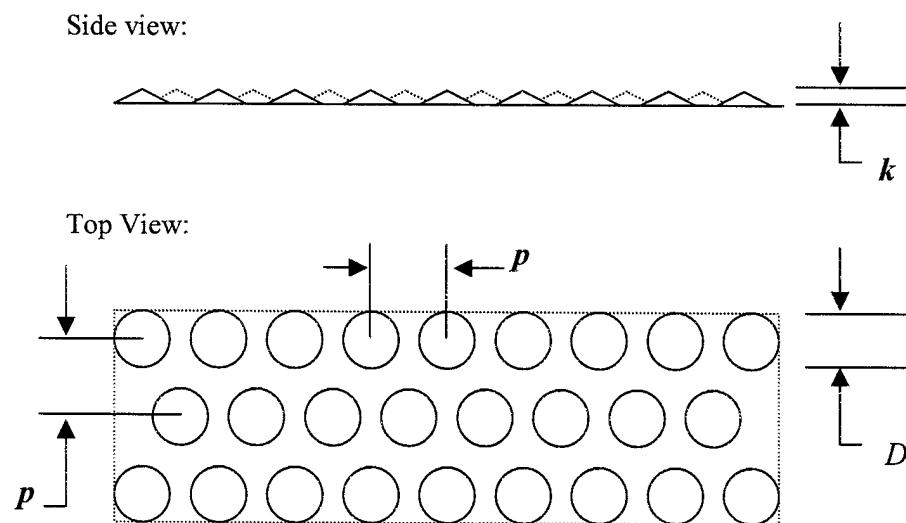


Figure 2.6: Surface Roughness Design Schematic

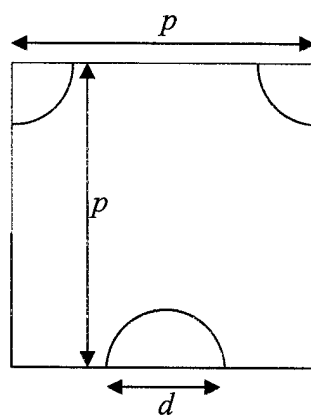


Figure 2.7: Smallest Repeating Element in Roughness Design

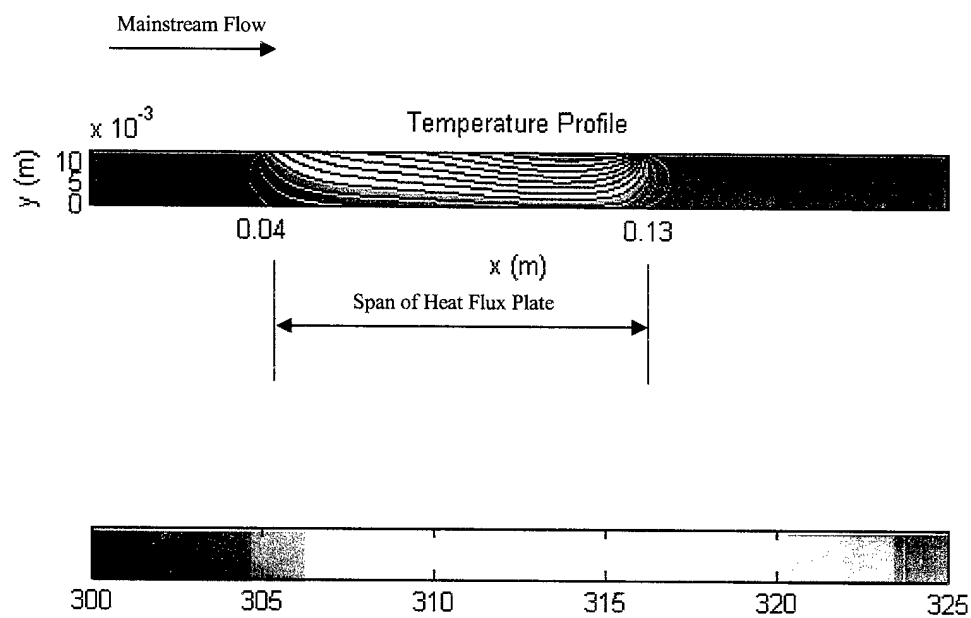


Figure 2.8: Numerically determined typical temperature profile within the vane wall under the heat flux plate. The applied electrical heat flux was  $1619 \text{ W/m}^2$ .

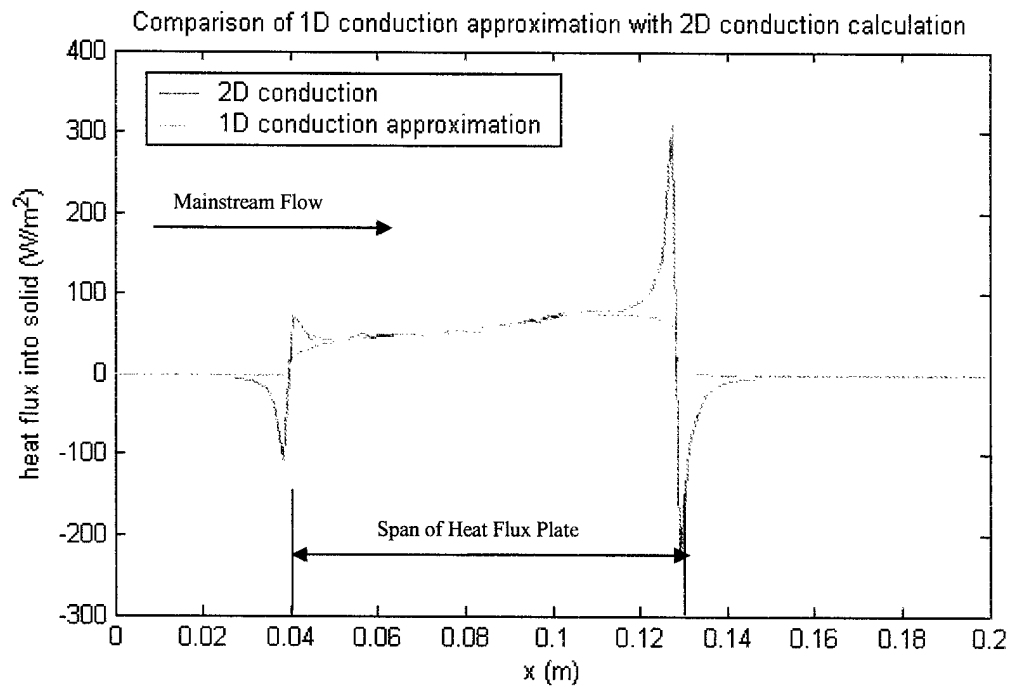


Figure 2.9: Comparison of conductive heat flux into the vane as computed with the one dimensional approximation and the two dimensional approximation. The applied electrical heat flux was  $1619 \text{ W/m}^2$ .

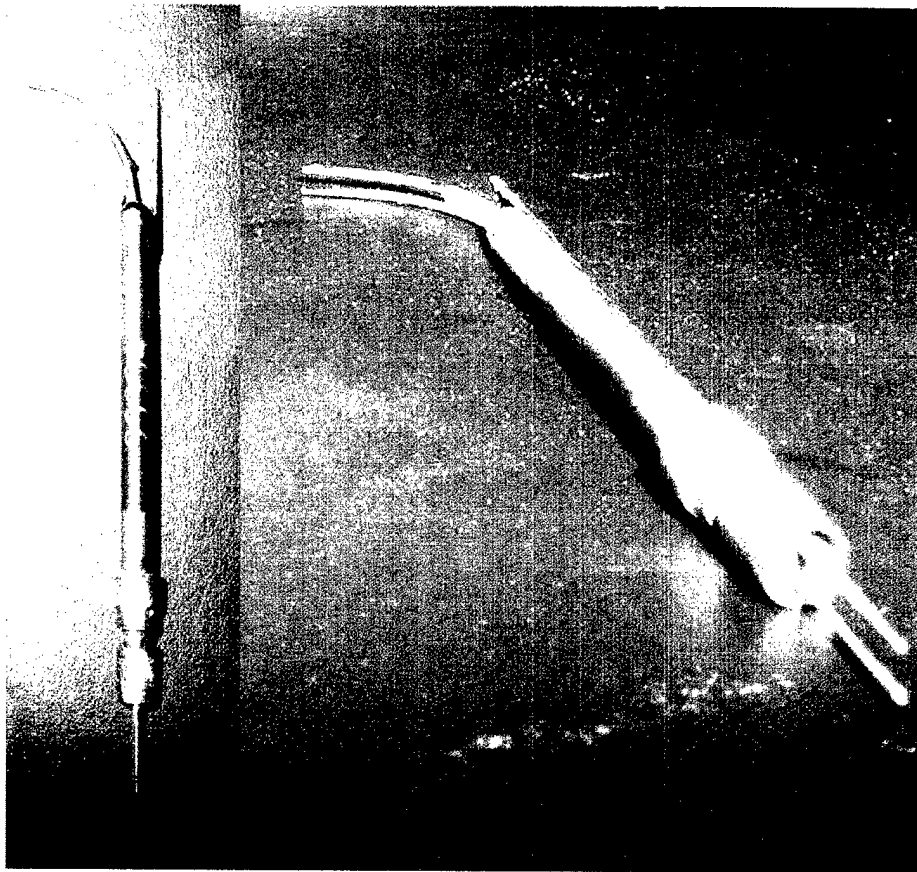


Figure 2.10: A boundary layer hot wire probe

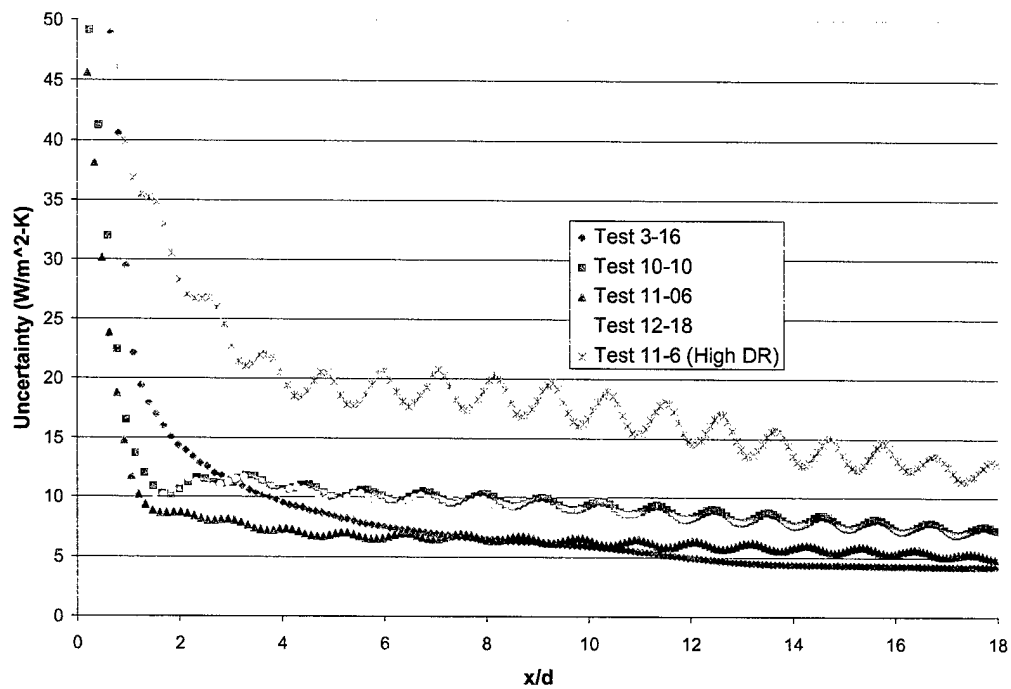


Figure 2.11: Uncertainties for each test calculated using the method of Kline and McClintock (1953)

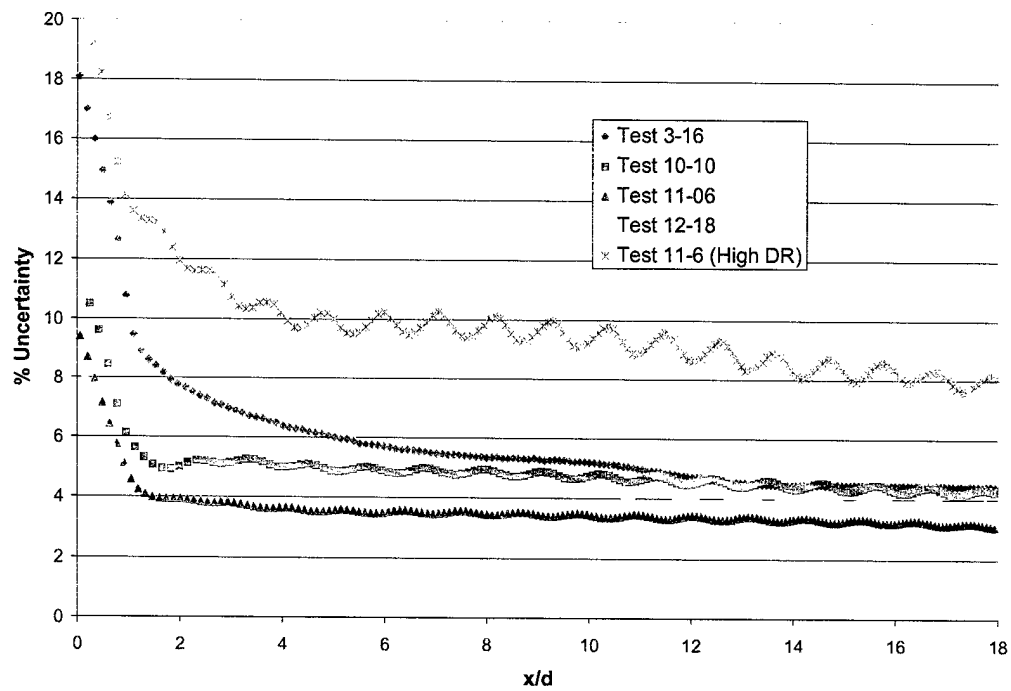


Figure 2.12: Percent Uncertainties for each test calculated using the method of Kline and McClintock (1953)

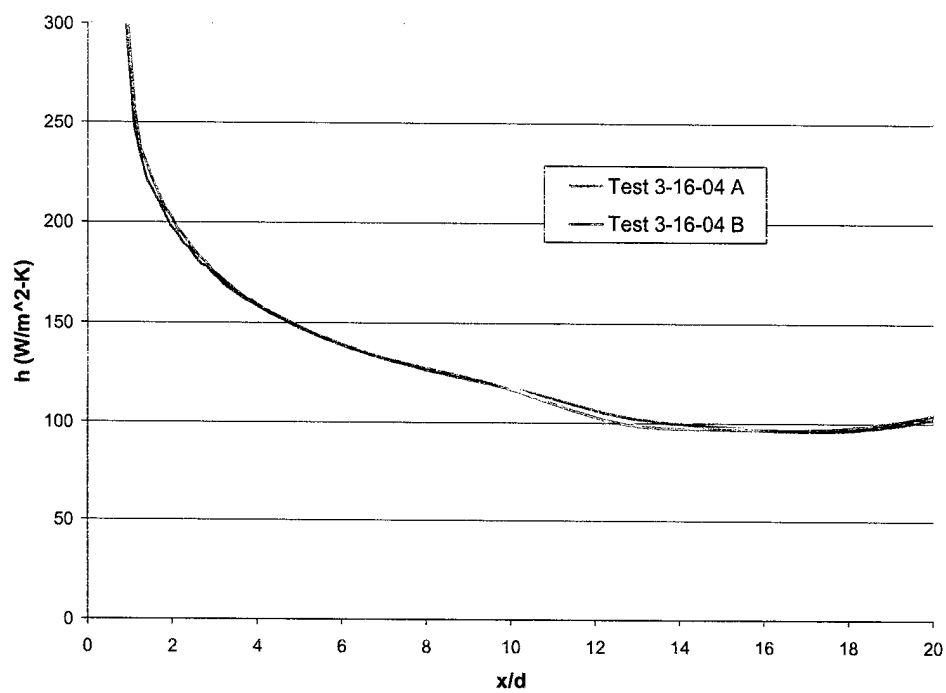


Figure 2.13: Repeatability within a test

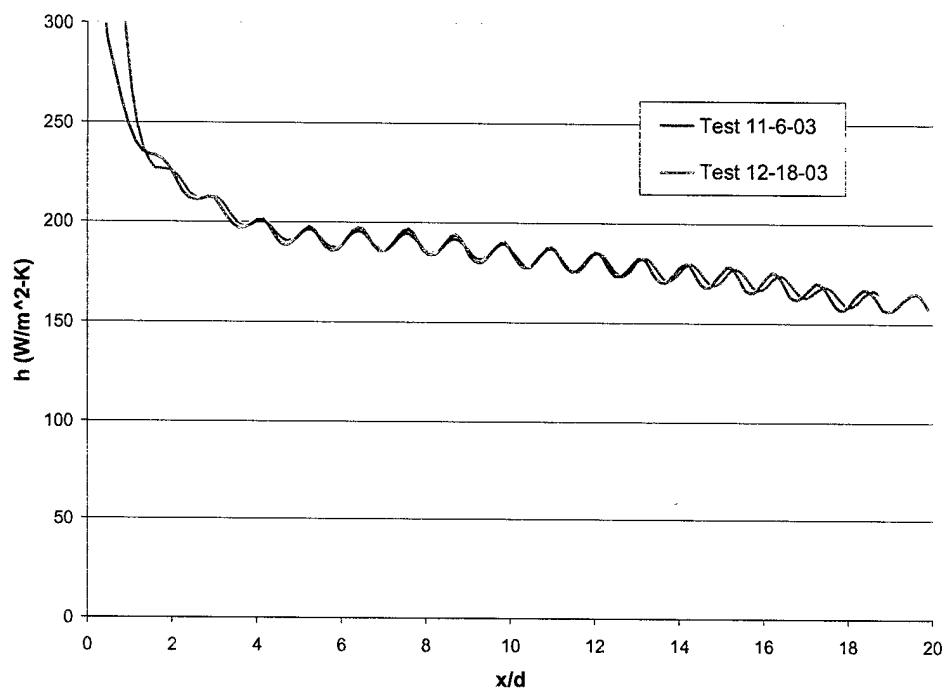


Figure 2.14: Repeatability between tests



## CHAPTER THREE

### EXPERIMENTAL RESULTS

This chapter presents the results of the heat transfer experiments and the boundary layer measurements from the present study. Results are organized by experimental condition. The boundary layer measurements are presented first in order to provide insight into the hydrodynamics of the flow that carries out the heat transfer. The heat transfer results are presented next, beginning with the baseline smooth wall condition and moving on to the rough conditions (one of which is a high density ratio test for comparison purposes). Finally, the heat transfer data is merged with the adiabatic effectiveness data from Robertson (2004) to provide net heat flux reduction information.

#### 3.1 TEST CONDITIONS

Table 3.1 summarizes the test conditions that are discussed in greater detail in Chapter 2. Tables 3.2 and 3.3 provide a list of the experiments used to generate the data. Low freestream turbulence refers to a freestream turbulence intensity of  $Tu_{\infty} = 5.2\%$  at  $0.18 C$  upstream of the vane leading edge. High freestream turbulence refers to a freestream turbulence level of  $Tu_{\infty} = 21\%$ . Turbulence length scales were  $\Lambda_f/C = 0.074$  and  $\Lambda_f/C = 0.069$  for the low and high turbulence levels, respectively. One heat transfer test was performed at a density ratio of  $DR = 1.6$ . All other tests were performed at a density ratio of  $DR = 1.0$ . Due to the subtlety of the effects of showerhead blowing, freestream turbulence, and upstream roughness, several tests were performed in which all of these parameters were varied in order to resolve those effects without the interference of test-to-test repeatability issues. For all measurements made without the showerhead, the showerhead was completely covered with 0.3 mm thick tape in order to avoid boundary layer disturbance upstream of the test area

from the showerhead holes. When the showerhead was in operation, it was operated at  $M_{sh} = 1.6$ .

Table 3.1: Test Conditions

Chord Length	59.4 cm
Span	54.9 cm
Pitch	45.7 cm
Inlet Velocity	5.8 m/s
Exit Reynolds Number	$1.06 \times 10^6$
High Freestream Turbulence at Inlet	$Tu = 21\%$ $\Lambda_f = 4.1$ cm
Low Freestream Turbulence at Inlet	$Tu = 5.2\%$ $\Lambda_f = 4.4$ cm
Showerhead Blowing Ratio (when in use)	$M_{sh} = 1.6$
Film Cooling Hole Diameter	4.11 mm

Table 3.2: Boundary Layer Experiments

Date	s/C	Baseline Condition	Additional Conditions
1/29/2004	0.19	Low Tu, No Roughness, No Cooling	Roughness; High Tu; Showerhead; Trip Rod
2/20/2004	0.19	Low Tu, No Roughness, No Cooling	Vane covered in a plastic sheet
2/26/2004	0.19	High Tu, No Roughness, No Cooling	Roughness; Showerhead; Roughness and Showerhead; Trip Rod
2/27/2004	0.22	Low Tu, No Roughness, No Cooling, Between Holes	Behind Hole (no blowing); Behind Hole (with blowing)
3/5/2004	0.35	Low Tu, No Roughness, No Cooling	Upstream Roughness; Showerhead

Table 3.3: Heat Transfer Experiments

Date	Freestream Turbulence Intensity	Showerhead	Upstream Condition	Downstream Condition	Density Ratio
10/10/2003	High / Low	On / Off	Smooth	Rough	1.0
11/6/2003	High / Low	On / Off	Rough	Rough	1.0
11/12/2003	Low	Off	Rough	Rough	1.6
12/18/2003	High / Low	On / Off	Rough / Smooth	Rough	1.0
3/16/2004	High / Low	On / Off	Rough / Smooth	Smooth	1.0

### 3.2 BOUNDARY LAYER MEASUREMENTS

This section presents the results of the boundary layer measurements. These measurements were conducted at four locations—two hole diameters upstream of the coolant holes ( $s/C = 0.19$ ), one hole diameter downstream of a hole ( $s/C = 0.22$ ), one hole diameter downstream of the holes between two holes, and at  $s/C = 0.35$ , which was  $1.5 d$  upstream of the second row of coolant holes. The high rate of acceleration in the region caused the measured velocity to be very sensitive to position. Therefore it is desirable to compare data acquired on the same day, during which the probe traverse was clamped in a fixed position.

Inviscid flow around a vane has its highest velocity adjacent to the vane. However, the no slip condition at the wall causes the actual flow to deviate from the inviscid flow, thus there is a boundary layer. This phenomenon is clearly seen in Figure 3.1 and creates difficulty in defining the boundary layer. Although the location of the peak velocity is a tempting definition of the boundary layer thickness, the influence of the wall clearly extends beyond the

peak as the velocity profile asymptotically approaches the inviscid profile. The boundary layer thickness,  $\delta_{99 \text{ inviscid}}$ , is defined as the location where the velocity was 99% of the velocity it would have been if the flow were inviscid. The inviscid velocity distribution was determined by fitting a linear curve through the outer data points in the inviscid flow regime. Radomsky and Thole (2002) defined the boundary layer thickness, called  $\delta_{99 \text{ peak}}$  in this document, as the location nearest the wall where the velocity was 99% of the peak velocity. This definition allows for comparison with the data of Radomsky and Thole.

The boundary layer measurements were conducted in collaboration with David Robertson. The results complement both the heat transfer study of this thesis and the adiabatic effectiveness study of Roberston (2004).

### **3.2.1 $s/C = 0.19$ Smooth Surface Check**

Measurements performed on 2/20/04 were conducted at low freestream turbulence, without any film cooling, without surface roughness, and without any heat flux plates. The purpose of the test was to determine how the standard smooth condition of the vane compared to the vane covered in transparency film. Duct tape (0.3 mm thick) was placed over the seam between the hatch and the rest of the vane approximately four cm upstream of the first row of suction side holes as part of standard procedure. Duct tape was also placed over the showerhead region as part of standard procedure. One set of measurements was performed with the vane in this standard condition. The other set of measurements was performed with overhead projector transparency covering the surface of the vane, providing a smoother vane surface without any duct tape. The velocity profiles are presented in Figure 3.1. At  $z/d < 0.2$ , it would appear that the velocities measured without the transparency film were less than the velocities measured with the transparency film. However, this conclusion

cannot be drawn due to the uncertainty in determining the position of the wall. The addition of transparency film to the vane surface altered the wall position and was difficult to locate due to the transparent nature of the film. If the velocity profiles were in fact identical, there would be an error of 0.1 mm (20 hot-wire diameters) in the wall location, which is reasonable, particularly with the transparency film. The turbulence levels in the boundary layer were also the same with and without the transparency film. This comparison demonstrates that the boundary layer flow around the imperfect vane (with duct tape covering the showerhead and the hatch seam) was equivalent to what it would be if the surface were covered in plastic for a greater degree of smoothness. Armed with this knowledge, we can proceed to consider the vane smooth as it was used in the remainder of experiments of this thesis.

### **3.2.2 $s/C = 0.19$ Tests With Low Turbulence Baseline**

This section presents the data that was acquired on 1/29/04. During this test, the individual effects of roughness, showerhead cooling, and the trip rod were compared against the baseline low turbulence case. Additionally, the effect of high turbulence was tested. The baseline condition was a smooth vane with no heat flux plates and low freestream turbulence. The trip rod was 1.59 mm in diameter and was placed approximately  $7d$  upstream of the suction side coolant holes for one of the conditions. The condition with the roughness used a rough plate whose downstream edge was approximately  $1d$  upstream of the hot wire probe. Mean velocity and turbulence level profiles are presented in Figures 3.2 and 3.3. The plotted turbulence levels are not based on the local velocity, but are based on the edge velocity of the baseline condition to facilitate direct comparison of the fluctuating velocities.

Radomsky and Thole (2002) made several boundary layer measurements on an identical vane geometry at Virginia Tech. Dr. Thole was kind enough to

provide their raw data files for direct comparison purposes. One of their measurements was at  $s/C = 0.21$ . Radomsky and Thole used a high turbulence condition ( $Tu_{\infty} = 19.5\%$ ) and a low turbulence condition ( $Tu_{\infty} = 0.6\%$ ). The lack of a hot streak generator allowed their low turbulence condition to be much lower than the low turbulence condition of the present study. Our measured boundary layer thickness at low turbulence of  $\delta_{99 \text{ peak}} = 0.58 \text{ mm}$  at  $s/C = 0.19$  is in good agreement with Radomsky and Thole who measured it to be  $0.61 \text{ mm}$  at their low turbulence condition. At high turbulence, for which the conditions were very similar ( $Tu_{\infty} = 19.5\%$  vs.  $Tu_{\infty} = 21\%$ ), the boundary layer thicknesses were  $\delta_{99 \text{ peak}} = 0.77 \text{ mm}$  and  $0.71 \text{ mm}$  for the present study and the study of Radomsky and Thole, respectively.

The turbulence level profiles shown in Figure 3.3 indicate that the turbulence intensities were elevated by the high turbulence case, particularly far from the wall. Sufficiently far from the vane, the turbulence intensity approached the freestream turbulence intensity, which was a function of streamwise position. From the inlet turbulence intensities given in Table 3.1, the freestream turbulence intensity decreased to  $Tu = 5.0\%$  and  $1.2\%$  (based on the local velocity) at  $s/C = 0.19$  for the high and low freestream turbulence intensities, respectively.

The effect of the showerhead was to decrease the velocity within the boundary layer (including the peak velocity) and decrease the velocity gradient in the vicinity of the edge of the boundary layer. The addition of roughness caused the boundary layer to grow substantially. Boundary layer thicknesses are given in Table 3.4.

Table 3.4: Boundary Layer Thicknesses for Test 1-29  
(Baseline Condition Low  $Tu$ )

Condition	$\delta_{99 \text{ peak}} / d$ Present Study	$\delta_{99 \text{ peak}} / d$ Radomsky and Thole (2002)
Baseline Low $Tu$	0.14	0.15 ( $Tu_{\infty} = 0.6\%$ )
Roughness	0.45	
High $Tu$	0.19	0.17 ( $Tu_{\infty} = 19.5\%$ )
Showerhead	0.19	
Trip Rod	0.56	

In addition to thickening the boundary layer, the roughness also increased the turbulence intensity inside the boundary layer. From a heat transfer perspective, these two effects compete with one another. The showerhead also increased turbulence levels inside the boundary layer, but the most prominent characteristic of the showerhead was the increase in turbulence far outside of the boundary layer. The additional turbulence was detected as far out as 1.3 cm (3.2  $d$ ).

The trip rod was found to cause a very strong disturbance in the boundary layer, thickening the boundary layer by a factor of 4. Additionally, the trip rod caused higher turbulence intensities than either the showerhead or the roughness. However, the turbulence created by the trip rod was localized to  $z/d < 1$ .

Profiles of the integral length scale for the baseline low turbulence condition, the high turbulence condition, and low turbulence with the showerhead are presented in Figure 3.4. The integral length scale of the turbulence caused by the showerhead was generally about half the size of the integral length scale of the high turbulence condition.

Figures 3.5 and 3.6 are plots of the high and low turbulence velocity profiles nondimensionalized by  $\delta_{99 \text{ inviscid}}$  and  $\delta_{99 \text{ peak}}$ , respectively. Also plotted are turbulent and laminar profiles given by the following equations:

$$\frac{u}{U_e} = \left( \frac{y}{\delta} \right)^{1/7} \quad (3.2.2.1)$$

$$\frac{u}{U_e} = 2 \left( \frac{y}{\delta} \right) - \left( \frac{y}{\delta} \right)^2 \quad (3.2.2.2)$$

At low turbulence,  $\delta_{99 \text{ inviscid}}$  was 30% larger than  $\delta_{99 \text{ peak}}$ . At high turbulence,  $\delta_{99 \text{ inviscid}}$  was 15% larger than  $\delta_{99 \text{ peak}}$ . Despite these differences, the two boundary layer profiles of Figures 3.5 and 3.6 are very similar. Because the shape of the boundary layer does not depend on the definition of the boundary layer thickness, the focus throughout the remainder of the document is on  $\delta_{99 \text{ peak}}$ . In addition to the high and low turbulence conditions tested on 1/29/04, a repeat of the low turbulence profile is presented. The repeated profile appears more laminar than the original. The repeatability between the tests indicates that boundary layer state conclusions cannot be formulated with the present data. Probe vibration and uncertainty in determining the wall location may have caused the inconsistency in the boundary layer profiles nondimensionalized by the boundary layer thickness.

Also plotted on Figure 3.6 are the boundary layer profiles of Radomsky and Thole (2002). At their lowest inlet turbulence intensity ( $Tu_\infty = 0.6\%$ ), Radomsky and Thole obtained a boundary layer profile very near that of the parabolic laminar profile. Radomsky and Thole obtained a boundary layer at their high turbulence condition ( $Tu_\infty = 19.5\%$ ) that exhibited traits characteristic



of a transitional boundary layer. Although their low turbulence intensity was much lower than the low turbulence case of the present study, their high turbulence intensity was nearly the same as the high turbulence intensity of the present study.

### **3.2.3 $s/C = 0.19$ Tests With High Turbulence Baseline**

On 2/26/04, a test was performed using high turbulence as the baseline condition. The baseline high turbulence condition had no surface roughness and no showerhead blowing and was identical to the high turbulence condition tested on 1/19/04. The four additional parameters used were roughness, showerhead blowing, the trip rod, and combined showerhead blowing and roughness. Note that low turbulence was not tested. Velocity and turbulence intensity profiles (based on the edge velocity of the baseline condition) are presented in Figures 3.7 and 3.8, respectively. Table 3.5 gives the boundary layer thicknesses for this experiment. Again, the roughness caused the boundary layer to thicken. The showerhead caused a much smaller increase in the boundary layer thickness. The combined roughness / showerhead test demonstrates that roughness effects dominated in the behavior of the boundary layer.

Table 3.5: Boundary Layer Thicknesses for Test 2-26  
(Baseline Condition High  $Tu$ )

Condition	$\delta_{99 \text{ peak}} / d$
Baseline High $Tu$	0.16
Showerhead	0.19
Roughness	0.44
Roughness / Showerhead	0.45
Trip Rod	0.57

As with low freestream turbulence, roughness again caused a large increase in turbulence intensity within the boundary layer. However, the showerhead did virtually nothing to the turbulence intensity. For the low freestream turbulence case, the turbulence intensity at the edge of the boundary layer with showerhead blowing was less than 5%. Under the high freestream turbulence condition, the turbulence intensity far from the wall approached approximately 5%. Furthermore, the integral length scale of the turbulence created by the showerhead at low freestream turbulence was shown to be smaller than the integral length scale of the high turbulence condition alone. Thus it is not surprising that the turbulence of the high turbulence condition dominated over the turbulence created by the showerhead.

At high turbulence, the effect of the trip on the boundary layer again was strong. For  $z/d < 0.4$ , the velocity with the trip was less than the velocity without roughness, but greater than the velocity with roughness. However, the boundary layer with the trip was much thicker and the peak velocity was 4% higher than the baseline condition without the trip.

Figure 3.9 presents turbulence intensities from the low turbulence test (1/29/04) and the high turbulence test (2/26/04) to compare the effects of roughness and freestream turbulence intensity on the turbulence intensity. The

plotted turbulence intensities are based on the edge velocity of the smooth low turbulence condition. Roughness combined with high freestream turbulence yielded the highest turbulence intensities in the boundary layer. This seems to indicate that there may be an interaction between the roughness and the high freestream turbulence.

The baseline high turbulence condition of Test 2/26 was the same as the high turbulence condition during Test 1/29 (for which the baseline condition was low turbulence). The boundary layer thicknesses differ by 17%. This discrepancy is primarily due to uncertainty in the position of the wall. Furthermore, Test 2/26 occurred at a position slightly upstream of the position used for Test 1/29. The peak velocities for these similar conditions between the two tests differ by 0.5 m/s. Through examination of the data in Radomsky (2000), one can estimate that the acceleration in that region was about 0.8 m/s/mm, indicating a difference in streamwise position of about 0.6 mm.

#### **3.2.4 Measurements Downstream of the Row of Holes**

In order to gain an improved understanding of how coolant jets affect the boundary layer, additional measurements were made at a location one hole diameter downstream of the coolant holes ( $s/C = 0.22$ ). Figure 3.10 shows the velocity profiles between two holes and directly behind a coolant hole with and without blowing. The velocity behind a hole with  $M = 0$  was within 2% of the velocity between two holes. Similarly, the turbulence profiles (based on the edge velocity of the "between holes" condition) in Figure 3.11 show that the presence of a hole that was not blowing had little effect on the turbulence. The results were much different when the coolant hole was blowing. The jet caused a great increase in the turbulence intensities and a decrease in velocity.

Pietrzyk et al. (1989) used a LDV to obtain hydrodynamic measurements of jets in crossflow. The jets were on a flat plate and were

inclined  $35^\circ$ . Blowing ratios of  $M = 0.25$ ,  $0.5$ , and  $1.0$  were studied. The authors found a wake region downstream of the jet. With  $M = 0.5$ , a local minimum in the mean velocity occurred at approximately  $0.2 d$  off of the surface, with a mean velocity of approximately half of what it would have been without the jet. In the present study with  $M = 0.7$ , the local minimum in mean velocity occurred at  $0.13 d$  off of the surface with a velocity of approximately  $1/3$  what it would have been without the jet. In both studies, the peaks in the turbulence intensity corresponded to the location of the strong shear layer between the relatively slow velocity of the wake and the faster mainstream.

### 3.2.5 Measurements at $s/C = 0.35$

Several boundary layer measurements were performed at  $s/C = 0.35$ , which would have been near the end of the heat flux plate, had the heat flux plate been installed. The location was approximately  $1.5 d$  upstream of the second row of suction side coolant holes. The incentive of these measurements was to gauge how quickly upstream effects decay. Measurements were made without suction side blowing with the suction side holes covered so that measurements would be insensitive to spanwise location. For these tests, the baseline condition was low turbulence, no showerhead blowing, and no roughness. The effects of high turbulence, showerhead blowing, upstream roughness, and the trip rod were tested individually. It must be emphasized that the term "upstream roughness" refers to roughness upstream of the suction side coolant holes at  $s/C = 0.21$ ; the region  $0.21 \leq s/C \leq 0.35$  was smooth. The results are presented in Figures 3.12 and 3.13. The equivalent velocity profile at  $s/C = 0.19$  is repeated in Figure 3.12 for comparison purposes.

Due to strong acceleration on the suction side, the peak velocity increased by 52% for the low turbulence baseline conditions between  $s/C = 0.19$  and  $s/C = 0.35$ . At  $s/C = 0.35$ , effects of the roughness and the showerhead had

not completely attenuated. The roughness, the trip rod, and the showerhead all caused velocity defects near the wall as well as elevated turbulence intensities away from the wall. Similar to  $s/C = 0.19$ , the roughness caused the higher velocity defect near the wall and the showerhead caused the higher turbulence intensity away from the wall. Although the trip caused a greater velocity defect in the boundary layer than the roughness did at  $s/C = 0.19$ , the effect of the trip decayed faster than the effect of the roughness. Consequently, at  $s/C = 0.35$ , the velocity profile with the trip was closer to the baseline velocity profile than roughness velocity profile. Also, the turbulence intensity profiles with the roughness and with the trip were nearly identical. At  $s/C = 0.19$ , the increase in turbulence due to the showerhead was limited to less than  $3.2 d$  from the surface, whereas at  $s/C = 0.35$ , there was still a noticeable turbulence augmentation at  $3.2 d$ , the farthest location from the surface where data was acquired. Aside from the trip rod case, the rest of the boundary layer thicknesses grew between  $s/C = 0.19$  and  $s/C = 0.35$ . Boundary layer thicknesses at  $s/C = 0.35$  are presented in Table 3.6. In the baseline and showerhead conditions, the boundary layer thicknesses each grew by a factor of 2.4 between  $s/C = 0.19$  and  $s/C = 0.35$ . The boundary layer thickness with upstream roughness grew only by a factor of 1.3. The boundary layer thickness with the trip rod decreased 5% due to the decay of the trip effect.

Table 3.6: Boundary Layer Thicknesses at  $s/C = 0.35$

	$\delta_{99 \text{ peak}} / d$
<b>Baseline Low Tu</b>	0.34
<b>Upstream Roughness</b>	0.58
<b>Showerhead</b>	0.46
<b>Trip Rod</b>	0.53

### 3.3 SMOOTH VANE HEAT TRANSFER RESULTS

In order to gain an appreciation for the effects of surface roughness on heat transfer, the baseline smooth wall data is presented first. The data presented in this section was acquired on 3/16/04.

#### 3.3.1 Smooth Heat Transfer Without Showerhead Blowing

Figure 3.14 presents the spanwise averaged heat transfer coefficients for the completely smooth surface with high freestream turbulence. Figure 3.15 shows the effect of blowing on the spanwise averaged heat transfer coefficient at  $x/d = 12$ . The "holes covered" condition was accomplished by covering the holes with a piece of 3M Scotch tape 0.004 cm thick. The tape thickness was about 7% of the boundary layer thickness, thus the tape was presumed to have no effect on the heat transfer coefficient. The figures indicate that merely exposing the holes caused an increase in the heat transfer coefficient. Although the boundary layer measurements indicate that the holes cause no additional turbulence, a small effect of the holes on the heat transfer coefficient was evident by comparing the heat transfer coefficient contour plots, Figures 3.16 and 3.17.

The addition of blowing caused a significant increase in the heat transfer coefficient. This phenomenon is noticeable both in Figure 3.14 and the contour plots of Figures 3.18 through 3.20. Figures 3.21 through 3.23 are augmentation plots showing the ratio  $h_f/h_o$  for several blowing ratios. The large amount of turbulence created by the jet at  $M = 0.7$  that was detected by the boundary layer measurements may have been the mechanism that caused this increase in  $h$  behind the film cooling holes. Recall that the coolant temperature was nominally the same as the mainstream temperature and that there was no heated starting length, so the effects of blowing reported here are due only to hydrodynamic effects of the jets and not thermal effects. Interestingly, the

spanwise averaged heat transfer coefficient was insensitive to changes in the blowing ratio that corresponded to the tested range,  $0.3 \leq M \leq 1.4$ . However, when the coolant flow rate was turned up as high as it would go in the facility, a noticeable increase in  $h$  was observed. This blowing ratio is unknown due to measurement equipment limitations, however it has been confirmed to be in the range  $3 < M < 4$ . According to Robertson (2004), the jets were detached in the region of interest for  $M \geq 1.0$ . Since there was not a significant increase in  $\bar{h}$  for  $M = 1.4$  compared to  $M = 0.3$ , we cannot conclude that jet detachment is the key to a large increase in  $h$ . Instead we can conclude that either there is a critical blowing ratio above  $M = 1.4$  where  $\bar{h}$  increases, or that the rate of increase in  $\bar{h}$  with  $M$  is more constant, but too small to detect in the range  $0.3 \leq M \leq 1.4$ . The large effect of a small amount of suction side blowing and the lack of effect of adjusting the blowing ratio indicates that the film cooling may trip the boundary layer.

Figure 3.24 presents the spanwise averaged heat transfer coefficients for the completely smooth surface with low freestream turbulence. Figure 3.25 shows the effect of blowing on the laterally averaged heat transfer coefficient at  $x/d = 12$ . Again we see that exposure of the holes increased the heat transfer coefficient and blowing caused another increase. The spanwise averaged heat transfer coefficient was insensitive to adjustments in the blowing ratio. As expected, high freestream turbulence increased  $\bar{h}$  slightly for the no blowing, no holes case. The measured increase was about 6%. However, effects of blowing dominated over freestream turbulence and the augmentation in  $\bar{h}_f$  was not seen with high turbulence.

The contour plot of low freestream turbulence heat transfer coefficient in Figure 3.26 reveals a characteristic of turbulence when compared with the high freestream turbulence contour plots. The regions of high heat transfer

downstream of the coolant holes exhibit greater spanwise spreading under high freestream turbulence conditions. As demonstrated with the boundary layer measurements, the shear layer created by a jet caused elevated turbulence intensities. The turbulent shear layer was spread wider under high freestream turbulence conditions. Figure 3.27 shows the augmentation in  $h$  due to blowing at  $M = 0.7$  under low freestream turbulence conditions. Compared to the high turbulence condition, the augmentation at low turbulence was more confined to regions directly downstream of the coolant holes. The contour plot of Figure 3.28 shows  $h/h_o$ , or the augmentation in the heat transfer coefficient due to high freestream turbulence. An augmentation that approached 15% toward the downstream end of the heat flux plate was apparent between the holes. However, the heat transfer coefficient was decreased along the hole centerlines. As the jets were dispersed in the spanwise directions, the intensity of the jets was decreased on the centerline, resulting in turbulence having little effect on  $\bar{h}$  with suction side blowing.

The present study detected that the high turbulence condition produced heat transfer coefficients only 6% higher than the low turbulence condition. Schmidt and Bogard (1996) (see Section 1.3.6.2) reported increases of between 15% and 30% with high freestream turbulence (turbulence intensities were  $Tu_\infty = 0.3\%$ , 10%, and 17%) in their flat plate studies. However, the two turbulence intensities at the film cooling holes in the current study are  $Tu_\infty = 1.2\%$  and 5%, a small difference relative to the wider range turbulence intensities used by Schmidt and Bogard. The reported influence of turbulence of Schmidt and Bogard applied to the reference condition without film cooling and the condition with film cooling. The present study detected no difference in the spanwise averaged heat transfer coefficient between the two turbulence intensities for film cooled cases. At both  $Tu_\infty = 0.3\%$  and 10% (bracketing the



turbulence intensities of the present study), Schmidt and Bogard found that blowing at  $I = 1.1$  ( $M = 1.0$ ) increased the heat transfer coefficient by approximately 20% near the hole, whereas blowing at  $I = 0.3$  ( $M = 0.5$ ) decreased the heat transfer coefficient by approximately 10%. For all blowing conditions and both turbulence intensities, the present study detected increases in the centerline heat transfer coefficient of approximately 30% downstream of the hole. In no case on the smooth surface was film cooling found to decrease the heat transfer coefficient in the present study. Since it is possible that the boundary layer of the present study was not turbulent, the confirmed turbulent boundary layer of Schmidt and Bogard may have prevented the jets from having the same magnitude of influence on the heat transfer coefficient as the jets of the current study.

Ammari et al. (1990) found larger augmentations in the centerline heat transfer coefficient in their flat plate studies than the present study. Ammari et al. had a confirmed turbulent boundary layer. At  $M = 1.46$ , blowing caused an increase of 60% near the hole, 45% at  $x/d \approx 3$ , 20% at  $x/d \approx 10$ , and 10% at  $x/d \approx 15$ . The present study found lower centerline heat transfer coefficient augmentations in the near hole region, but the influence of blowing in the current study did not decay as rapidly. The heated starting length used by Ammari et al. might have caused the higher augmentations in the near hole region. Ammari et al. also found an interaction between the jets resulting in heat transfer coefficient augmentation between the holes that could not be predicted via superposition. Although the present study did not compare the effect of a row of holes versus a single hole, elevated heat transfer coefficients were detected between the film cooling holes.

Radomsky (2000) performed heat transfer measurements on a nearly identical vane geometry with a uniform heat flux on the entire vane surface. The only difference from the geometry of the present study was the fact that

Radomsky's vane had no film cooling holes and no hatch, thus it was a smoother surface. The turbulence intensity  $Tu_{\infty} = 19.5\%$  of Radomsky is comparable to the high turbulence condition of the present study. At  $s/C \approx 0.3$ , Radomsky measured  $St \approx 0.0077$  ( $St$  was based on  $U_{approach}$ ), or  $h \approx 55 \text{ W/(m}^2 \text{ K)}$ . This location corresponds to  $x/d \approx 13$ , where the heat transfer coefficient of the present study (with the smooth surface and no film cooling) was measured to be  $h \approx 87 \text{ W/(m}^2 \text{ K)}$ , or  $St \approx 0.012$ . The 58% higher heat transfer coefficient of the present study may be attributed to the unheated starting length. A correlation presented by Kays and Crawford (1993) indicates that if the vane were a flat surface in zero pressure gradient and had a laminar boundary layer, the heat transfer coefficient with an unheated starting length would be 56% higher than with a heated starting length.

### 3.3.2 Smooth Heat Transfer With Showerhead Blowing

Figure 3.29 shows the effect of the showerhead on the spanwise averaged heat transfer coefficient when the suction side coolant holes were covered. The figure also clearly shows the effect of turbulence. The showerhead caused an increase in the heat transfer coefficient for the low turbulence condition. An increase in  $\bar{h}$  was not evident for the high turbulence condition.

Like the case without showerhead cooling, Figures 3.30 and 3.31 show that  $\bar{h}$  was insensitive to changes in the suction side blowing ratio with showerhead cooling. Contour plots of the heat transfer coefficient with showerhead blowing at high and low turbulence are presented in Figures 3.32 through 3.35. For the low turbulence condition, the showerhead promoted lateral mixing of the jets, similar to the effect of high turbulence without the showerhead. The showerhead coolant holes were oriented with a compound

angle of  $90^\circ$ , therefore the velocity of the flow around the vane had a small spanwise component. The flow out of the suction side coolant holes was influenced by this and is evident in the contour plots of the heat transfer coefficient.

### **3.3.3 Trip Rod Effects on Heat Transfer**

A 1.59 mm diameter rod was placed  $7d$  upstream of the first row of suction side holes in order to determine how that rod affects the heat transfer coefficient. Figure 3.36 presents the heat transfer coefficient augmentation that occurred for the trip under high and low turbulence conditions. Additionally, data was taken for a case with film cooling to determine if the wake from the rod changed how the jet affects the heat transfer coefficient. In all cases, the effect of the trip was within the uncertainty of the measurements. This lack of effect of the trip on the heat transfer coefficient was rather surprising considering the large effect of the trip on the boundary layer thickness and the turbulence level.

### **3.3.4 Surface Imperfections**

The data presented for the smooth case was obtained on 3/16/04, although several smooth tests had been performed on earlier dates. Earlier test data was disregarded due to imperfections in the surface of the heat flux plate. It turns out that the smooth wall heat transfer coefficient distribution was very sensitive to those surface imperfections. As discussed in Section 2.4, the heat flux plate had to precisely follow the contours of the surface. Nearly imperceptible wrinkles (with smooth contours) in the heat flux plate would cause anomalous accelerations and decelerations to occur in the boundary layer, thus giving anomalous heat transfer coefficient distributions. These height of the wrinkles were estimated to be on the order of 0.1 mm with surface length

scales of approximately 3 cm. Scaled down another order of magnitude to the actual size of the vane and the wrinkle height would be of order 0.01 mm. Under these circumstances, the heat transfer coefficient would exhibit spanwise variations of 10%, even with the suction side holes covered. The test data presented in this section was gathered under the most ideal surface conditions possible. These ideal surface conditions may or may not be representative of actual new turbine vanes.

In addition to maintaining a wrinkle-free surface, it was also determined that a step at the leading edge of the smooth heat flux plate could cause an undesired increase in the heat transfer coefficient. A smooth heat transfer experiment was performed on 2/3/04 that did not have the surface upstream of the heat flux plate built-up to eliminate the step at the heat flux plate. The step up to the heat flux plate was approximately 0.3 mm, or half the boundary layer height. The results of the test are unusable except for demonstrating the importance of a smooth transition from the surface of the vane to the heat flux plate. Figure 3.37 compares the results of the test with the step (2/3/04) and the test without the step (3/16/04). The step caused an increase in the heat transfer coefficient of as much as 30%.

### **3.4 HEAT TRANSFER RESULTS WITH DOWNSTREAM ROUGHNESS**

This section discusses the results of the heat transfer tests conducted with roughness downstream of the holes, but with the upstream region smooth. Data presented in this section was acquired on 10/10/2003.

#### **3.4.1 Downstream Rough Heat Transfer Without Showerhead Blowing**

Figure 3.38 presents laterally averaged heat transfer coefficient plots for several blowing ratios in addition to the holes covered condition. The first feature to notice about these plots is the oscillatory nature of the heat transfer

coefficient. Although the rows of conical roughness elements were staggered in the streamwise direction, there was no spanwise staggering. The peaks in the oscillations correspond to rows of cones.

Like the smooth wall data, blowing had little effect on  $\bar{h}$ , especially at low blowing ratios. However, it is interesting to note that the laterally averaged heat transfer coefficient was not reduced by covering the suction side coolant holes. Aside from the blowing ratio  $M = 1.4$ , all the spanwise averaged heat transfer coefficients lie within uncertainty. Roughness was the dominant effect on the boundary layer, thus a large amount of coolant was required to augment the effect of roughness. Figure 3.39 shows the effect of blowing ratio at several streamwise locations. These figures also demonstrate the attenuation of blowing effects as distance from the holes was increased. This attenuation was not observed with the smooth wall data nearly to the extent that it was with the rough wall data. As Robertson (2004) shows, the roughness causes a great deal of mixing between the jets and the freestream. As this mixing occurs, the severity of the shear layer may decrease, resulting in less turbulence caused by the jet with distance downstream.

The analogous data for the low turbulence case is presented in Figures 3.40 and 3.41. The laterally averaged heat transfer coefficient was virtually unaffected by the freestream turbulence. The differences between the  $\bar{h}$  values are within the experimental uncertainty. This fact indicates that roughness effects dominated over turbulence effects.

Figures 3.42 through 3.45 are contour plots of the heat transfer coefficient on the rough surface. An important difference between the heat transfer coefficient distributions on the rough surface and the smooth surface was the effect of the jets. On the rough surface, lower heat transfer coefficients existed in the regions downstream of the jets than in between the jets. By

comparing the  $M = 0$  plots with the  $M = 0.7$  plots, it is clear that the jet actually decreased the heat transfer coefficient from what it would have been without the jet. However, this was not the case at  $M = 1.4$ , for which the jet was completely detached (in the region of interest) and it increased the heat transfer coefficient as seen in Figure 3.38. Figures 3.46 and 3.47 show the spatial augmentation of  $h$  due to blowing at  $M = 0.7$  for the high and low turbulence cases, respectively. The effect of blowing was most pronounced at low freestream turbulence than for high freestream turbulence. The heat transfer coefficient was decreased along the hole centerline, but increased between the holes, particularly in the upstream region of the heat flux plate. As the boundary layer measurements of Section 3.2.4 demonstrate, the velocity behind a blowing hole is lower than it would be if the hole were not blowing. The decrease in velocity behind the hole may cause a decrease in the effective roughness Reynolds number on the rough heat flux plate. Thus, the roughness may not have the ability to augment the heat transfer coefficient as much as it does without the film cooling jet. However, some mainstream flow goes around the slow jet, causing an increase in the velocity between adjacent film cooling jets and a higher effective roughness Reynolds number in those locations. This hypothesis may explain the unexpected phenomenon of the jets' effect on the  $h$  distribution.

Figure 3.48 presents spanwise averaged heat transfer coefficients for both the smooth case and the downstream rough case. The magnitude of the heat transfer coefficient with roughness downstream of the suction side coolant holes was higher than the equivalent smooth vane values. Figure 3.49 shows the  $\bar{h}$  augmentation realized with downstream roughness for conditions with and without film cooling. We see that there was very little augmentation at the leading edge of the heat flux plate, but a growing augmentation with distance downstream. As the thermal boundary layer grew, the heat transfer coefficient

dropped. With roughness, the drop in  $\bar{h}$  tapered off relatively quickly before the heat transfer enhancement effects of the roughness retarded the drop. However, the smooth surface allowed the heat transfer coefficient to continue to decrease at a higher rate than with the roughness. Past  $x/d \approx 4$ , the heat transfer coefficient was increased by between 50% and 150% for the case with film cooling holes covered. Blair (1994) obtained similar augmentations due to roughness, reporting that roughness approximately doubled the heat transfer coefficient in his experiments. Film cooling decreased the heat transfer augmentation somewhat. Although the film cooling had very little effect on  $\bar{h}$  with roughness, it did increase  $\bar{h}$  for the smooth wall case. Therefore, the heat transfer coefficient augmentation with roughness was lower with film cooling than without.

Figures 3.50 and 3.51 show how roughness augmented the heat transfer coefficient locally with high and low turbulence, respectively. The blowing ratio used in both figures was  $M = 0.7$ . As the laterally averaged augmentation plots suggested, areas with film cooling experienced a lower augmentation than areas without film cooling. As seen earlier, the high turbulence condition induced greater spanwise dispersion of the coolant. Because areas with film cooling experienced less  $h$  augmentation, the greater spanwise coolant dispersion of the high turbulence condition suppressed the  $h$  augmentation due to roughness.

### 3.4.2 Downstream Rough Heat Transfer With Showerhead Blowing

Data comparing the effects of the showerhead and turbulence on laterally averaged heat transfer coefficient are presented in Figure 3.52. The showerhead caused a slight increase in  $h$  that rapidly decayed. An unusual observation is that the high turbulence  $\bar{h}$  values tend to be two or three percent

lower than the low turbulence  $\bar{h}$  values. Although this difference is within uncertainty, the phenomenon was also observed in the test that took place on 12/18/03, but again only with the showerhead on.

Figure 3.53 presents laterally averaged heat transfer coefficients for the high turbulence case with showerhead blowing. Again we see that the heat transfer coefficient was insensitive to blowing ratio except within a few hole diameters of injection. Figure 3.54 shows the laterally averaged heat transfer coefficients for the low turbulence case. In order to be certain that blowing had an effect on  $\bar{h}$ , the blowing ratio was increased to an immeasurably high value in the range  $3 < M < 4$ . We do see a marked increase in  $\bar{h}$  at this extremely high blowing ratio.

Figure 3.55 shows how roughness increased the heat transfer coefficient from the smooth wall values when the showerhead was in operation. The results are similar to the case without the showerhead. The augmentation plot emphasizes that turbulence had a greater effect on  $\bar{h}$  with a smooth vane than with a rough vane. Even with showerhead blowing, the addition of suction side blowing still caused a decrease in the augmentation because of the subtlety of the showerhead effects on both the rough and smooth surfaces. At low turbulence, there was a slightly greater  $\bar{h}$  augmentation with showerhead cooling than without showerhead cooling. However, at high turbulence, the showerhead had no effect on the  $\bar{h}$  augmentation.

Figures 3.56 and 3.57 show how roughness augmented the heat transfer coefficient locally with showerhead blowing at high and low turbulence, respectively. The blowing ratio in both figures is  $M = 0.7$ . Again we see that areas downstream of the jets experienced a lower augmentation than areas between the jets. Also, the high turbulence condition decreased the augmentation as it did without showerhead cooling.



### **3.5 UPSTREAM ROUGHNESS EFFECTS ON HEAT TRANSFER**

This section presents the effects of upstream roughness both when the downstream area was smooth and when the downstream area was rough. Early in the course of this study, it was determined that upstream roughness effects were subtle. In order to resolve these effects, it was necessary to eliminate experiment to experiment variability by running with and without upstream roughness in the same tests. The tests that took place on 12/18/03 and 3/16/04 were each executed with and without upstream roughness. Data was first acquired with upstream roughness and then the upstream roughness was removed during the test without turning off the tunnel, the IR camera, or the heat flux plate. The test on 12/18/03 was executed with an abbreviated set of blowing ratios; however, a more complete set of blowing ratios for the completely rough condition was used during the test of 11/6/03.

#### **3.5.1 Downstream Smooth**

With a smooth surface upstream of the suction side holes, the presence of the suction side holes was enough to alter the heat transfer coefficient downstream of the holes. Thus it was necessary to tape over the suction side holes in order to determine what the heat transfer coefficient would be on an uncooled vane. However, roughness upstream of the holes caused a sufficiently large boundary layer disturbance that the holes caused no additional disturbance to affect the heat transfer coefficient. This fact is apparent in Figure 3.58, a contour plot of  $h$  with high freestream turbulence, roughness upstream of the holes, and no suction side blowing with the holes exposed. There was no significant spanwise variation in  $h$ , particularly with a repetition that corresponds to the suction side hole locations. This result holds true regardless of showerhead blowing, freestream turbulence intensity, or downstream surface condition. Because suction side holes without coolant ejection had no influence

on  $h$ , there is no need to distinguish between the "holes covered" and "holes exposed" conditions.

Figure 3.59 shows the effect of upstream roughness on the spanwise averaged heat transfer coefficient without suction side blowing. The upstream roughness caused a significant increase in the heat transfer coefficient along the entirety of the heat flux plate. At  $x/d = 3$ , the upstream roughness caused a 26% increase in  $\bar{h}$  relative to the all smooth, holes covered condition. The boundary layer measurements indicated that the turbulence caused by the roughness was attenuated as the flow moved downstream. Consequently, at  $x/d = 18$ , the increase in  $\bar{h}$  due to upstream roughness was 19%.

Figures 3.60 and 3.61 show how suction side blowing affected the spanwise averaged heat transfer coefficient for high and low turbulence, respectively. Suction side blowing increased the spanwise averaged heat transfer coefficient, but not to the extent as without upstream roughness. The spanwise averaged heat transfer coefficient was insensitive to reasonable adjustments in the blowing ratio. An immeasurably high blowing ratio was used (for which  $M > 3$ ) to demonstrate that the spanwise averaged heat transfer coefficient was not completely insensitive to adjustments in blowing ratio.

From the contour plots of  $h$  in Figures 3.62 and 3.26, it is apparent that upstream roughness had a similar (but stronger) effect as high freestream turbulence on  $h$  when there was film cooling. The additional turbulence from the roughness caused increased spanwise dispersion of the coolant. There was always greater  $h$  where there was a jet than where there was not a jet. With upstream roughness, the spanwise area of influence of the jets is increased, but the magnitude of the  $h$  augmentation along the jet centerline was decreased. Figure 3.63 shows the  $h$  distribution with upstream roughness at high turbulence. The increase in turbulence caused further spanwise coolant

dispersion, but the effect was small relative to the effect of upstream roughness alone. Figure 3.64 is a contour plot of the heat transfer coefficient augmentation realized with upstream roughness at low turbulence. Clearly,  $h$  was decreased along the hole centerline at the expense of increased  $h$  between the holes. Figure 3.65 is the analogous plot at high freestream turbulence. Although the high freestream turbulence alone caused some spanwise dispersion of the coolant, the roughness caused additional spanwise dispersion.

Figure 3.66 summarizes the effects of turbulence on the spanwise averaged heat transfer coefficient with upstream roughness. Showerhead effects are also presented. The effects of turbulence and showerhead blowing were less than the uncertainty until approximately  $x/d > 14$ . As was the case without upstream roughness, both the showerhead and high freestream turbulence tended to increase the heat transfer coefficient, with the high turbulence having a greater effect than the showerhead. Suction side blowing effects with showerhead blowing are presented in Figures 3.67 and 3.68 for high and low turbulence, respectively. The same trends continue, with a small amount of blowing causing an increase in the spanwise averaged heat transfer coefficient and further increases having virtually no effect.

With showerhead blowing and high freestream turbulence, there is a great deal of turbulence to cause spanwise dispersion of the coolant, even without upstream roughness. Therefore, the addition of upstream roughness cannot have as great of a heat transfer coefficient augmentation as without showerhead blowing and high freestream turbulence. In this case, the  $h$  augmentation due to roughness was under 10% as shown in Figure 3.69.

### 3.5.2 Downstream Rough

Data used to determine the effects of upstream roughness with downstream roughness present were obtained on 12/18/03. Figure 3.70

compares the upstream rough data with the upstream smooth data. Interestingly, the addition of upstream roughness reduced the heat transfer coefficient. From the boundary layer measurements, it is clear that roughness thickens the boundary layer in addition to increasing the turbulence intensity in the boundary layer. The higher turbulence intensity may be responsible for the increase in  $h$  with the downstream region smooth. However, the downstream roughness alone caused a significant increase in the boundary layer turbulence intensity and the addition of upstream roughness probably cannot increase it much more. The thicker boundary layer created by the upstream roughness means that the velocity near the surface was slower than without the upstream roughness. The lower velocity near the surface with the upstream roughness can be thought of as decreasing the roughness Reynolds number. Therefore, the downstream roughness could not augment the heat transfer as much as it could without the upstream roughness.

Contour plots of the heat transfer coefficient with both upstream and downstream roughness are presented in Figures 3.71 through 3.74. The upstream roughness combined with the downstream roughness caused such a large amount of jet deterioration that the influence of the jets on  $h$  is hardly distinguishable. However, the regions downstream of the holes had slightly higher  $h$  than between the holes, particularly in the far hole region. The case of combined downstream / upstream roughness with high freestream turbulence, showerhead film cooling, and suction side film cooling simulates engine representative conditions on a rough vane. Figure 3.75 shows the augmentation in  $h$  that occurs with upstream roughness. In the zone of reliable data ( $x/d > 3$ , where the conduction correction is applicable) the heat transfer coefficient was decreased. The strongest decrease in  $h$  occurred between the jets. The additional spanwise dispersion of the coolant from the upstream roughness

caused the area of influence of the jet to increase. For the rough wall case, that influence was to decrease the heat transfer coefficient.

A contour plot of the  $h$  augmentation that occurred due to full surface roughness in an engine representative environment (high freestream turbulence, showerhead on) is presented in Figure 3.76. The results indicate that a rough vane experiences localized augmentations in  $h$  that can reach as high as 100%.

### 3.6 HIGH DENSITY RATIO EFFECTS ON HEAT TRANSFER

A heat transfer test with  $DR = 1.6$  was conducted on 11/12/03. The low turbulence condition was used. The rough heat flux plate was used in addition to roughness upstream of the suction side coolant holes. The smooth heat flux plate was not used because wide range of surface temperatures ( $\sim 100\text{K}$ ) present during the high density ratio heat transfer test would cause wrinkles in the heat flux plate that would cause unacceptable anomalies in the smooth wall heat transfer coefficient.

Figure 3.77 presents the spanwise averaged heat transfer coefficients for  $M=0.5, 0.7$ , and  $1.4$  obtained by both high and low density ratio experiments. The low density ratio data was obtained on 11/6/03. The peaks of the roughness were offset by approximately  $0.5 d$  between the two experiments. By comparing corresponding peak values, the high density ratio and low density ratio  $\bar{h}$  values agree within 5%. Varying the blowing ratio had no significant effect on  $\bar{h}$  at either density ratio.

The lack of effect of density ratio on the spanwise averaged heat transfer coefficient is deceptive. The spatial distribution of  $h$  was quite dependent on the density ratio. Figures 3.78 through 3.81 are contour plots of the heat transfer coefficient at high density ratio and  $M = 0.3, 0.7, 0.85$ , and  $1.0$ , respectively. The heat transfer coefficient was clearly lower along the jet

centerline than between the jets. However, the effect of jets on  $h$  were rendered barely discernable with the upstream roughness at low density ratio. At high density ratio, the effect of the jets was quite prominent. Figures 3.82 and 3.83 present the ratio  $h_{high\ DR} / h_{low\ DR}$  at  $M = 0.7$  and  $1.4$ . At  $M = 0.7$ , it is clear that the heat transfer coefficient was typically about 20% higher between the holes at high density ratio than at low density ratio. But the affected area was narrow and  $h$  along the hole centerline was about 10% lower at the high density ratio. At  $M = 1.4$ , there was almost no difference in the  $h$  distribution obtained at the low and high density ratios. The oscillation of  $h_{high\ DR} / h_{low\ DR}$  about 1 at  $x/d > 8$  was caused by an offset in the positioning of the roughness.

These limited high density ratio heat transfer results indicate that the physics governing jet behavior is related to density ratio. Spanwise averaging of the heat transfer coefficient gave similar results at both density ratios. Ethridge et al. (2001) suggested the use of the momentum flux ratio,  $I$ , to scale adiabatic effectiveness for  $I > 0.4$ . It can be shown that the momentum flux ratio is related to blowing ratio through the following equations:

$$I = M^2 \quad \text{for } DR = 1.0 \quad (3.6.1)$$

$$I = \frac{M^2}{1.6} \quad \text{for } DR = 1.6 \quad (3.6.2)$$

To test the validity of  $h$  scaling with the momentum flux ratio on a rough surface, consider the case of  $M = 0.7$  at  $DR = 1.0$ , for which  $I \approx 0.5$ . If the momentum flux is matched, the blowing ratio at  $DR = 1.6$  would be  $M \approx 0.9$ . Although a blowing ratio of  $M = 0.9$  was not tested, data for  $M = 0.85$  and  $M = 1.0$  is available in Figures 3.80 and 3.81. Comparison with Figure 3.73 reveals

that the jets were better defined at high density ratio than low density ratio, even when the momentum flux ratio is matched.

Ammari et al. (1990) suggested the use of velocity ratio for scaling the heat transfer coefficient on a flat plate with inclined film cooling holes. The following equations related the velocity ratio,  $VR$ , to the blowing ratio for the two density ratios used in this research:

$$VR = M \quad \text{for } DR = 1.0 \quad (3.6.3)$$

$$VR = \frac{M}{1.6} \quad \text{for } DR = 1.6 \quad (3.6.4)$$

If velocity ratios are matched  $M = 0.5$  at  $DR = 1.0$  corresponds to  $M = 0.8$  at  $DR = 1.6$ . Comparison of Figures 3.73 and Figures 3.79 and 3.80 reveal that the velocity ratio is also an inadequate scaling parameter for the spatial heat transfer coefficient distribution.

### 3.7 NET HEAT FLUX REDUCTION

Up to this point, results have been presented that have demonstrated how both film cooling and roughness influence the heat transfer coefficient on the suction side of a gas turbine vane. In order to predict how film cooling and roughness influence the heat flux into a real vane, the adiabatic wall temperature and actual vane surface temperature must be known. The data of Robertson (2004) was used along with an assumption about the actual vane surface temperature ( $\phi = 0.6$ ) to provide this critical information. Equation 1.2.6 was used to determine the effect of film cooling on the heat flux and Equation 2.6.3.2 was used to determine the effect of roughness on heat flux.

Recall that  $\Delta q_r$  and  $\Delta q_{r,rough}$  indicate the fractional decrease in heat flux due to the addition of film cooling or roughness, respectively. For example,  $\Delta q_r = 0.2$  indicates a 20% decrease in heat flux due to the addition of film cooling. If  $\Delta q_{r,rough} = -0.3$ , a 30% increase in heat flux is realized due to the addition of surface roughness. The net heat flux reduction was calculated spatially and then spanwise averaged.

Due to the practical importance of the net heat flux reduction results, the calculations were performed on the data most representative of actual operating conditions (high turbulence and fully smooth or fully rough). Additionally, the low turbulence condition and operation without the showerhead are presented. Blowing ratios of  $M = 0.0, 0.3, 0.7$ , and  $1.4$  were considered. The showerhead was assumed to be in operation at  $M_{sh} = 1.6$  for cases with showerhead cooling. The “no holes” condition was used for the heat transfer data representative of uncooled vanes.

Figure 3.84 shows how the addition of showerhead and suction side film cooling to an otherwise uncooled smooth vane changes the heat flux. At  $M = 0.3$ , the heat load is reduced by nearly 40% in the near hole region. A blowing ratio of  $M = 0.7$  provides a maximum reduction in heat flux of only 30%, but the performance is better than  $M = 0.3$  past  $x/d \approx 11$ . The blowing ratio  $M = 1.4$  is far too high for the condition as evidenced by the fact that the showerhead alone provides better cooling. In all cases, the net benefit from film cooling decays with  $x/d$  as the film cooling adiabatic effectiveness decreases.

Figure 3.85 shows how the addition of suction side coolant only (without the showerhead) changes the heat load. The blowing ratio,  $M = 1.4$  was found to be detrimental to the heat flux. Although the heat transfer coefficient was fairly insensitive to showerhead blowing, the showerhead decreased the adiabatic wall temperature. Without the showerhead, the



maximum net heat flux reduction at  $M = 0.7$  was only half of what it was when the showerhead was in operation.

The effect of the low turbulence condition is presented in Figure 3.86. The net heat flux reduction was generally lower at high turbulence, primarily because the coolant mixes with the mainstream faster at high turbulence. However, the high blowing ratio,  $M = 1.4$ , performs worse at low turbulence in the far hole region because the detached jet requires turbulent mixing to return to the surface.

Figure 3.87 shows how the addition of showerhead and suction side film cooling to an otherwise uncooled fully rough vane changes the heat flux. Again, the best performer in the near hole region is  $M = 0.3$ . The higher blowing ratio,  $M = 0.7$  has better performance past  $x/d \approx 11$  again. This time the blowing ratio  $M = 1.4$ , is able to provide a nearly uniform net heat flux reduction of about 30%. The showerhead alone provides a net heat flux reduction of between 15% and 20%. With all blowing ratios, the decay in the benefit from film cooling is less than with the smooth surface. As Robertson (2004) described, turbulent mixing caused by the roughness causes coolant from separated or partially separated jets to return to the surface, thereby reducing the decay in adiabatic effectiveness.

Figure 3.88 is the analogous plot for the case of no showerhead cooling on the rough surface. Again, we observe that the net heat flux reduction is decreased appreciably by turning off the showerhead.

The effect of the low turbulence condition on the rough surface is presented in Figure 3.89. Film cooling performance was better at low turbulence than high turbulence everywhere for all blowing ratios. Unlike it did on the smooth surface, even  $M = 1.4$  performed better at low turbulence than it did at high turbulence on the rough surface.

Figure 3.90 shows how the change from a completely smooth to a fully rough vane affects the heat load for several different blowing rates. The results indicate that an uncooled vane would experience an increase in heat load of about 130% as the surface finish changes from smooth to rough. The predicted increase in heat load decreases with increasing blowing ratios. There are two mechanisms responsible for this phenomenon. Increasing the film cooling on a smooth surface increases the spanwise averaged heat transfer coefficient, whereas the blowing ratio has little effect on a rough surface. Therefore, at high blowing ratios the change from smooth to rough does not cause as great of a heat transfer augmentation as it does without film cooling. The other mechanism is the effect of roughness on the adiabatic effectiveness. The roughness decreases the adiabatic effectiveness for low to moderate blowing ratios ( $M \leq 0.7$ ). However, at high blowing ratios, exemplified by  $M = 1.4$ , the roughness increases the adiabatic effectiveness as described earlier. At  $M = 1.4$ , the heat load is increased by approximately only 70% due to roughness. It must be emphasized that although high blowing ratio results in the smallest increase in heat load, the lower heat load is obtained with a low to moderate blowing ratio as shown in Figures 3.84 and 3.87.

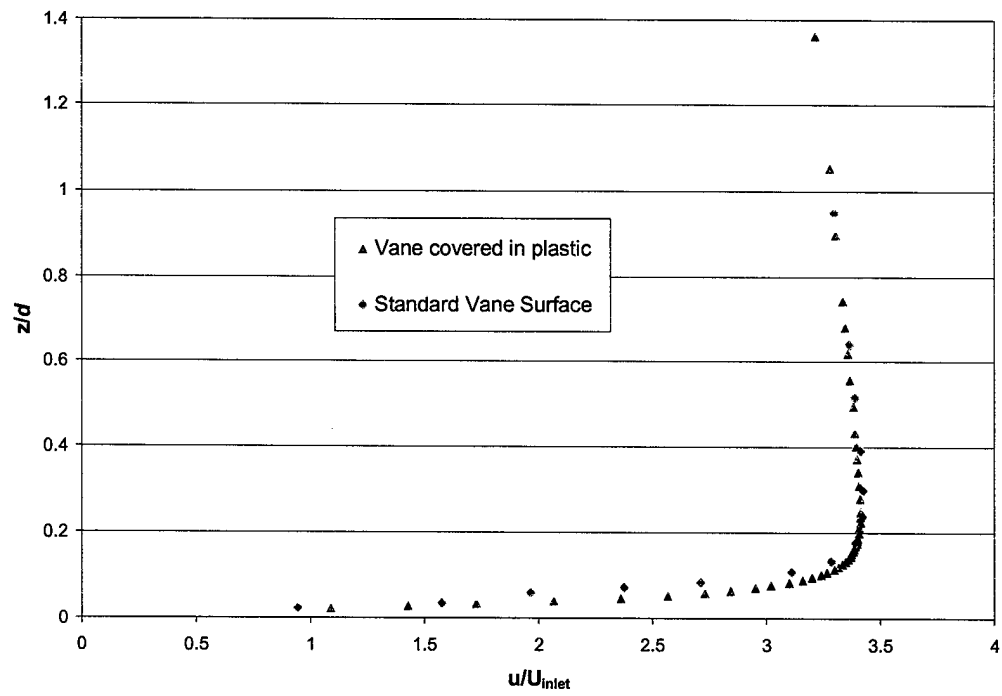


Figure 3.1: Velocity profiles at  $s/C = 0.19$ . Conditions are low turbulence, no roughness, and no film cooling.

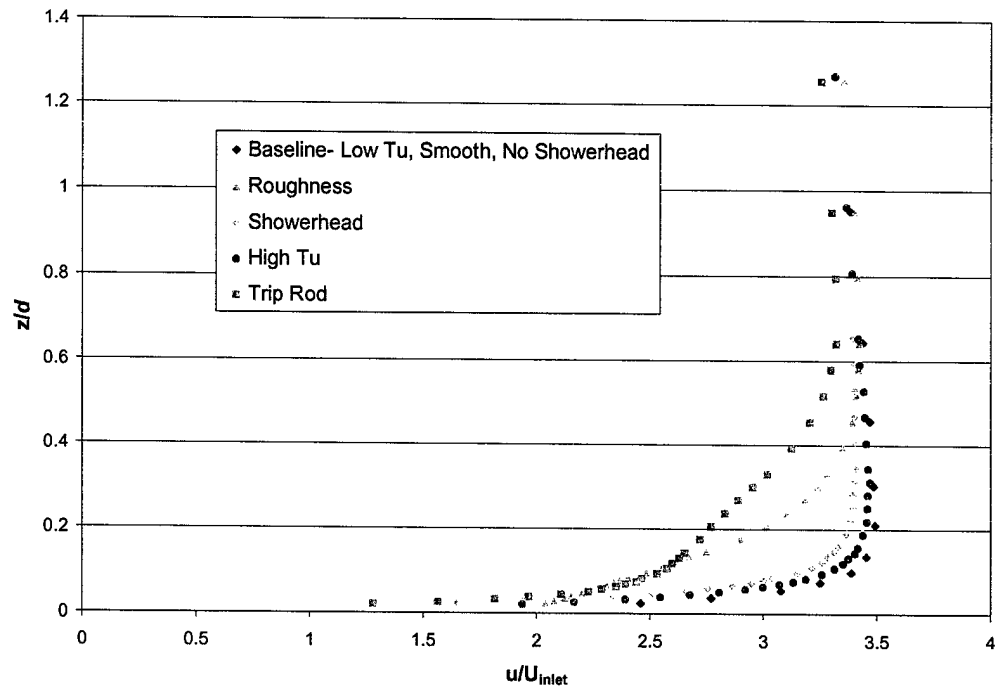


Figure 3.2: Velocity profiles at  $s/C = 0.19$ . The baseline condition is low turbulence, no roughness, and no film cooling.

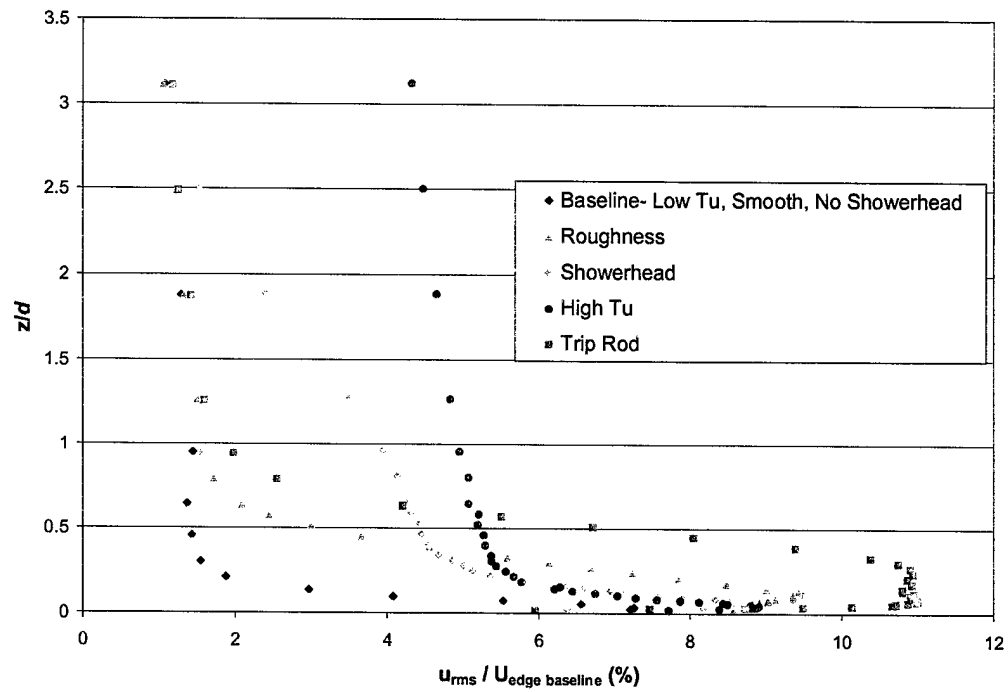


Figure 3.3: Turbulence level profiles at  $s/C = 0.19$ . The baseline condition is low turbulence, no roughness, and no film cooling.

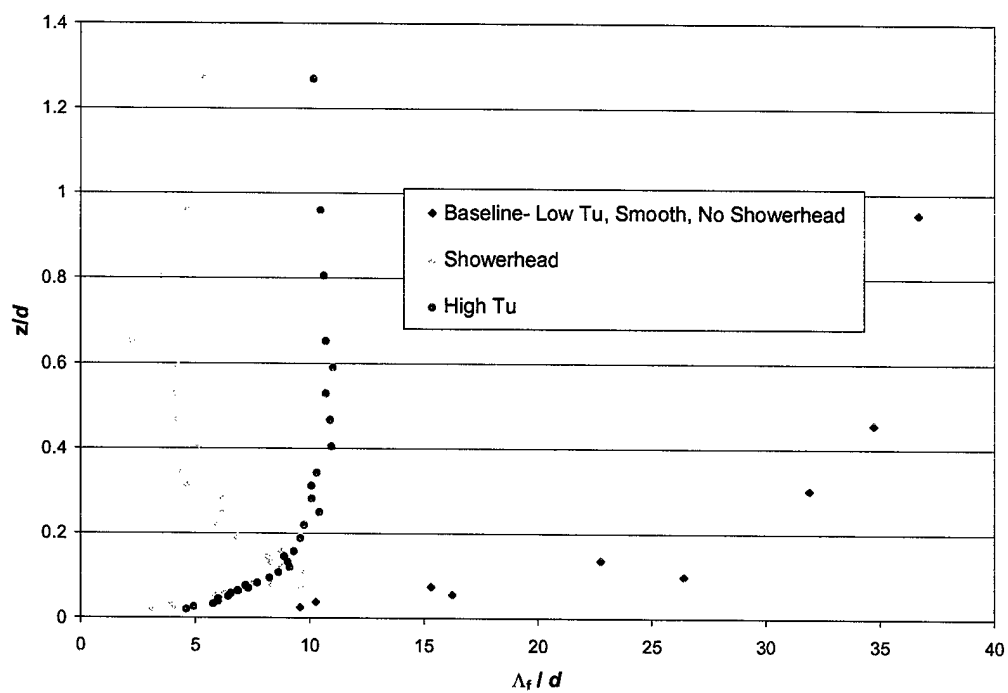


Figure 3.4: Turbulence integral length scale profiles at  $s/C = 0.19$ . The baseline condition is low turbulence, no roughness, and no film cooling.

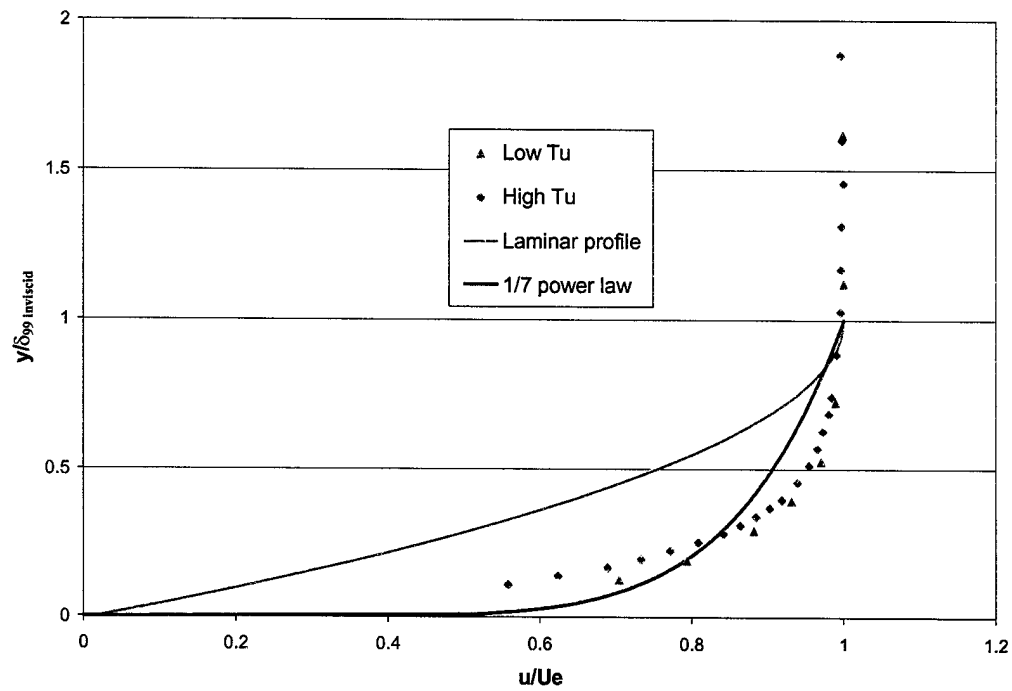


Figure 3.5: Velocity profiles at  $s/C = 0.19$  nondimensionalized by  $\delta_{99 \text{ inviscid}}$ . Conditions are smooth and no film cooling.

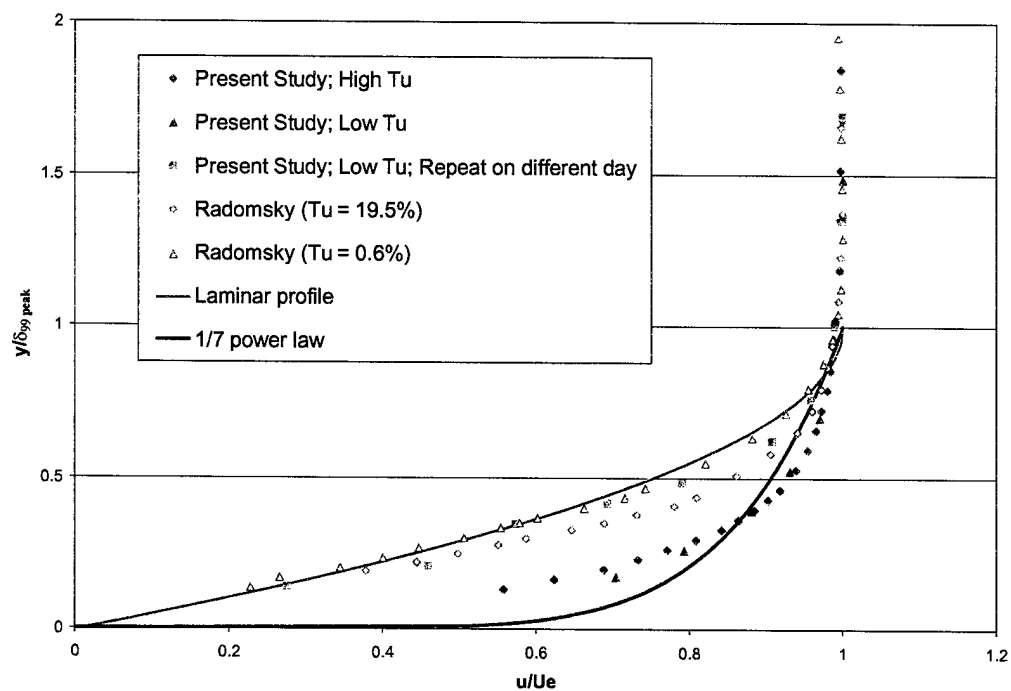


Figure 3.6: Velocity profiles at  $s/C = 0.19$  nondimensionalized by  $\delta_{99 \text{ peak}}$ . Conditions are smooth and no film cooling.



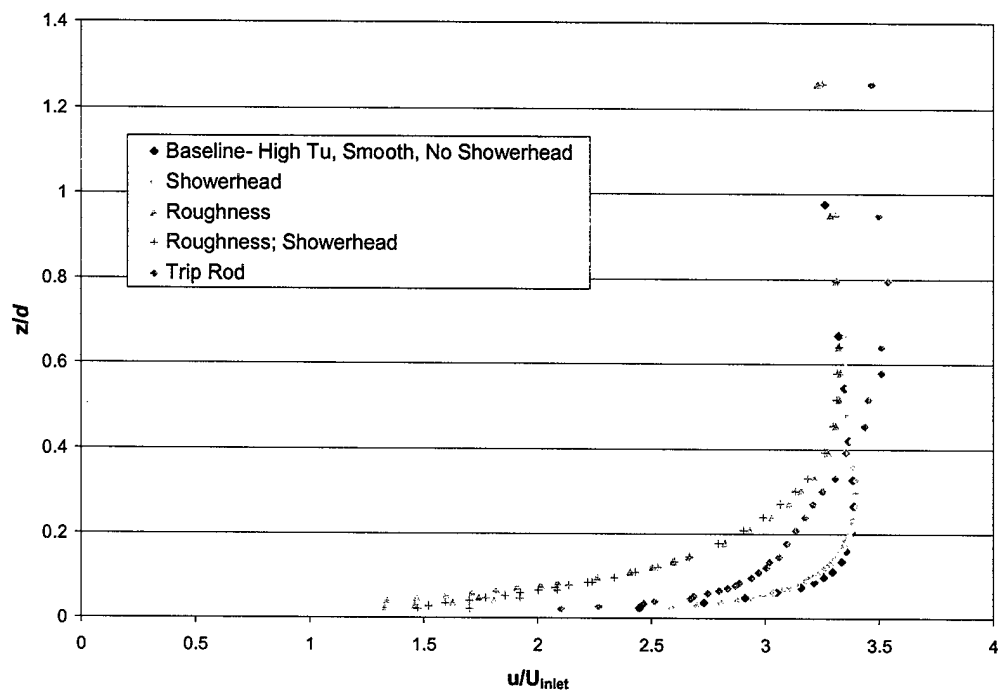


Figure 3.7: Velocity profiles at  $s/C = 0.19$ . The baseline condition is high turbulence, no roughness, and no film cooling.

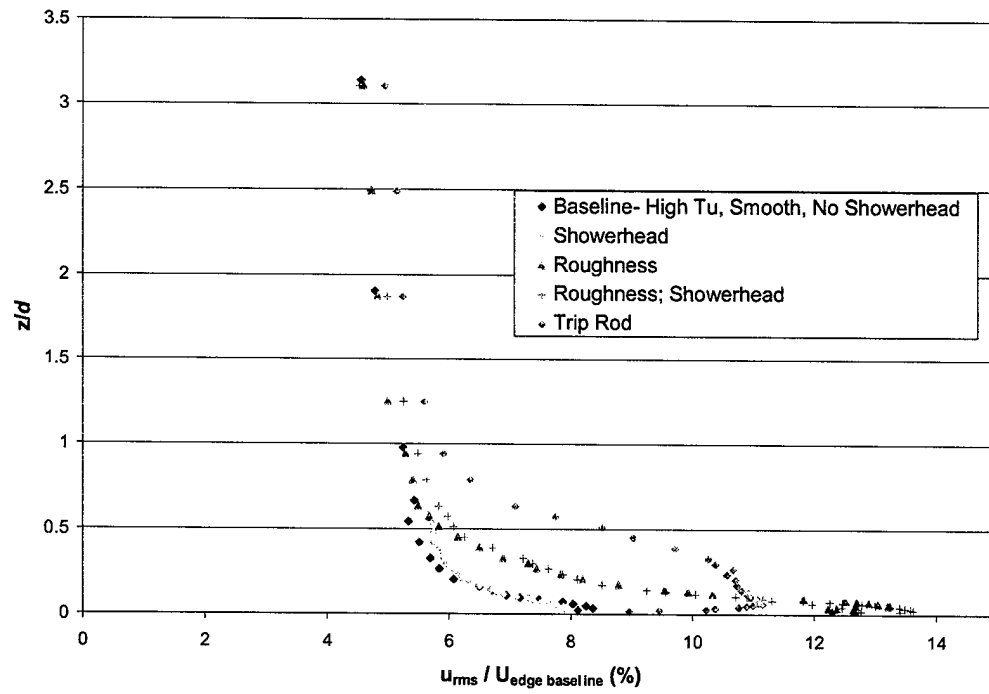


Figure 3.8: Turbulence level profiles at  $s/C = 0.19$ . The baseline condition is high turbulence, no roughness, and no film cooling.

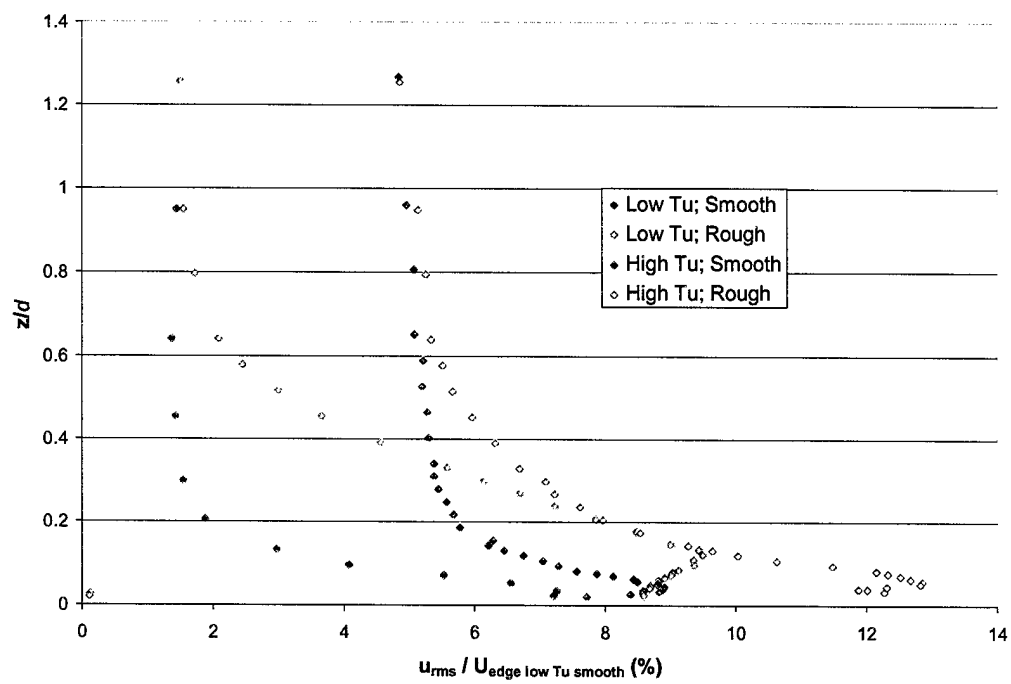


Figure 3.9: Turbulence level profiles at  $s/C = 0.19$ .

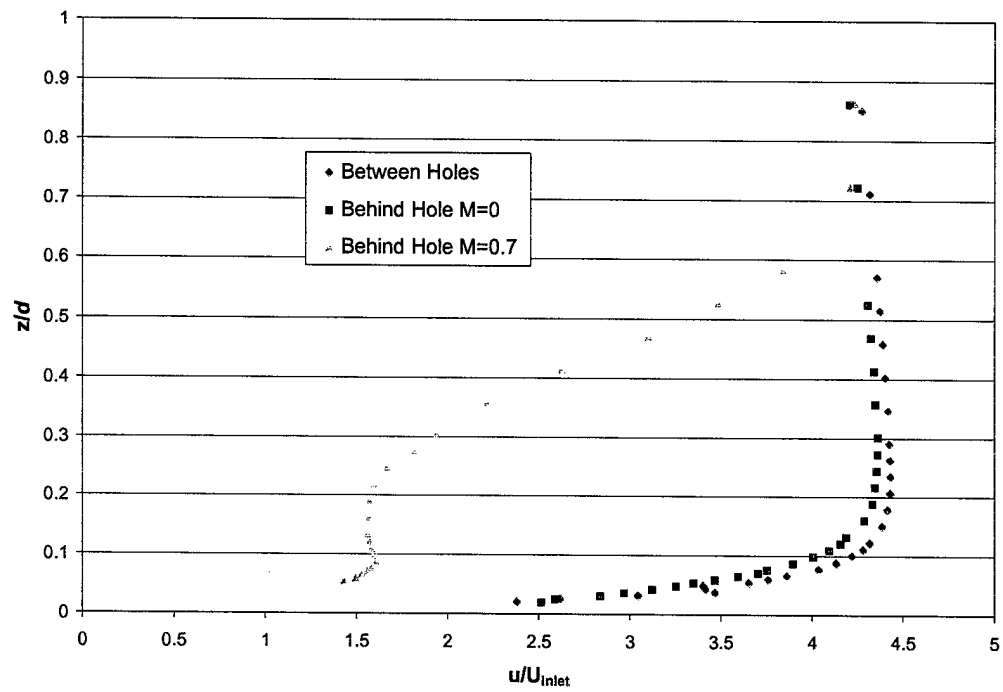


Figure 3.10: Velocity profiles at  $s/C = 0.22$ ,  $1 d$  downstream of the 1<sup>st</sup> row of suction side coolant holes, low freestream turbulence, smooth, no showerhead.

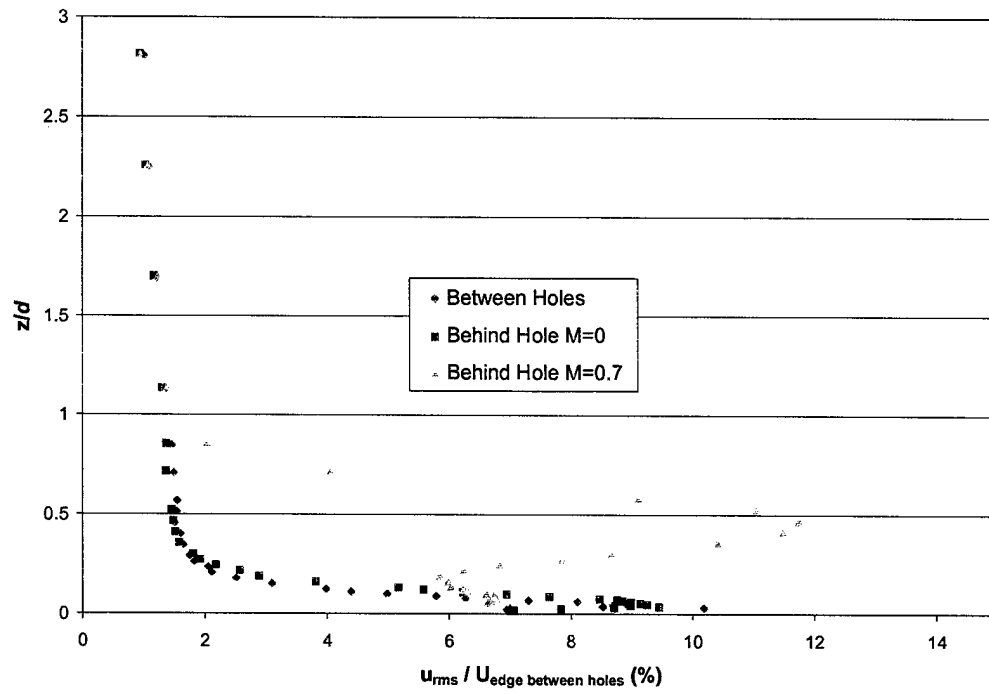


Figure 3.11: Turbulence level profiles at  $s/C = 0.22$ ,  $1 d$  downstream of the 1<sup>st</sup> row of suction side coolant holes, low freestream turbulence, smooth, no showerhead.

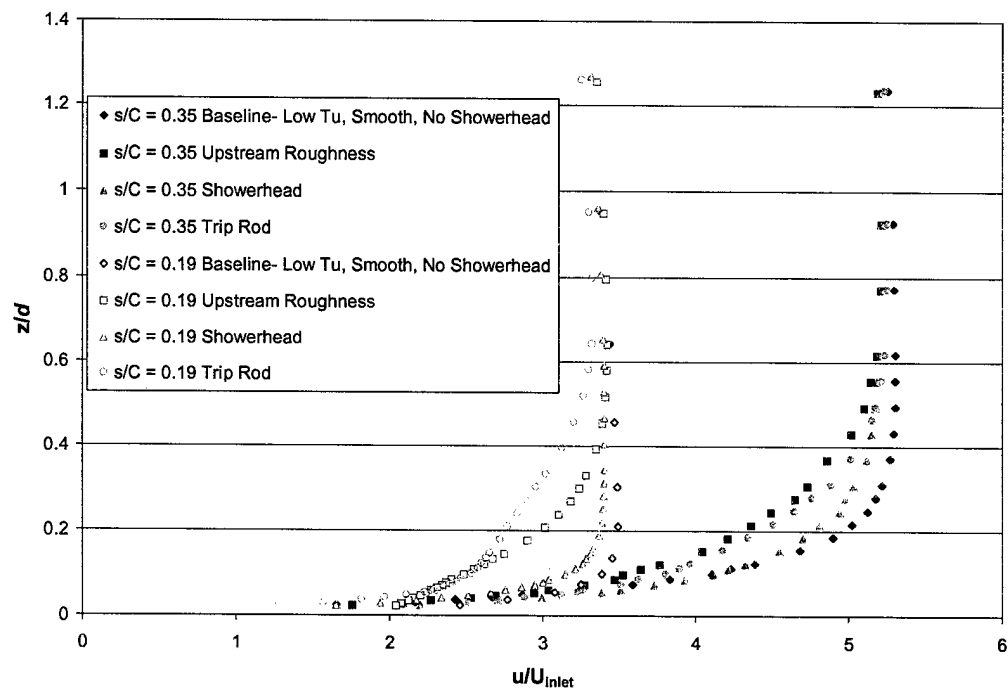


Figure 3.12: Velocity profiles at  $s/C = 0.35$  and  $s/C = 0.19$ . The baseline condition is low turbulence, no roughness, and no film cooling.

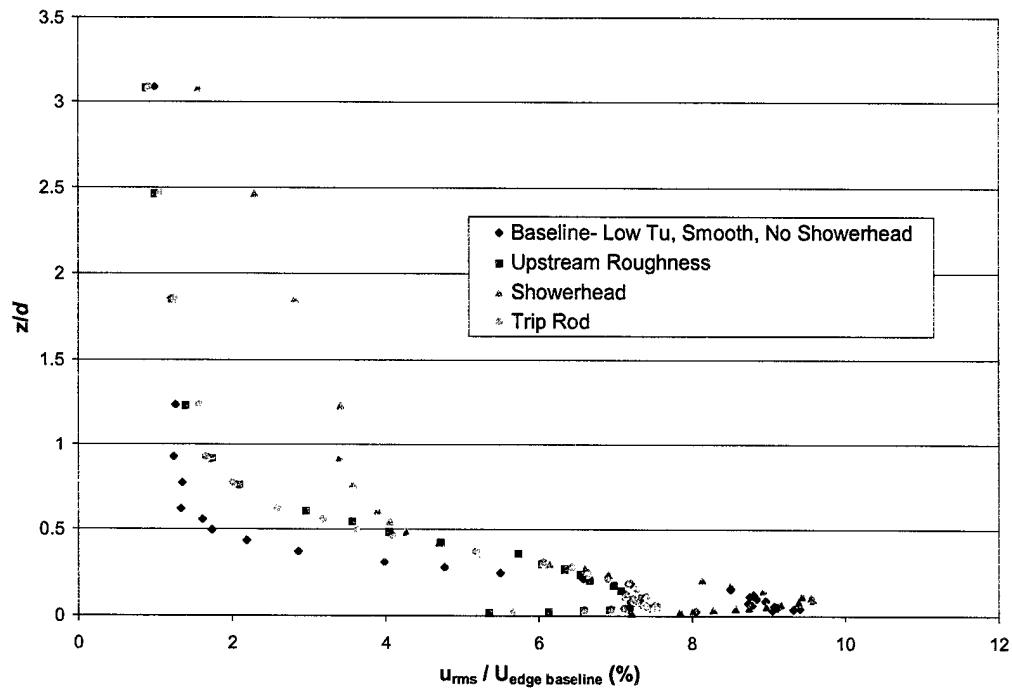


Figure 3.13: Turbulence level profiles at  $s/C = 0.35$ . The baseline condition is low turbulence, no roughness, and no film cooling.

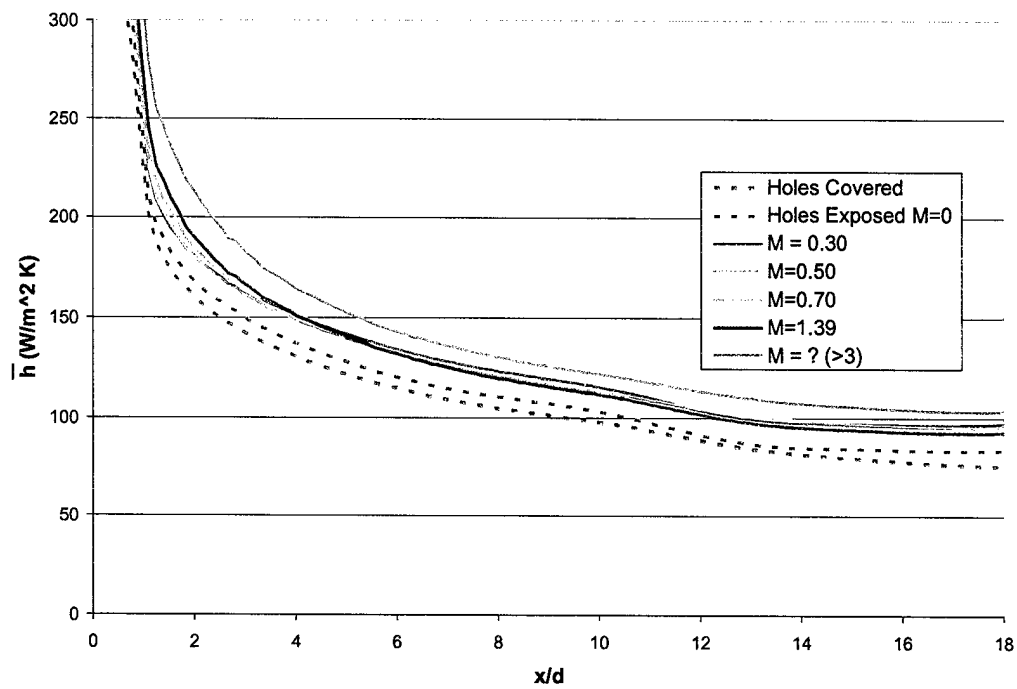


Figure 3.14: Spanwise averaged heat transfer coefficients. All smooth, showerhead off, high turbulence.



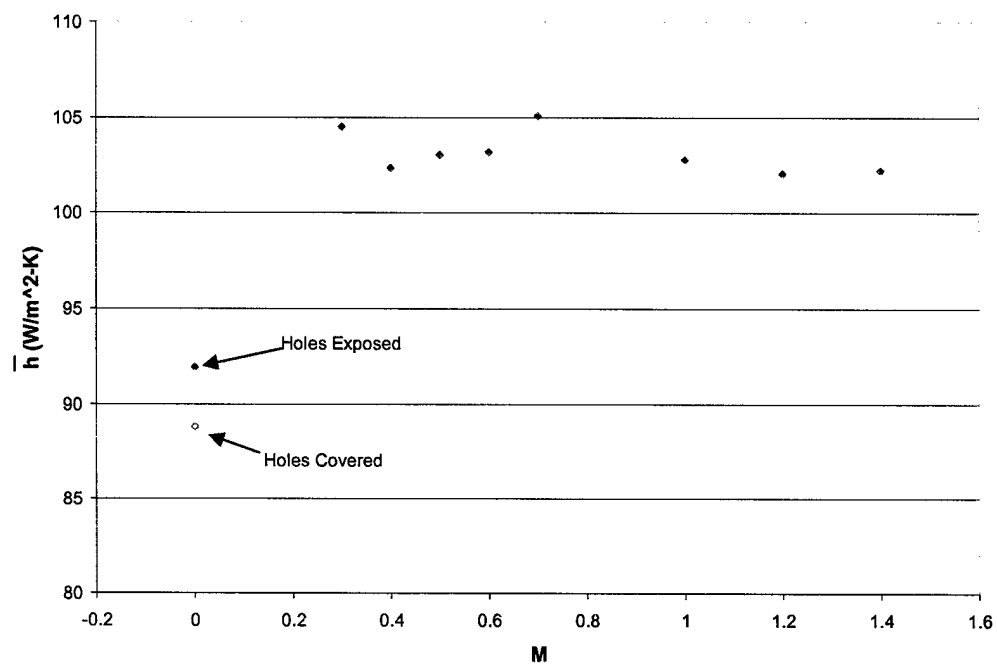


Figure 3.15: Spanwise averaged heat transfer coefficients at  $x/d = 12$ . All smooth, showerhead off, high turbulence.

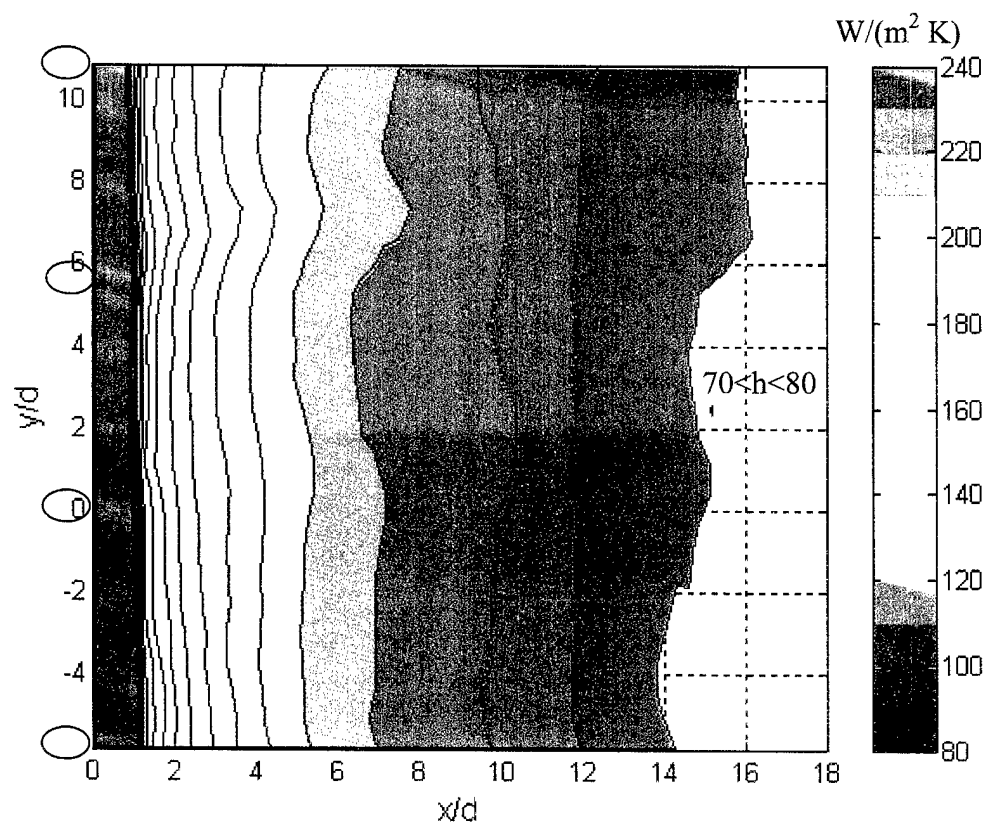


Figure 3.16: Heat transfer coefficient distribution,  $M = 0$ , holes covered. All smooth, showerhead off, high turbulence.

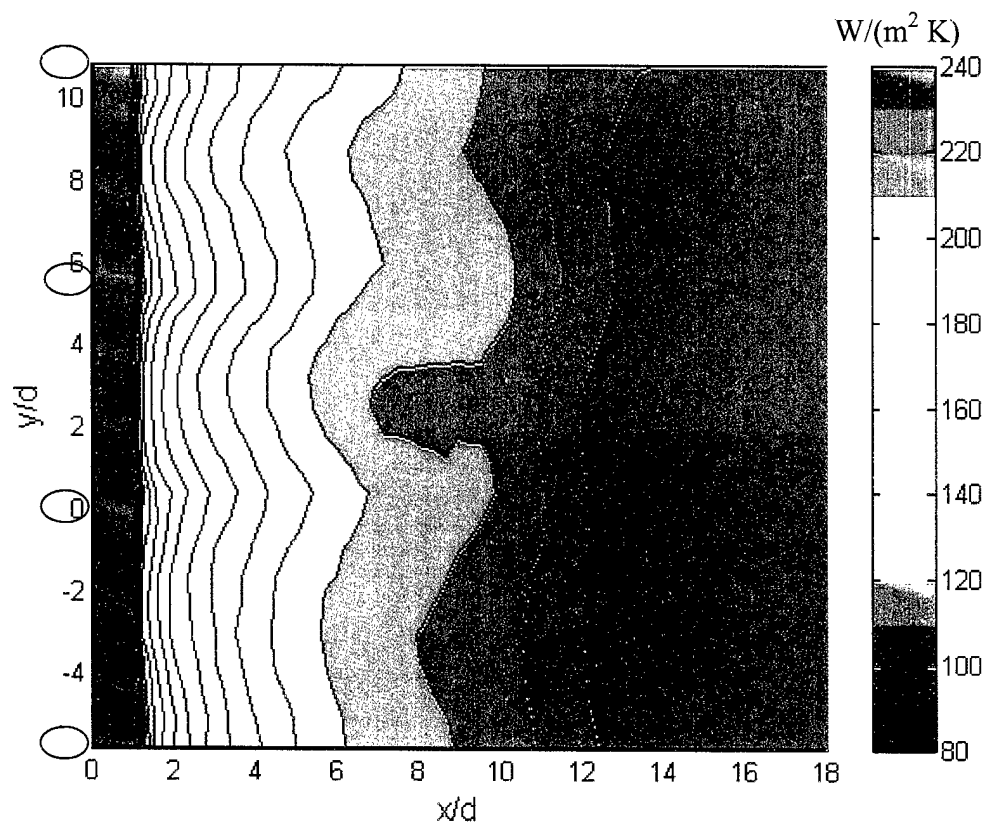


Figure 3.17: Heat transfer coefficient distribution,  $M = 0$ , holes exposed. All smooth, showerhead off, high turbulence.

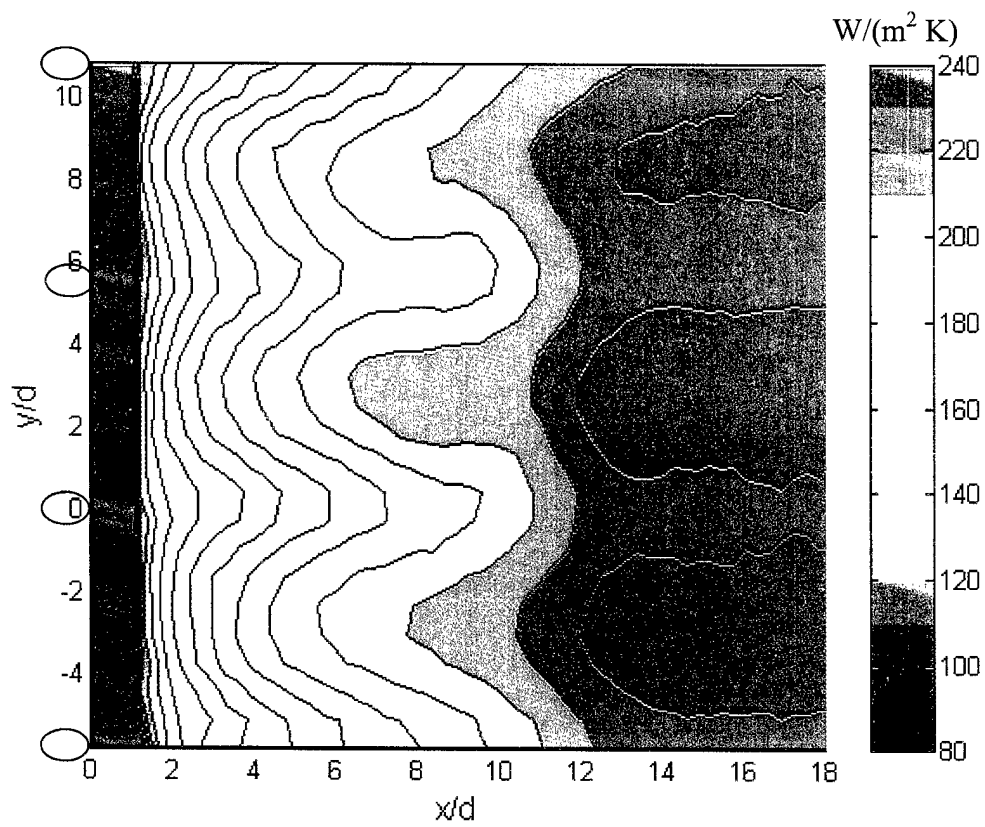


Figure 3.18: Heat transfer coefficient distribution,  $M = 0.3$ . All smooth, showerhead off, high turbulence.

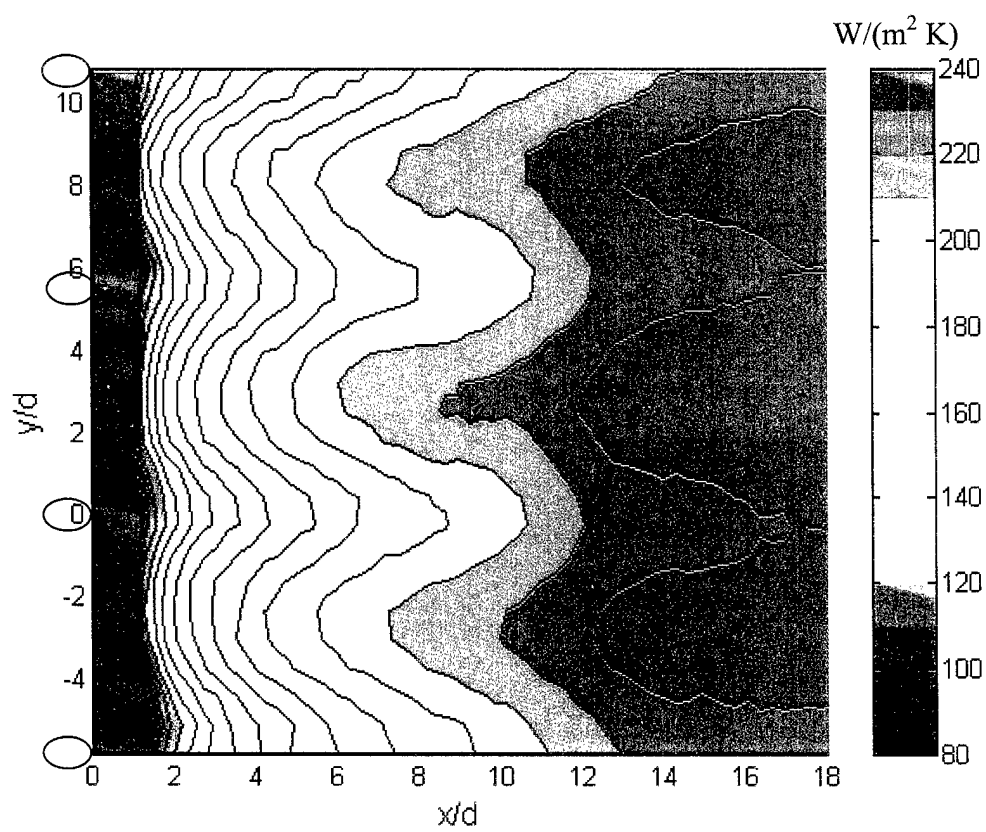


Figure 3.19: Heat transfer coefficient distribution,  $M = 0.7$ . All smooth, showerhead off, high turbulence.

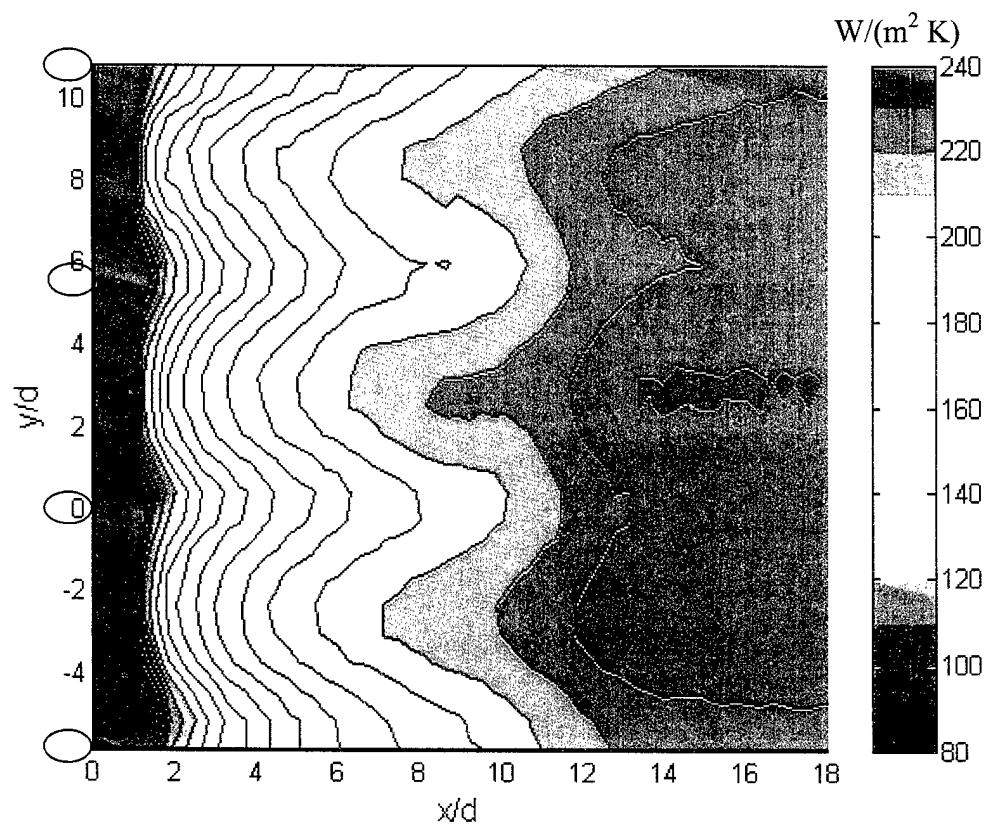


Figure 3.20: Heat transfer coefficient distribution,  $M = 1.4$ . All smooth, showerhead off, high turbulence.

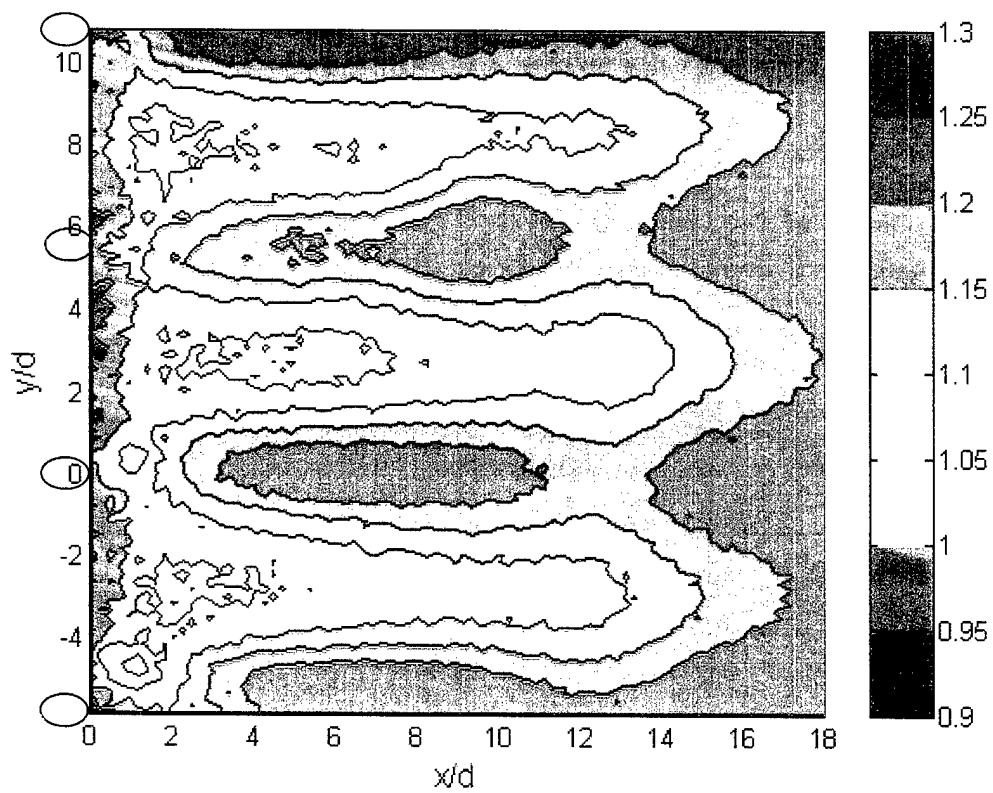


Figure 3.21: Heat transfer coefficient augmentation due to blowing at  $M = 0.3$  ( $h_f/h_o$ ). All smooth, showerhead off, high turbulence.

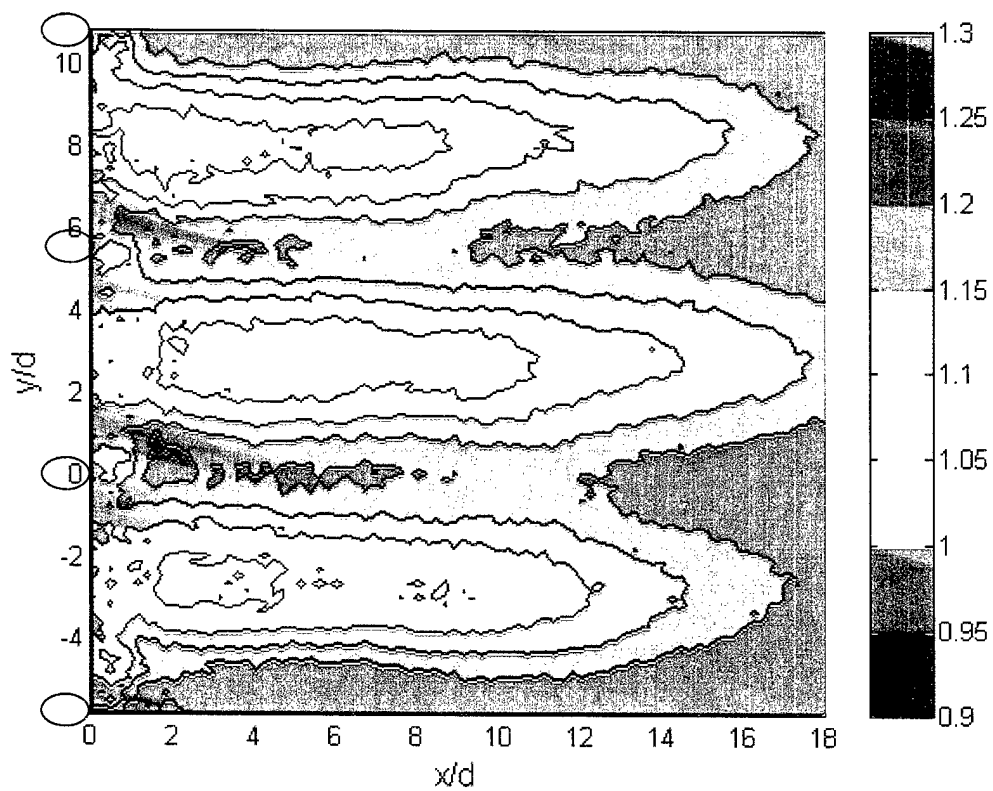


Figure 3.22: Heat transfer coefficient augmentation due to blowing at  $M = 0.7$  ( $h_f/h_o$ ). All smooth, showerhead off, high turbulence.



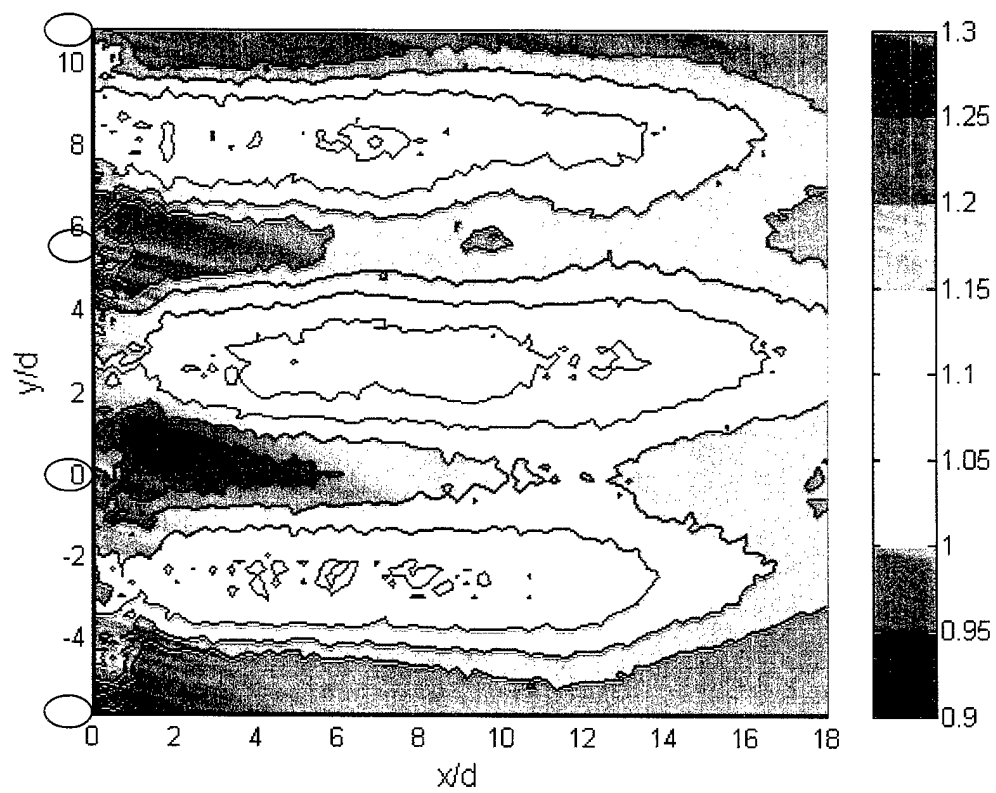


Figure 3.23: Heat transfer coefficient augmentation due to blowing at  $M = 1.4$  ( $h_f/h_o$ ). All smooth, showerhead off, high turbulence.

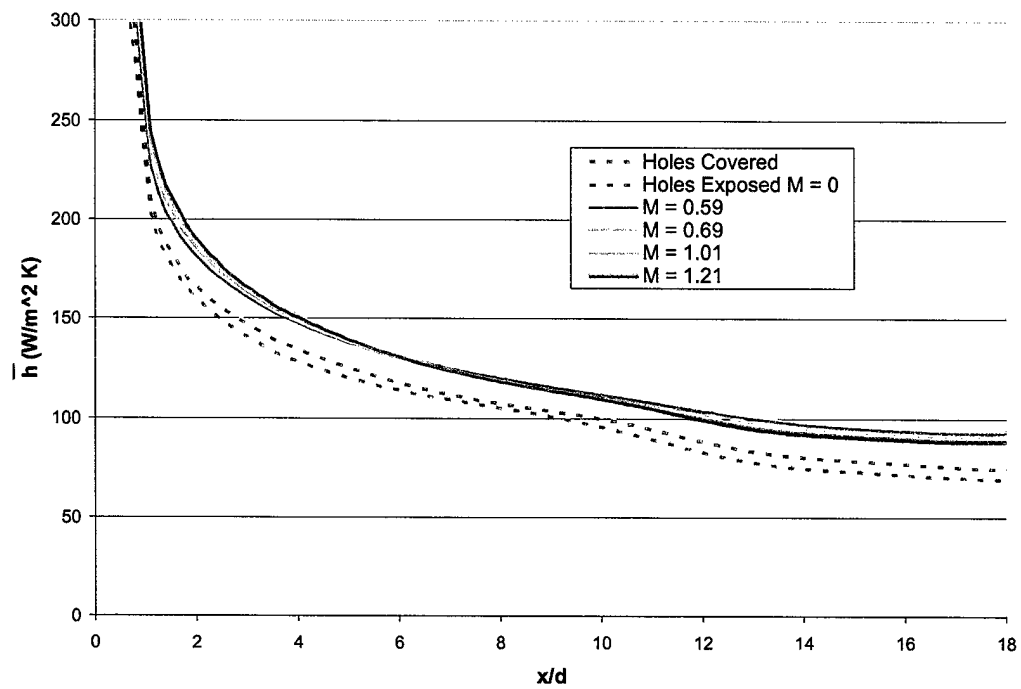


Figure 3.24: Spanwise averaged heat transfer coefficients. All smooth, showerhead off, low turbulence.

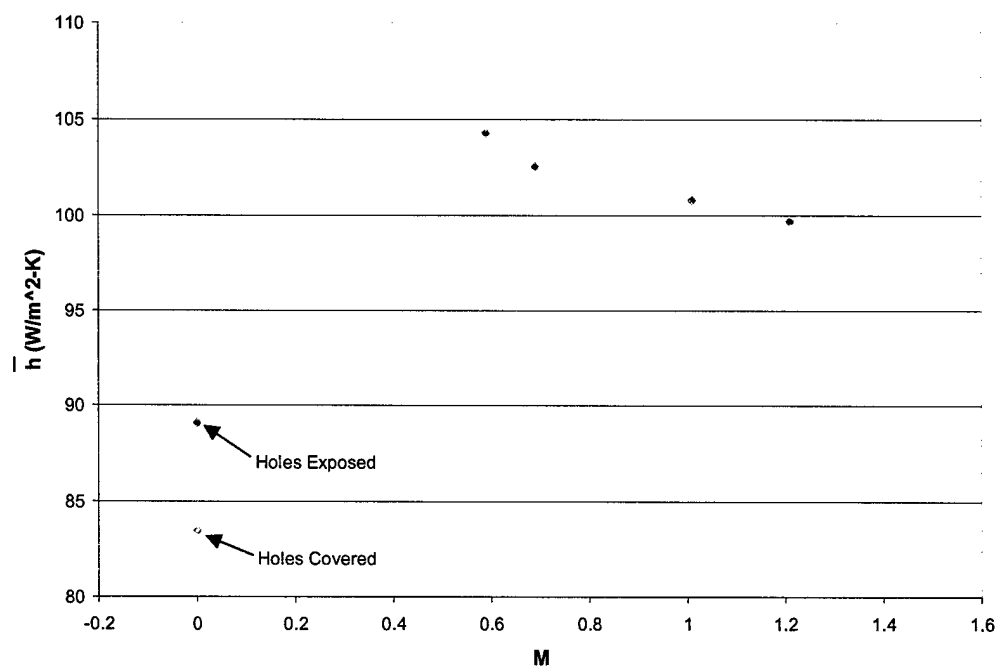


Figure 3.25: Spanwise averaged heat transfer coefficients at  $x/d = 12$ . All smooth, showerhead off, low turbulence.

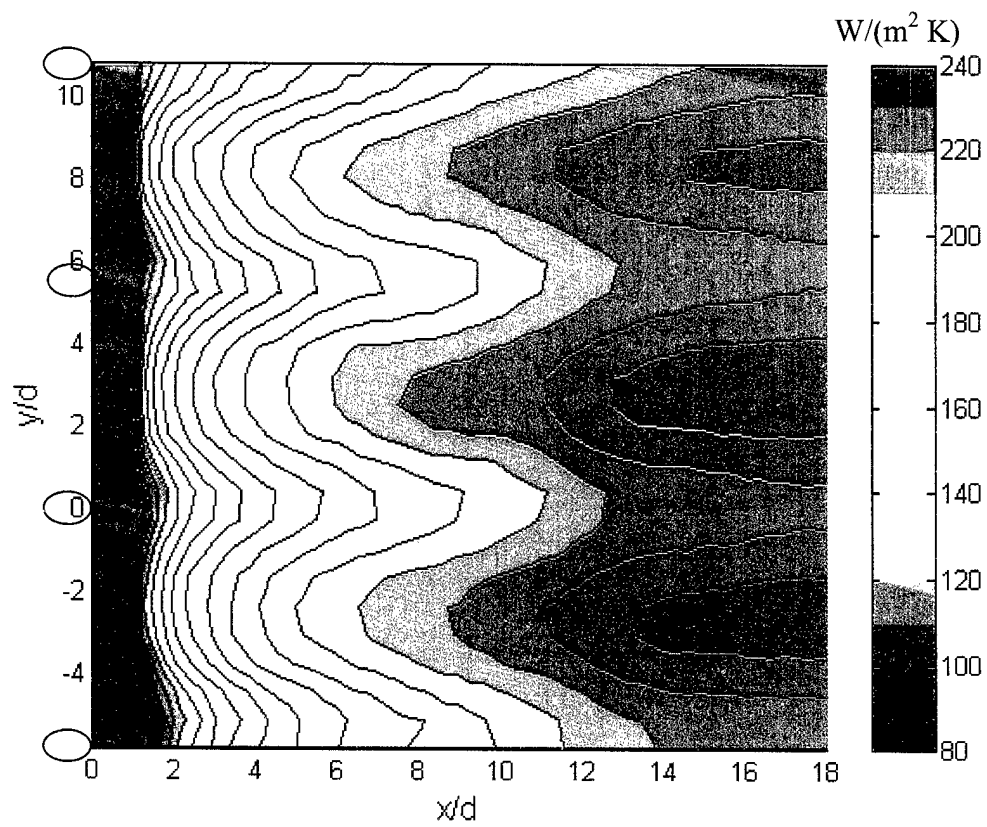


Figure 3.26: Heat transfer coefficient distribution,  $M = 0.7$ . All smooth, showerhead off, low turbulence.

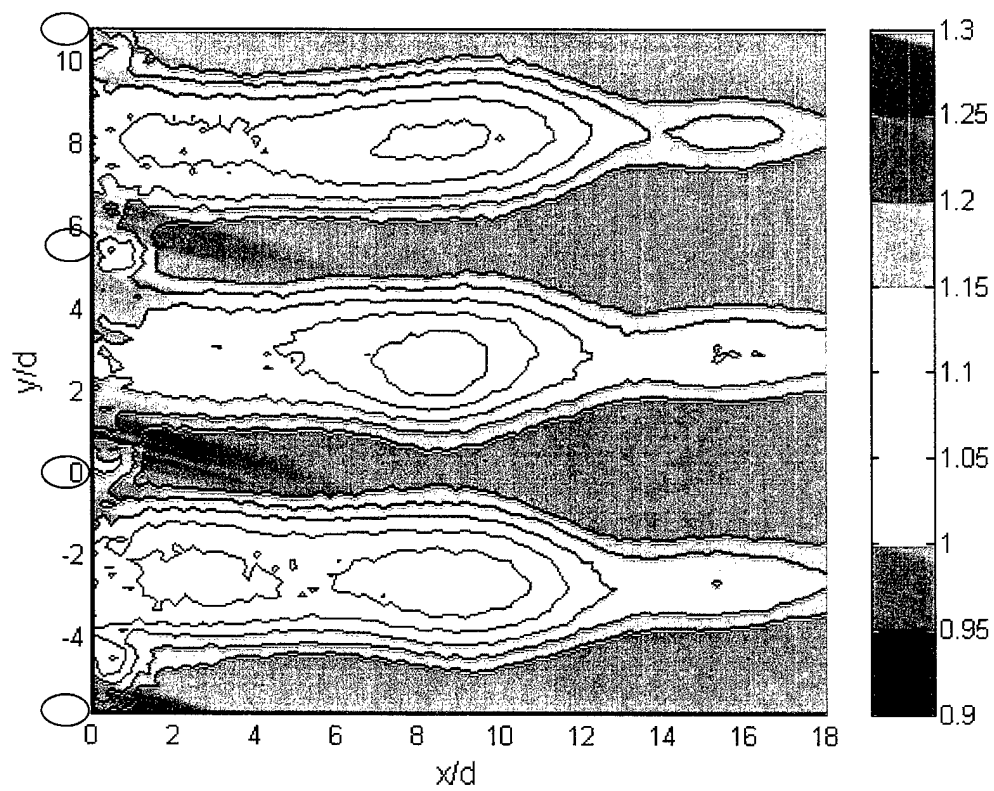


Figure 3.27: Heat transfer coefficient augmentation due to blowing at  $M = 0.7$  ( $h_f/h_o$ ). All smooth, showerhead off, low turbulence.

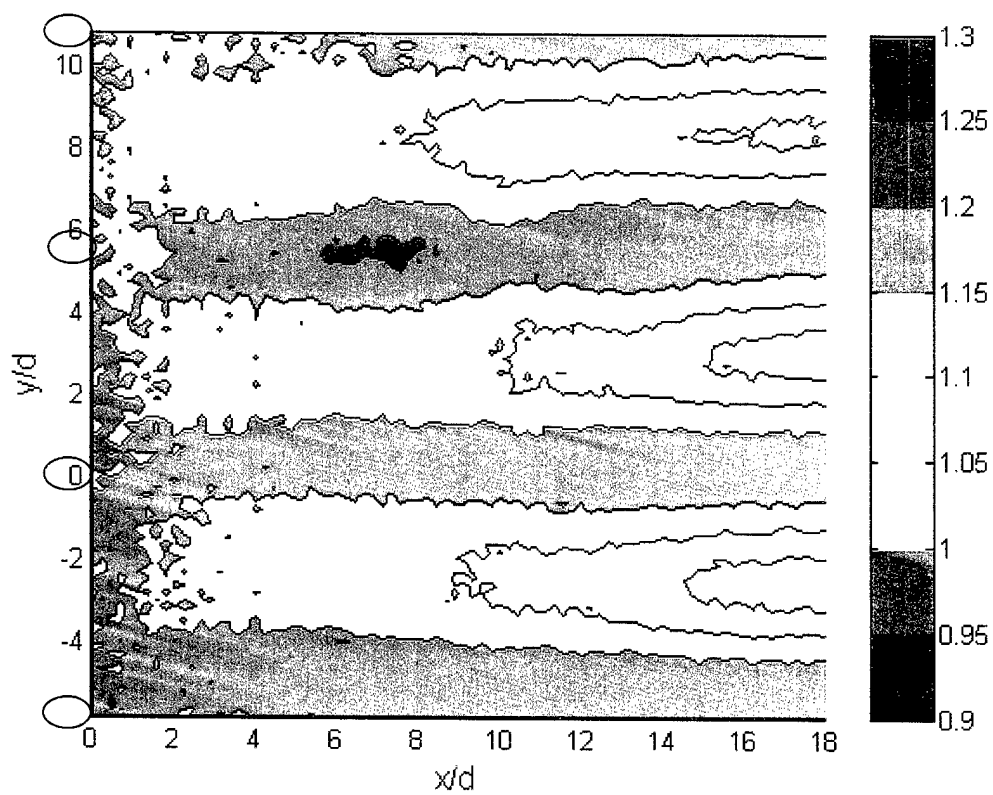


Figure 3.28: Heat transfer coefficient augmentation due to high turbulence ( $h_{high\ Tu}/h_{low\ Tu}$ ),  $M = 0.7$ . All smooth, showerhead off.

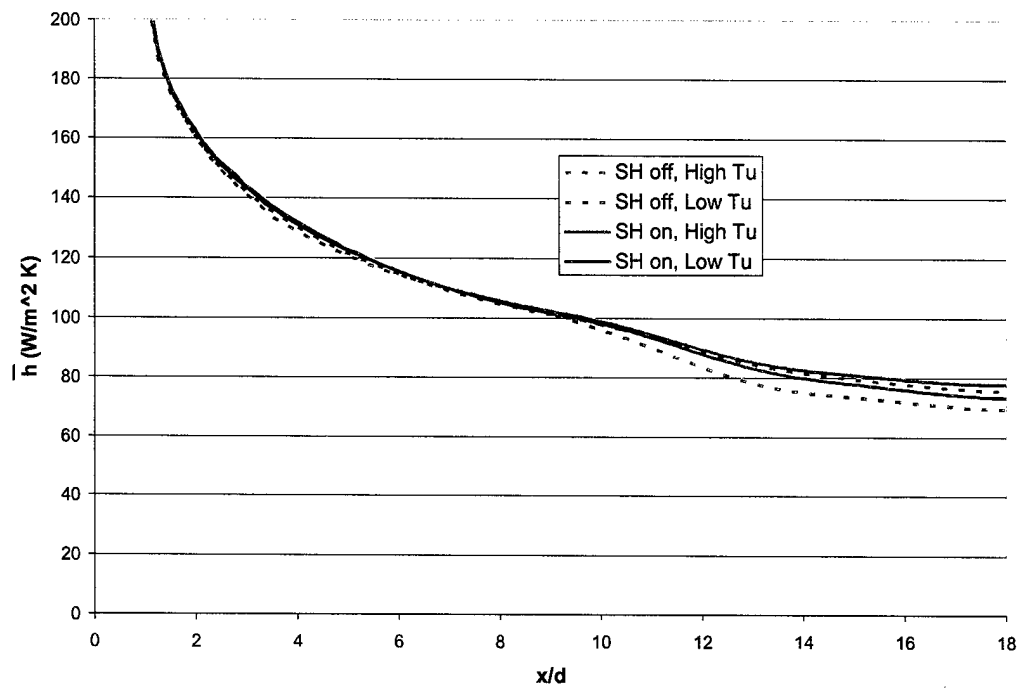


Figure 3.29: Effects of turbulence and showerhead cooling on spanwise averaged heat transfer coefficients. All smooth,  $M = 0$ , holes covered.

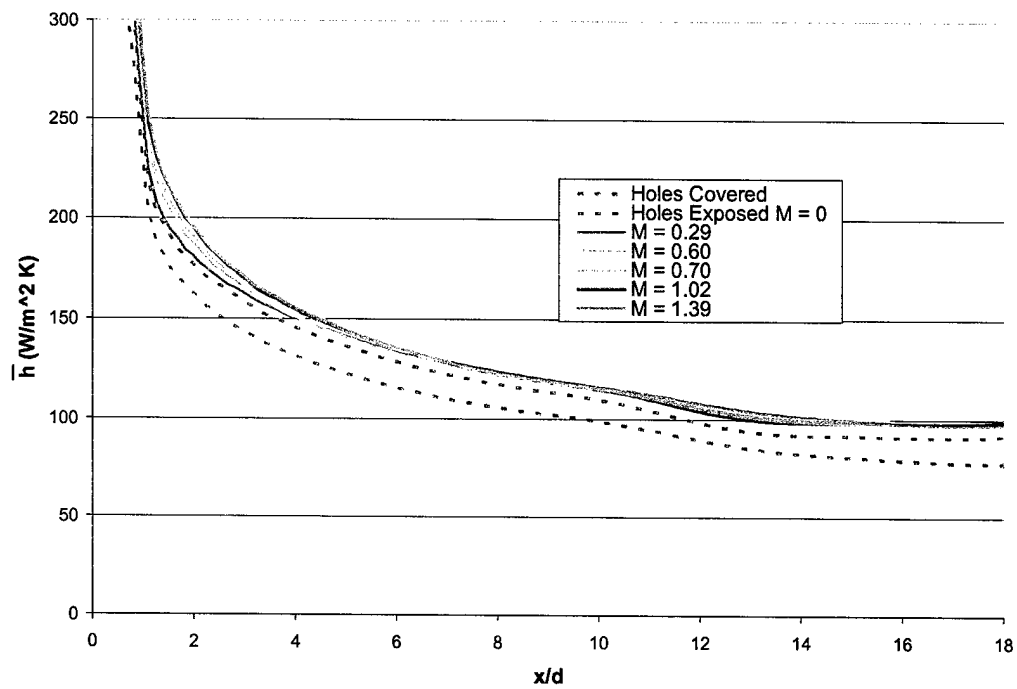


Figure 3.30: Spanwise averaged heat transfer coefficients. All smooth, showerhead on, high turbulence.



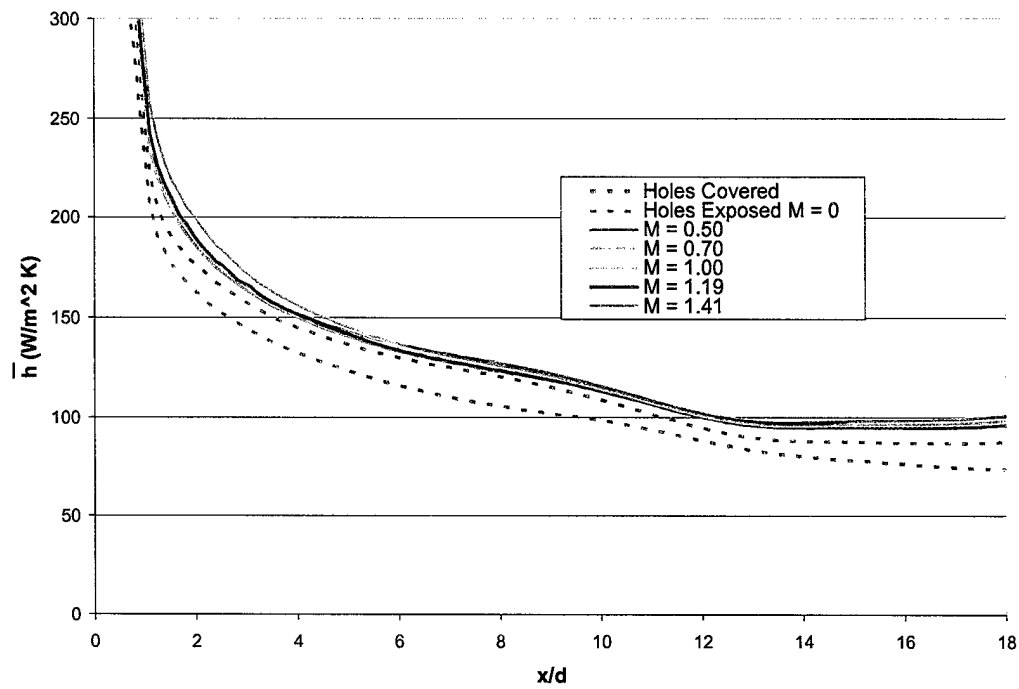


Figure 3.31: Spanwise averaged heat transfer coefficients. All smooth, showerhead on, low turbulence.

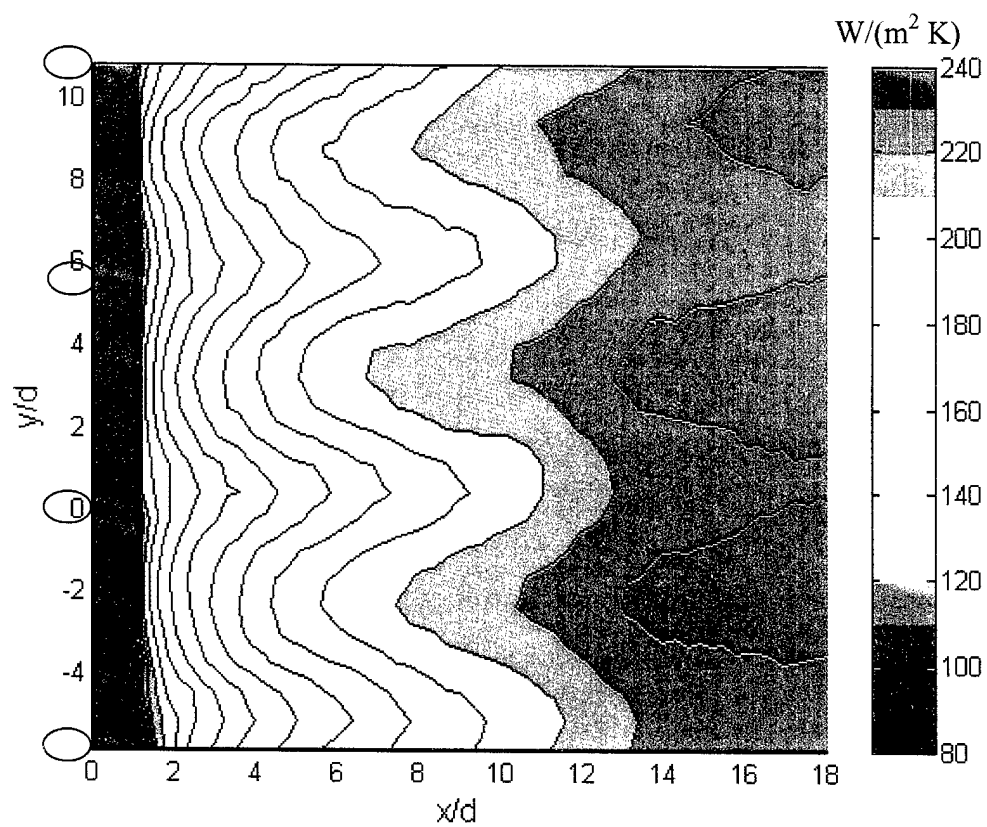


Figure 3.32: Heat transfer coefficient distribution,  $M = 0.3$ . All smooth, showerhead on, high turbulence.

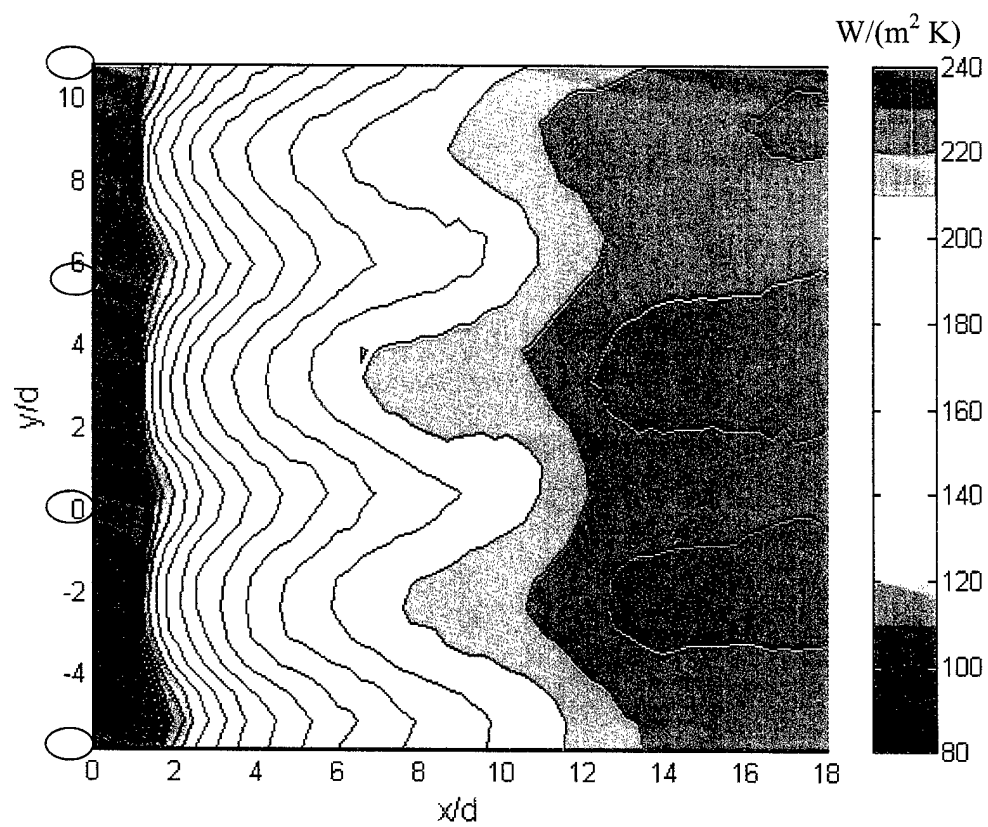


Figure 3.33: Heat transfer coefficient distribution,  $M = 0.7$ . All smooth, showerhead on, high turbulence.

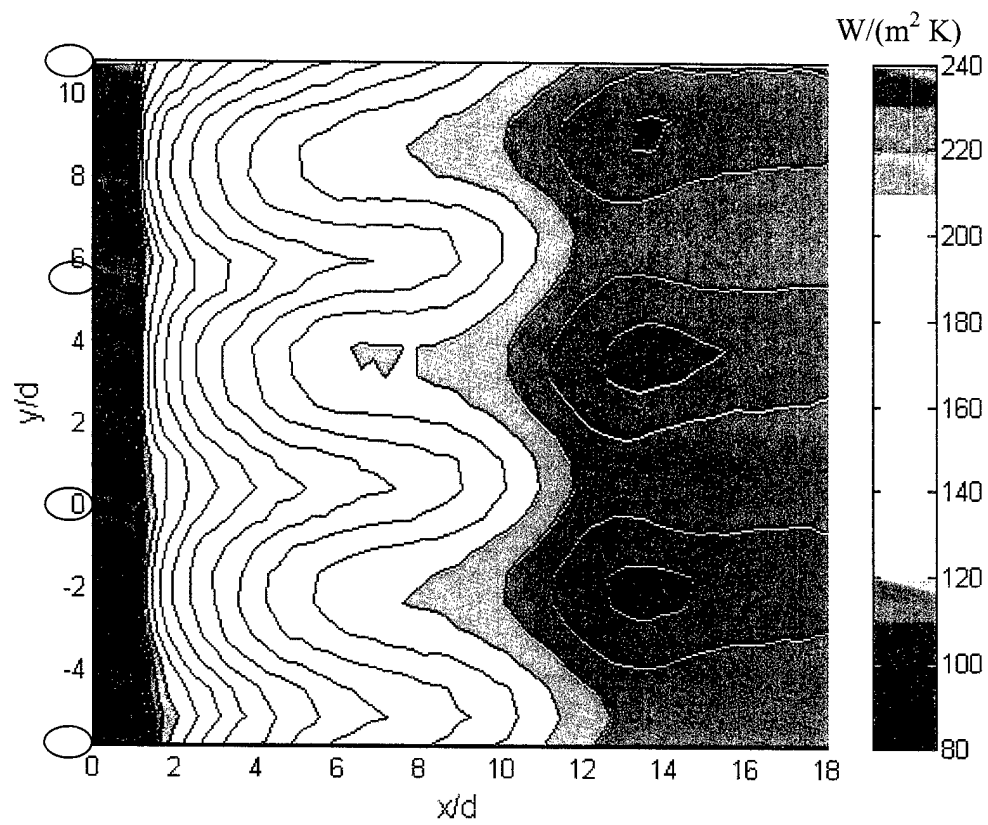


Figure 3.34: Heat transfer coefficient distribution,  $M = 0.3$ . All smooth, showerhead on, low turbulence.

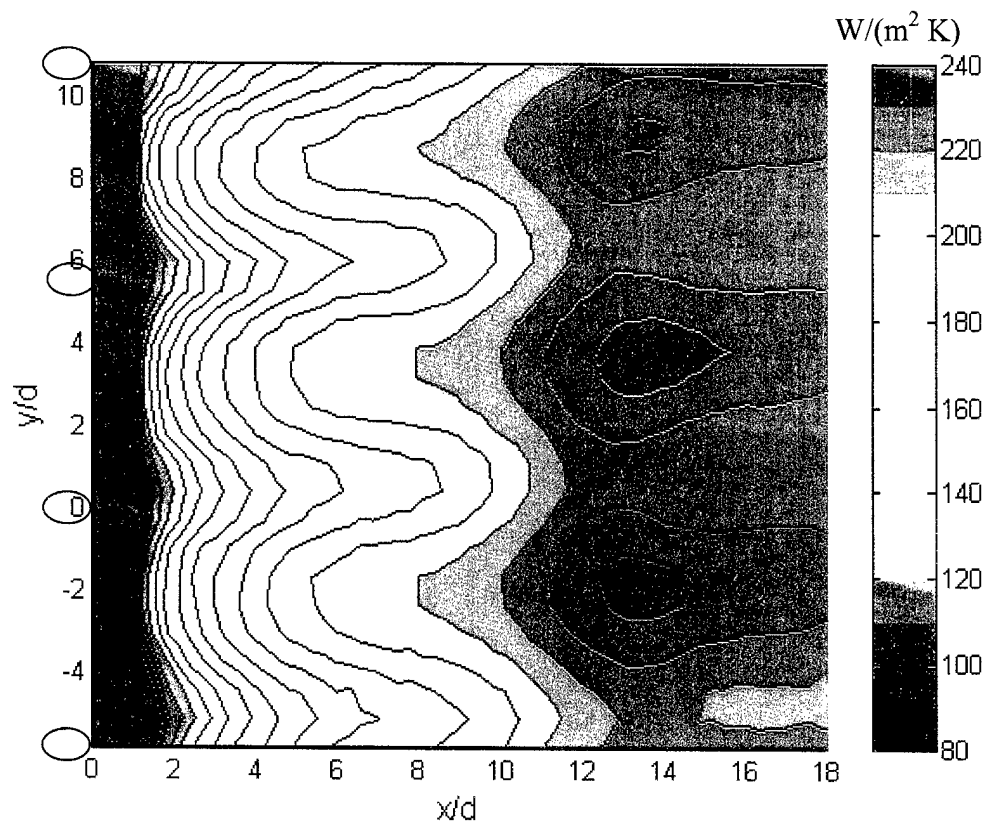


Figure 3.35: Heat transfer coefficient distribution,  $M = 0.7$ . All smooth, showerhead on, low turbulence.

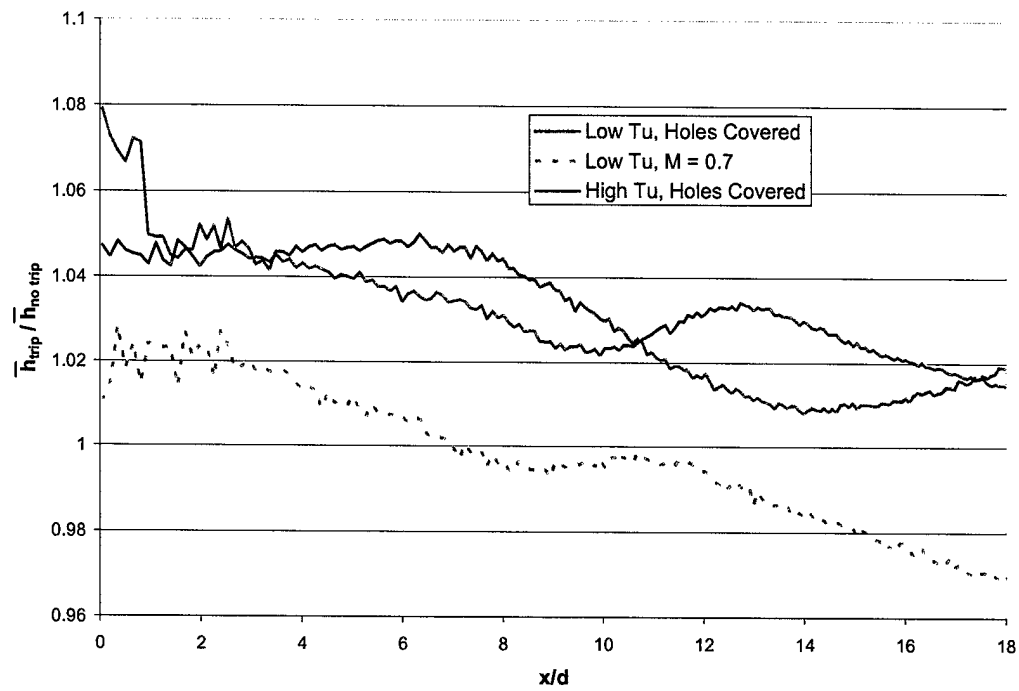


Figure 3.36:  $\bar{h}$  augmentation due to the trip rod (all smooth, showerhead off)

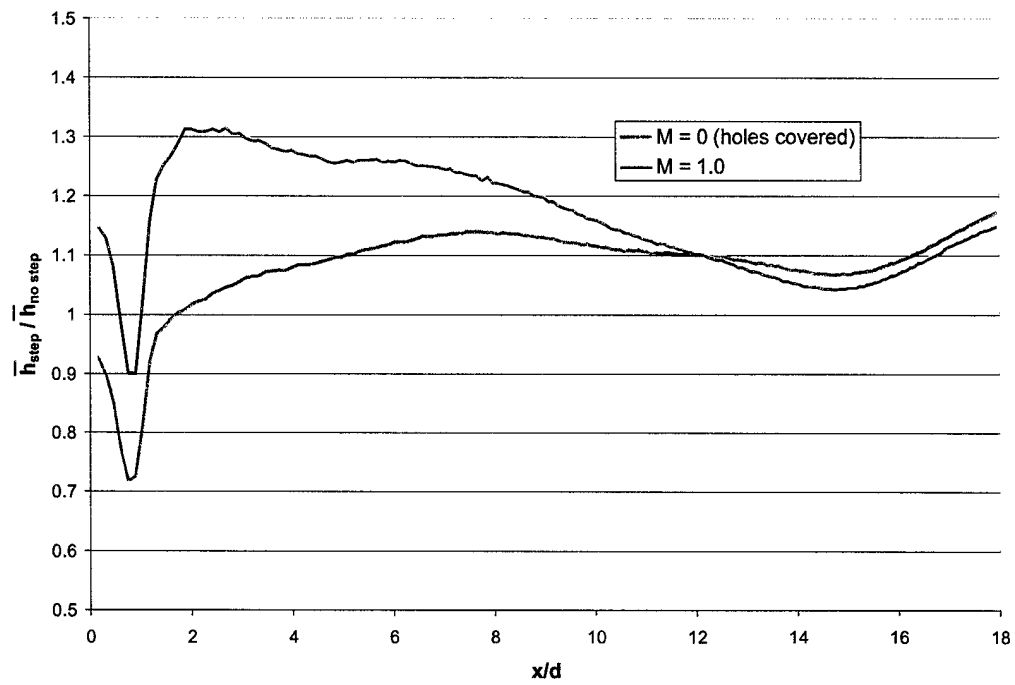


Figure 3.37:  $\bar{h}$  augmentation due to step change in surface height of approximately 0.3 mm (all smooth, showerhead off, high Tu)

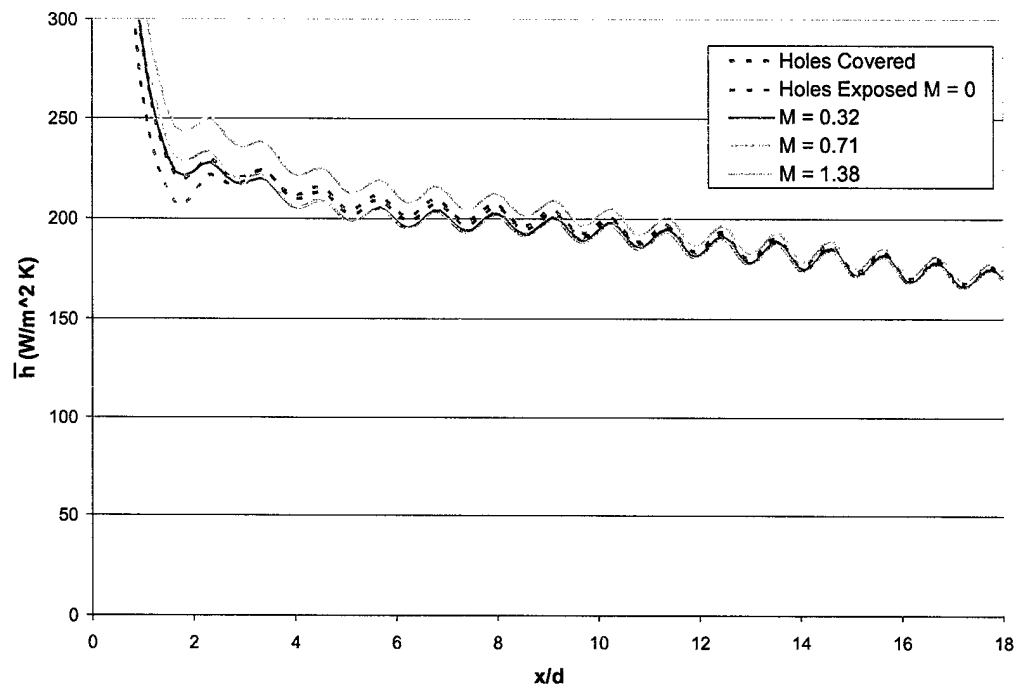


Figure 3.38: Spanwise averaged heat transfer coefficients. Downstream rough, showerhead off, high turbulence.



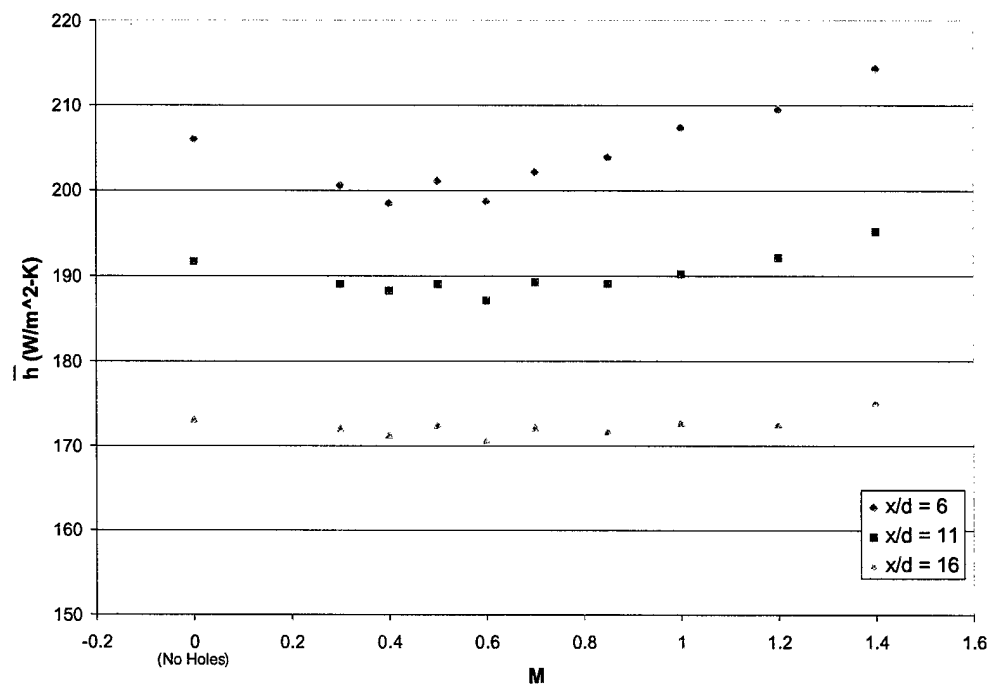


Figure 3.39: Spanwise averaged heat transfer coefficients at  $x/d = 6, 11$ , and  $16$ .  
Downstream rough, showerhead off, high turbulence.

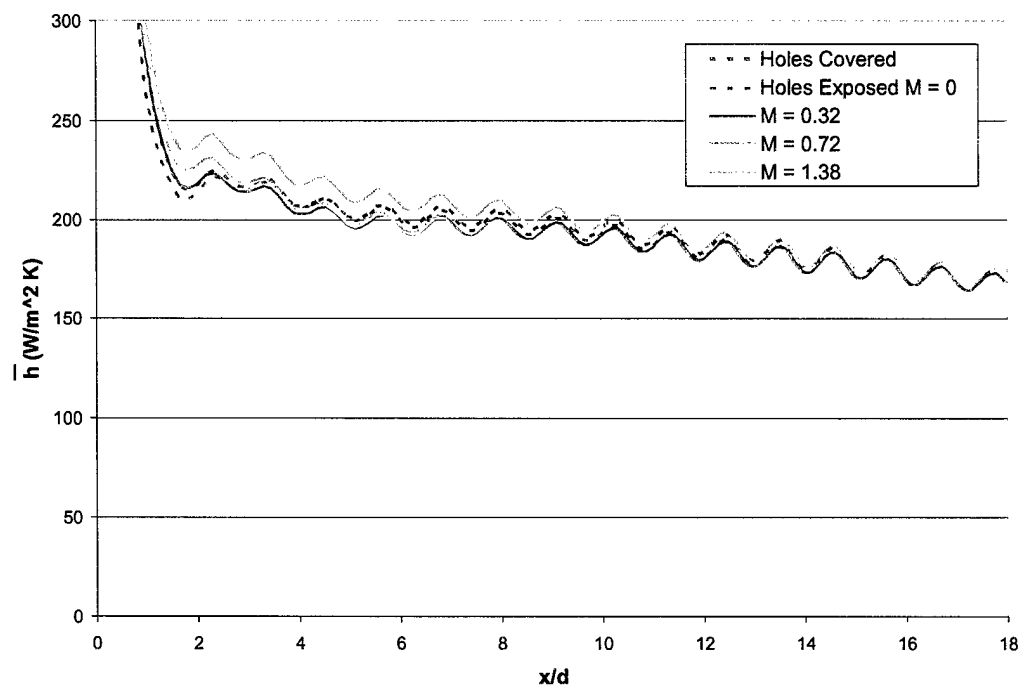


Figure 3.40: Spanwise averaged heat transfer coefficients. Downstream rough, showerhead off, low turbulence.

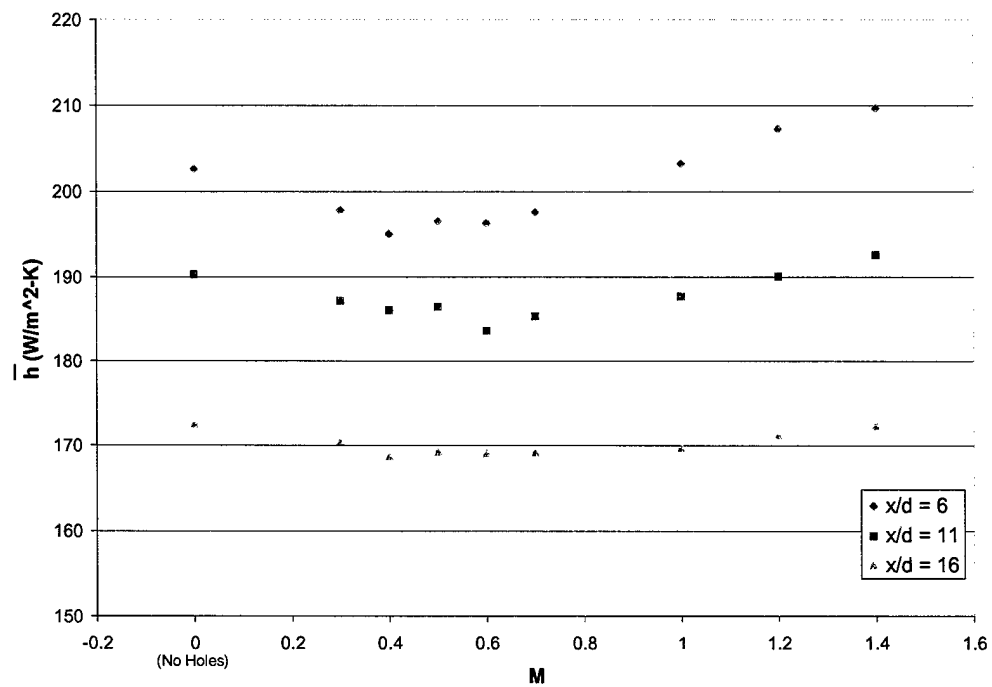


Figure 3.41: Spanwise averaged heat transfer coefficients at  $x/d = 6, 11$ , and  $16$ .  
Downstream rough, showerhead off, low turbulence.

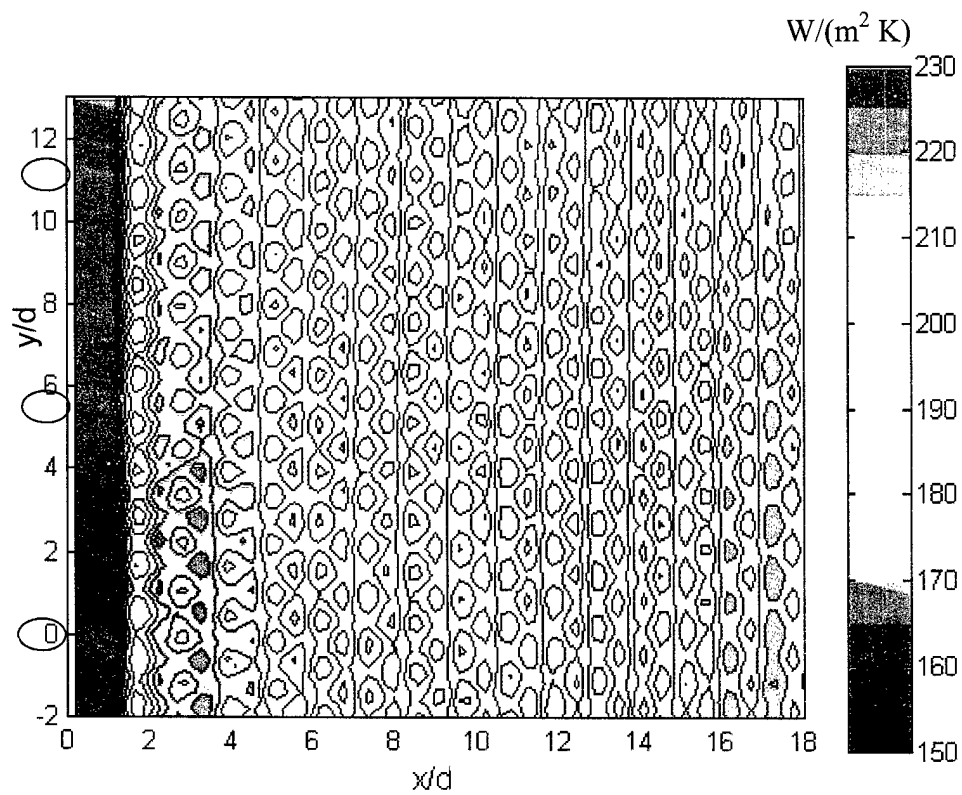


Figure 3.42: Heat transfer coefficient distribution,  $M = 0$ , holes covered.  
Downstream rough, showerhead off, high turbulence.

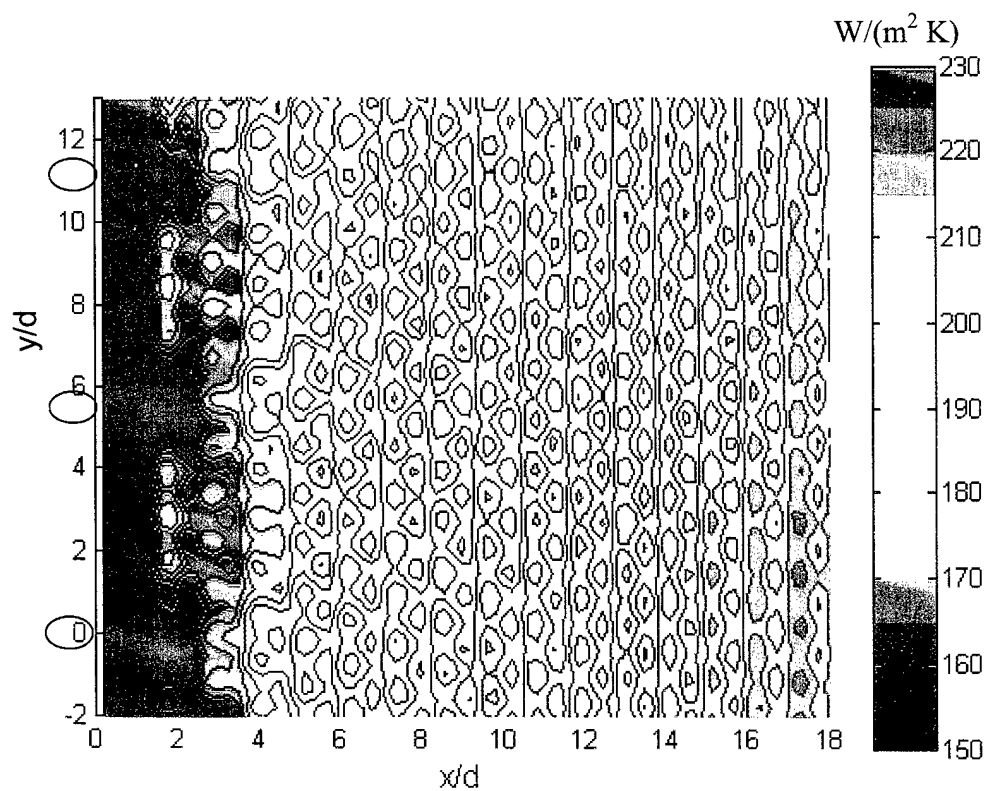


Figure 3.43: Heat transfer coefficient distribution,  $M = 0.7$ . Downstream rough, showerhead off, high turbulence.

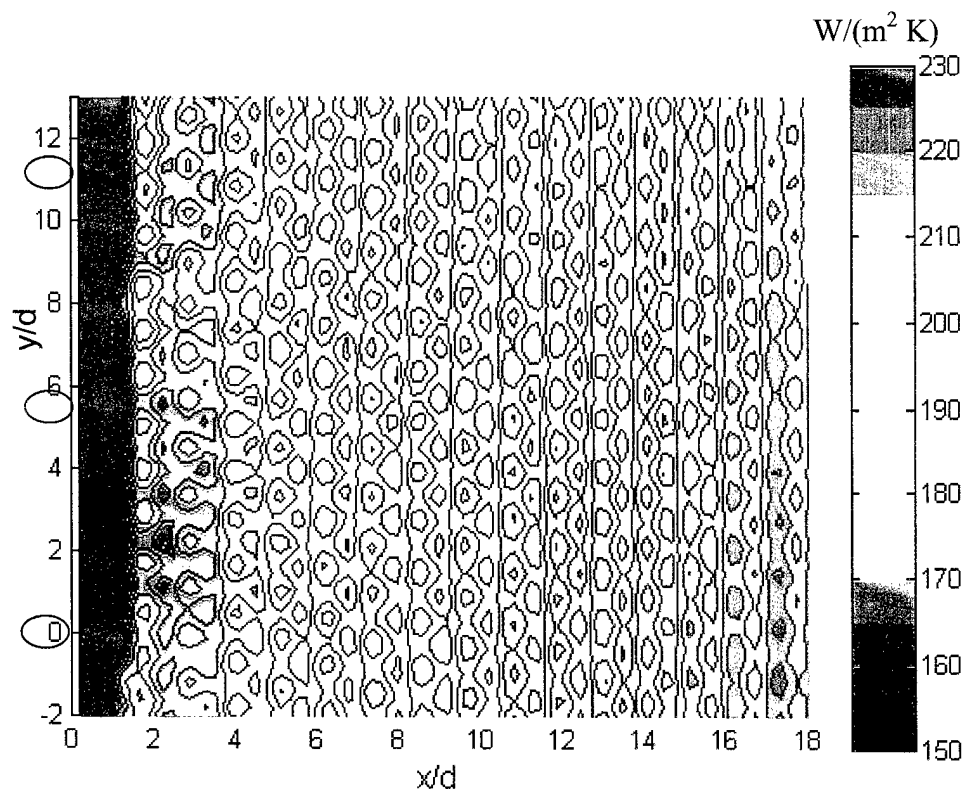


Figure 3.44: Heat transfer coefficient distribution,  $M = 0$ , holes covered.  
Downstream rough, showerhead off, low turbulence.

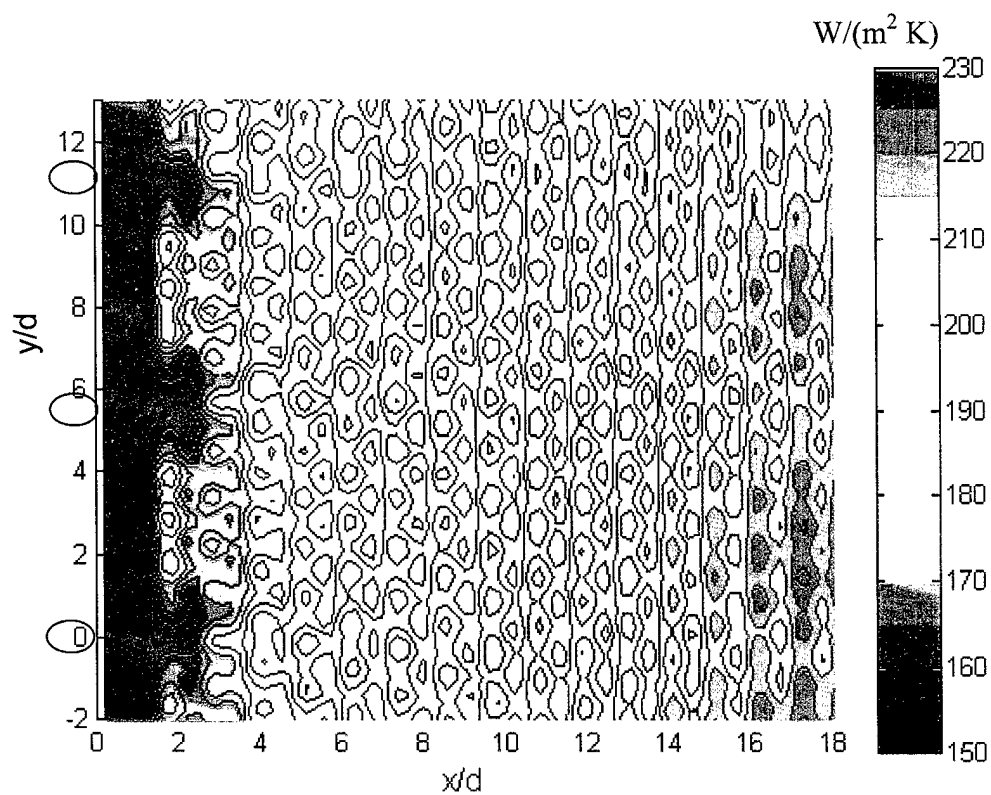


Figure 3.45: Heat transfer coefficient distribution,  $M = 0.7$ . Downstream rough, showerhead off, low turbulence.

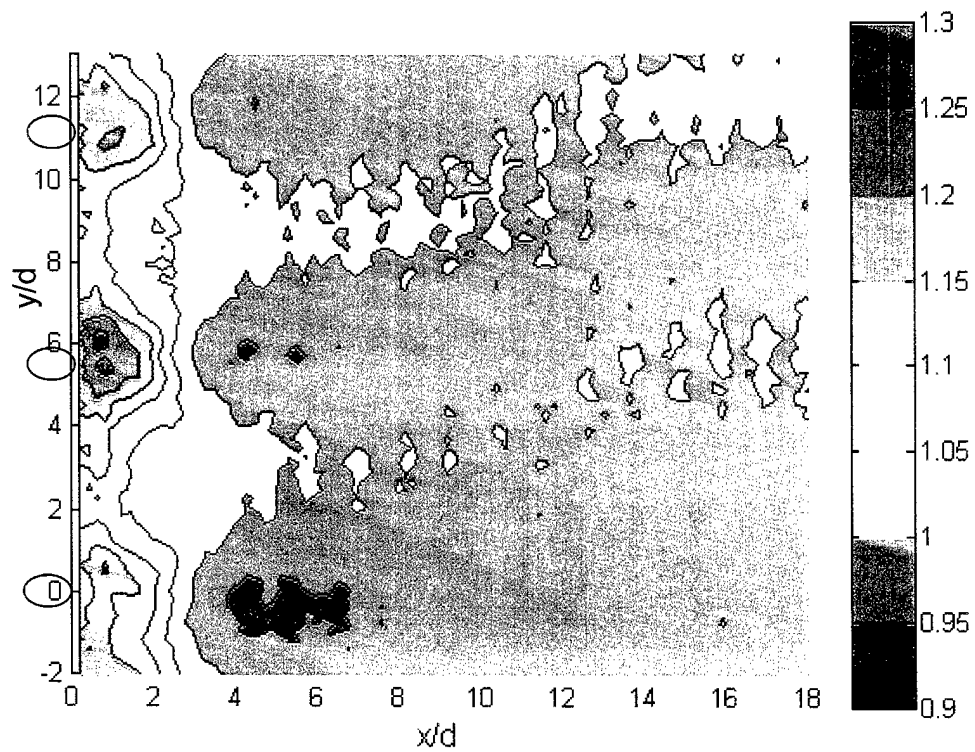


Figure 3.46: Heat transfer coefficient augmentation due to blowing at  $M = 0.7$  ( $h_f/h_o$ ). Downstream rough, showerhead off, high turbulence.



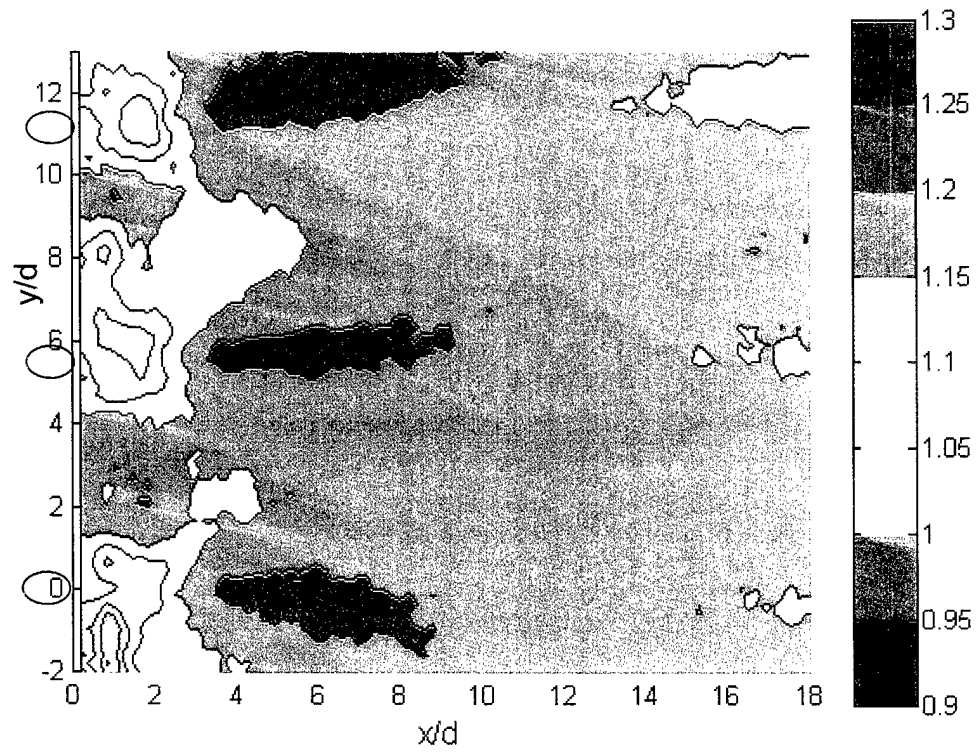


Figure 3.47: Heat transfer coefficient augmentation due to blowing at  $M = 0.7$  ( $h_f/h_o$ ). Downstream rough, showerhead off, low turbulence.

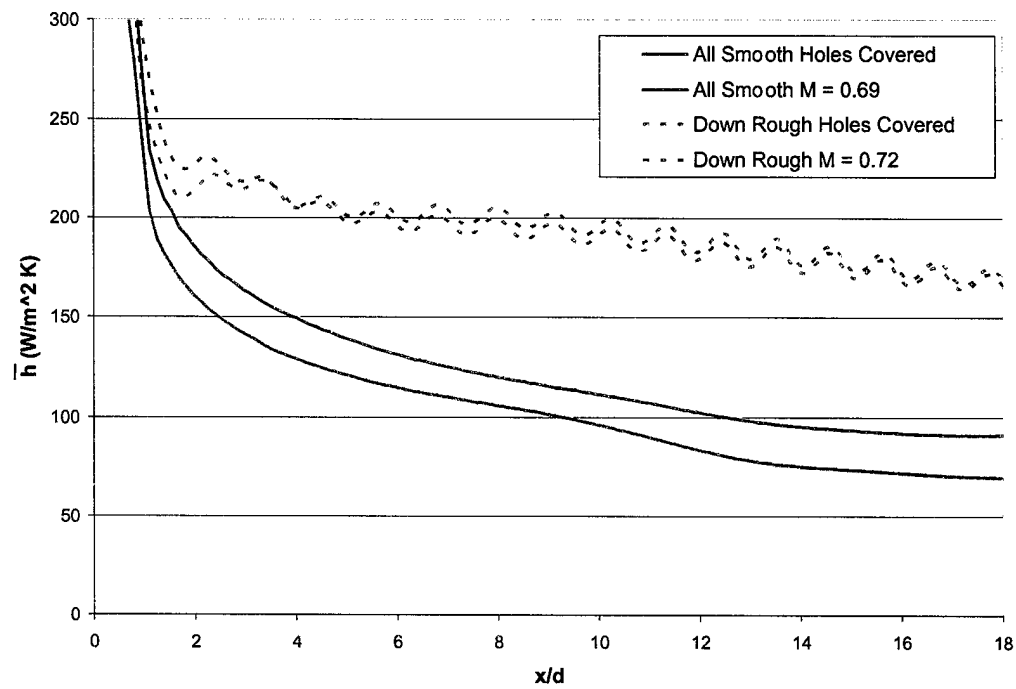


Figure 3.48: Influence of downstream roughness on spanwise averaged heat transfer coefficients. Upstream smooth, showerhead off, low turbulence.

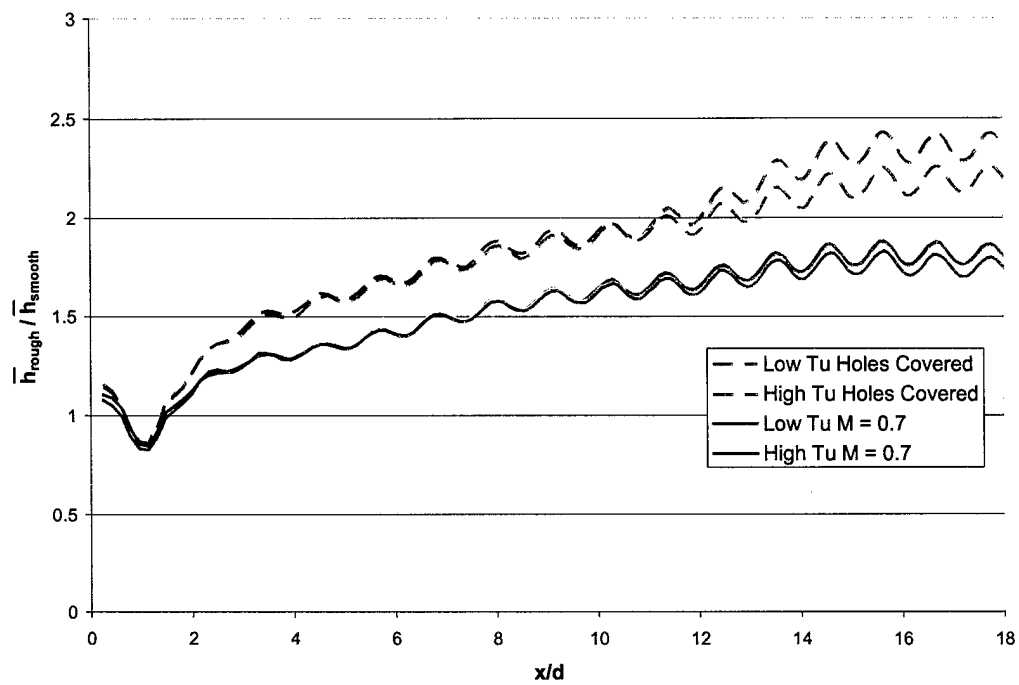


Figure 3.49: Spanwise averaged heat transfer coefficient augmentation due to downstream roughness ( $\bar{h}_{rough}/\bar{h}_{smooth}$ ). Upstream smooth, showerhead off.

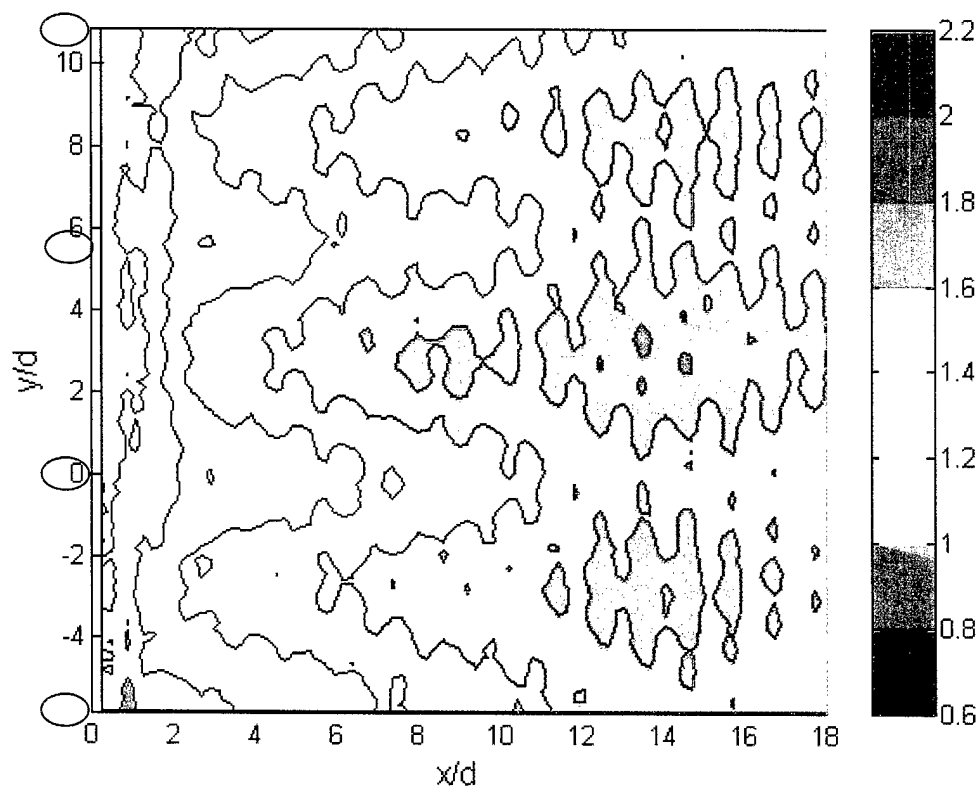


Figure 3.50: Heat transfer coefficient augmentation due to downstream roughness ( $h_{rough}/h_{smooth}$ ).  $M = 0.7$ , upstream smooth, showerhead off, high turbulence.

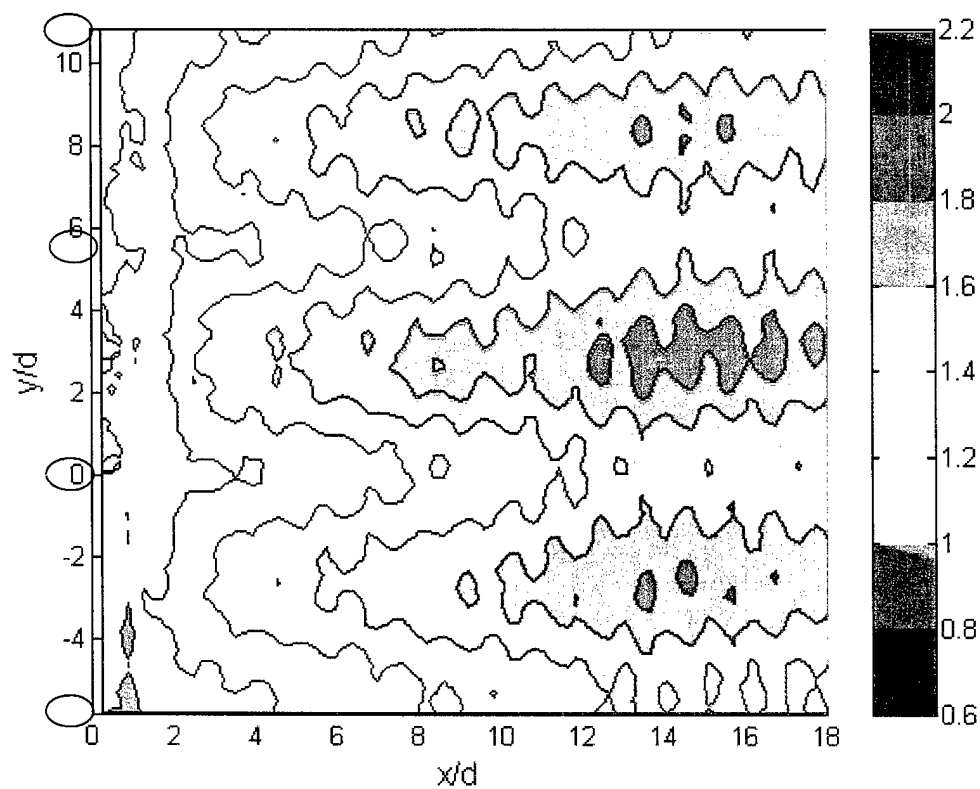


Figure 3.51: Heat transfer coefficient augmentation due to downstream roughness ( $h_{rough}/h_{smooth}$ ).  $M = 0.7$ , upstream smooth, showerhead off, low turbulence.

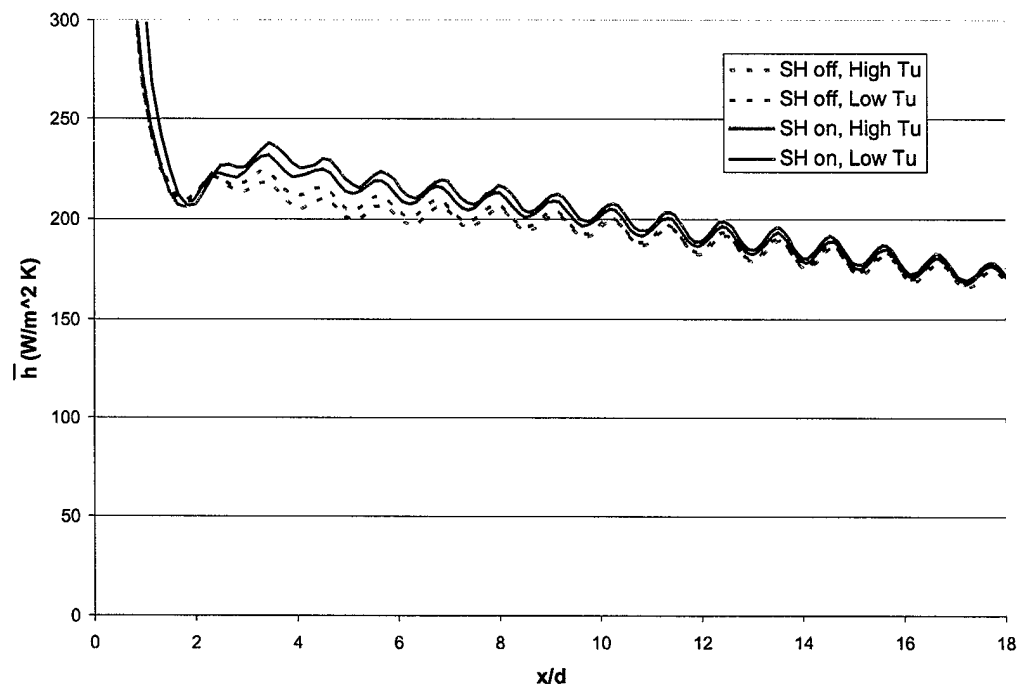


Figure 3.52: Effects of turbulence and showerhead cooling on spanwise averaged heat transfer coefficients. Downstream rough,  $M = 0$ , holes covered.

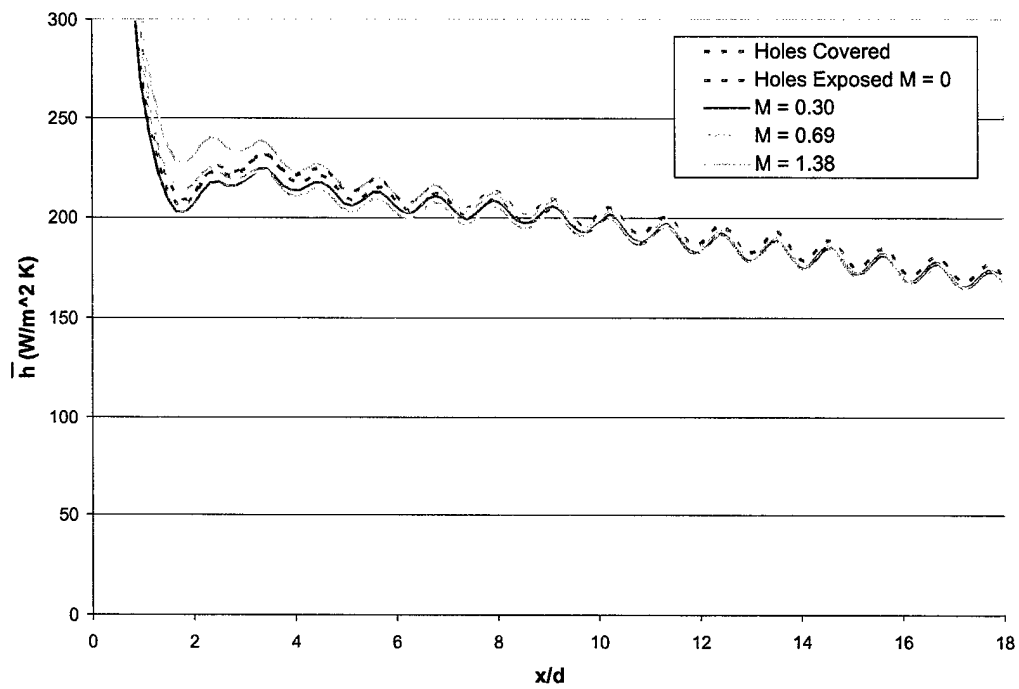


Figure 3.53: Spanwise averaged heat transfer coefficients. Downstream rough, showerhead on, high turbulence.

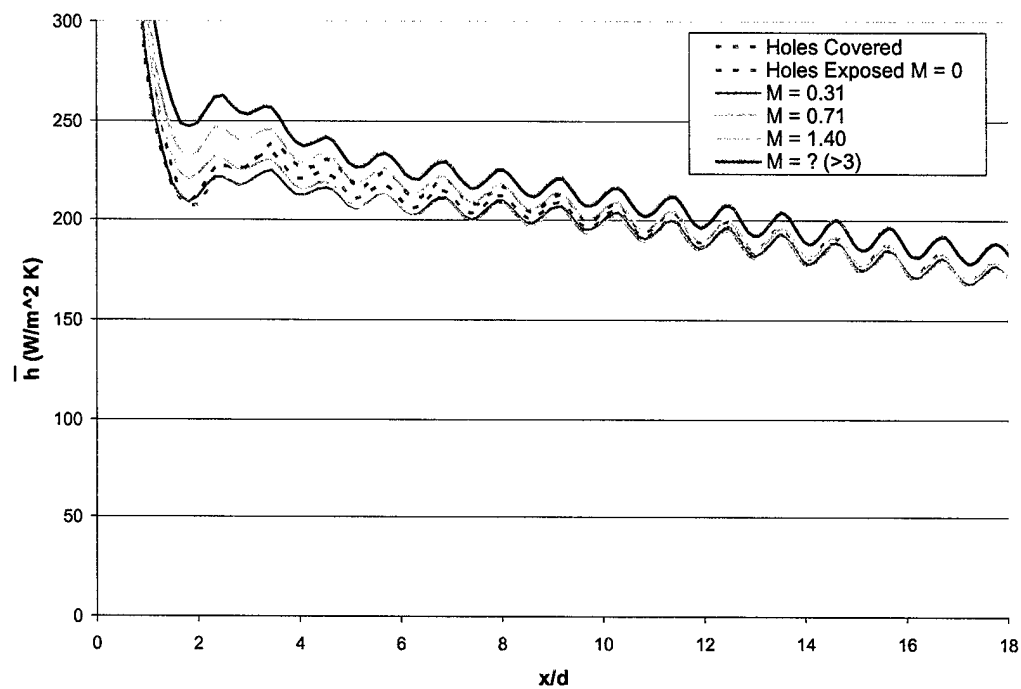


Figure 3.54: Spanwise averaged heat transfer coefficients. Downstream rough, showerhead on, low turbulence.



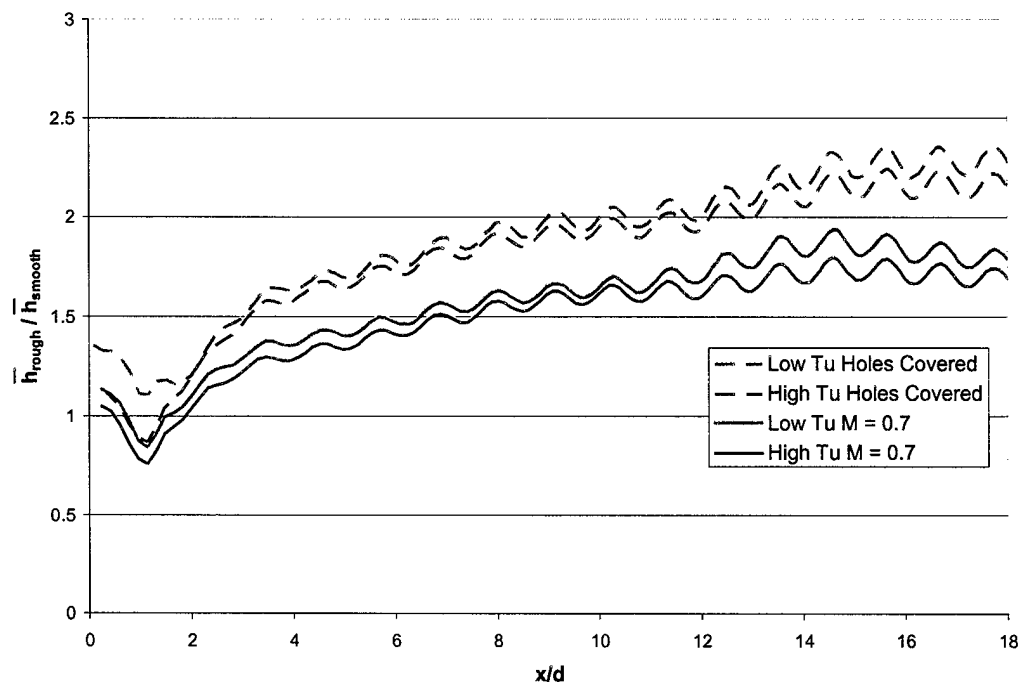


Figure 3.55: Spanwise averaged heat transfer coefficient augmentation due to downstream roughness ( $h_{rough}/h_{smooth}$ ). Upstream smooth, showerhead on.

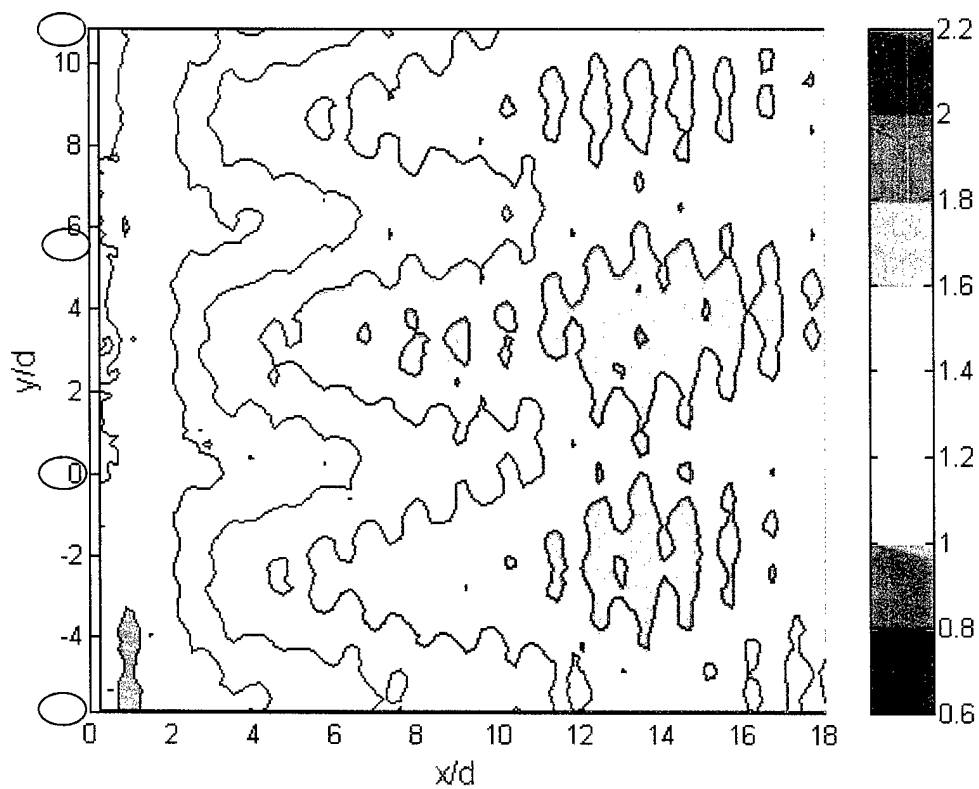


Figure 3.56: Heat transfer coefficient augmentation due to downstream roughness ( $h_{rough}/h_{smooth}$ ).  $M = 0.7$ , upstream smooth, showerhead on, high turbulence.

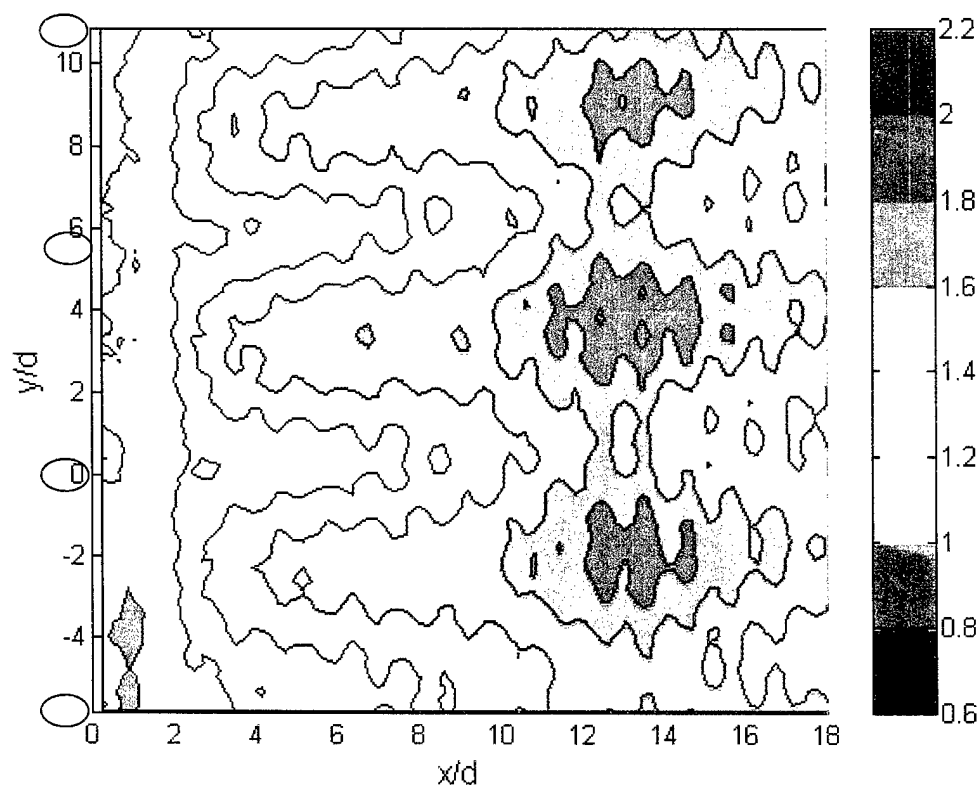


Figure 3.57: Heat transfer coefficient augmentation due to downstream roughness ( $h_{rough}/h_{smooth}$ ).  $M = 0.7$ , upstream smooth, showerhead on, low turbulence.

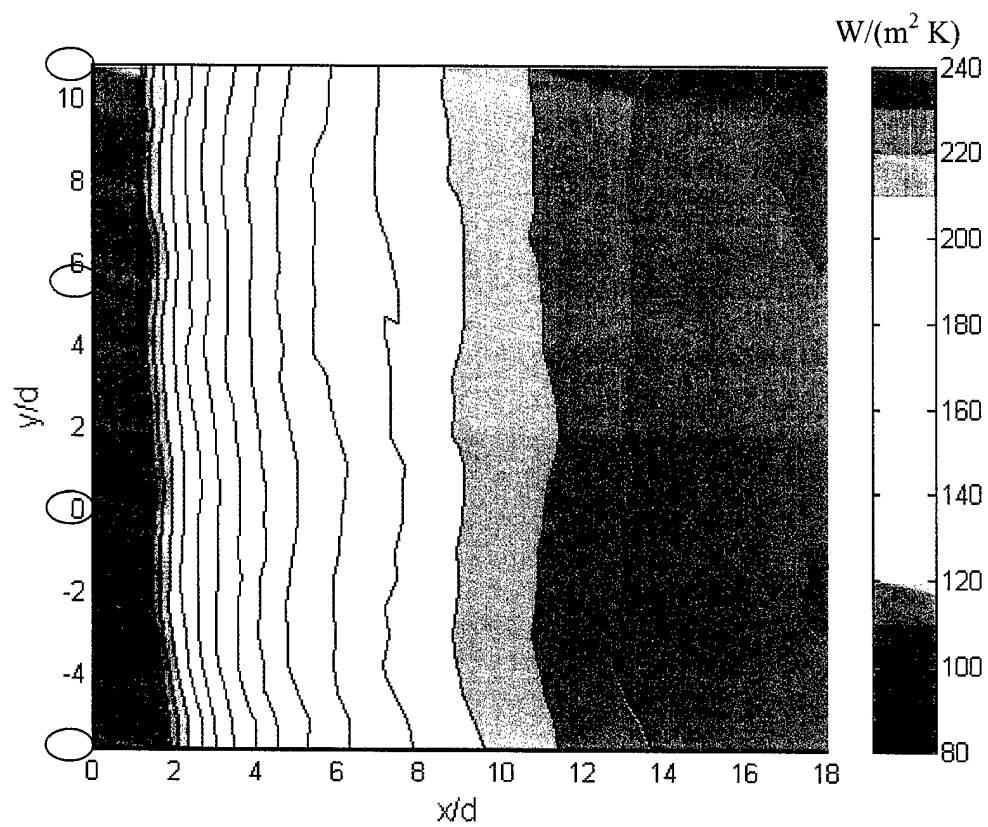


Figure 3.58: Heat transfer coefficient distribution,  $M = 0$ , holes exposed. Upstream rough, downstream smooth, showerhead off, high turbulence.

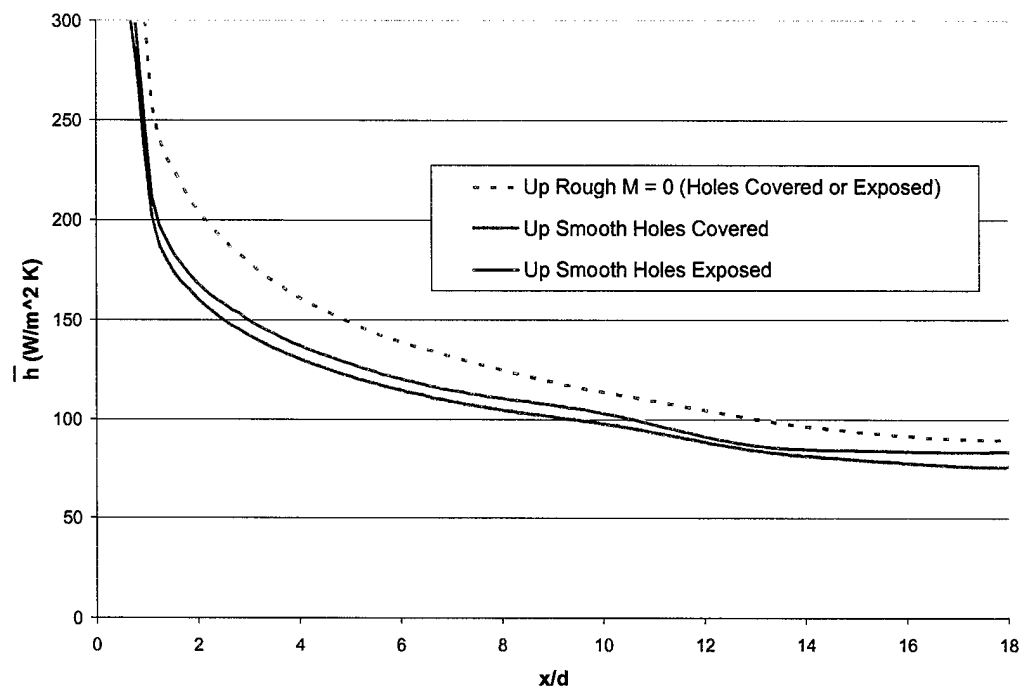


Figure 3.59: Influence of upstream roughness on spanwise averaged heat transfer coefficients. Downstream smooth, showerhead off, high turbulence.

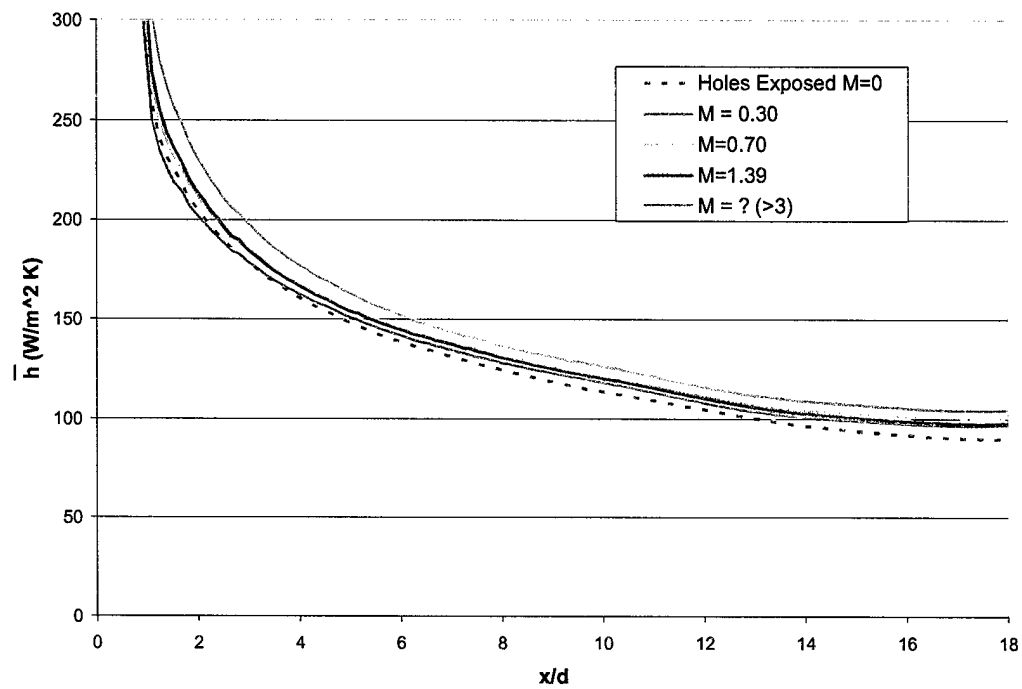


Figure 3.60: Spanwise averaged heat transfer coefficients. Upstream rough, downstream smooth, showerhead off, high turbulence.

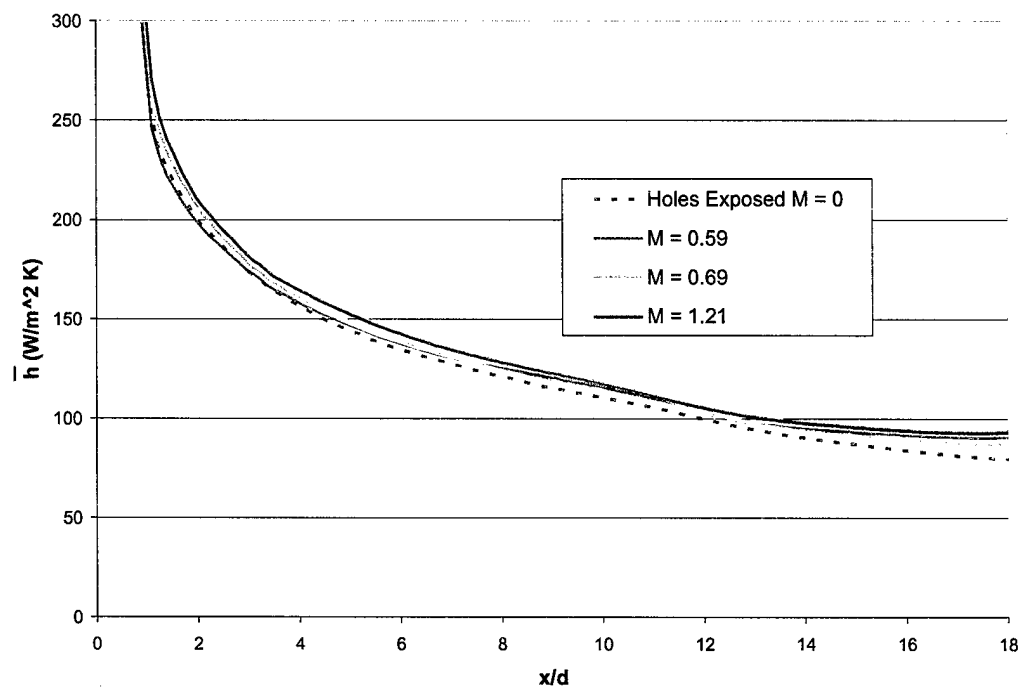


Figure 3.61: Spanwise averaged heat transfer coefficients. Upstream rough, downstream smooth, showerhead off, low turbulence.

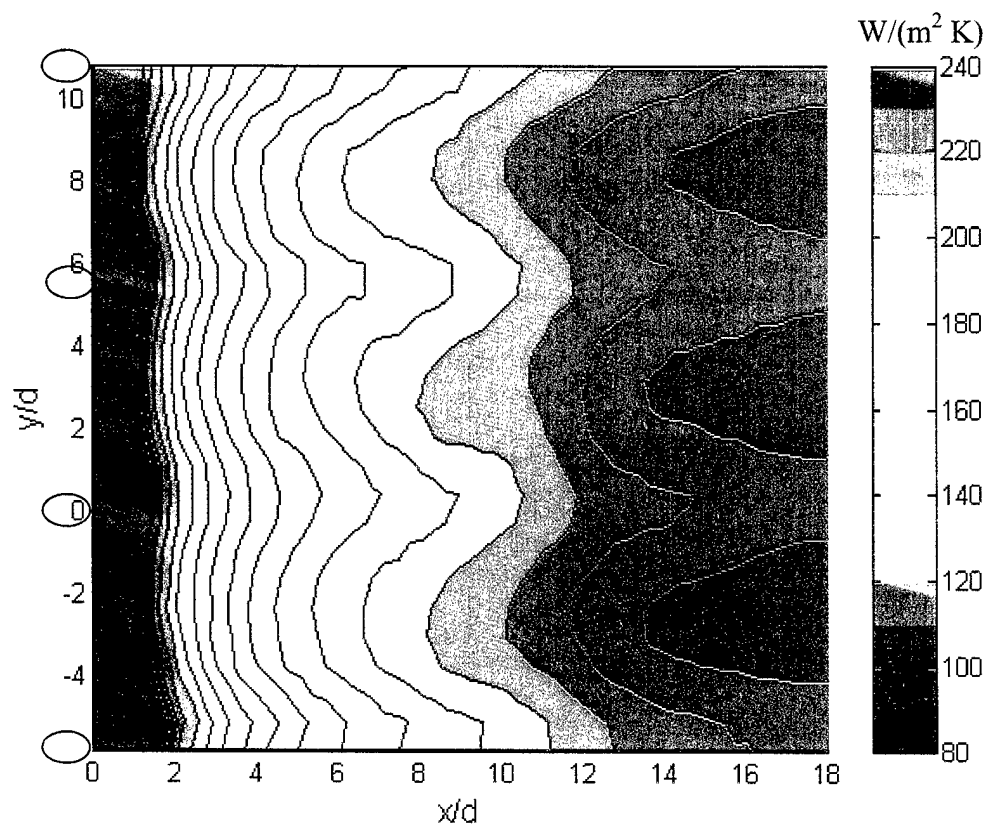


Figure 3.62: Heat transfer coefficient distribution,  $M = 0.7$ . Upstream rough, downstream smooth, showerhead off, low turbulence.



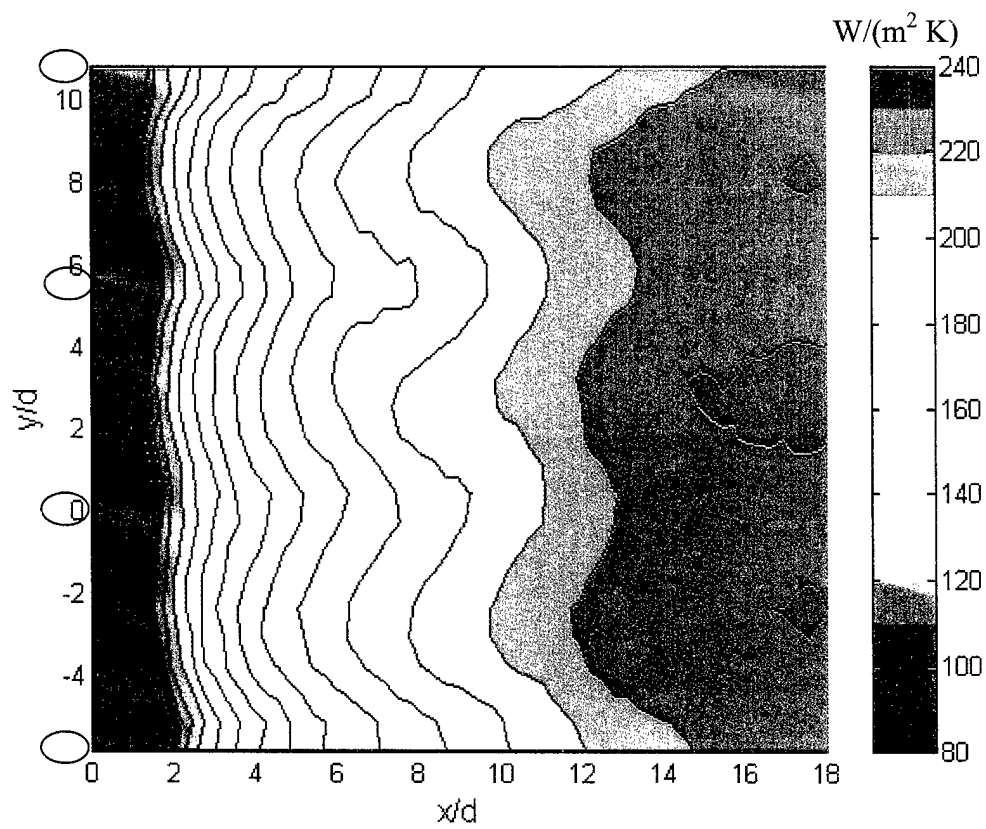


Figure 3.63: Heat transfer coefficient distribution,  $M = 0.7$ . Upstream rough, downstream smooth, showerhead off, high turbulence.

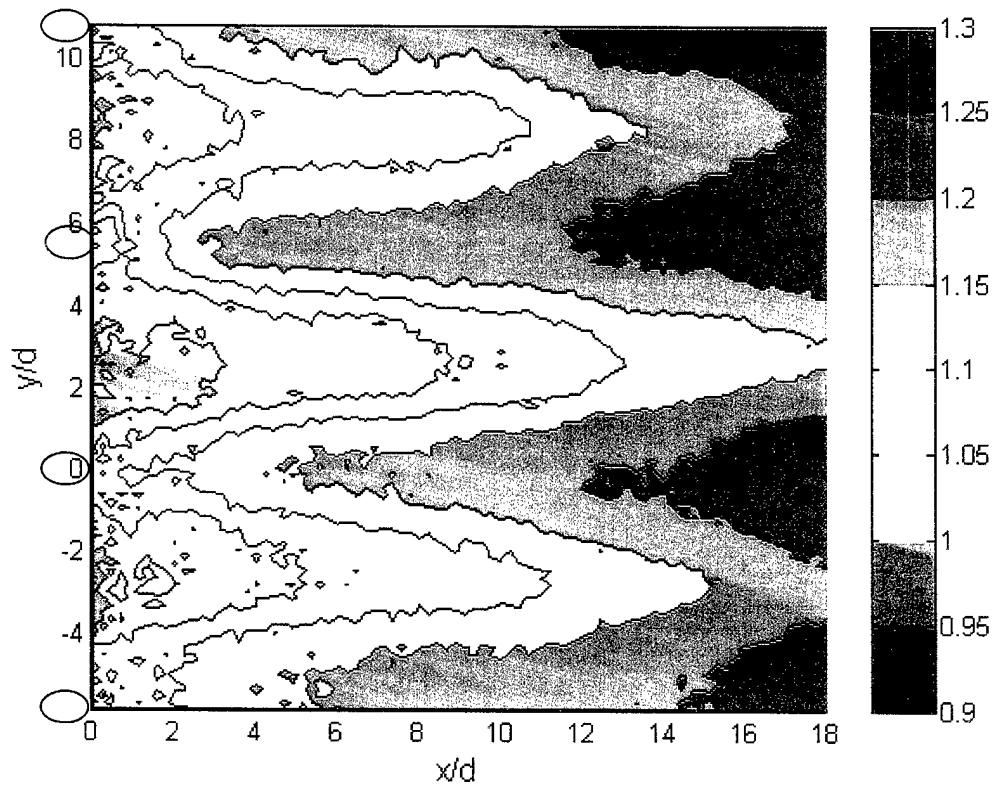


Figure 3.64: Heat transfer coefficient augmentation due to upstream roughness ( $h_{rough}/h_{smooth}$ ).  $M = 0.7$ , downstream smooth, showerhead off, low turbulence.

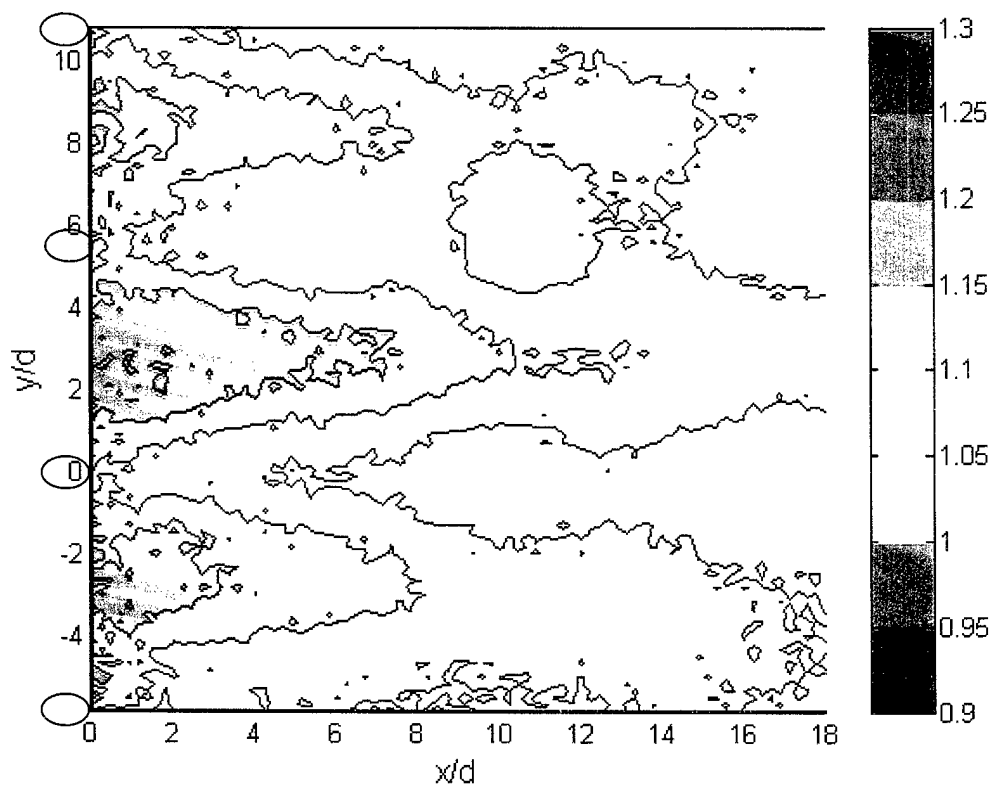


Figure 3.65: Heat transfer coefficient augmentation due to upstream roughness ( $h_{rough}/h_{smooth}$ ).  $M = 0.7$ , downstream smooth, showerhead off, high turbulence.

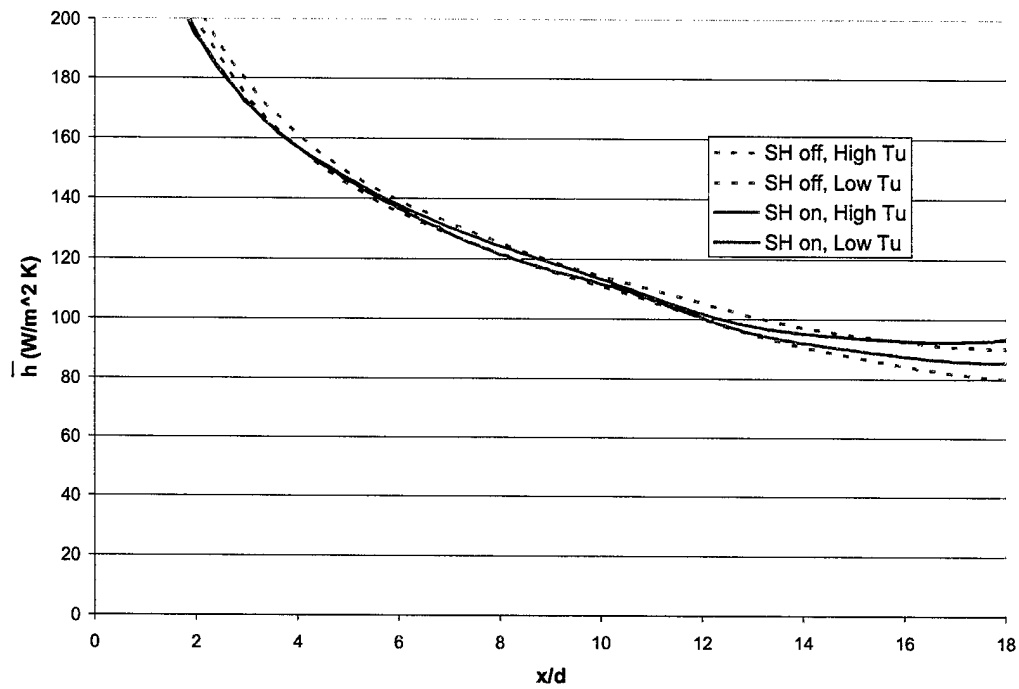


Figure 3.66: Effects of turbulence and showerhead cooling on spanwise averaged heat transfer coefficients. Upstream rough, downstream smooth,  $M = 0$  holes exposed (or covered).

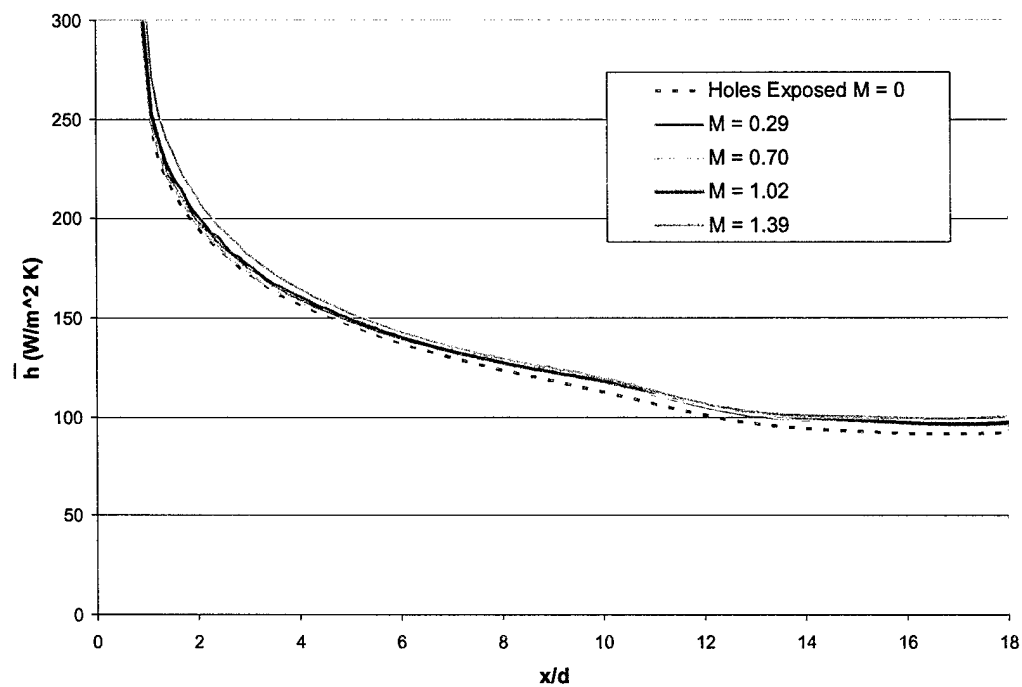


Figure 3.67: Spanwise averaged heat transfer coefficients. Upstream rough, downstream smooth, showerhead on, high turbulence.

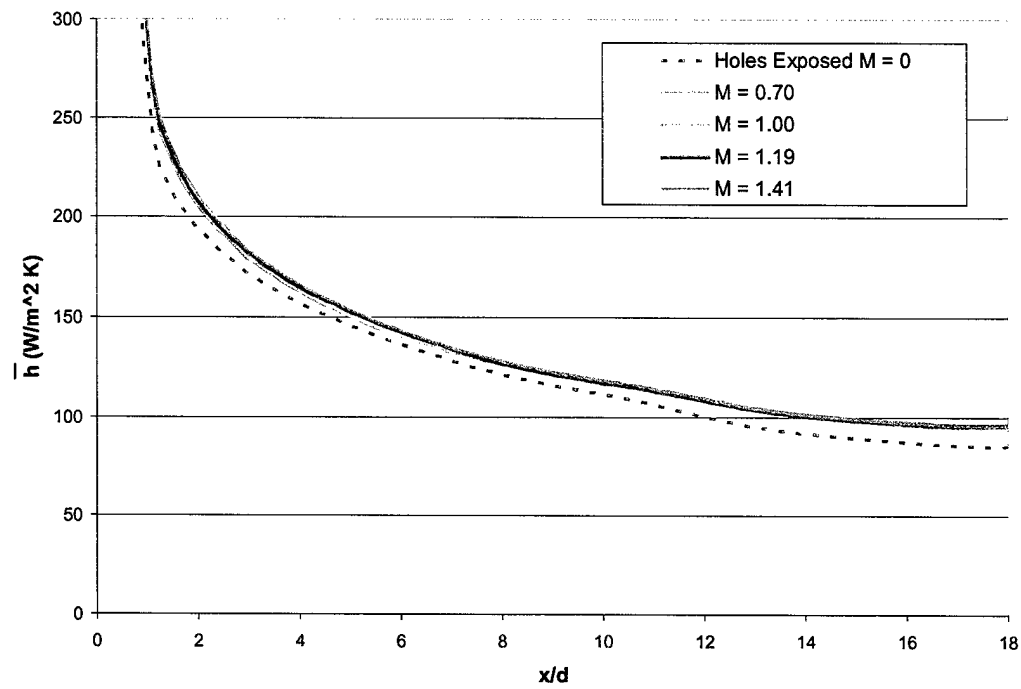


Figure 3.68: Spanwise averaged heat transfer coefficients. Upstream rough, downstream smooth, showerhead on, low turbulence.

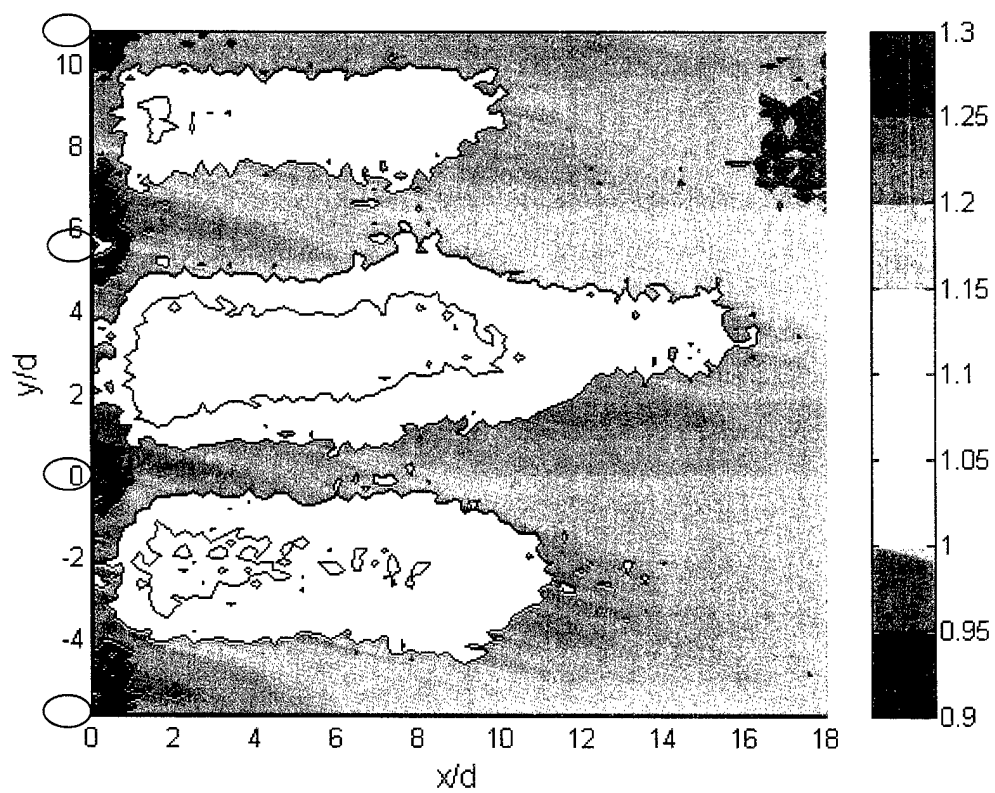


Figure 3.69: Heat transfer coefficient augmentation due to upstream roughness ( $h_{rough}/h_{smooth}$ ).  $M = 0.7$ , showerhead on, downstream smooth, high turbulence.

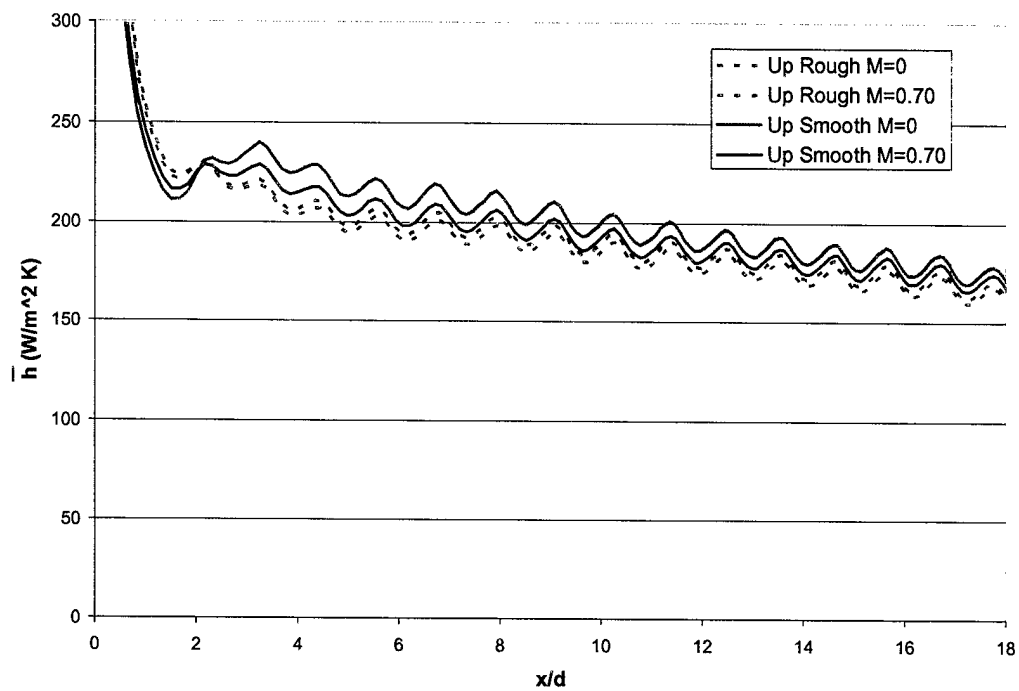


Figure 3.70: Influence of upstream roughness on spanwise averaged heat transfer coefficients. Downstream rough, showerhead off, high turbulence.



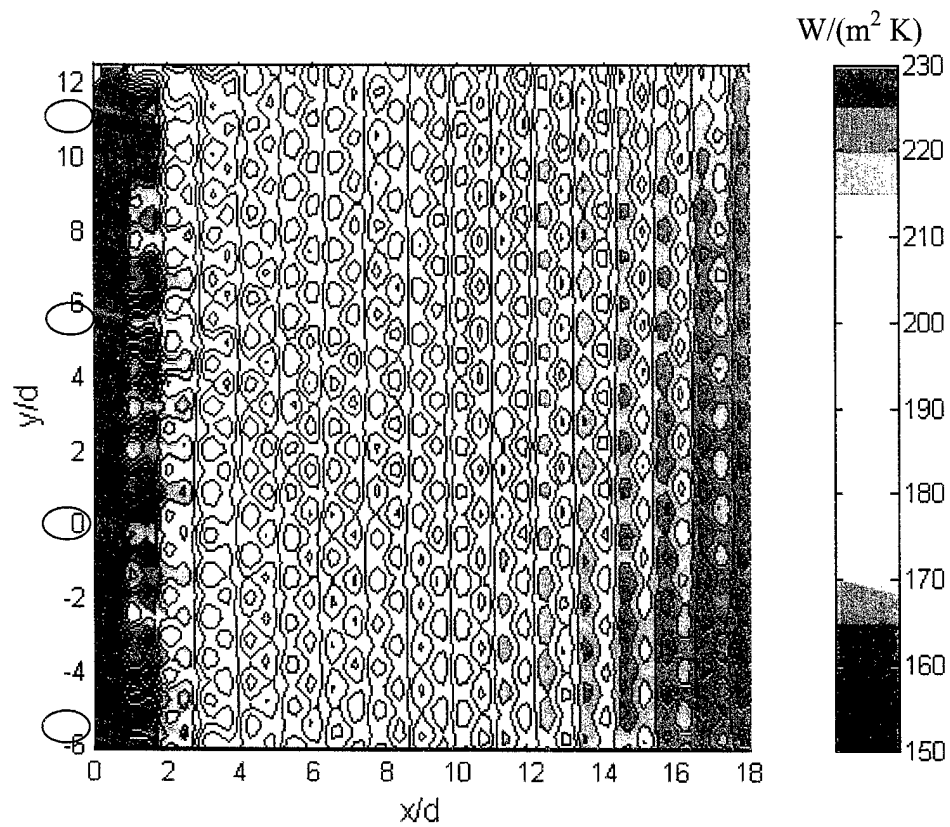


Figure 3.71: Heat transfer coefficient distribution,  $M = 0.7$ . All rough, showerhead off, high turbulence.

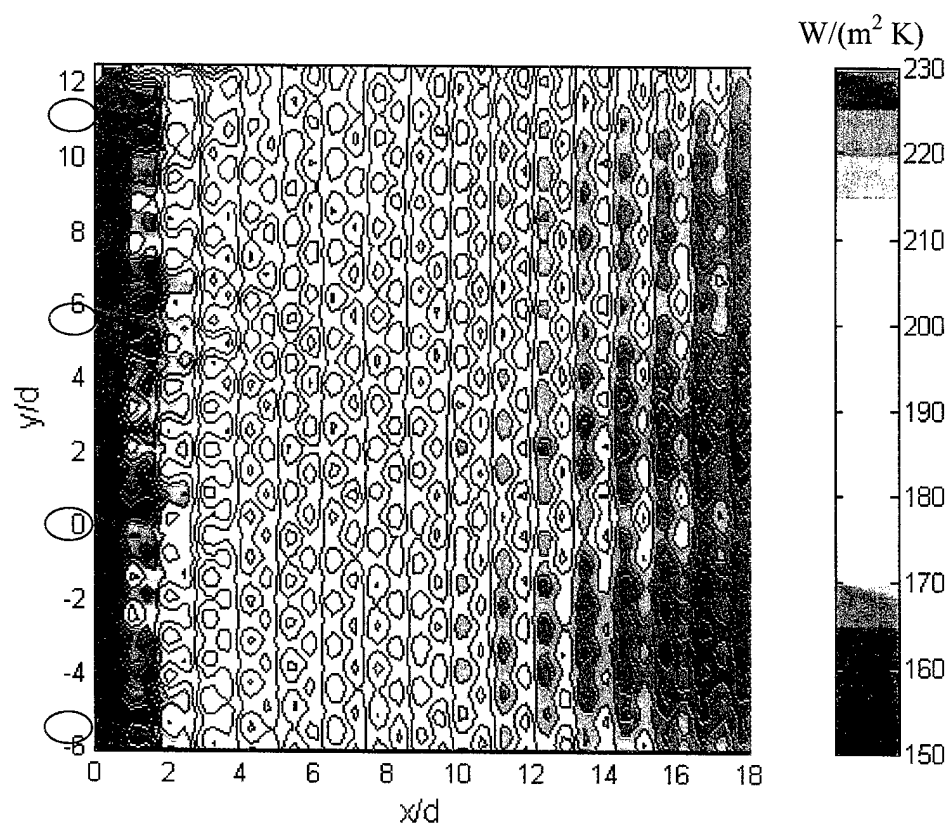


Figure 3.72: Heat transfer coefficient distribution,  $M = 0.7$ . All rough, showerhead off, low turbulence.

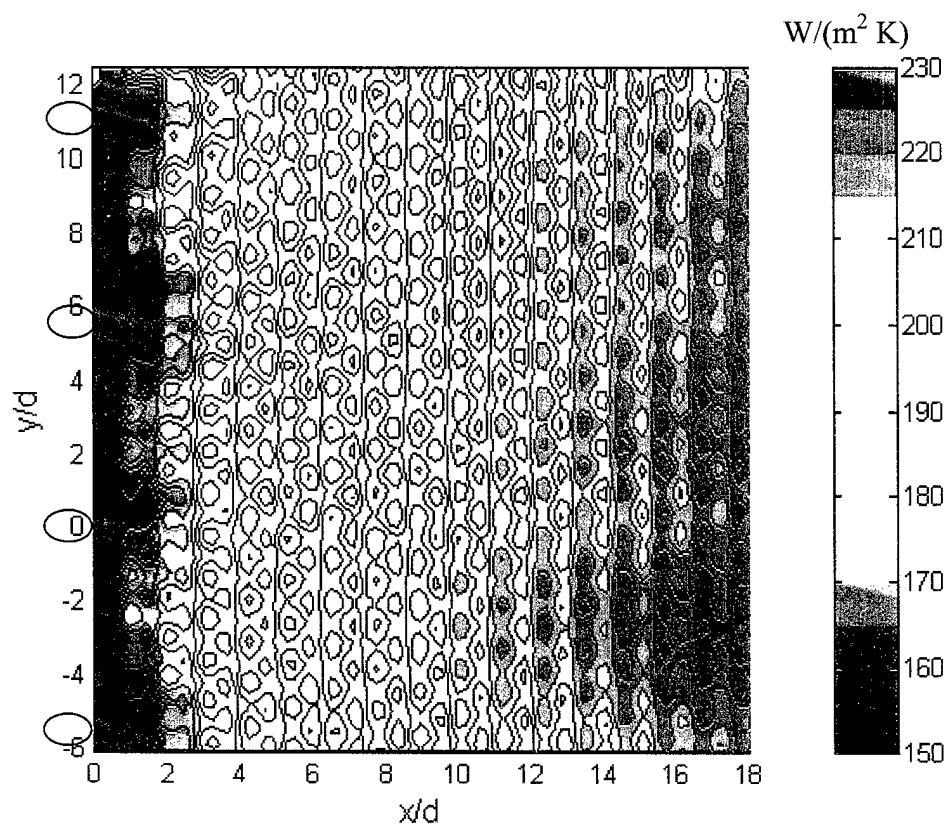


Figure 3.73: Heat transfer coefficient distribution,  $M = 0.85$ . All rough, showerhead off, low turbulence.

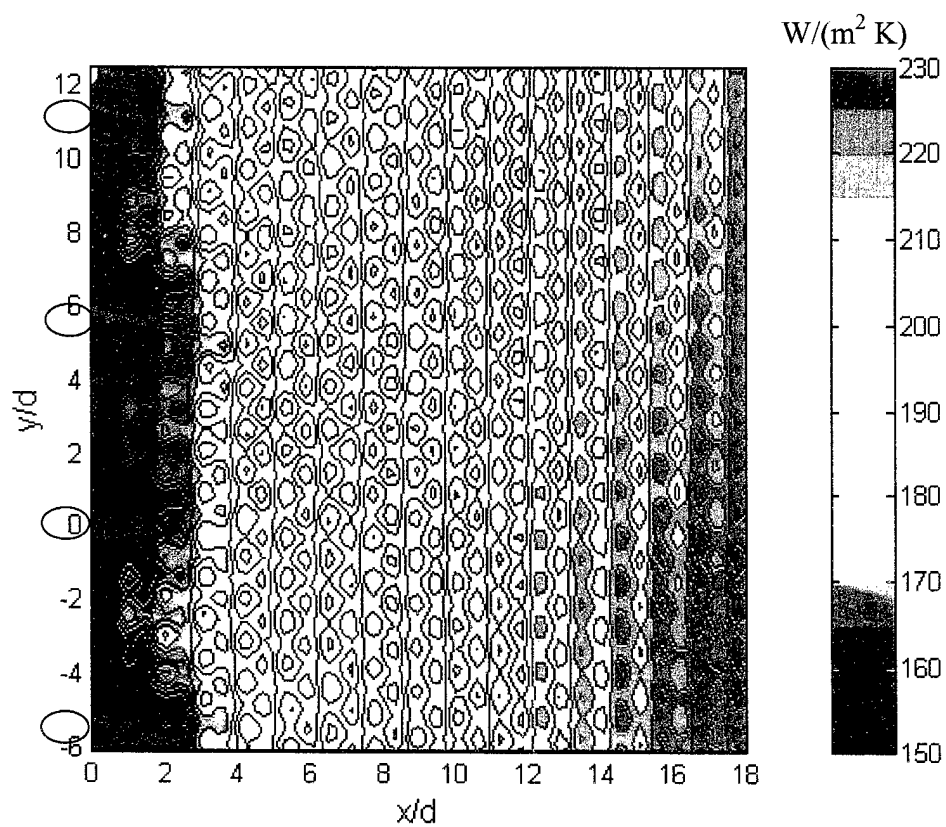


Figure 3.74: Heat transfer coefficient distribution,  $M = 0.7$ . All rough, showerhead on, high turbulence.

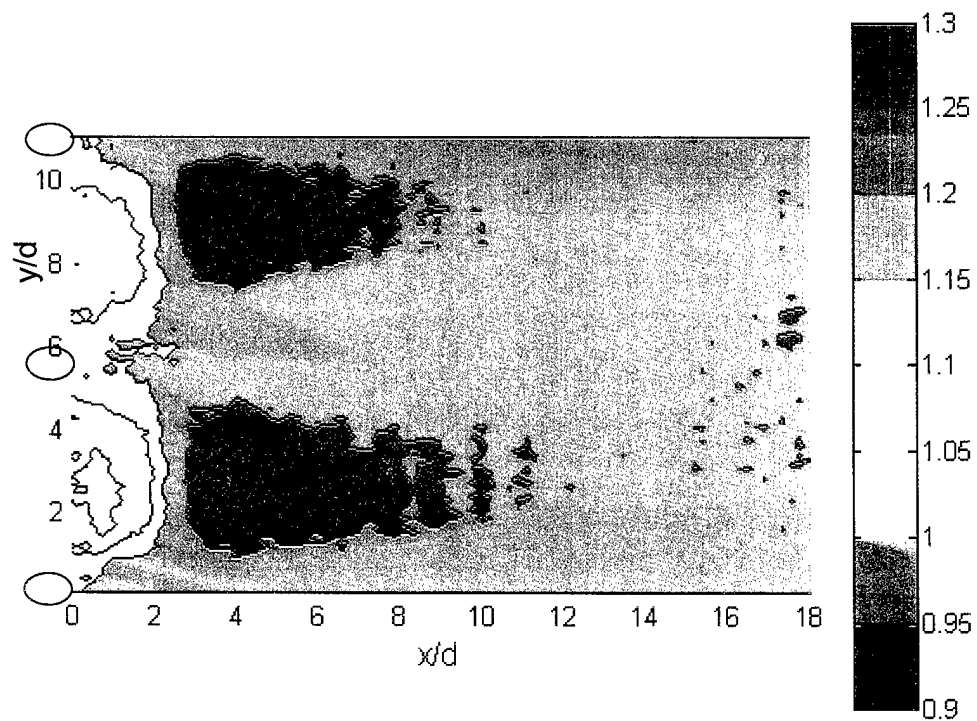


Figure 3.75: Heat transfer coefficient augmentation due to upstream roughness ( $h_{up\ rough}/h_{up\ smooth}$ ).  $M = 0.7$ , showerhead on, high turbulence, downstream rough.

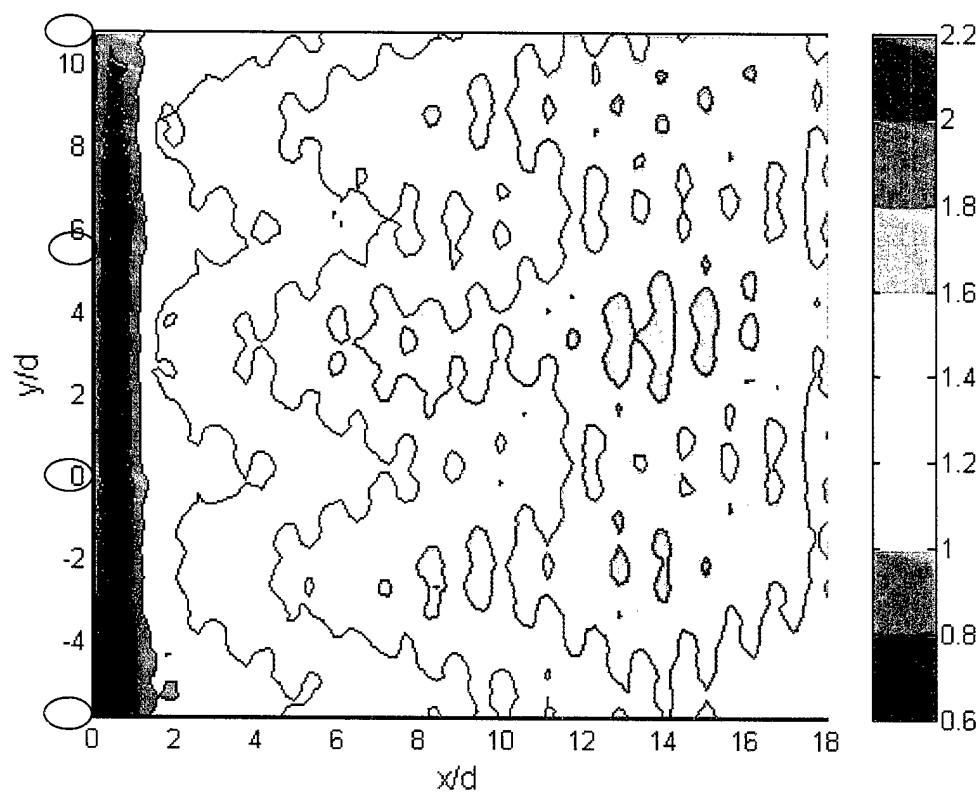


Figure 3.76: Heat transfer coefficient augmentation due to upstream and downstream roughness ( $h_{rough}/h_{smooth}$ ).  $M = 0.7$ , showerhead on, high turbulence.

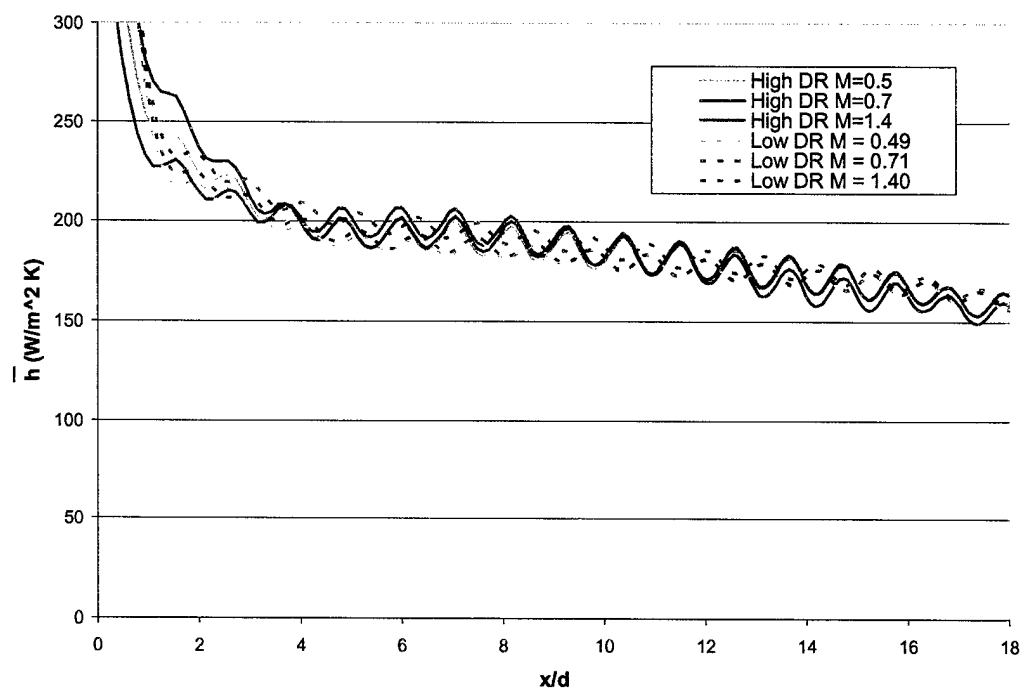


Figure 3.77: Spanwise averaged heat transfer coefficients at  $DR = 1.6$  and  $DR = 1.0$ . All rough, showerhead off, low turbulence.

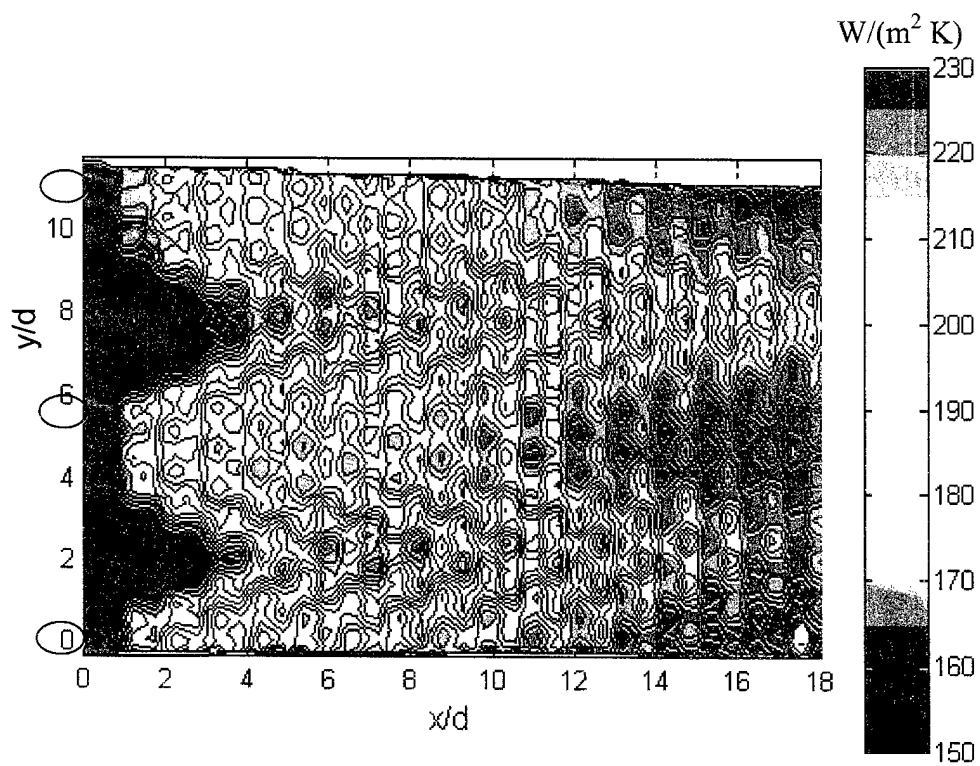


Figure 3.78: Heat transfer coefficient distribution,  $M = 0.3$ . All rough, showerhead off, low turbulence,  $DR = 1.6$ .



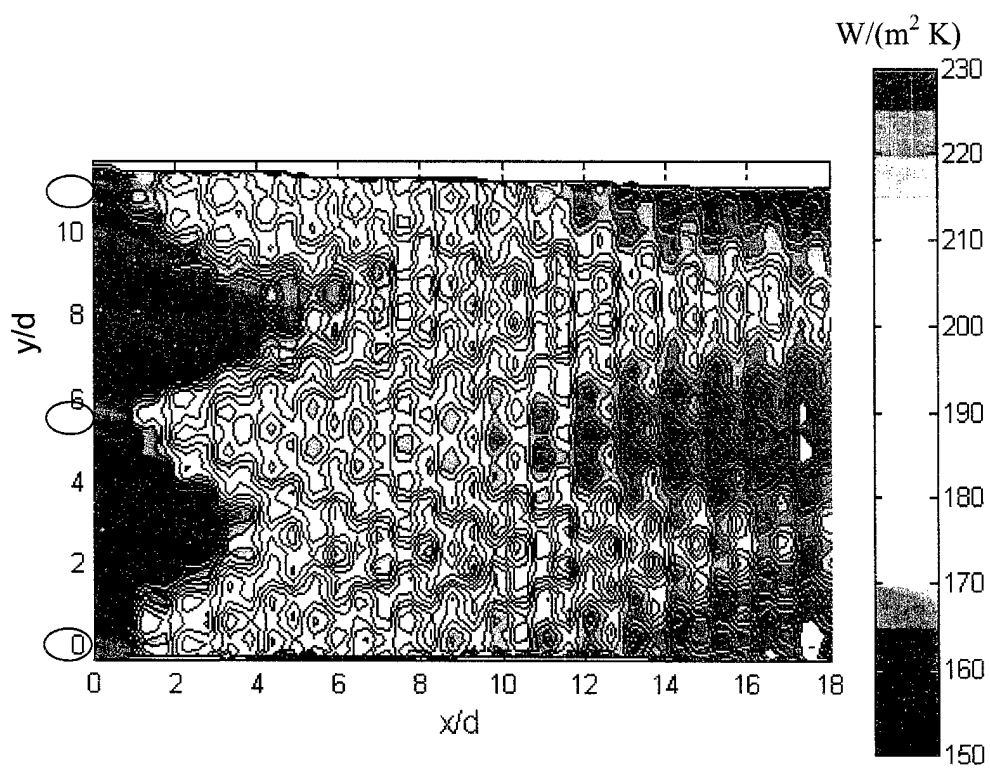


Figure 3.79: Heat transfer coefficient distribution,  $M = 0.7$ . All rough, showerhead off, low turbulence,  $DR = 1.6$ .

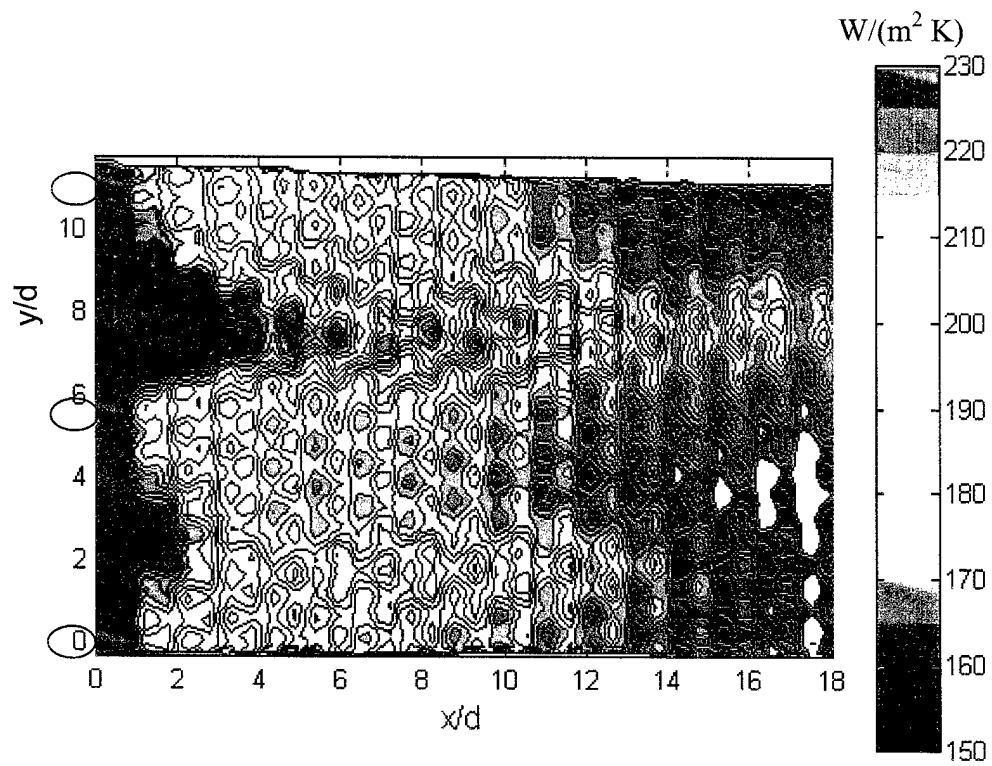


Figure 3.80: Heat transfer coefficient distribution,  $M = 0.85$ . All rough, showerhead off, low turbulence,  $DR = 1.6$ .

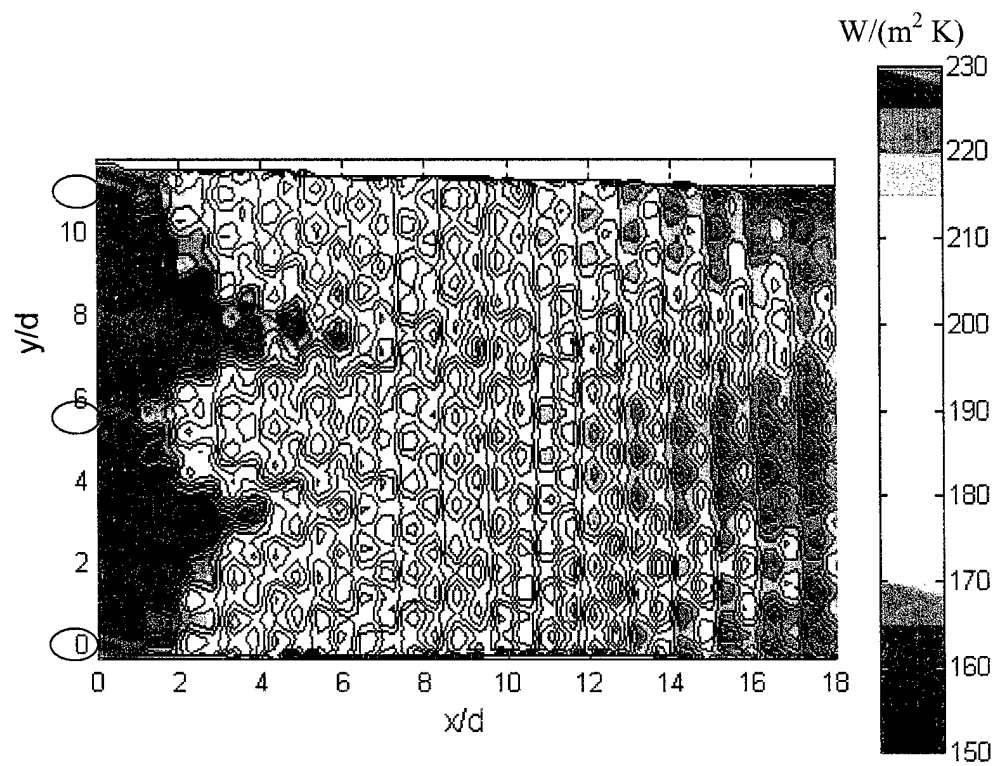


Figure 3.81: Heat transfer coefficient distribution,  $M = 1.0$ . All rough, showerhead off, low turbulence,  $DR = 1.6$ .

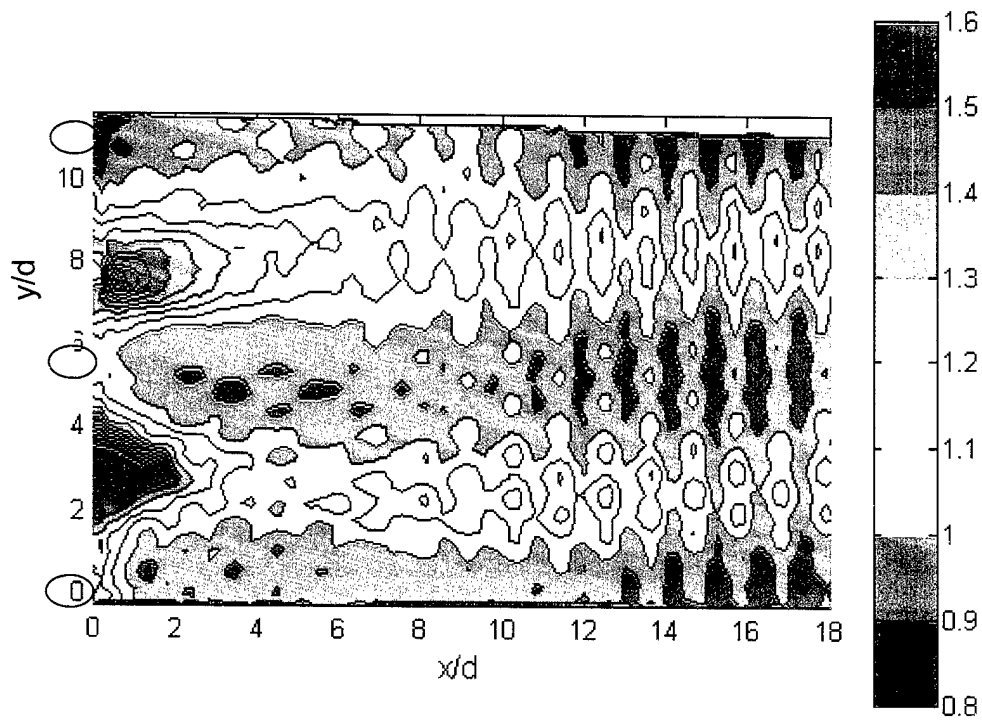


Figure 3.82: Heat transfer coefficient augmentation due to high density ratio ( $h_{high\ DR}/h_{low\ DR}$ ).  $M = 0.7$ , showerhead on, low turbulence.

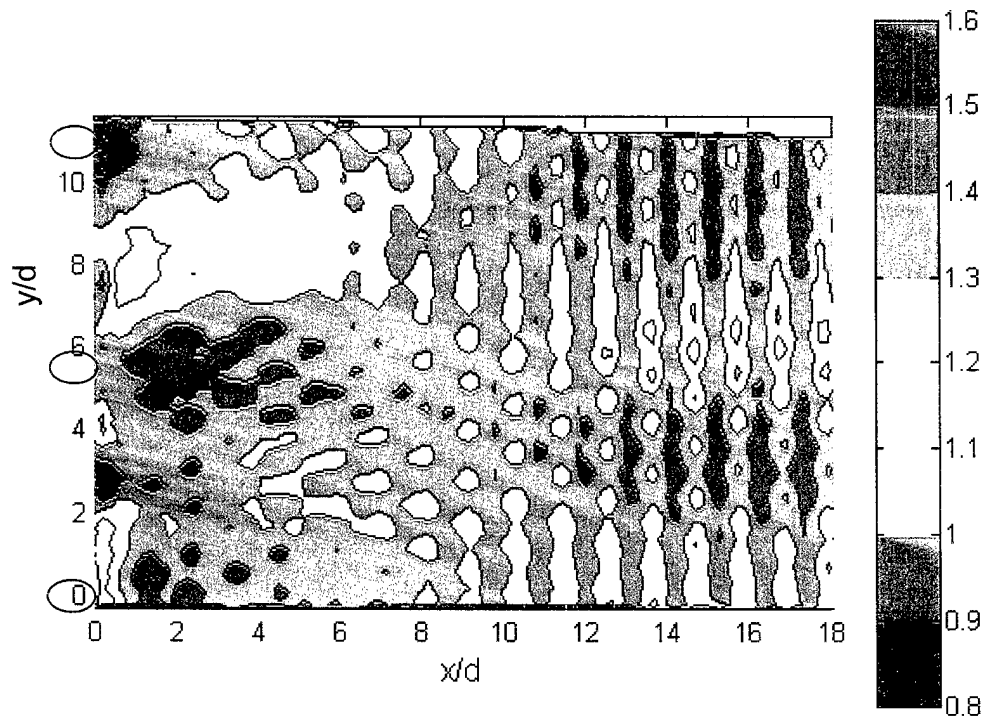


Figure 3.83: Heat transfer coefficient augmentation due to high density ratio ( $h_{high\ DR}/h_{low\ DR}$ ).  $M = 1.4$ , showerhead on, low turbulence.

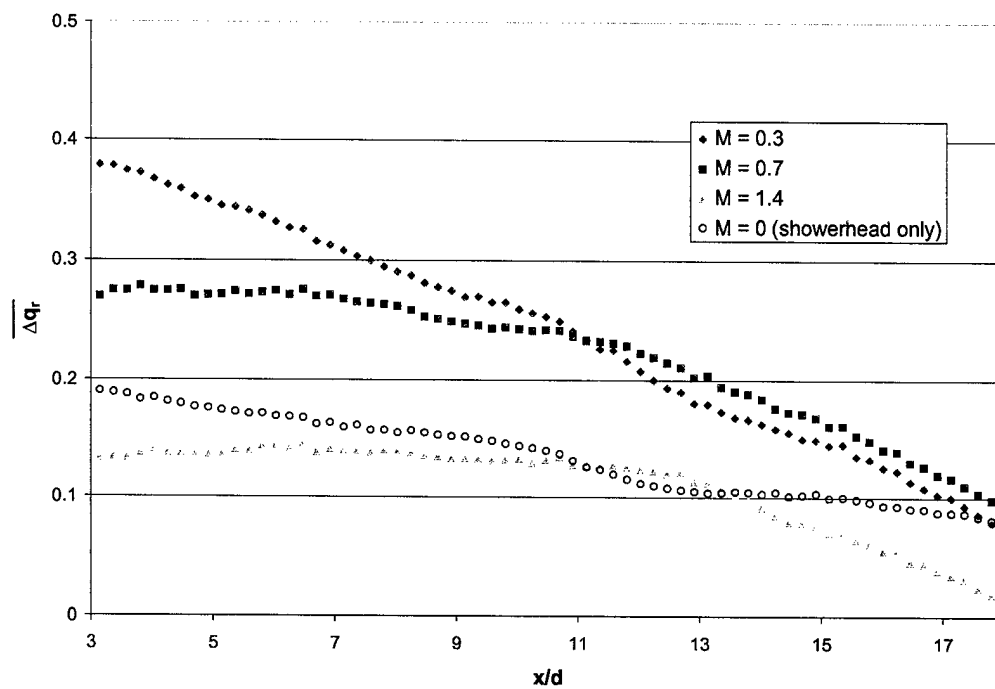


Figure 3.84: Net heat flux reduction due to adding suction side and showerhead blowing. All smooth, high turbulence, showerhead on for cases with suction side cooling.

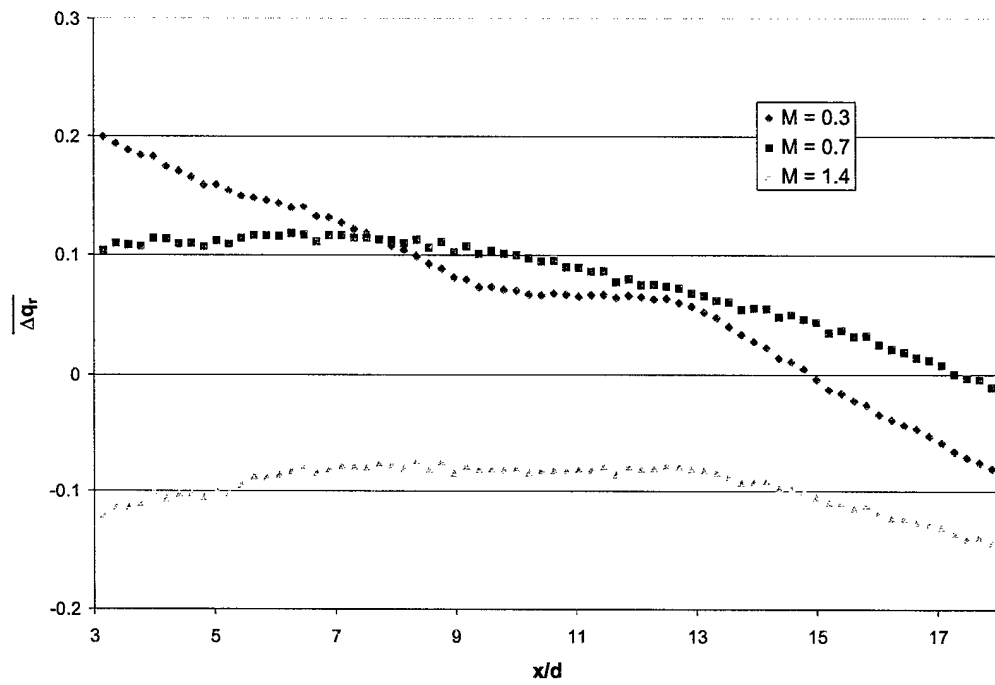


Figure 3.85: Net heat flux reduction due to adding suction side blowing no showerhead blowing. All smooth, high turbulence, showerhead off.

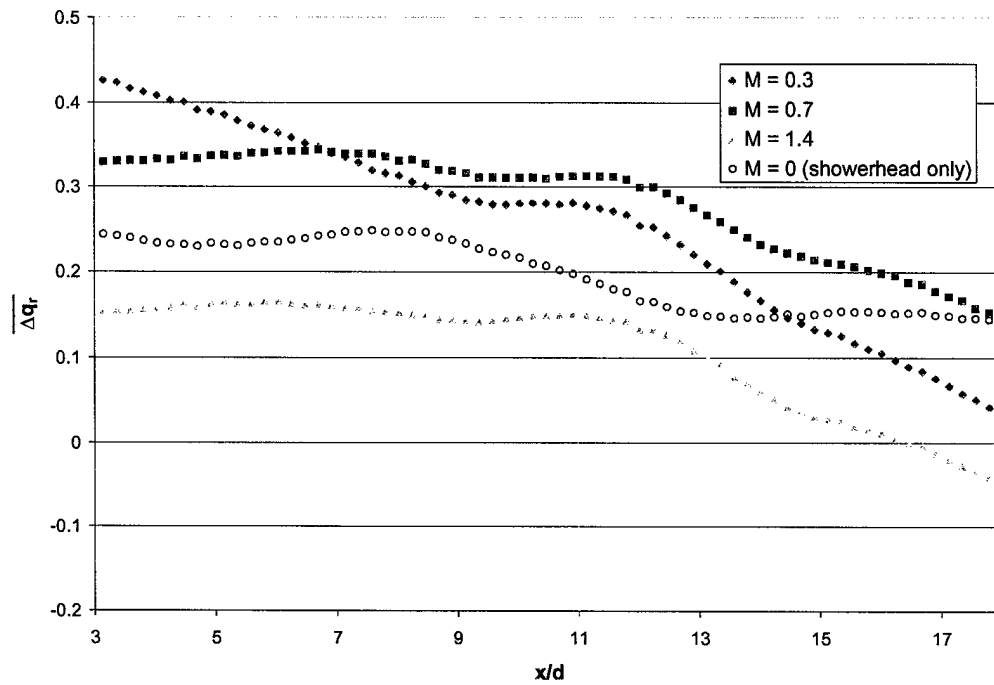


Figure 3.86: Net heat flux reduction due to adding suction side and showerhead blowing. All smooth, low turbulence, showerhead on for cases with suction side cooling.



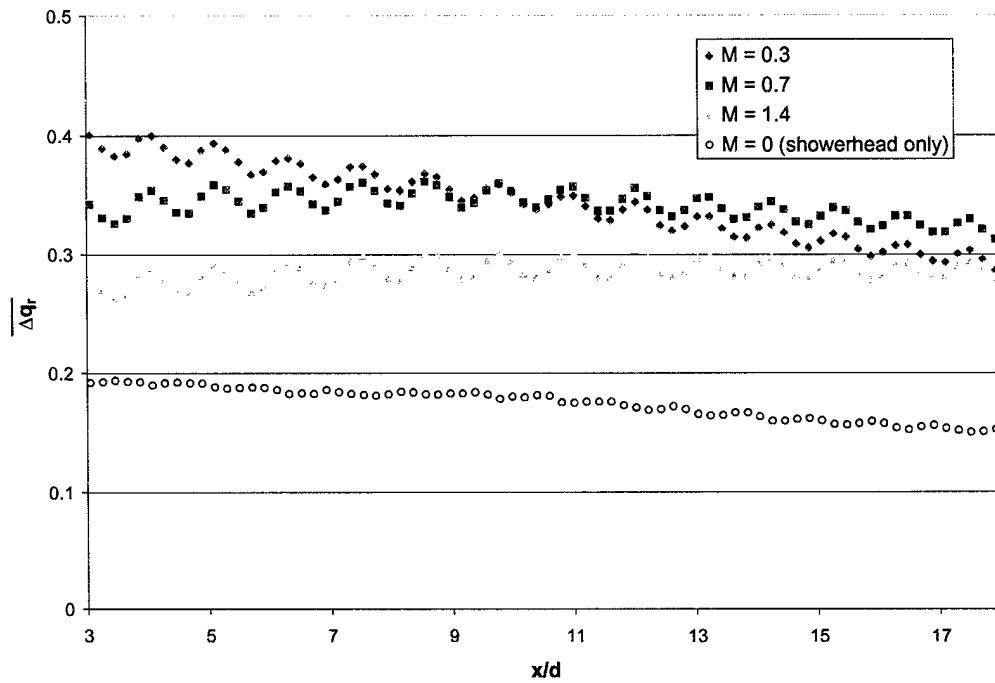


Figure 3.87: Net heat flux reduction due to adding suction side and showerhead blowing. All rough, high turbulence, showerhead on for cases with suction side cooling.

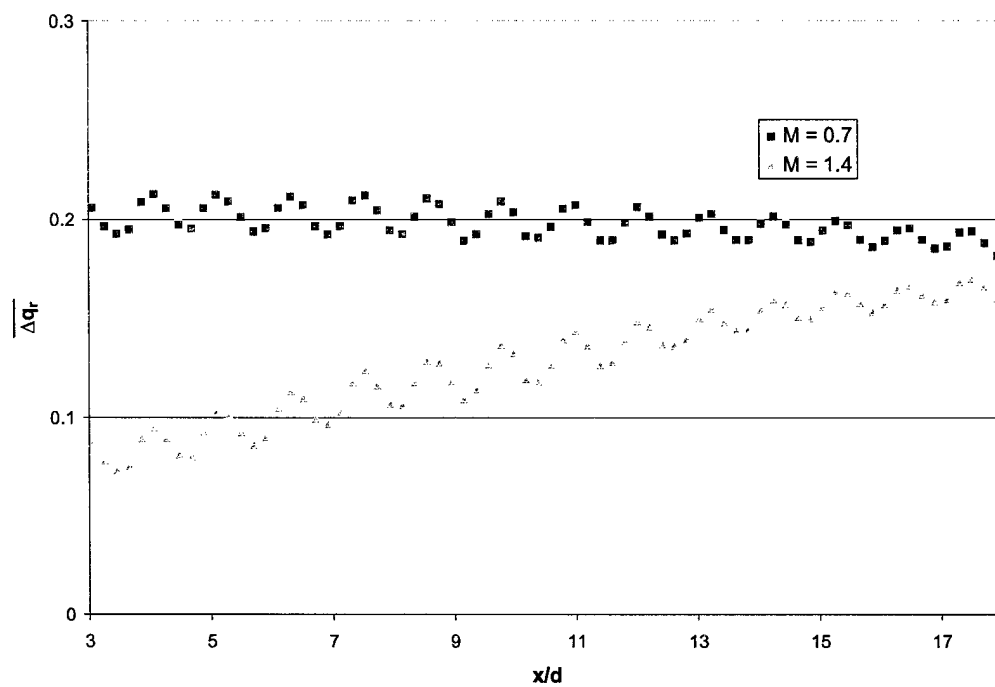


Figure 3.88: Net heat flux reduction due to adding suction side blowing. All rough, high turbulence.

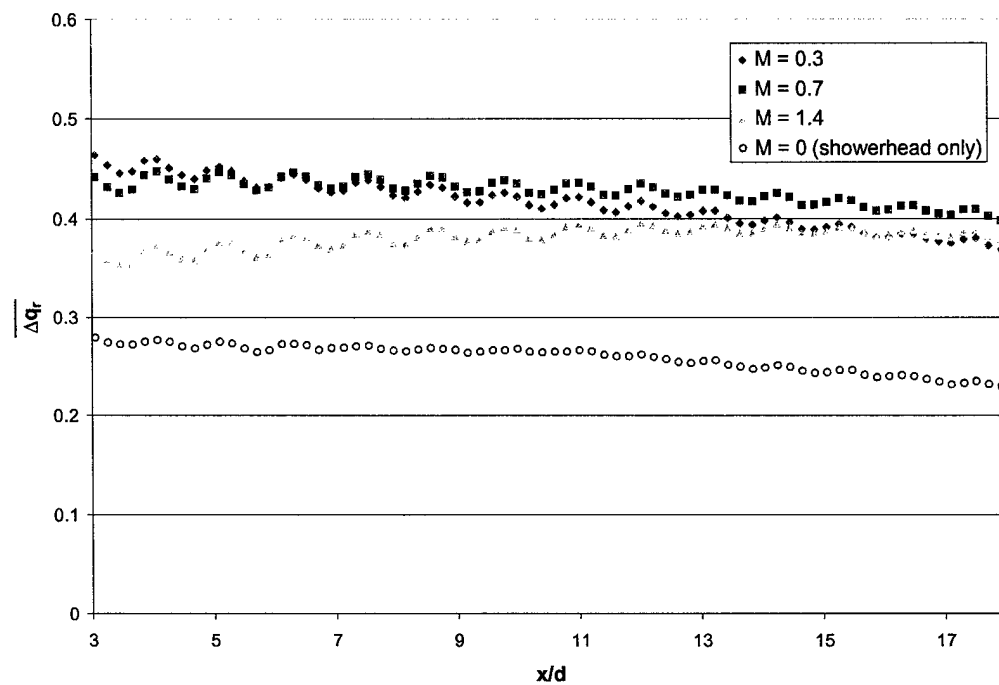


Figure 3.89: Net heat flux reduction due to adding suction side and showerhead blowing. All rough, low turbulence, showerhead on for cases with suction side cooling.

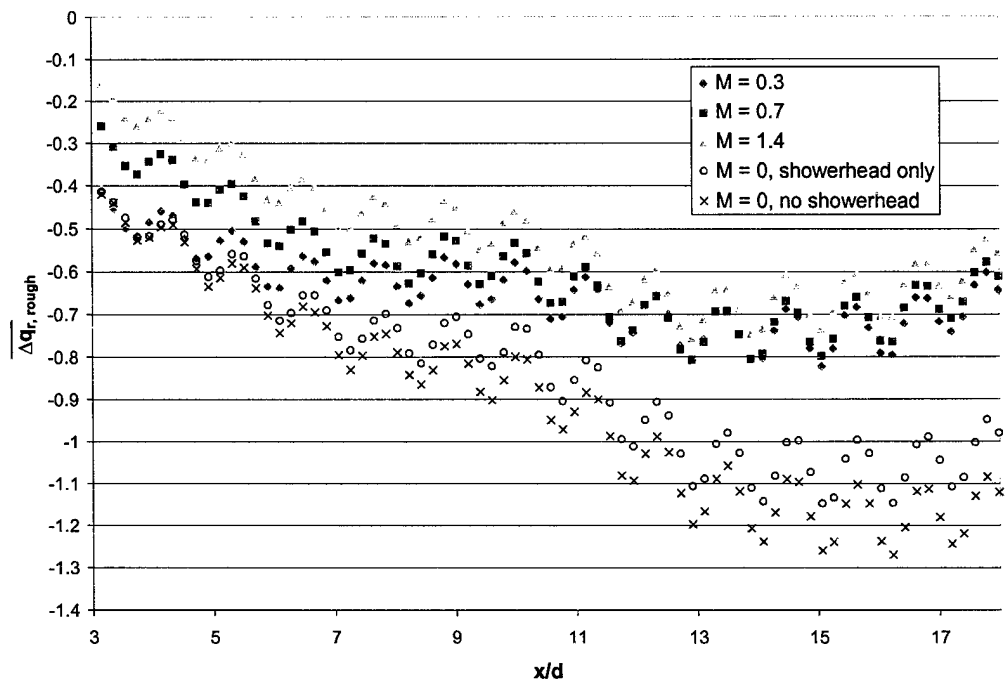


Figure 3.90: Net heat flux reduction due to adding upstream and downstream roughness. High turbulence, showerhead on for cases with suction side cooling.

## CHAPTER FOUR

### CONCLUSIONS

This chapter presents the major conclusions of the present study as well as ideas of possible future studies that would complement this one.

#### 4.1 SUMMARY OF RESULTS

Heat transfer coefficient measurements were made downstream of the first row of coolant holes on the suction side of a nozzle guide vane. The significant results show how film cooling and surface roughness influence the heat transfer coefficient in the region of interest.

When the suction side surface was smooth, suction side film cooling caused the heat transfer coefficient to elevate from its value for an uncooled surface. Locally, the increase was as high as 30%. The largest augmentations occurred directly downstream of the holes, with smaller augmentations ( $< 15\%$ ) between the holes. Although film cooling was shown to increase  $h$ , it turned out that  $h$  was fairly insensitive to the blowing ratio.

The heat transfer coefficient on the uncooled smooth vane was approximately 6% higher at the high freestream turbulence intensity ( $Tu_{\infty} = 21\%$  at inlet) than the low freestream turbulence intensity ( $Tu_{\infty} = 5.2\%$  at inlet). With film cooling, turbulence caused spanwise dispersion of the jets, elevating the heat transfer coefficient between the jets. However, the high turbulence condition caused a decrease in the heat transfer coefficient along the jet centerlines.

The showerhead caused an increase in  $h$  of 8% at low turbulence, but only toward the downstream end of the heat flux plate. The showerhead caused increased turbulence intensities near the wall, but not as high as the high

freestream turbulence condition caused. Consequently, the showerhead had no perceptible effect on  $h$  under high freestream turbulence conditions.

The addition of roughness upstream of the holes to the otherwise smooth surface caused the heat transfer coefficient to increase by 26% in the near hole region. The upstream roughness caused an increase in the turbulence levels in the boundary layer along with a thickening of the boundary layer. The effects of the roughness were dissipated until the augmentation in  $h$  due to upstream roughness was only 19% at  $x/d = 18$ . The additional turbulence caused by the upstream roughness had a similar effect as the high freestream turbulence condition in that it promoted spanwise dispersion of the coolant.

Downstream roughness caused an increase in  $h$  of nearly 150% for an uncooled surface at low freestream turbulence. With film cooling, local increases in  $h$  due to roughness reached 100%. In an unusual twist from the smooth wall data, film cooling was found to cause local decreases in the heat transfer coefficient downstream of the jets. These local depressions in  $h$  were accompanied by elevated  $h$  between the jets, thus the spanwise averaged heat transfer coefficients were virtually unaffected by the coolant. The decrease in  $h$  downstream of the holes was hypothesized to be caused a reduction in the local roughness Reynolds number due to the velocity deficit caused by the jet. Because the velocity is decreased by the jet downstream of the hole, mass may be conserved by having higher velocities between the holes. Higher velocity in these regions possibly resulted in a higher roughness Reynolds number. The increase in  $h$  between the film cooling jets is particularly unfortunate, as those locations receive little or no film cooling.

With downstream roughness present, the addition of upstream roughness caused a 5% to 10% decrease in the heat transfer coefficient. This decrease can be explained by the thicker boundary layer with the upstream roughness and therefore the lower velocity near the rough surface. Upstream roughness

rendered the effects of the jets on  $h$  to be barely discernable, although the heat transfer coefficient was elevated in the regions downstream of the jets.

A high density ratio ( $DR = 1.6$ ) experiment was run with roughness upstream and downstream of the row of coolant holes. At low density ratio, the upstream roughness combined with the downstream roughness resulted in the effects of the jets being nearly indistinguishable on spatial  $h$  plots. However, the high density ratio jets were very distinguishable, decreasing  $h$  along the hole centerline and increasing  $h$  between the holes. The high density ratio test gave  $h$  values between the holes that were approximately 20% higher than the low density ratio tests, but  $h$  values along the centerline that were approximately 10% lower. The regions were balanced such that the end result was that the spanwise averaged values were within about 5%.

Net heat flux reduction calculations were performed using the adiabatic effectiveness data of Robertson (2004). The benefits due to film cooling were found to be higher with surface roughness than without. On a completely smooth surface, the blowing ratio  $M = 0.7$  gave a reduction in heat flux that ranged from over 25% in the near hole region to 10% in the far hole region. When the surface was rough, the net heat flux reduction was fairly uniform at about 35%. However, this does not imply that roughness is beneficial, only that film cooling becomes more valuable with surface roughness present. The transition to surface roughness at a fixed blowing ratio of  $M = 0.7$  caused an increase in heat load of 80% (maximum) at  $x/d \approx 13$ .

## 4.2 RECOMMENDATIONS FOR FUTURE WORK

This section suggests future studies that would complement the present study in advancing understanding of heat transfer on a turbine vane.

#### 4.2.1 The Effect of a Heated Starting Length

The heat transfer experiments of this study involved heat transfer downstream of the first row of coolant holes. This practice was a way of ensuring that only the hydrodynamic effects of film cooling / the presence of film cooling holes would be measured. If there were a heat flux plate upstream of the film cooling holes, the coolant would displace the already finite thermal boundary layer and new boundary layers would be initiated in the regions downstream of the film cooling holes. This experiment would provide valuable data regarding thermal boundary layer effects. However, this hypothetical experiment could be modified to give data that shows the effect of the heated starting length without the thermal boundary layer displacement. One would run the case with upstream and downstream heating and then turn off only the downstream heat flux plate, allowing sufficient time for thermal equilibrium to be achieved. Data taken at this point would yield the adiabatic wall temperature distribution downstream of the holes with upstream heating. This adiabatic wall temperature distribution will take into account the thermal effects of the jets, much in the same way the high density ratio heat transfer test of this study was performed. A test such as the one I described would yield important information about film cooling heat transfer such as whether kidney vortices cause significant mixing between the thermal boundary layer and the mainstream in the upstream region of the downstream heat flux plate, where my thermal boundary layer may have been too small to see such a phenomenon.

There is another benefit of a heated starting length. A flaw with the heat transfer experiments of the present study are the two-dimensional conduction effects at the upstream and downstream edge of the heat flux plate. Accurate accounting of the two-dimensional conduction effects proved to be prohibitively difficult. As a result, the heat transfer data was reliable only in the range  $3 < x/d < 18$ . A heated starting length could rid the situation of two-dimensional



conduction at the upstream edge, giving reliable data very near the coolant holes.

#### **4.2.2 High Density Ratio Effects on a Smooth Surface**

Only one high density ratio heat transfer test was performed in this study. Due to problems caused by surface wrinkles at low temperatures, the test was limited to a rough surface condition. The more fundamental condition of a smooth surface was not studied. Improvements in the heat flux plate material and / or the attachment method may allow high density ratio tests to be conducted on a smooth surface. Alternatively, a foreign gas injectant with a density greater than that of air could be used at the mainstream temperature.

#### **4.2.3 Different Roughness Characteristics**

The roughness used in this study was a uniform array of protruding cones. This type of roughness may best be representative of foreign material deposition. Additional types of roughness that simulate thermal barrier coating spallation, pitting, and erosion might be valuable for the turbine design community. Furthermore, real turbine roughness is nonuniform. Erosion furrows downstream of the coolant holes might be particularly interesting features to study.

#### **4.2.4 Heat Transfer Downstream of the Second Row of Coolant Holes**

The present study considered the heat transfer between the first and second row of suction side film cooling holes on the suction side of the vane. The heat transfer coefficients were found to vary little with  $x$  at the downstream end of the heat flux plate where  $x/d = 18$ . It would be interesting to see how this trend in  $h$  continues downstream  $x/d = 18$  and how the second row of coolant holes influences the heat transfer coefficient. The second row has compound

angle coolant holes, thus their influence on  $h$  may be somewhat different from the influence of the first row.

## APPENDIX A

### ROUGHNESS REYNOLDS NUMBER

This appendix describes the techniques used to determine the roughness Reynolds number. The roughness Reynolds number can be written:

$$Re_k = \frac{u_e k_s}{\nu} \left( \frac{c_f}{2} \right)^{1/2} \quad (\text{A.1})$$

The only term that was somewhat difficult to obtain was the skin friction coefficient. The skin friction coefficient can be estimated through the use of standard correlations (from White (1991), Schlichting (1979) or Mills(1999)). Unfortunately these three correlations were developed for flat plates and require a distance from the leading edge. For the purposes of this study, this distance was estimated to be the surface distance from the stagnation point.

Alternatively, the skin friction can be determined by experimentally measuring either the momentum thickness or the boundary layer thickness and using a correlation developed in Kays and Crawford (1993). A benefit of the Kays and Crawford technique is that it does not rely on a distance from the leading edge of the plate. Unfortunately, the technique of Kays and Crawford assumed a zero pressure gradient wake strength of 2.3. In a favorable pressure gradient, the wake strength is less than 2.3. The procedure of determining the momentum thickness was performed using hot wire anemometry as discussed in Section 2.7. Another technique of Kays and Crawford was a correlation between the Stanton number and the skin friction coefficient on rough surfaces.

A lower bound on the roughness Reynolds number was determined by using the smooth wall skin friction coefficient of Radomsky and Thole (2002),

but also using the equivalent sand grain roughness of the rough surface. Since the smooth wall skin friction coefficient must be lower than the rough wall skin friction coefficient, the roughness Reynolds number determined in this fashion must be a lower bound.

Table A.1 Different Approximations for the Roughness Reynolds Number

Correlation	Description	$Re_k$
White (1991)	Flat plate assumption	51.6
Schlichting (1979)	Flat plate assumption	49.5
Mills (1999)	Flat plate assumption	45.3
Kays and Crawford (1993)	Based on momentum thickness (wake strength = 2.3)	52.5
Kays and Crawford (1993)	Based on boundary layer thickness (wake strength = 2.3)	53.8
Kays and Crawford (1993)	Based on boundary layer thickness (limiting case of wake strength = 0)	64.6
Kays and Crawford (1993)	Based on Stanton numbers of rough and smooth surfaces	47.6
Lower bound	Uses skin friction from smooth surface (Radomsky and Thole (2002))	31.7

The lower bound indicates that the roughness Reynolds number is at least 31.7. The various methods for obtaining  $Re_k$  give results that are in good agreement, generally indicating that  $Re_k \approx 50$ .

## **APPENDIX B**

### **BUS BAR SOLDERING**

The material properties of stainless steel can cause a great deal of difficulty in soldering anything to it. A successful soldering technique was developed in order to attach the copper bus bars to the stainless steel heat flux plate. This appendix describes the procedure.

The first step is to fabricate the bus bars. The bus bars are originally stripped 10 gauge wire. The portion of the wire to be soldered to the heat flux plate is pounded flat using a hammer and an anvil. The bus bar is then cleaned to ensure good electrical contact. A bus bar soldered to a heat flux cannot be bent appreciably without inducing serious wrinkles in the heat flux plate. Therefore, it is imperative that the bus bars are formed to the appropriate shape prior to soldering.

The soldering procedure requires a hot plate to provide the necessary heat. Because soldering is performed on a curved surface, a curved hot plate is needed. The area of interest on the suction side of the vane has a radius of curvature of approximately 11 cm. A thick walled pipe with outer radius 11 cm was obtained and cut such that a flat surface is available to place on a hot plate. The flat surface allows heat to conduct from the hot plate into the pipe piece and the curved surface is used as the soldering surface.

A piece of silver bearing solder the length of the contact area is cut from a roll of solder. Like the bus bar, it is pounded flat cleaned, and formed to the appropriate shape. Radio Shack model 64-021A rosin soldering paste flux is applied to both sides of the solder. Other types of flux were tested, but only the Radio Shack flux produces satisfactory results. The fluxed solder is sandwiched between the bus bar and the heat flux plate. The flux should hold the solder to the bus bar, but probably not the heat flux plate because the thin heat flux plate

will not hold the proper curvature. The rig is then set down on the curved hot plate while pushing down on the bus bar. As soon as the solder melts, water is sprayed at the bus bar to quench it. Some parts of the solder may melt before others. In general it is okay to quench one area while waiting for another area to melt. If it is not quenched fast enough, the solder can flow away from where it is needed.

Once both bus bars are attached, the heat flux plate must be cleaned. The rosin flux may be easily removed with acetone. Because the round ends of the bus bars will be connected to the power supply, electrical connectors should be soldered at the ends of the bus bars using conventional soldering techniques (i.e. with a soldering iron).

## **APPENDIX C**

### **HEAT TRANSFER TEST PROCEDURE**

The following is the checklist that was completed prior to any data acquisition on each day a heat transfer test was run.

1. Expose holes on top of tunnel.
2. Hook up a nitrogen tank, ensure other switching valve is closed.
3. Seal hatch; ensure all screws are screwed in.
4. Tape hatch including non-hatch suction side holes.
5. Tape over all holes not to be used in experiment (suction side, pressure side, and showerhead).
6. Turn on blower and do hole count- ensure Labview hole settings are correct.
7. Install trip rod if showerhead is not to be used.
8. Install heater power wires.
9. Install IR window.
10. Turn on 2<sup>nd</sup> computer monitor
11. Ensure thermocouples, pressure transducers, and voltage leads are properly hooked up.
12. Ensure IR Memory card is empty.
13. Ensure Tripod feet are level.
14. Ensure Camera is level.
15. With a hot stick ensure IR camera is in correct location.
16. Focus IR camera with hot stick
17. Rigidly fix IR camera.
18. Ensure focus and field of view are still good.
19. Install Black Box
20. Initial X/D measurements, hole locations, and top and bottom bounds.
21. Ensure all windows/ports are secure
22. Ensure all tape is still smooth and attached.
23. Turn tunnel water on.
24. Turn on secondary loop.
25. Turn on tunnel
26. run test
27. Final X/D and hole locations
28. calibration
29. Turn off everything (tunnel, tunnel water, heaters, nitrogen, pressure transducer boxes, secondary loop)

## REFERENCES

- Abuaf, N., Bunker, R.S., Lee, C.P., 1998, "Effects of Surface Roughness on Heat Transfer and Aerodynamic Performance of Turbine Airfoils," *Journal of Turbomachinery*, Vol. 120, pp. 522-529.
- Ames, F. E., 1997, "The Influence of Large-Scale High-Intensity Turbulence on Vane Heat Transfer," *Journal of Turbomachinery*, Vol. 199, pp. 23-30.
- Ammari, H. D., Hay, N., Lampard, D., 1990, "The Effect of Density Ratio on the Heat Transfer Coefficient from a Film Cooled Flat Plate," *Journal of Turbomachinery*, Vol 112, pp. 444-450
- Blair, M. F., 1994, "An Experimental Study of Heat Transfer in a Large-Scale Turbine Rotor Passage," *Journal of Turbomachinery*, Vol. 116, pp. 1-12.
- Bogard, D. G., Schmidt, D. L., Tabbita, M., 1998, "Characterization and Laboratory Simulation of Turbine Airfoil Surface Roughness and Associated Heat Transfer," *Journal of Turbomachinery*, Vol. 120, pp. 337-342.
- Bogard, D. G., Snook, D., Kohli, A., 2003, "Rough Surface Effects on Film Cooling of the Suction Side Surface of a Turbine Vane," ASME Paper No. EMECE2003-42061.
- Bons, J. P., Taylor, R. P., McClain, S. T., Rivir, R. B., 2001, "The Many Faces of Turbine Surface Roughness," ASME Paper No. 2001-GT-0163.
- Bons, J. P., 2002, "St and  $c_f$  Augmentation for Real Turbine Roughness with Elevated Freestream Turbulence," ASME Paper No. GT-2002-30198.
- Boyle, R. J., Spuckler, C. M., Lucci, B. L., Camperchioli, W. P., 2001, "Infrared Low-Temperature Turbine Vane Rough Surface Heat Transfer Measurements," *Journal of Turbomachinery*, Vol. 123, pp. 168-177.
- Cutbirth, J. M., 2000, "Turbulence and Three-Dimensional Effects on a Fully Film Cooled Turbine Vane," Ph.D. Dissertation, The University of Texas at Austin.



- Cutbirth, J. M., Bogard, D. G., 2002, "Thermal Field and Flow Visualization Within the Stagnation Region of a Film-Cooled Turbine Vane," *Journal of Turbomachinery*, Vol. 124, pp. 200-206.
- Ethridge, M. I., Cutbirth, J. M., Bogard, D. G., 2001, "Scaling of Performance for Varying Density Ratio Coolants on an Airfoil With Strong Curvature and Pressure Gradient Effects," *Journal of Turbomachinery*, Vol. 123, pp 231-237.
- Goldstein, R. J., 1983, "Velocity and Turbulence Measurements in Combustion Systems," *Experiments in Fluids*, Vol. 1, pp. 93-99.
- Guo, S. M., Lai, C. C., Jones, T. V., Oldfield, M. L. G., Lock, G. D., Rawlinson, A. J., 1998, "The Application of Thin-Film Technology to Measure Turbine-Vane Heat Transfer and Effectiveness in a Film-Cooled, Engine-Simulated Environment," *International Journal of Heat and Fluid Flow*, Vol. 19, pp. 594-600.
- Guo, S. M., Lai, C. C., Jones, T. V., Oldfield, M. L. G., Lock, G. D., Rawlinson, A. J., 2000, "Influence of Surface Roughness on Heat Transfer and Effectiveness for a Fully Film Cooled Nozzle Guide Vane Measured by Wide Band Liquid Crystals and Direct Heat Flux Gages," *Journal of Turbomachinery*, Vol. 122, pp. 709-716.
- Han, J. C., Dutta, S., and Ekkad, S. V., 2000, *Gas Turbine Heat Transfer and Cooling Technology*, Taylor & Francis.
- Jenkins, S. C., Varadarajan, K., and Bogard, D.G., 2004, "The Effects of High Mainstream Turbulence and Turbine Vane Film Cooling on the Dispersion of a Simulated Hot Streak," *Journal of Turbomachinery*, Vol. 126, pp. 203-211.
- Kays, W. M., and Crawford, M. E., 1993, *Convective Heat and Mass Transfer*, 3<sup>rd</sup> ed., McGraw-Hill, New York.
- Kline, S. J., and McClintock, F. A., 1953, "Describing Uncertainties in Single Sample Experiments," *Mechanical Engineering* Vol. 75.
- Kuotmos, P. and McGuirk, J. J., 1989, "Isothermal Flow in a Gas Turbine Combustor- A Benchmark Experimental Study," *Experiments in Fluids*, Vol. 7, pp. 344-354.

- Mattingly, J. D., 1996, *Elements of Gas Turbine Propulsion*, McGraw-Hill.
- Mills, A. F., 1999, *Heat Transfer*, Second Edition, Prentice Hall, New Jersey.
- Nikuradse, J., 1933, *Forsch. Arb. Ing.-Wes.*, Nr. 361.
- Pietrzyk, J. R., Bogard, D. G., Crawford, M. E., 1989, "Hydrodynamic Measurements of Jets in Crossflow for Gas Turbine Film Cooling Applications," *Journal of Turbomachinery*, Vol. 111, pp. 139-145.
- Polanka, M., 1999, "Detailed Film Cooling Effectiveness and Three Component Velocity Field Measurements on a First Stage Turbine Vane Subject to High Freestream Turbulence", Ph.D. Dissertation, The University of Texas at Austin.
- Radomsky, R. W., 2000, "High Freestream Turbulence Studies on a Scaled-Up Stator Vane," Ph.D. Dissertation, The University of Wisconsin – Madison.
- Radomsky, R. W. and Thole, K. A., 2002, "Detailed Boundary Layer Measurements on a Turbine Stator Vane at Elevated Freestream Turbulence Levels," *Journal of Turbomachinery*, Vol. 124, pp. 107-118.
- Robertson, D. R., 2004, "Roughness Impact on Turbine Vane Suction Side Film Cooling Effectiveness," Masters Thesis, The University of Texas at Austin.
- Schlichting, H., 1936, *Ing.-Arch.*, Vol. 7, pp. 1-34.
- Schmidt, D. L., Bogard, D. G., 1996, "Effects of Free-Stream Turbulence and Surface Roughness on Film Cooling," ASME Paper No. 96-GT-462.
- Schmidt, D. L., Sen, B., Bogard, D. G., 1996, "Effects of Surface Roughness on Film Cooling," ASME Paper No. 96-GT-299.
- Sen, B., Schmidt, D. L., Bogard, D. G., 1996, "Film Cooling With Compound Angle Holes: Heat Transfer," *Journal of Turbomachinery*, Vol 118, pp. 800-806.

- Sigal, A., and Danberg, J. E., 1990, "New Correlation of Roughness Density Effect on the Turbulent Boundary Layer," *AIAA Journal*, Vol. 28, No. 3, pp. 554-556.
- Snook, D. S., 2002, "Effects of Surface Roughness on Suction Side Film Cooling Effectiveness of a Gas Turbine Vane," Masters Thesis, The University of Texas at Austin.
- Taylor, R. P., Taylor, J. K., Hosni, M. H., Coleman, H., W., 1991, "Heat Transfer in the Turbulent Boundary Layer with a Step Change in Surface Roughness," ASME Paper No. 91-GT-266.
- Teekaram, A. J. H., Forth, C. J. P., Jones, T. V., 1988, "The Use of Foreign Gas to Simulate the Effects of Density Ratios in Film Cooling," ASME Paper No. 88-GT-37.
- Whitaker, S., 1972, "Forced convection heat transfer correlations for flow in pipes, past flat plates, single cylinders, single spheres, and for flow in packed beds and tube bundles," *AIChE Journal*, 18, pp. 361-371.
- White, F. M., 1991, *Viscous Fluid Flow*, Second Edition, McGraw-Hill, New York, NY.
- Zimmerman, D. R., 1979, "Laser Anemometer Measurements at the Exit of a T63-C20 Combustor," National Aeronautics and Space Administration, NASA Lewis Research Center, Contract NAS 3-21267.